UV Induced Processes in Biomolecules, Hydrated Clusters and Stark Deflected Beams

Thesis

A THESIS SUBMITTED FOR THE DEGREE OF
DOCTOR OF PHILOSOPHY

RAHUL KUMAR PANDEY (BSc, MSc, MTech)

UV Induced Processes in Biomolecules, Hydrated Clusters and Stark Deflected Beams

---

THE OPEN UNIVERSITY

DEPARTMENT OF PHYSICAL SCIENCES

MILTON KEYNES (UNITED KINGDOM)

June 2017

Supervisors:

Dr Samuel Eden
Dr Jimena Gorfinkiel

The Open University
Department of Physical Sciences

Abstract

The nanoscale processes by which UV irradiation initiates damage in biological material have not yet been fully elucidated. This represents a barrier to innovations in radiotherapy and also limits our understanding of the molecular origins of life. Experiments on gas-phase biological building blocks can reveal detailed information via comparisons with high-level calculations, while parallel studies of biomolecular clusters offer a route to assess the effects of condensed biological environments. This thesis investigates the stabilities and relaxation pathways of isolated and clustered nucleobases in neutral electronic excited states and ionic states. Furthermore, it presents a new *laser thermal desorption* facility and reports advances in applying *Stark deflection* to narrow the range of molecular and cluster configurations in continuous supersonic beams.

The key analytical tool in this thesis is UV *multi-photon ionization time-of-flight mass spectrometry* (MPI-TOF). High-resolution measurements on the RNA base uracil and its fully-deuterated analogue provide new evidence supporting a ring-opening process in a neutral electronic excited state. Comparing experiments on uracil in supersonic beams and from the laser thermal desorption source show that the MPI channel that marks this ring-opening process is not sensitive to the vaporization method and aid comparisons with time-resolved experiments at Heriot Watt University.

Exploiting the capabilities of *reflectron* mass spectrometry to study the metastable dissociation of excited ions and cluster ions is a major theme in this thesis. Photon energy thresholds for metastable dissociation from multi-photon ionized uracil and thymine are reported for the first time. We argue that these thresholds can provide a new route to deduce the adiabatic energies of neutral electronic excited states. Further metastable dissociation experiments and detailed comparisons with *ab initio* calculations provide the most detailed study of the stable configurations of thymine-water cluster ions to date.

The variety of different structural configurations of biomolecules and clusters in neutral target beams presents a major challenge in the experimental study of radiation-induced processes. Stark deflection in electric field gradients offers a powerful method to address this challenge and has previously been used to select specific polar species from mixed pulsed supersonic beams. However, the low pulsing frequencies of such beams are unsuitable to study many collision-induced processes. This thesis reports on the development of a system at the Open University that uses Stark deflection to manipulate continuous beams with the ultimate aim of probing electron attachment processes in selected clusters. Controlled deflection of nitromethane is demonstrated in a helium beam with 94% recovery of the deflected molecules. The manipulation of nucleobases using Stark deflection is achieved for the first time, with continuous argon and krypton expansions providing the necessary rotational cooling. Isolated and clustered nucleobases show very different responses to the deflecting fields, providing a method to gain insights into the origins of specific fragment ions in MPI and electron impact ionization experiments.

Acknowledgements

During my PhD, I have had the privilege to work with many scientists, technical and non-technical staff. I also come to meet many generous and friendly people during my PhD. I would like to take this opportunity to acknowledge their effort on this PhD project, as it would not be possible to complete it without them.

First and foremost, I would like to thank my supervisor, Sam Eden for his guidance and support throughout my PhD period, and an introduction to the cutting edge of science. Many thanks go to Sam for giving me the opportunity to attend many conferences, workshops and scientific community meetings, and for introducing me to the members of the scientific communities we participate in. Also, I would like to thank my second supervisor, Jimena Gorfinkiel for very useful discussions during group meetings. Special thanks go to Nigel Mason for all his efforts and diverse contributions during my PhD. I am very grateful to the EPSRC and the Department of Physical Sciences at the Open University for co-funding my PhD studentship.

I would also like to extend my gratitude to Michal Ryszka, I learnt a lot from him as I was new to the field and he has also worked with me on the experiments. I would also like to thank Marcin Dampc for his help with ion trajectory simulations during his stay in The Open University. I am grateful to Bartek Barc for building the compact MPI/EII experiment during his PhD that I was then able to exploit and develop.

I would like to express my special thanks of gratitude to Jean-Christophe Poully, for the invitation to work on experiments at the BESSY-II Synchrotron (Berlin, Germany) and whose visits to The Open University and calculations were always very beneficial for me. I also wish to thank Thomas Schlatholter and his group (University of Groningen, Netherlands) for welcoming me to use his incredible tandem mass spectrometry set-up for synchrotron experiments. I am very grateful to Jochen Küpper for his role in the Stark deflection experiment. Also I would like to acknowledge here Violaine Vizcaino, for interesting and helpful discussions. Paulo Limao-Vieira is acknowledged for his

contributions to journal manuscripts. I am thankful to Dave Townsend for his advice on the design of the OU laser thermal desorption system.

I am very grateful for the technical support at the Open University. My thanks go to Fraser Robertson and Robert Seaton for electronics, Chris Hall and his team (Kevin Dewar and Michael Abbott), and also Martin Percy for patiently making, and then remaking many parts for the experiments. I am also very grateful for the support from laboratory managers, Jill Clarke and later Shabbir Ahmad, and for the help with orders from Beverley Bishop and Rebecca Coster.

I wish to thank Mathieu Lalande, Chris Rizk, Tiago da Fonseca Cunha, Andre Rebelo, Bogumil Zalewski, Sandor Kovacs, Lily Ellis-Gibbings and Janka Bockova: some incredible people I worked with. Special thanks go to Gosia Smialek-Telega for all of her support. I would like to also thank all my friends and colleagues, in particular Rishi Kesh Sinha, Ewelina Szymanska, Safaa Lebjioui, Alex Nominé, Katarzyna Krzyzanowska, Agnieszka Sieradzka, Adetokunbo Ayilaran, Calum Maccormick, Rudy Romain, Panchayat and, last but not least, the OU 6-a-side cricket organizers for making my life in Milton Keynes very enjoyable.

At home, I am very grateful to Dropadi, Premlal, Arti, Rajkumar, Sanjay, Garima, Devna, Demaira and Jyoti for their support throughout my education. Finally, I thank Stuti for all her support and everything else that really matters.

"Dream is not that which you see while sleeping, it is something that does not let you sleep."

A. P. J. Abdul Kalam

Contents

List of Figures

List of Tables

CHAPTER 1

Introduction

This thesis investigates radiation-induced processes in biomolecules and their clusters. Electronic excitation, ionization, and fragmentation pathways of DNA/RNA bases, nitromethane, and 3-aminophenol are studied following exposure to UV light and ionizing electrons. It also reports on the development of a new apparatus to select specific biomolecules and clusters for crossed-beam experiments using *Stark deflection*. The common goal of the work is to contribute to our understanding of the fundamental processes by which electronic excitation and ionization can initiate structural and chemical changes in biological molecules. Despite the applied interest related to radiochemistry and the molecular origins of life, our understanding of the radiation-response of key biomolecular building blocks in the gas phase is far from complete and our knowledge of the effects of intermolecular bonding on these critical processes is even more limited. This chapter introduces the motivations and context for the research in this thesis.

1.1 Radiation induced processes in fundamental biomolecular building blocks

Most of the results presented in this PhD thesis probe the electronic excited state dynamics and the ionic states of isolated biomolecules. In particular, the experiments applied multi-photon ionization (MPI) to investigate UV induced processes in DNA and RNA bases. Radiation interactions with gas phase biomolecular building blocks have attracted considerable interest in order to better understand the fundamental processes that can initiate lesions in key macromolecules [Smialek et al. 2012, Boniol et al. 2012]. Sanche and co-workers' [2000] sub-ionization energy electron irradiation experiments on gas phase DNA bases and on condensed DNA provide a striking example of how studying isolated building blocks can lead to new insights into radiation damage processes on the macromolecular scale. They revealed local maxima in the production of DNA strand breaks at electron energies that approximately matched resonances for dissociative electron attachment (DEA) in gas-phase nucleobases. This provided the strongest evidence to date that the interactions of low-energy *secondary* electrons (the products of local ionization events) with DNA play an important role in its damage by ionizing radiation. More generally, it showed that understanding and, where possible, quantifying the dynamics and reactivity of excited nucleobases is important for building molecular-scale models of DNA damage [Alloni et al. 2010]. DNA damage had previously been understood essentially in terms of reactions with secondary radicals (notably OH), with a smaller contribution from direct interactions with the radiative particles [Von Sonntag 1989, Chatgilialoglu et al. 2001]. Biological radiation damage is discussed further in section 1.3.

Solar radiation at sea level is limited to photons of energy below 4.25 eV (wavelength greater than 292 nm) [Demore et al. 1997], below the range studied in this thesis (5.59-5.64 eV). This upper energy limit rises at higher altitudes. For example, UV radiation at 5.5 eV is not negligible at the cruising altitudes of commercial aircraft (just below 12 km). It should also be noted that the Earth's atmosphere afforded far less UV protection before photosynthesis led to a dramatic increase in oxygen (the thence ozone) levels in the atmosphere around 2.45 billion years ago [Farquhar et al. 2000]. Therefore, the UV stability of key biomolecules can have implications for understanding the molecular origins of life on Earth. Nonetheless, we use 5.59-5.64 eV photons (230-220 nm) in this thesis primarily as a convenient tool to investigate the relaxation of biomolecules after electronic excitation (specifically to the high vibrational levels of the S_2 states of nucleobases). The same states can be accessed in interactions with other types of radiation that are more prevalent at the Earth's surface. In particular they are accessed in collisions with secondary electrons produced by ionizing radiation such as the X-rays, electrons, and ions used in radiotherapy; the X-rays used in hospital diagnostics; and cosmic rays.

UV induced photochemistry has been the subject of extensive studies in recent years and demonstrated that irradiation of ice analogues can lead to the synthesis of biological building blocks including amino acids [Bernstein et al. 2002, Muñoz Caro et al. 2002, Ciesla and Sandford 2012]. In addition to amino acids and sugar-related compounds, nucleobases were recently detected in the Murchison meteorite [Martins et al. 2008]. Compound-specific carbon isotope data of measured uracil and xanthine compounds revealed a non-terrestrial origin for these compounds [Martins et al. 2008]. Consequently, nucleobases delivered to these worlds by cometary dust, meteorites or

interplanetary dust particles [Muñoz Caro et al. 2002] might have played an important role in the origin of life on Earth, Mars, or elsewhere [Martins et al. 2008]. Therefore, it is important to understand the possible mechanisms by which biological building blocks can survive irradiation in space and radiostabilization in the presence of water is expected to contribute. This hypothesis is supported by recent results showing that the organic composition in carbonaceous meteorites is dependent on aqueous alteration processes [Martins et al. 2007, Glavin and Dworkin 2009]. UV-irradiation experiments on key biomolecules in the gas phase, on surfaces, and in hydrated clusters can therefore contribute to understanding their origins on Earth and indeed to predict their possible presence on other planets or moons [Mason et al. 2014].

The present MPI and electron impact ionization (EII) experiments on gas-phase molecules have probed uracil, thymine (and its hydrated clusters, discussed further below), nitromethane, and 3-aminophenol. The latter two molecules were primarily studied here as test cases for Stark deflection instead of due to their applied or fundamental interest. In uracil and thymine, ultrafast (sub-picosecond) relaxation to the vibrationally-hot electronic ground state is the dominant relaxation pathway following electronic excitation in the near UV [Middleton et al. 2009] and this plays a central role in their radio-stability. However, competing relaxation routes can lead to relatively long-lived electronic excited states and / or to significant structural changes such as ring-opening [Nachtigallová et al. 2011]. These relatively long-lived excited states and structural changes can be an important source of radiation damage in DNA and RNA. This thesis probes a dissociative multi-photon ionization channel that has previously been proposed as an indicator of a ring-opening process in neutral electronically-excited uracil [Ryszka 2015, Barc et al. 2013] (see Chapters 4, 6, and 7). To our knowledge,

this extends the only experimental study in the literature that reports evidence for major structural changes (e.g. bond breaking on the aromatic ring as opposed to hydrogen abstraction and / or the modification of bond lengths / angles) in electronically excited nucleobases.

In addition to neutral electronic excitation, ionization is a key process in radiation damage to biological tissue. Therefore, the dissociative ionization pathways of DNA and RNA bases have been studied for many years, stretching back to the 1960s [Rice et al. 1965, Rice and Dudek 1967]. Nonetheless, various details remain unresolved including the identification of certain fragment ions. The MPI results presented in Chapter 4 answer some of these questions, taking advantage of good mass resolution, high signal to noise ratios, and comparisons with deuterated molecules.

Chapter 5 describes our experiments probing metastable dissociation pathways of multi-photon ionized uracil, thymine and thymine-water clusters. We have also built a *laser thermal desorption* source based on systems at Queen's University Belfast and Heriot Watt University [Camillis 2015]) for two purposes: (1) to enable the best possible comparisons between the OU experiments and the Heriot Watt experiments (see Chapter 6 and Chapter 2) to enable future work on larger biomolecules that are typically thermally damaged in a more conventional heating source (e.g. nucleosides and nucleotides). Comparing the radiation response of sequentially more complex biomolecules in the gas phase provides a natural approach to linking fundamental nanoscale processes and effects in biological systems.

1.2 Radiation induced processes in biomolecular clusters

Studies of isolated molecules generally provide the clearest interpretations of radiation-induced process [Bald et al. 2008] but it is very challenging to relate these insights to more complex systems such as DNA in its natural environment. One strategy to help bridge this *complexity gap* is to study molecular clusters in the gas phase. Clearly, the intermolecular bonding (particularly hydrogen bonds and π-stacking) within clusters enables analogies to be drawn with condensed biological environments. Simultaneously, experiments on clusters in the gas phase enable key nanoscale processes such as fragment ion production and (photo-) electron emission to be observed directly without many of the complications that can affect experiments on surfaces (e.g. surface charging, cumulative modification of the exposed layer during measurements, and the need for ultrahigh vacuum to limit the impurities condensing on the surface). This enables very close comparisons to be drawn between experiments on isolated molecules and those on clusters in the gas phase. In quantum chemical calculations [Szwacki et al. 2007], research of this kind can provide valuable insights to relate the specific information gained from studies of isolated molecules to a nanoscale understanding of radiation-induced processes in condensed media.

Clustering effects on molecular geometries [Screen et al. 2007], electronic configurations [Kjellberg et al. 2010], and diverse types of reactivity [Martin et al. 2009, Boatwright et al. 2007] have emerged as major areas of interdisciplinary research. Indeed cluster research has demonstrated important new fundamental molecular interactions, notably Intermolecular Coulombic Decay [Kreidi et al. 2009]. A selection of significant research topics on molecular clusters are listed below.

1. Creation and geometric form of clusters [Kim et al. 2002, Qiu et al. 2009,Yanson et al. 1979, Rajabi et al. 2009]

2. Changes of ionization potentials, as well as the energies and vibrational coupling of excited and ionic states upon clustering [Kim et al. 1996, Belau et al. 2007, Close et al. 2005]

3. The transfer of vibrational energy from intra-molecular modes to inter-molecular modes (extending to evaporation) [Lan et al. 2008, Grégoire et al. 2001, Cukier 2002]

4. The dissociation pathways of clusters and of molecules within clusters [Gador et al. 2007, Gord et al. 1990, Mons et al. 2002]

5. Radiation induced intermolecular reactivity, including proton transfer [Khistyaev et al. 2013, Liu et al. 2008, Fuciarelli et al. 1994, Bobrowski et al. 1990, Sjödin et al. 2005, Dee and Baur 1974]

6. Characteristic properties of cluster-assembled materials [Jena et al. 2006, Claridge et al. 2009, Alivisatos 2008]

7. Microscopic aspects of nucleation [Castleman and Wei 1994]

Topics 1-4 above are particularly important from the perspective of understanding radiation-induced processes in molecular clusters. The experiments and calculations on thymine-water cluster ions in Chapter 5 explore aspects of topics 1-4 (stable cluster ion geometries, ionization energies. vibrational excitation, and evaporation / dissociation). Proton transfer in ionized hydrogen-bonded clusters and their subsequent dissociation (linking to topics 4 and 5 above) are important processes in Chapter 7 as the signals for protonated nucleobases provide the key indicators of clusters in our Stark-manipulated beams.

Comparing measurements with theory in the topic of radiation interactions with clusters is severely compromised by the experimental difficulty of selecting distinct neutral cluster targets as opposed to a broad distribution of monomer and cluster configurations. In response to this challenge, we are developing a system at The Open University that allows for better control over the molecular and cluster targets. This experiment uses a Stark deflection method developed by Küpper (DESY, Hamburg), Meijer (Fritz Haber Inst., Berlin), and co-workers [Filsinger et al. 2009A, Filsinger et al. 2009B, Trippel et al. 2012, Filsinger et al. 2011] for the manipulation of neutral molecular beams using inhomogeneous electric fields. This has been used successfully to separate specific cluster configurations in pulsed supersonic jets [Trippel et al. 2012], as well as to separate out different structural isomers/conformers [Filsinger et al. 2009B]. The method is based on accelerating molecules or clusters in strong electric field gradients as a function of their *effective dipole moment* / mass ratios. The effective dipole moment is a function of the permanent electric dipole moment, the polarizability, and the level of rotational excitation of a molecule or cluster. The permanent dipole moments and polarizabilities of DNA base monomers (including their different tautomeric forms), their dimers, their heterogeneous base pairs (notably the Watson-Crick pairs), and their hydrates [Riahi et al. 2010] vary significantly. Hence Stark deflection has great potential to control mixed beams of isolated and clustered nucleobases, and indeed many other important biomolecules.

1.3 Radiation damage in biological systems

The effects of radiation in living material are complex and involve a very wide range of processes. Therefore, elucidating biological radiation damage requires multidimensional

research with both bottom-up and top-down approaches. Key radiation induced damage events can be grouped into *stages* according to of their timeframes. As shown in Table 1.1, these timeframes span 24 orders of magnitude [Nikjoo 2003] from 10^{-15} s to 10^{9} s.

Table 1.1: Stages of radiation damage in biological material. Adapted from [Nikjoo 2003, Ryszka 2015].

Stage	Approximate timescale	Events
Physical stage	10^{-15} s	Electronic excitation and ionization
	10^{-14} s	Vibrational excitation, dissociation (including dissociative electron attachment) and electron thermalization
Chemical stage	10^{-12} s	Diffusion of free radicals
	10^{-10} s	Free radical reactions with the solute
	10^{-8} s	Formation of molecular products
	10^{-5} s	Completion of chemical reactions
Biochemical	1 s - 1 hr	Enzymatic reactions, repair processes
Biological	1 hr -100 yrs	Genomic instability, aberration, mutation, cell killing, appearance of tumours and secondary tumours

This thesis provides information to help understand processes in the physical stage of radiation damage, most of all electronic and / or vibrational excitation, ionization, and dissociation. The temporal scales in Table 1.1 are broadly linked to increasing spatial dimensions, with the physical stage occurring on the nanoscale and the biological stage extending to whole-body-scale processes such as the formation of secondary tumours, formations known as metastases. In the bottom-up approach, understanding and modelling large-scale harmful effects (in a cell, tissue, an organism, or even a population) requires detailed knowledge of all the key nanoscale processes [Smialek 2012, Sanz et al. 2012]. Cellular damage begins with radiation interactions with molecular constituents, notably DNA or proteins [Dawley and Ptasinska 2014]. The molecules studied in this thesis play essential biological roles: nucleobases are subunits

of DNA and RNA, while their hydrated clusters provide model systems for the aqueous conditions within a cell. The experiments mainly analogise *direct* (sometimes described as *primary*) radiation interactions with nucleobases within DNA, notably near-UV absorption and *high-energy* (defined here as sufficiently energetic to ionize a molecule) electron impact. The electrons that are excited (or removed) from molecules in this thesis are exclusively from valence states; we do not investigate any inner-shell processes.

Watson and Crick [1953] were the first to identify the right-handed double helix DNA structure. The helix is made of a sequence of nucleotides. Each nucleotide consists of a nucleoside and a phosphate group [Schermann 2008] and each nucleoside consists a five-carbon sugar, deoxyribose, and a nucleobase (adenine, thymine, guanine and cytosine in DNA) as shown in Fig. 1.1. Based on their central ring structures, nucleobases are classed as *pyrimidine* bases (uracil, thymine, and cytosine) or *purine* bases (adenine and guanine). The genetic information coding is based on the sequence of the nucleobases and the first human chromosome (human cells have 23 pairs of chromosomes (22 pairs of autosomes, look the same in both males and females and one pair of sex chromosomes), giving a total of 46 per cell) contains approximately 224 million nucleotides [Gregory et al. 2006]. The two strands of DNA are held together by hydrogen bonds between individual bases, with adenine always binding to thymine (2H-bonds), and guanine to cytosine (3H-bonds) as shown in Fig. 1.1.

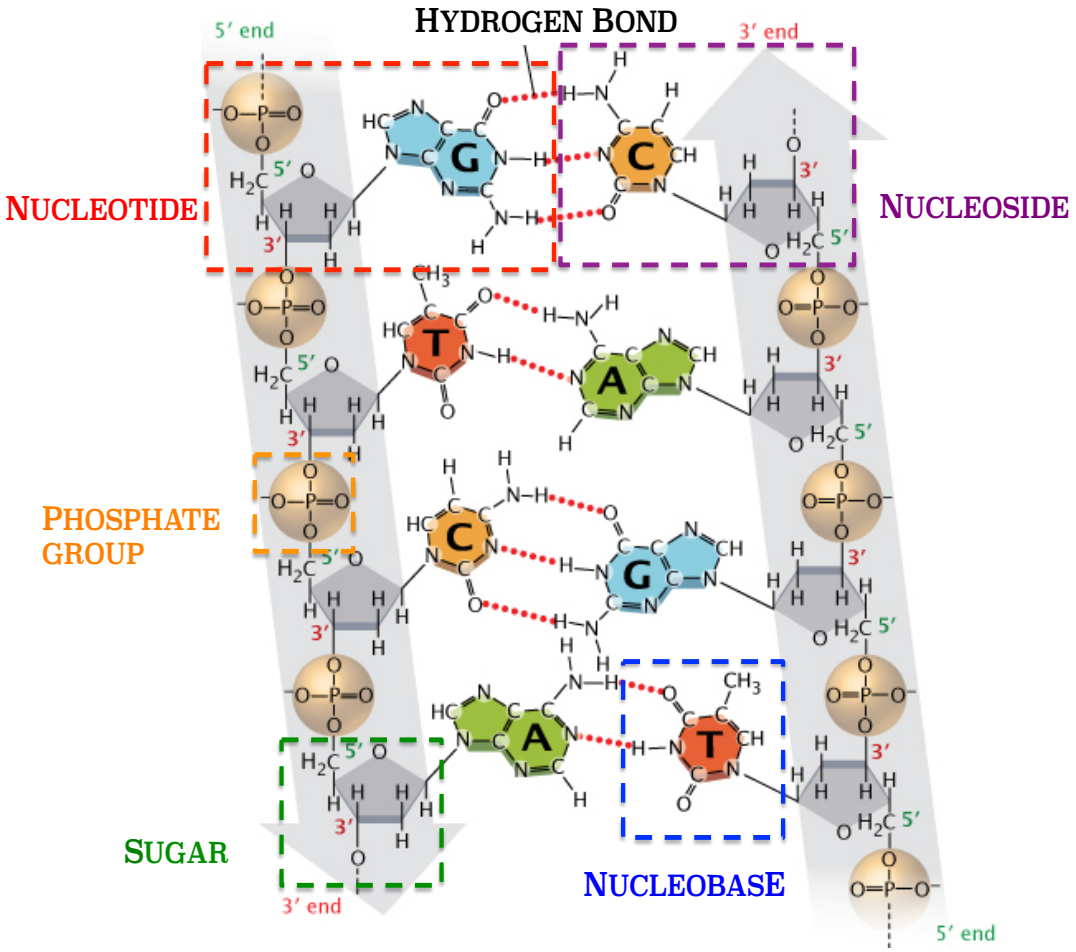

Figure 1.1: The chemical structure of DNA: The dashed lines correspond to hydrogen bonds (O•••HN or N•••HN). Starting in the top left quadrant and moving round clockwise, the nucleobases shown are guanine, cytosine, adenine, and thymine. The sugar-phosphate backbones (grey) run anti-parallel to each other, so that the 3' and 5' ends of the two strands are aligned. Reproduced from [Clancy 2008].

All these hydrogen bonds are strengthened and protected from solvent hydration due to the hydrophobic stacking nature of the nucleobases, which is a major contributor to the helix stability. In the absence of this arrangement, the base pairs would rapidly separate and hydrate with solvent water. The interaction between nucleobases in DNA is not limited to hydrogen bonding, however. The π-stacking of nucleobases along the length of a DNA strand also plays an important role in the structure and dynamics of DNA, for example in the case of Proton-Coupled Electron Transfer (PCET) [Kumar and Sevilla 2010]. It is also noteworthy that nucleosides of the strands are bonded to the phosphate

groups in two different carbon places (see Fig. 1.1). Hence, the two strands have opposite directionality [Dampc 2012] and this plays critical role in DNA replication. Most types of cell in the human body replicate numerous times during their lifetimes. This is important in the context of this thesis, because these replications significantly change the chemical environment surrounding a nucleobase. Therefore, we should not only consider the most stable structure of DNA when considering its nanoscale radio-sensitivity. Indeed, cellular radio-sensitivity is well known to vary between different stages of the cell cycle [Pawlik and Keyomarsi 2004].

The surrounding chemical environment plays an important role determining the structure of DNA, with the adequate hydration (~ 30 % by mass) being crucial to support the double-helical structure of the DNA [Chaplin 2006, Dickerson et al. 1982]. Nucleic acid hydration is particularly very important for their conformation and utility [Chaplin 2006], as shown by Watson and Crick [1953]. The strength of these aqueous interactions is far greater than those for proteins due to their highly ionic nature [Makarov et al. 2000]. The DNA double helix can take up various conformations depending upon the hydration level [Porschke 2016]. Nucleic acids have numerous groups that can hydrogen bond with water, with RNA having a greater scope of hydration than DNA due to its extra oxygen atoms and unpaired base sites (see Fig. 1.3). These extra hydroxyl groups also create additional hydration in duplex RNA [Rozners and Moulder 2004]. All these hydrogen bonded nucleobases (except for the hydrogen-bonded ring nitrogen atoms (pyrimidine N3 and purine N1)) are capable of one further hydrogen-bonding link to water within the major or minor grooves in DNA. A molecular dynamics simulation indicated that both grooves were roughly equally hydrated as shown in Fig. 1.2 [Bonvin et al. 1998].

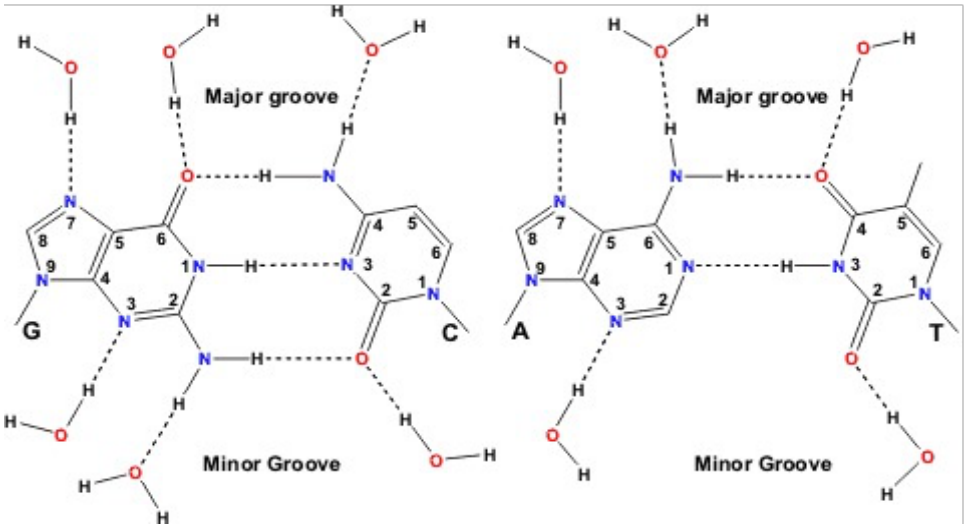

Figure 1.2: DNA base pairs showing hydration sites, in particular G-C pair have three hydration sites in minor groove compared to two in A-T site [Bonvin et al. 1998].

Moreover, solvation of the bases creates a unique pattern of water molecules, depending on the nucleotides' sequence. This helps the proteins to sense the base sequence from the outside of DNA [Pal and Zewail 2004, Khesbak et al. 2011, Chaplin 2006]. The solvation around the double helix also allows specialised proteins to slide along the strands more easily [Chaplin 2006]. Furthemore, water molecules have been shown to lower ionisation energy [Close et al. 2005], stabilise neutral excited states [Blancafort and Migani 2007], and mediate proton transfer reactions [Khistyaev et al. 2013]. However, while extensive studies have been carried out on condensed hydrated DNA and on its subunits in solution, there is scarcity in previous experimental research on hydrated clusters of DNA/RNA bases, particularly offering more direct detection of radiation products.

The key function of DNA is the storage of the genetic information. Ribonucleic nucleic acid, RNA, plays a fundamentally important role in a variety of biological processes, such as enzymatic catalysis [Kruger et al. 1982], protein synthesis [Klein et al. 2004]

and gene regulation [Serganov and Nudler 2013]. The structure of RNA is similar to DNA, but with several key differences. Unlike DNA, RNA is usually a single-stranded molecule. Also, the sugar in RNA is ribose instead of deoxyribose (ribose contains one more hydroxyl group on the second carbon), which accounts for the molecule's name. Furthermore, thymine (studied in Chapters 5 and 7) is replaced in RNA by uracil (studied in Chapters 4-7). RNA molecules fold in a well-defined three-dimensional structure controlled by their nucleotide sequence [Tinoco and Bustamante 1999], that can be determined by X-ray crystallography or nuclear magnetic resonance experiments [Tinoco 1996]**.** Fig. 1.3 a shows chemical structure of RNA and Fig. 1.3 b illustrates an example of folding. There are a variety of forms of RNA [Clancy 2008], including messenger RNA (mRNA), transfer RNA (tRNA), and ribosomal RNA (rRNA) and each form has different functions and activities. Messenger RNA is essentially a copy of a section of DNA and serves in the manufacture of proteins. Transfer RNA binds to both mRNA and amino acids, based on the nucleotide sequence of the mRNA, and brings the appropriate amino acids into the growing polypeptide chain during protein synthesis. Proteins synthesis process is called translation. Translation occurs on ribosomes (serves as the sites for translation of mRNA into protein), which are cellular organelles composed of protein and rRNA [Clancy 2008]. In 1956, Alexander Rich and David Davies discovered that single strands of RNA can "hybridize," sticking together to form a double-stranded molecule [Rich and Davies 1957]. Later, in 1960, Rich discovered that an RNA molecule and a DNA molecule could form a hybrid double helix. This was the first experimental demonstration showing that information could be transferred from DNA to RNA [Rich 1960].

It is also worth noting that RNA preceded DNA as the vessel to store genetic information in early life forms. Greater radio- and chemical-stability is believed to have the evolutionary transition from RNA to DNA [Alberts et al. 2002], although the specific nanoscale mechanisms responsible for the increased radio-stability of DNA are not yet fully understood. Apart from its important role as an RNA base, another reason to study uracil comes from the role of its derivatives (notably halogenated uracil) in chemo-radiotherapy as *radiosensitisers* [Byfield et al. 1982, Lawrence et al. 1994]. For example, Krook et al. [1991] showed that a combination of postoperative local therapy with radiation plus flurouracil (systematic therapy with a flurouracil based regimen) significantly improved the results of therapy for patients suffering from rectal carcinoma with a poor prognosis, as compared with postoperative radiation alone. A number of studies have demonstrated an increased sensitivity to X-irradiation after incorporation of 5-chloro-, 5-bromo-, or 5-iodo-deoxyuridine into the deoxyribonucleic acid (DNA) of human cells in tissue culture [Djordjevic and Szybalski 1960, Erikson and Szybalski 1961]. In 1962, Delihas et al. found that incorporation of 5-bromo-deoxyuridine into the DNA of a human cell line produced a twofold increase of the sensitivity to X-rays [Delihas et al. 1962]. Despite the fact that the initial research dated back to 1950's radiation interactions with halogenated uracils (in isolation and in doped cellular environments) are not fully understood.

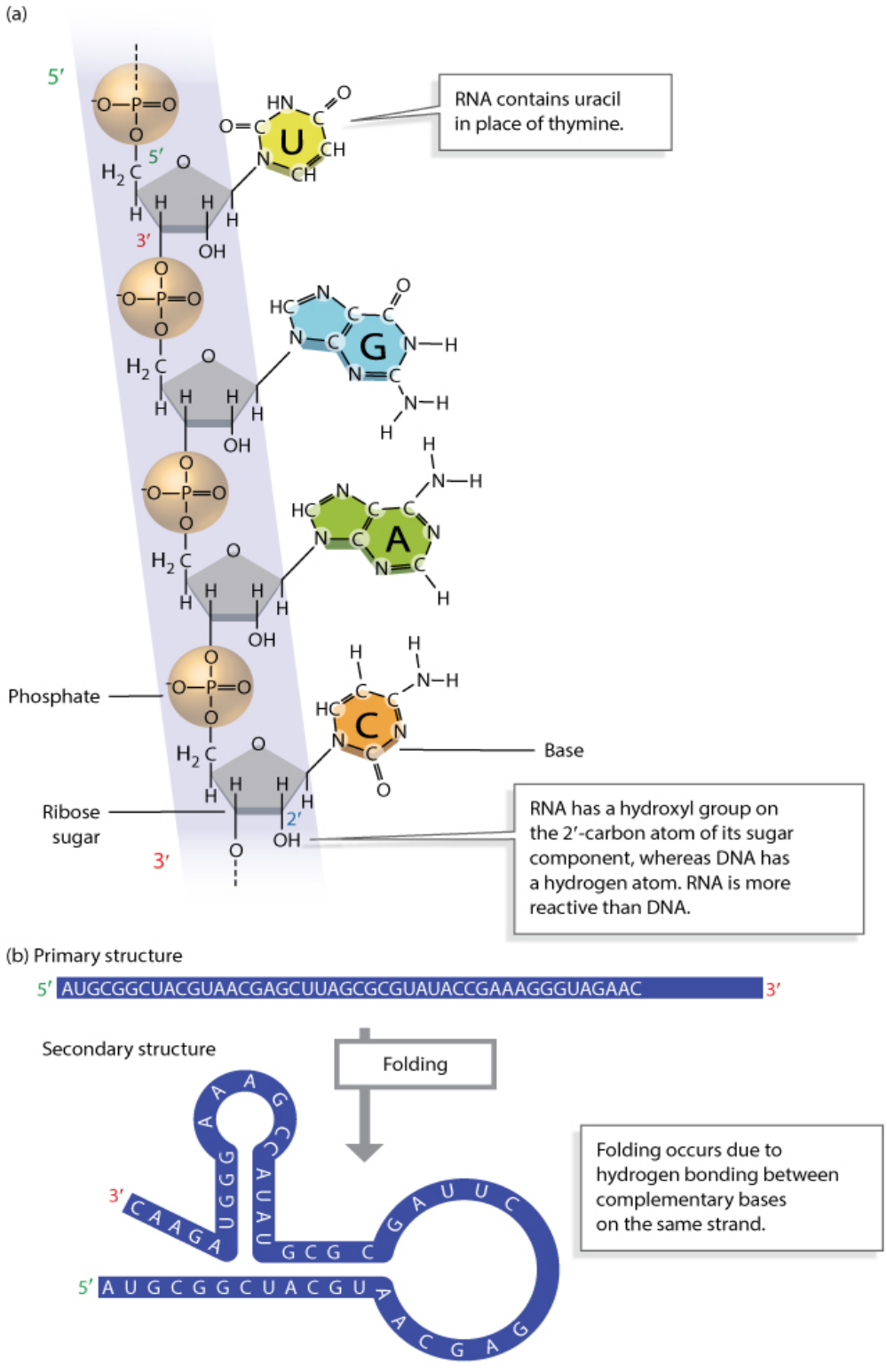

Figure 1.3: (a). The chemical structures of single-stranded RNA. (b). The primary and secondary structures of RNA. The primary structure refers to the molecule's nucleotide sequence; the secondary structure refers to its three-dimensional conformation after folding has occurred. Adapted from [Clancy 2008].

Fig. 1.4 shows the most common types of DNA damage initiated by means of irradiation. The formation of nucleobase radical cations and the formation of dimers via covalent bonding between the neighbouring pyrimidine bases, make up 80 % of the UV induced damage [Whitmore et al. 2001]. In the context of this thesis, the ionization measurements on isolated and clustered nucleobases are particularly relevant to these damage routes. Other important types of damage include DNA- protein cross links intra-strand and inter-strand, where the sequence of links between the two strands is corrupted. The insertion of molecules between the stacked bases is called "intercalations" and can also play a significant role. Moreover, DNA can go through either loss or addition of bases, or base damage by dissociative ionisation. Although these damages are identifiable macroscopically, the underlying physical pathways leading to their creation are only partially understood. The study of biomolecules (notably nucleobases, nucleosides, and nucleotides) and clusters in the gas phase can provide insights to better understand these processes.

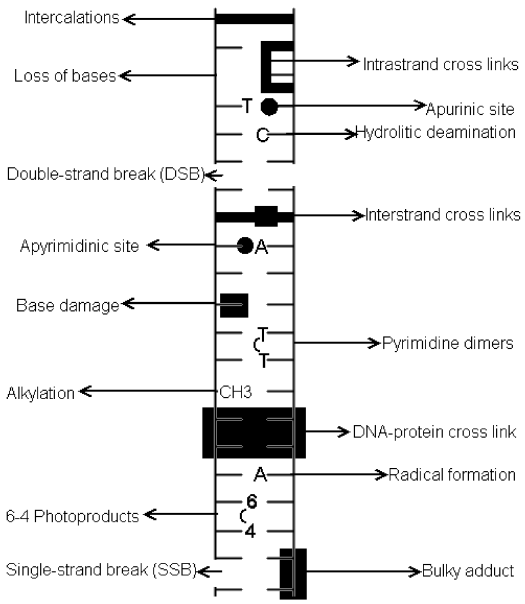

Figure 1.4: Common types of DNA damage. Adapted from [Ryszka 2015].

Double-strand breaks (DSB) and single-strand breaks (SSB) are recognized as particularly important classes of DNA damage. DSB happen when single strand breaks on opposite complimentary strands occur in close proximity. The cellular repair mechanisms for strand breaks are mainly homologous recombination [Sung and Klein 2006] and nonhomologous end joining [Lieber 2008]. However, the latter can be viewed as imprecise because the break can be rebuilt with a different sequence of nucleotides. The agarose gel electrophores method can be used to measure SSBs and DSBs macroscopically [Yokoya et al. 2008]. However, the electrophoresis method does not provide any information regarding the location of the strand break or on the specific interaction that initiated it. Hence, it is very important to complement these studies with more fundamental experiments and calculations. For example, Boudaïffa et al. [2000] were able to show that DEA plays a central role in radiation damage to DNA by matching electrophoresis results with DEA measurements on gas-phase nucleobases (as mentioned in section 1.1).

Biologically relevant conclusions cannot be drawn from understanding the physical stage of radiation damage alone. In particular, physical damage to DNA or other key macromolecules (notably RNA) must be considered in the context of biochemical repair. For example, the majority of cells possess defence mechanisms against oxidative damage, like excision repair (BER) and nucleotide excision repair (NER) enzymes. Different types of DNA damage can be more or less dangerous according to their repairing efficiency. Therefore the propagation of harmful radiation effects is highly dependent to the specific nanoscale damage process. This highlights the fundamental drawback and limitation of using macroscopic measures of radiation interactions with material to predict biological effects. Radiation dose, energy deposited per unit mass, is such a macroscopic measure and the cornerstone of clinical radiation application.

Currently radiobiology and radiotherapy depends on empirical correction factors to adjust dose-based predictions according to radiation type (for example incident X-ray photons compared ions) and tissue type. Nanoscale models of radiation damage are required to advance beyond these approximations. In particular, the evidence base is widely recognized as being inadequate to support dose-based predictions of the low-intensity radiation exposure effects.

1.4 Summary

The physical stages of radiation damage in biological material (in particular the electronic excitation, ionisation and dissociation of important biological molecules due to radiation interactions) have not been fully understood. This represents a significant barrier to building multi-dimensional simulations of radiation effects that can overcome the limitations based on macroscopic models only. Furthermore, understanding the radiation response of fundamental biological building blocks in isolation and in diverse chemical environments can provide insight into the molecular origins of life. This thesis explores UV and electron-induced process in two DNA / RNA bases as well as in nitromethane and 3-aminophenol. Studies of pure and hydrated clusters (in a *classic* supersonic jet and also in *Stark deflected* beams) can contribute to bridging the complexity gap between understanding radiation effects in isolated molecules and in condensed biological media.

1.5 Layout of the thesis

Chapter 2 introduces the fundamental concepts that govern radiation interactions with isolated molecules and clusters, as well as the principles of Stark deflection. Chapter 3 gives a detailed description of the experimental setups that I have exploited and developed during PhD. High resolution multi-photon ionization (MPI) performed on uracil and compared with deuterated uracil measurements is the subject of Chapter 4, with a particular focus on assignment of several fragment ions that were subject to debate in the available literature. Chapter 5 focuses on the metastable dissociation pathways of isolated uracil, thymine and hydrated thymine clusters. A Newly built laser thermal desorption apparatus, and our first results with this system are presented in Chapter 6. MPI and EII results obtained from Stark deflection experiments are presented in Chapter 7, with a particular focus on manipulation of nucleobases, 3-aminophenol and nitromethane. Chapter 8 summarizes the main results in the thesis and discusses future work.

References:

- B. Alberts, A. Johnson, J. Lewis, J. Lewis, M. Raff, K. Roberts and P. Walter, *Molecular biology of the cell, Garland Science, New York,* **4th edition**, 2002.
- A. P. Alivisatos, *ACS Nano*, 2008, **2**, 1514-1516.
- D. Alloni, A. Campa, M. Belli, G. Esposito, A. Facoetti, W. Friedland, M. Liotta, L. Mariotti, H. G. Paretzke and A. Ottolenghi, *Radiat. Res*., 2010, **173**, 263-271.
- I. Bald, J. Langer, P. Tegeder and O. Ingólfsson, *Int. J. of Mass Spectrom.*, 2008, **277**, 4-25.
- B. Barc, M. Ryszka, J. Spurrell, M. Dampc, P. Limão-Vieira, R. Parajuli, N. J. Mason and S. Eden, *J. Chem. Phys.*, **139**, 2013, 244311.
- L. Belau, K. R. Wilson, S. R. Leone and M. Ahmed, *J. Phys. Chem. A*, 2007, **111**, 7562-7568.
- M. P. Bernstein, J. P. Dworkin, S. A. Sandford, G. W. Cooper and L. J. Allamandola, *Nature*, 2002, **416**, 401-403.
- L. Blancafort and A. Migani, *J. Photochem. Photobiol., A,* 2007, **190**, 283-289.
- A. Boatwright, J. Jeffs and A. J. Stace, *J. Phys. Chem. A,* 2007, **111**, 7481-7488.
- K. Bobrowski, K. L. Wierzchowski, J. Holcman and M. Ciurak, *Inter. J. Radiat. Biol.,* 1990, **57**, 919-932.
- M. Boniol, P. Autier, P. Boyle and S. Gandini, *British Medical Journal*, 2012, **345**, 4757.
- A. M. J. J. Bonvin, M. Sunnerhagen, G. Otting and W. F. van Gunsteren, *J. Mol. Biol.,* 1998, **282**, 859-873.
- B. Boudaïffa, P. Cloutier, D. Hunting, M. A. Huels and L. Sanche, *Science,* 2000, **287**, 1658-1660.
- P. Byfield, E. John and Calabro-Jones, I. Klisak, and F. Kulhanian, *Int. J. Radiat. Oncol. Biol. Phys.*, 1982, **8**, 1923-1933.
- S. D. Camillis, J. Miles, G. Alexander, O. Ghafur, I. D. Williams, D. Townsend and Jason B. Greenwood, *Phys. Chem. Chem. Phys.,* 2015, **17**, 23643-23650.
- A. W. Castleman and S. Wei, *Annu. Rev. Phys. Chem.,* 1994, **45**, 685-719.
- M. F. Chaplin, *Nature Rev. Mol. Cell Biol.,* 2006, **7**, 861-866.
- C. Chatgilialoglu and P. O'Neill, *Exp. Gerontol*. 2001, **36**, 1459-1471.
- F. J. Ciesla and S. A. Sandford. *Science*, 2012, **336**,452-454.
- S. Clancy, *Nature Education*, 2008, **7**, 60.

- S. A. Claridge, J. A. W. Castleman, S. N. Khanna, C. B. Murra, A. Sen and P. S. Weiss, *ACS Nano*, 2009, **3**, 244-255.
- D. M. Close, C. E. Crespo-Hernández, L. Gorb and J. Leszczynski, *J. Phys. Chem. A,* 2005, **109**, 9279-9283.
- R. I. Cukier, *J. Phys. Chem. B,* 2002, **106**, 1746-1757.
- M. Dampc, Politechnika Gdaiska, Wydziaa Fizyki Technicznej i Matematyki Stosowanej, Katedra Fizyki Zjawisk Elektronowych, *PhD thesis*, 2012.
- M. M. Dawley and S. Ptasinska, *Int. J. of Mass Spectrom.,* 2014, **365**, 143-151.
- D. Dee and M. E. Baur, *J. Chem. Phys.,* 1974, **60**, 541-560.
- N. Delihas, M. A. Rich and M.L. Eidinoff, *Rad. Res.,* 1962, **27**, 479-491.
- W. B. DeMore, S. P. Sander, D. M. Golden, R. F. Hampson, M. J. Kurylo, C. J. Howard, A. R. Ravishankara, C. E. Kolb, and M. J. Molina, Jet Propul. Lab Publ., 1997, 97-4.
- R. E. Dickerson, H. R. Drew, B. N. Conner, R. M. Wing, A. V. Fratini and M. L. Kopka, *Science*, 1982, **216**, 475-485.
- B. Djordjevic and W. Szybalski, *J. Exp. Med.,* 1960, **222**, 509-531.
- R. L. Erikson and W. Szybalski, *Biochem. Biophys. Res. Commun.,* 1961, **1**, 258-261.
- J. Farquhar, H. Bao, and M. Thiemens, *Science*, 2000, **289**, 756-758.
- F. Filsinger, J. Küpper, G. Meijer, J. L. Hansen, J. Maurer, J. H. Nielsen, L. Holmegaard and H. Stapelfeldt, *Angewandte Chemie International Edition*, 2009A, **48**, 6900-6902.
- F. Filsinger, J. Küpper, G. Meijer, L. Holmegaard, J. H. Nielsen, I. Nevo, J. L. Hansen and H. Stapelfeldt., *J. Chem. Phys*., 2009B, **131**, 064309.
- F. Filsinger, G. Meijer, H. Stapelfeldt, H. N. Chapman and J. Küpper, *Phys. Chem. Chem. Phys.,* 2011, **13**, 2076-2087.
- A. F. Fuciarelli, E. C. Sisk, J. H. Miller and J. D. Zimbrick, *Inter. J. Radiat. Biol.,* 1994, **66**, 505-509.
- N. Gador, E. Samoylova, V. R. Smith, A. Stolow, D. M. Rayner, W. Radloff, I. V. Hertel and T. Schultz, *J. Phys. Chem. A*, 2007, **111**, 11743-11749.
- D. P. Glavin and J. P. Dworkin, *Proceedings of the National Academy of Sciences*, 2009, **106**, 5487-5492.
- N. G. Szwacki, A. Sadrzadeh and B. I. Yakobson, *Phys. Rev. Lett.,* 2007, **98**, 166804.
- J. R. Gord, A. W. Garrett, R. E. Bandy and T. S. Zwier, *Chem. Phys. Lett.,* 1990, **171**, 443-450.

- G. Grégoire, C. Dedonder-Lardeux, C. Jouvet, S. Martrenchard, and D. Solgadi, *J. Phys. Chem. A,* 2001, **105**, 5971-5976.
- S. G. Gregory, K. F. Barlow, K. E. McLay, R. Kaul, D. Swarbreck, A. Dunham, C. E. Scott, K. L. Howe, K. Woodfine, C. C. A. Spencer, M. C. Jones, C. Gillson, S. Searle, Y. Zhou, F. Kokocinski, L. McDonald, R. Evans, K. Phillips, A. Atkinson, R. Cooper, C. Jones, R. E. Hall, T. D. Andrews, C. Lloyd, R. Ainscough, J. P. Almeida, K. D. Ambrose, F. Anderson, R. W. Andrew, R. I. S. Ashwell, K. Aubin, A. K. Babbage, C. L. Bagguley, J. Bailey, H. Beasley, G. Bethel, C. P. Bird, S. Bray-Allen, J. Y. Brown, A. J. Brown, D. Buckley, J. Burton, J. Bye, C. Carder, J. C. Chapman, S. Y. Clark, G. Clarke, C. Clee, V. Cobley, R. E. Collier, N. Corby, G. J. Coville, J. Davies, R. Deadman, M. Dunn, M. Earthrowl, A. G. Ellington, H. Errington, A. Frankish, J. Frankland, L. French, P. Garner, J. Garnett, L. Gay, M. R. J. Ghori, R. Gibson, L. M. Gilby, W. Gillett, R. J. Glithero, D. V. Grafham, C. Griffiths, S. Griffiths-Jones, R. Grocock, S. Hammond, E. S. I. Harrison, E. Hart, E. Haugen, P. D. Heath, S. Holmes, K. Holt, P. J. Howden, A. R. Hunt, S. E. Hunt, G. Hunter, J. Isherwood, R. James, C. Johnson, D. Johnson, A. Joy, M. Kay, J. K. Kershaw, M. Kibukawa, A. M. Kimberley, A. King, A. J. Knights, H. Lad, G. Laird, S. Lawlor, D. A. Leongamornlert, D. M. Lloyd, J. Loveland, J. Lovell, M. J. Lush, R. Lyne, S. Martin, M. Mashreghi-Mohammadi, L. Matthews, N. S. W. Matthews, S. McLaren, S. Milne, S. Mistry, M. J. F. M oore, T. Nickerson, C. N. O'Dell, K. Oliver, A. Palmeiri, S. A. Palmer, A. Parker, D. Patel, A. V. Pearce, A. I. Peck, S. Pelan, K. Phelps, B. J. Phillimore, R. Plumb, J. Rajan, C. Raymond, G. Rouse, C. Saenphimmachak, H. K. Sehra, E. Sheridan, R. Shownkeen, S. Sims, C. D. Skuce, M. Smith, C. Steward, S. Subramanian, N. Sycamore, A. Tracey, A. Tromans, Z. Van Helmond, M. Wall, J. M. Wallis, S. White, S. L. Whitehead, J. E. Wilkinson, D. L. Willey, H. Williams, L. Wilming, P. W. Wray, Z. Wu, A. Coulson, M. Vaudin, J. E. Sulston, R. Durbin, T. Hubbard, R. Wooster, I. Dunham, N. P. Carter, G. McVean, M. T. Ross, J. Harrow, M. V. Olson, S. Beck, J. Rogers and D. R. Bentley, Nature, 2006, **441**, 315-321.
- P. Jena and A. W. Castleman, *Proceedings of the National Academy of Sciences,* 2006, **103**, 10560-10569.
- H. Khesbak, O. Savchuk, S. Tsushima and K. Fahmy, *J. Am. Chem. Soc.,* 2011, **133**, 5834-5842.
- K. Khistyaev, A. Golan, K. B. Bravaya, N. Orms, A. I. Krylov and M. Ahmed, *J. Phys. Chem. A,* 2013, **117**, 6789-6797.
- S. K. Kim, W. Lee and D. R. Herschbach, *J. Phys. Chem.,* 1996, **100**, 7933-7937.
- N. J. Kim, Y. S. Kim, G. Jeong, T. K. Ahn and S. K. Kim, *Int. J. of Mass Spectrom.,* 2002, **219**, 11-21.
- M. Kjellberg, O. Johansson, F. Jonsson, A. V. Bulgakov, C. Bordas, E. E. B. Campbell and K. Hansen, *Phys. Rev. A*, 2010, **81**, 023202.

- D. Klein, P. Moore and T. Steitz, *J. Mol. Biol.*, 2004, **340**, 141-177.
- K. Kreidi, P. V. Demekhin, T. Jahnke, T. Weber, T. Havermeier, X.J. Liu, Y. Morisita, S. Schössler, L. P. H. Schmidt, M. Schöffler, M. Odenweller, N. Neumann, L. Foucar, J. Titze, B. Ulrich, F. Sturm, C. Stuck, R. Wallauer, S. Voss, I. Lauter, H.K. Kim, M. Rudloff, H. Fukuzawa, G. Prümper, N. Saito, K. Ueda, A. Czasch, O. Jagutzki, H. Schmidt-Böcking, S. Scheit, L. S. Cederbaum and R. Dörner, *Phys. Rev. Lett.,* 2009,**103**, 033001.
- J. E. Krook, C. G. Moertel, L. L Gunderson, H. S Wieand, R. T. Collins, R. W. Beart, T. P. Kubista, M. A. Poon, W. C. Meyerns, J. A. Mailliard, D. I. Twito, R. F. Morton, M. H. Veeder, T. E Witzg, S. Cha and S. C. Vidyarthi, *N. Engl. J. Med.,* 1991, **324**, 709-715.
- K. Kruger, P. J. Grabowski, A. J Zaug, J. Sands, D. E. Gottschling and T. R. Cech, *Cell*, 1982, **31**, 147-157.
- A. Kumar and M. D. Sevilla*, Chem. Rev.,* 2010, **110**, 7002-7023.
- Z. Lan, L. M. Frutos, A. L. Sobolewski and W. Domcke, *Proceedings of the National Academy of Sciences,* 2008, **105**,12707-12712.
- T. S. Lawrence, M. A. Davis and J. Maybaum, *Int. J. Radiat. Oncol. Biol. Phys.*, 1994, **29**, 519-523.
- M. R. Lieber, *J. Biol. Chem.,* 2008, **283**,1-5.
- M. Liu, T. Li, F. S. Amegayibor, D. S. Cardoso, Y. Fu and J. K. Lee, *J. Org. Chem.*, 2008, **73**, 9283–9291.
- Z. Martins, O.D. Alexander, G. Orzechowska, M. Fogel and P. Ehrenfreund, *Meteoritics and Planetary Sci.,* 2007, **42**, 2125-2136.
- Z. Martins, O. Botta, M.L.Fogel, M.A. Sephton, D.P. Glavin, J.S .Watson, J.P. Dworkin, A.W. Schwartz and P. Ehrenfreund*, Earth and Planetary Sci Lett*., 2008, **270**, 130-136.
- I. Martin, J. Langer, M. Stano and E. Illenberger, *Int. J. of Mass Spectrom.,* 2009, **280**, 107-112.
- C. T. Middleton, K. de La Harpe, C. Su, Y.K. Law, C.E. Crespo-Hernández and B. Kohler. *Annu. Rev. Phys. Chem.,* 2009, **60**, 217-239.
- V. Makarov, B. K. Andrews, P. E. Smith and B. M. Pettitt, *Biophys. J.*, 2000, **79,** 2966-2974.
- N. J. Mason, B. Nair, S. Jheeta and E. Szymanska, *Faraday Discussions*, 2014, **168**, 235-247.
- M. Mons, I. Dimicoli and F. Piuzzi, *Int. Rev. Phys. Chem.,* 2002, **21**,101-135.
- G. M. Muñoz Caro, U. J. Meierhenrich, W. A. Schutte, B. Barbier, A. Arcones Segovia, H. Rosenbauer, W. H. P. Thiemann, A. Brack and J. M. Greenberg,

Nature, 2002, **416**, 403-406.

- D. Nachtigallová, A. J. A. Aquino, J. J. Szymczak, M. Barbatti, P. Hobza and H. Lischka, *J. Phys. Chem. A*, 2011, **115**, 5247-5255.
- H. Nikjoo, *Iran J. Radiat. Res.,* 2003, **1**, 3-16.
- S. K. Pal and A. H. Zewail, *Chem. Rev.,* 2004, **104**, 2099-2124.
- T. M. Pawlik and K. Keyomarsi, *Int. J. Radiat. Oncol. Biol. Phys.,* 2004, **59**, 928-942.
- D. Porschke, *Eur. Biophys. J*., 2016, **45**, 413-421.
- B. Qiu, J. Liu, Z. Qin, G. Wang and H. Luo, *Chem. Commun*., 2009, **20**, 2863-2865.
- K. Rajabi, K. Theel, E. A. L. Gillis, G. Beran and T. D. Fridgen, *J. Phys. Chem. A,* 2009, **113**, 8099-8107.
- S. Riahi, S. Eynollahi, M. Ganjali and P. Norouzi, *Int. J. Electrochem. Sci,* 2010, 355-366.
- J. M. Rice, G. O. Dudek and M. Barber, *J. Am. Chem. Soc.,* 1965, **87**, 4569-4576.
- J. M. Rice and G. O. Dudek. J. Am. Chem. Soc., 1967, **89**, 2719-2725.
- A. Rich and D.R. Davies, *Journal of the American Chemical Society,* 1956, **78**, 3548-3549.
- A. Rich, *Proceedings of the National Academy of Sciences* **46**, 1960, 1044-1053.
- E. Rozners and J. Moulder, *Nucleic Acids Res.,* 2004 **32**, 248-254.
- M. Ryszka, Radiation induced processes in biomolecules and clusters in controlled beams, Department of Physical Sciences, The Open University, Milton Keynes, United Kingdom, *PhD thesis*, 2015.
- A. G. Sanz, M. C. Fuss, A. Muñoz, F. Blanco, P. Limão-Vieira, M. J. Brunger, S.J. Buckman and G. García *Int. J. Radiat. Biol.,* 2012, **88**, 71-76.
- J. P. Schermann, *Spectroscopy and Modelling of Biomolecular Building Blocks*, *Elsevier, Amsterdam, Boston*, 2008.
- M. A. Smialek. *Journal of Physics: Conference Series*, 2012, **373**, 012013.
- P. Sung and H. Klein, *Nat. Rev. Mol. Cell Biol.,* 2006, **7**, 739-750.
- J. Screen, E. Stanca-Kaposta, D. Gamblin, B. Liu, N. A. Macleod, L. C. Snoek, B. G. Davis and J. P. Simons, *Angew. Chem. Int. Ed.,* 2007, **46**, 3644-3648.
- A. Serganov and E. Nudler, *Cell*, 2013, **152**, 17-24.
- M. Sjödin, S. Styring and H. Wolpher, *J. Am. Chem. Soc.,* 2005, **127**, 3855-3863.
- S. Trippel, Y. P. Chang, S. Stern, T. Mullins, L. Holmegaard and J. Küpper, *Phys. Rev. A*, 2012, **86**, 033202.

- I. Tinoco, *J. Phys. Chem.*, 1996, **100**, 13311-13322.
- I. Tinoco and C. Bustamante, *J. Mol. Biol.*, 1999 **293**, 271-281.
- C. Von Sonntag, *The chemical basis of radiation biology, Taylor and Francis, London*, 1989.
- J. D. Watson and F. H. C. Crick, *Nature*, 1953, **171**, 737-738.
- S. E. Whitmore, C. S. Potten, C. A. Chadwick, P. T. Strickland and W. L. Morison, *Photodermatology, Photoimmunology and Photomedicine,* 2001, **17**, 213-217.
- I. K. Yanson, A. B. Teplitsky and L. F. Sukhodub, *Biopolymers*, 1979, **18**, 1149-1170.
- A. Yokoya, N. Shikazono, K. Fujii, A. Urushibara, K. Akamatsu and R. Watanabe, *Radiat. Phys. Chem.,* 2008, **77**, 1280-1285.

CHAPTER 2

Theory

The central aim of this chapter is to give a short overview of the behaviour of molecules and molecular clusters when they interact with photons and electrons. It starts with a brief introduction to molecular orbital theory, excitation, ionization, and fragmentation processes. The discussion then moves to the intermolecular forces responsible for clustering with a focus on hydrogen bonding, as this is the strongest bonding mechanism of the clusters studied in this thesis. The chapter then discusses the principles of rotational cooling in supersonic expansions and the manipulation of neutral molecules using the electric field gradient produced by a Stark deflector.

2.1 Molecules and clusters

2.1.1 Born-Oppenheimer approximation

Molecules can express changes in internal energy in terms of electronic, rotational, and vibrational excitation. These are known as the internal degrees of freedom and each can interact with electromagnetic radiation. The energy differences between electronic

states are of the order of a few eV, whereas vibrational levels are typically separated by several tens to hundreds of meV and rotational energy levels by a few meV. Although molecules can be simultaneously excited rotationally, vibrationally, and electronically, the large energy differences enable us to treat the three degrees of freedom separately. The separation can also be rationalized in terms of the large mass difference between electrons and nuclei leading to significantly different timeframes for changes in electronic motion compared with nuclear motion (rotation and vibration) [Born 1927, Seiler 1969, Lipson 2009]. Under the Born-Oppenheimer approximation, the total internal energy of a molecular system can be expressed as:

$$E_{total} = E_{electronic} + E_{vibrational} + E_{rotational} \qquad \text{[Eq. 2.1]}$$

This provides an invaluable framework to help us understand excited state dynamics of molecules. Naturally there are limitations in the applicability of Born-Oppenheimer approximation, like any other approximation. Electronic and vibrational coupling is discussed in section 2.1.4.4. Rotational motion influences vibrational excitation in a manner analogous to a centrifugal force, i.e. by elongating bonds [Piela 2007]. These couplings are weak, however, and can be treated effectively as perturbations in most situations.

2.1.2 Molecular orbital theory

Molecular orbital theory describes the distribution of the electrons in a molecule according to quantum mechanical principles. The quantum state of an electron is determined by its interactions with all the other electrons and the nuclei in the molecule. A molecular orbital represents this quantum state as a region of space with high probability of finding the electron at any given time. The measure of this

probability in space is known as the *electron density*. Molecular orbitals are combinations of atomic orbitals. Considering the wave-like behaviour of electrons, we can think of molecular orbitals as regions where atomic orbitals interfere constructively. In stable molecules, regions of high electron density are usually found around atoms and along bonds. As an example, Fig. 2.1 shows the density of the valence shell electrons for 14 electrons in 10 orbitals in active space of uracil using the complete active space self consistent field (CASSCF) method and the 6-31G basis set [Richter et al. 2014].

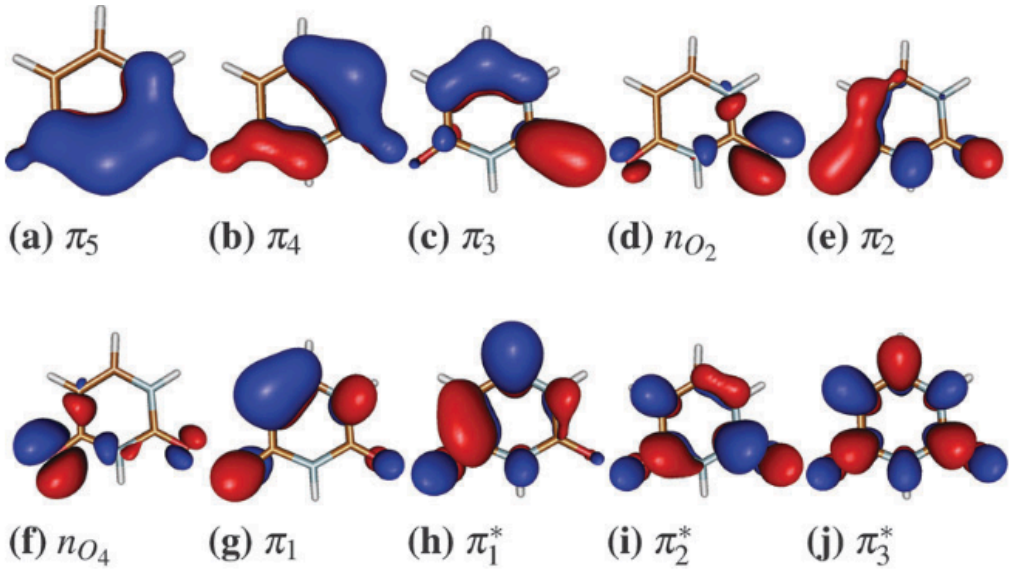

Figure 2.1: Electron density in active space of uracil (including 14 valence electrons in 10 orbitals). Adapted from reference [Richter et al. 2014].

Due to the current limits of computing power, solving the Schrödinger equation for molecular orbitals is not possible analytically except for the simplest molecules such as homo-nucleic diatomics. Therefore various numerical methods have been developed to approximate molecular orbitals. The simplest mathematical process of this kind is

called the *linear combination of atomic orbitals (LCAO)* [Piela 2007]. Equation 2.2 shows how single electron molecular orbitals, φ_i, are built in LCAO.

$$\varphi_i = \sum_s c_{si}\chi_s \qquad \text{[Eq. 2.2]}$$

Where c_{si} = weighing coefficient, and χ_s = atomic orbitals (Specific selection of χ_S is called a basis set).

Molecular orbitals in the valence shell are delocalized over two or more nuclei, allowing electrons to be *shared*, and lowering the total energy of the system. Delocalization of orbitals plays a critical role in chemistry, producing more complex shapes of molecular orbitals than atomic orbitals. The highest occupied molecular orbital is referred to as the HOMO and the lowest unoccupied molecular orbital is referred as the LUMO. Valence orbitals are given letter designations according to their shapes and function:

σ (bonding molecular orbital) - The shared electron density is concentrated along the internuclear axis.

π (bonding molecular orbital) - The bonding electron density is concentrated in *lobes* above and below, or in front of and behind, the internuclear axis. There is no electron density directly along the internuclear axis.

n - For orbitals not contributing to the binding energy of the molecule.

If the orbitals have *antibonding* character (tending to repel the nuclei that share the electron density instead of attracting them) the letter designations e.g. σ* or π*. These definitions are descriptive and not mutually exclusive for molecular orbitals. Hence, some orbitals are described with two-letter designation. For example, nucleobases all have excited states of nπ or σπ character, some of them also exhibiting antibonding character. Other types of orbitals (e.g. Rydberg) can also mix with valence orbitals. A

detailed description of molecular orbitals and molecular bonding is available in reference [Hollas 2003].

2.1.3 Intermolecular forces effects: clusters

Intermolecular forces are forces of attraction and repulsion between molecules. Throughout this PhD thesis, the term molecular cluster is used to represent a complex molecule consisting of two or more molecules. The molecules can be the same (homo-molecular) or different (hetero-molecular clusters), e.g. thymine-water complexes described in Chapter 5. Other types of clusters such as fullerenes with covalent bonds (Valance cluster) [Szwacki et al. 2007], or helium nano-droplets (Atomic clusters) [Leidlmair et al. 2012A, Leidlmair et al. 2012B, Bartl et al. 2013]), are not studied here. In this PhD thesis, hydrogen bonding plays a particularly important role as it is the strongest intermolecular attraction force in pure and hydrated clusters of DNA / RNA bases, and is responsible for binding Watson-Crick base pairs. The most important categories of intermolecular forces in the context of this thesis are listed in table 2.1 and described in the subsections below [Johnston 2002].

Table 2.1: Summary of the most important intermolecular forces for the cluster studies in this thesis and, type of species that interact.

Type of Interaction	Interacting Species
Dipole-Dipole	Polar Molecules (stationary ones have more energy than rotating ones)
Hydrogen Bonding	Between partial positive H atom and highly electronegative atom such as N, O, F of other molecules
Van der Waals Forces	All Molecules (just need electron cloud)
Ion-Dipole	Ions and Polar Molecules
Cation-π	π-Electron Cloud and Cation
π -Stacking	Two different π-Electron Clouds

2.1.3.1 Van der Waals forces

Van der Waals forces are the intermolecular attraction forces between the molecules. There are two kinds of Van der Waals forces: weak London Dispersion Forces (discussed below) and stronger Dipole-Dipole forces (discussed in section 2.1.3.2) [Petrucci et al. 2007]. An unequal charge distribution within a molecule caused by the electron motion in one nonpolar molecule (instantaneous dipole) can induce a dipole in a nearby nonpolar molecule, resulting in an intermolecular attraction. These dipole-induced dipole attractions are called London Dispersion Forces [Reger 2009].

$$V^{LD} = -\frac{C}{r^6} \qquad \text{[Eq. 2.3]}$$

Where r = intermolecular distance, and C = constant dependent on polarisability and ionization energy. At short intermolecular distances, repulsion due to electrostatic charge and the Pauli exclusion principle start to dominate. This repulsive interaction potential scales with $1/r^{12}$. Combining this with the London Dispersion potential gives the Lennard-Jones potential (V^{LJ}) , which is expressed as follows:

$$V^{LJ}(r) = \varepsilon\left(\frac{r_0}{r}\right)^{12} - 2\left(\frac{r_0}{r}\right)^{6} \qquad \text{[Eq. 2.4]}$$

Where ε and r_0 correspond to the binding energy and equilibrium distance, respectively. London dispersion forces are the weakest of all the intermolecular forces discussed here. Their strength generally increases with increasing numbers of electrons in the interacting molecules [Johnston 2002]. The resultant binding energies range from few meV to less than 100 meV.

2.1.3.2 Dipole-Dipole and higher multipole interactions

The interaction between polar molecules (molecules which possess permanent electric dipole moments) tends to orient the molecules to achieve the minimum total potential energy of the system. The dipole-dipole interaction energy of two co-linear dipoles μ_1 and μ_2 is given by:

$$V^{DD}(r) = -\frac{2\mu_1\mu_2}{4\pi\varepsilon_0 r^3} \qquad \text{[Eq. 2.5]}$$

Where r = distance between the centres of two dipoles. The dipole-dipole interaction potential energy between two parallel, non-co-linear dipoles is given by:

$$V^{DD}(r) = -\frac{2\mu_1\mu_2}{4\pi\varepsilon_0 r^3}(1 - 3\cos^2\theta) \qquad \text{[Eq. 2.6]}$$

Where θ = angle between the inter-molecular vector with the intra-molecular bond. The resultant binding energy for two interacting molecules with dipole moments of 1 Debye each is typically about 15 meV at room temperature [Johnston 2002]. Although higher multipole interactions usually contribute relatively weakly to the inter-molecular binding energy, they can play an important role in determining the structure of the cluster. For example, the structure of $(HF)_2$ determined exclusively by considering dipole-dipole interaction would be linear. However, Dyke et al. [1972] have experimentally determined that the angle between the molecular dipoles is approximately 60°. Dimers of benzene (C_6H_6) and perfluorobenzene (C_6F_6) are the example of clusters where quadrupole interactions dominate. Strong quadrupole moments can result in T-shaped geometries for clusters [Johnston 2002] or π-Stacking (i.e. non-covalent interactions between π-electrons).

2.1.3.3 Hydrogen bonding

A Dipole-Dipole interaction where a partially positive H atom of one molecule is attracted to a highly electronegative atom such as N, O, F of another molecule [Johnston 2002, Reger et al. 2009] is called hydrogen bonding. Hydrogen bonds are stronger than the dipole interactions described above, but weaker than covalent or ionic bonds. Binding energy is closely correlated to bond length and hence hydrogen bond lengths are significantly longer than covalent bonds. For example, the length of hydrogen bond in between water molecules is about 117 picometres whereas the length of the O-H covalent bond(s) is only 99 picometres [Reger 2009]. Hydrogen bonding is generally represented by dashed line as shown in Fig. 2.2. Fig. 2.2 shows the calculated eight lowest energy structures of hydrogen bonded G-C clusters along with the WC structure (very lowest energy structure in Fig 2.2 a). The two lowest G-C energy structures (red) were not observed in gas-phase experiments with nanosecond timescale Resonance Enhanced Multi-photon Ionization (REMPI) (i.e. the wavelength of the n photons matches the energy gap between the ground and the excited states), whereas two higher energy structures (yellow) were observed in IR–UV hole burning [Abo-Riziq et al. 2005, Nir et al. 2000, Nir et al. 2002]. Furthermore, white structures with higher energies were not observed in any experiment. Hydrogen bonds can occur in inorganic molecules such as H_2O, NH_3 and HF and in organic molecules like DNA and proteins. As mentioned above, hydrogen bonds are the strongest bonds that form between the neutral molecules in the expansions discussed in Chapters 5 and 6. In particular, water forms hydrogen bonds with the pyrimidine derivative, thymine. Hydrogen bonds provide a potential bridge for proton transfer and participate in determining secondary and tertiary structures of proteins.

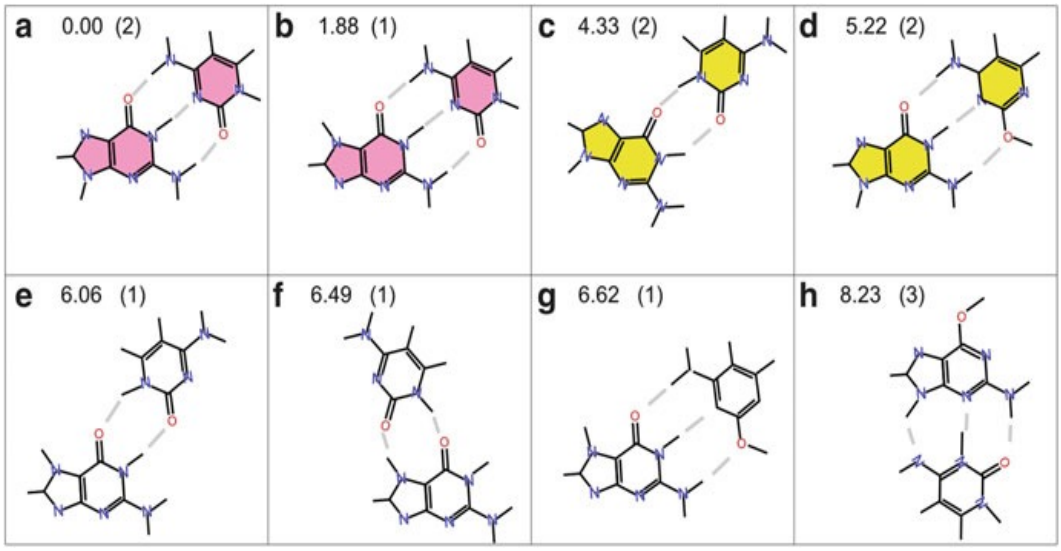

Figure 2.2: The calculated lowest energy structures of hydrogen bonded guanine-cytosine (G-C) clusters with energies in kcal/mol. Adapted from [Barbatti et al. 2014]

Hydrogen bonding can play three particularly important roles in the radiation-induced processes studied in this thesis. Firstly, it can modify the *potential energy surfaces* of a molecule (in its electronic ground state as well as in electronic excited states) and hence affect electronic excitation and relaxation pathways, including possible trajectories through *conical intersections* (potential energy surfaces and conical intersections are in sections 2.1.4.1 and 2.1.4.4 below) [Perun et al. 2005A, Perun et al. 2005B, Sobolewski and Domcke 2006, Shemesh et al. 2009A. Shemesh et al. 2009B]. Secondly, hydrogen bonds provide a *bridge* for the possible intermolecular transfer of a proton or a hydrogen atom in an excited complex [Liu et al. 2008]. Thirdly, hydrogen bonds (and indeed all other intermolecular bonds) provide an efficient mechanism for the dissipation of vibrational energy from intramolecular modes to intermolecular modes, often leading to intermolecular bond breaking and evaporation [Barc et al. 2014].

2.1.3.4 Other non-covalent forces

1). Ion-Dipole - An attraction that occurs when a dipole interacts with an ion. a negative ion attracts the positive dipole of another molecule, a positive ion attracts the negative dipole of another molecule. The interaction strength increases as ion charge or the dipole magnitude of the polar molecule increases. Ion-Dipole attraction is quite important in context of this thesis because it plays a very important role in the thymine$^{+}(H_2O)_n$ bonding discussed in Chapter 5.

2). Cation-π - A weak attraction that occurs between a cation and the electron-rich π orbital of an aromatic ring. Bond strength is relatively strong and similar to the strength of hydrogen bonding. It is a very important force in proteins. A detailed review of Cation-π interactions in structural biology is available in reference [Gallivan and Dougherty 1999].

3). π-Stacking - A weak attraction that results from the distortion of two different π - electron clouds. For example, when the π-electron cloud of one benzene ring becomes attracted to that of another, the negative dipoles repel each other so the electrons shift away from the other molecule. A positive dipole is created on the other side of the π-electron cloud. The negative dipole moment of a second benzene ring is attracted to this induced positive dipole. A detailed review of several types of π-Stacking is available in reference [Martinez and Iverson 2012].

2.1.4 Electronic excited state dynamics

2.1.4.1 Potential energy surfaces

A potential energy surface reflects the relationship between the energy and the geometry of a molecule in a specific electronic state. This surface is created by plotting the molecules' potential energy as a function of its internuclear distances for all degrees of freedom and its shape, its features, and its relation with other potential surfaces determine its evolution, notably with respect to radiationless deactivation from excited states. The main features commonly found on such hypersurfaces include (see Fig. 2.3) the Franck-Condon region, local minima, avoided crossings and conical intersections. In order to represent potential energy surfaces graphically, the internuclear distance dimensions are represented by just one (resulting in a potential energy curve) or two axes.

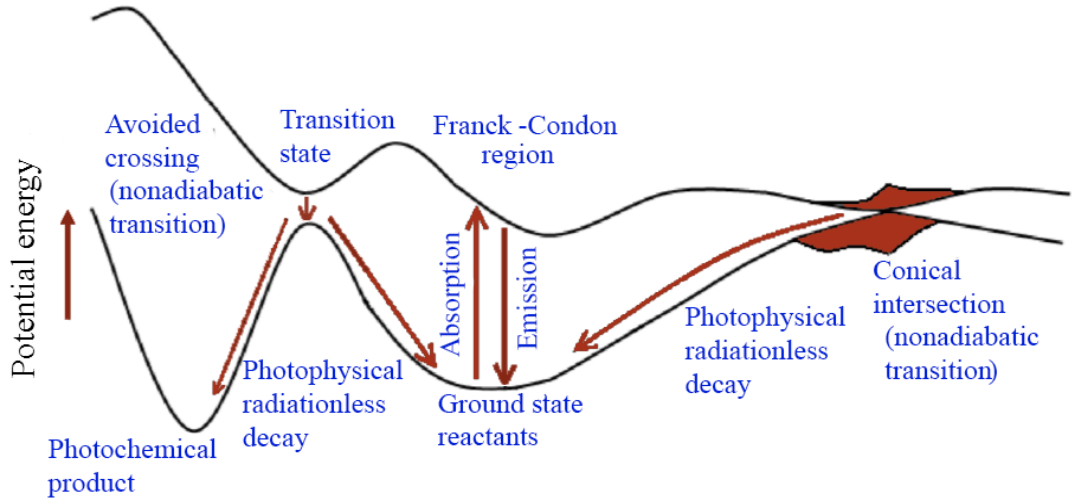

Figure 2.3: Graphical representation of potential energy curves for two electronic states. Such curves can be interpreted as key fragments of the full potential energy hypersurface, plotted in one dimension. Common features found on hypersurfaces are marked. Adapted from [Ryszka 2015].

2.1.4.2 Franck-Condon principle

Before the development of the Schrodinger equation in 1925, Franck put forward qualitative arguments to explain electronic transitions to vibrationally-excited states (a neutral electronic excited state or an ionic state). Such transitions are known as vibronic transitions. His proposal was based on the fact that an electronic transition in a molecule takes place much more rapidly than nuclear motion (see section 2.1.1) so that, in a vibronic transition, the nuclei have very nearly the same position and velocity before and after the transition. The most probable transition occurs from a point where vibrational motion is about to reverse, i.e. the kinetic energy associated with the vibration is at its minimum. We can also understand the maximum probability for a transition as corresponding to the molecular geometry where maximum overlap occurs between electronic wave functions of initial state and final state.

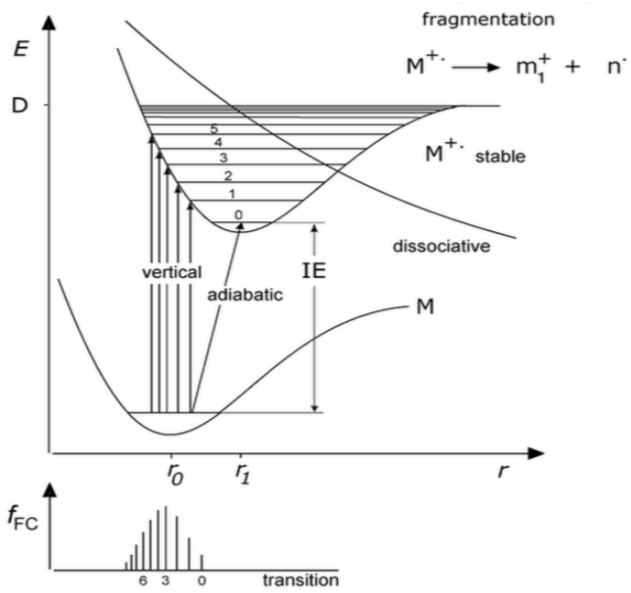

Figure 2.4: The Franck-Condon principle illustrated. The lower part schematically shows the distribution of Franck-Condon factors, f_{FC} for various transitions. Adapted from [Gross 2011].

The Franck-Condon factors, f_{FC} describe the probability of any particular transition and hence determine the distribution of vibrational states in the final state [Dunn 1966]. Fig. 2.4 illustrates a hypothetical Franck-Condon transition between the neutral electronic ground state of a molecule and its lowest-energy ionic state. The greater r_1 compared to r_0 the more probable will be the generation of ions excited to high vibrational states. The requirement that the nuclei have the same positions before and after an electronic excitation means that such transitions can be schematically represented by vertical lines in Fig. 2.4. The energy required for the most probable transition (with the highest f_{FC}) is called the "vertical energy". Conversely, the energy difference between the vibrational ground states of the origin and destination electronic ground states (sometimes referred to as the $(0 \leftarrow 0)$ transition) is named the *adiabatic energy* and is represented by a diagonal line in Fig. 2.4. The difference between vertical and adiabatic ionization energies ($IE_{vert} - IE_{ad}$) is typically of the order of 0.1–0.7 eV [Beynon and Gilbert 1979].

2.1.4.3 Radiative decay

An electronically excited molecule can relax to a lower-energy electronic state radiatively via the following processes:

1. Fluorescence - Deactivation involves states of the same multiplicity. The transition typically takes place 0.01 - 10 μs after the initial excitation.
2. Phosphorescence - Deactivation involves a change in the multiplicity of transition states, e.g. triplet-singlet. Phosphorescence generally occurs between low lying vibrational states of the excited triplet and the vibrationally-excited electronic ground

state. These are slow processes with lifetimes up to several minutes.

The two decay mechanisms described above are too slow to have a significant effect in our MPI experiments, as the molecules investigated in this thesis relax non-radiatively on much faster timescales.

2.1.4.4 Non-radiative decay

The physics of non-radiative decay of polyatomic molecules is an extensive subject and the reader is referred to Piela's [2007] book for thorough description. The following sections aim to introduce the most important concepts and terms that feature in the discussions of relaxation pathways in this thesis. Potential energy hypersurfaces derived under the Born-Oppenheimer approximation are referred to as *adiabatic potential energy surfaces*. When the energy gap between two states is low, the Born-Oppenheimer approximation fails [Makarewicz 1985, Johnson and Reinhardt 1986, Pisana et al. 2007] thus a representation using *diabatic surfaces* is more appropriate. Fig. 2.5 compares adiabatic and diabatic surfaces for describing the S_2-S_1 conical intersection in pyrazine, obtained using CASSCF (complete active space self consistent field) and MRCI (multi reference configuration interaction) techniques [Woywod et al. 1994].

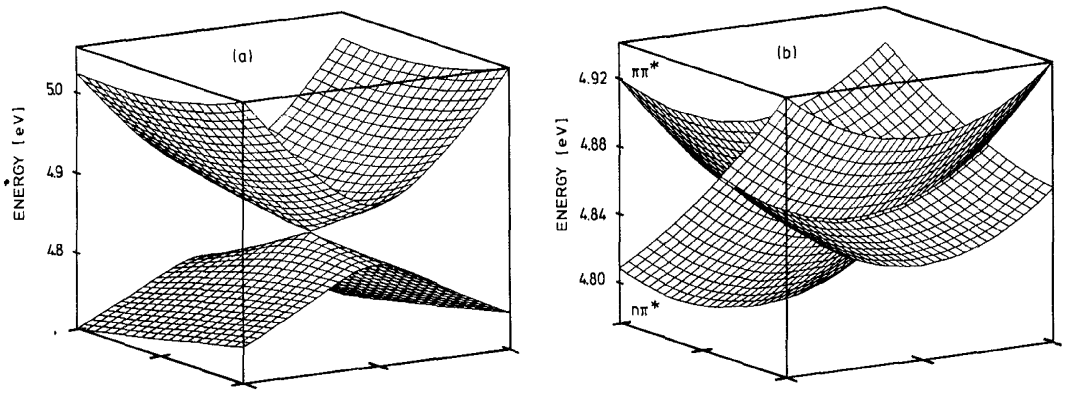

Figure 2.5: Diagrams showing a close-up of the S_2 -S_1 conical intersection in pyrazine. Adiabatic surfaces are shown in (a), and diabatic in (b). Adapted from [Ryszka 2015].

Fig. 2.6 illustrates the concept of a conical intersection between two states. The two adiabatic surfaces represent excited (upper, E_-) and ground (lower, E_+) electronic states. Each of these surfaces comprise two diabatic lobes - representing molecular breakup i.e. products (white) and more stable / strongly bonded molecule (grey). The crossing seam between the two surfaces is called a conical intersection (labelled C on the Fig. 2.6, but more commonly referred to as CI). After electronic excitation in the Franck-Condon region (FC), the system finds itself on a well-shaped part of the E_- potential energy hypersurface. The lowest local maximum around this well can be described as a saddle point or a transition point (TS on the Fig. 2.6). Depending upon the vibrational energy of the system, the system can pass through the local minimum (M^*) and then overcome the energy barrier of the saddle point. Alternatively, tunneling can penetrate this barrier. The system is then almost certain to relax to the electronic ground state through the conical intersection. At this stage, the system can either return to the ground state minimum (P') or it can follow the potential slope towards point (P). The latter path could either lead to dissociation or to more complicated dynamics. The total energy of the system must be conserved, so the transition only occurs if there is a way to dissipate the excess energy of the system to vibrational, rotational or

translational degrees of freedom. Furthermore, energy can be transferred to neighboring molecules.

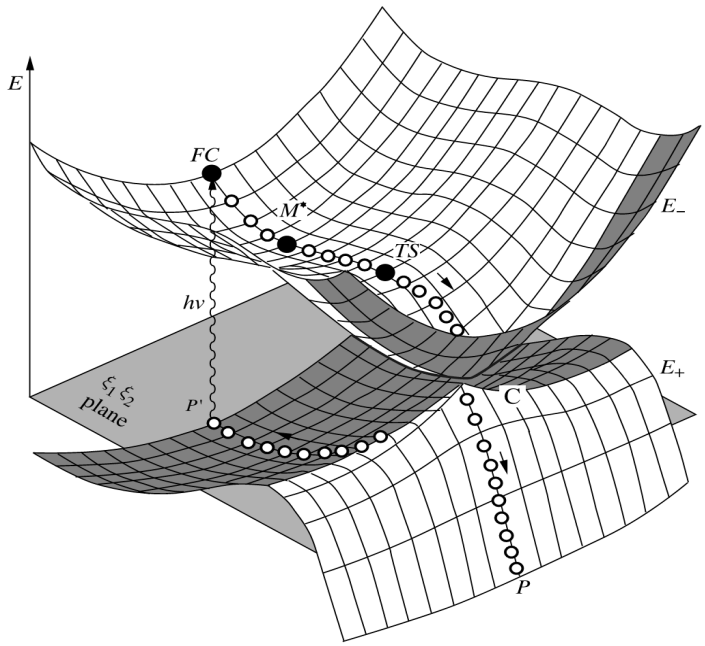

Figure 2.6: Illustration of non-radiative decay via a conical intersection. Adapted from [Ryszka 2015].

The multiplicity of a state of a molecule is given by:

$$\text{Multiplicity} = 2S + 1 \qquad \text{[Eq. 2.7]}$$

Where S = the sum of the spin quantum numbers of the electrons in the molecule. If all the electrons' spins are paired then S = 0 so the multiplicity = 1 and the state is called a *singlet state*. In the case of unpaired orientation of spins, S = 1 and multiplicity = 3. Such states are triply degenerate (i.e. there are 3 possible spin vector orientations) and are called *triplet states*. Depending upon the multiplicity of the states involved, a transition can be classed as:

- Internal conversion (IC) - No change in the multiplicity e.g. singlet-singlet

- Inter-system crossing (ISC) - Multiplicity changes during the transition, e.g. singlet-triplet

Transitions involving a change of multiplicity are normally forbidden because the spin-overlap integral is zero (spins are orthonormal). The spin overlap integral, M_S, is given by:

$$M_s = \int S_i S_j dr_s \qquad \text{[Eq. 2.8]}$$

Where, S_i and S_j = the spin functions of the initial and final states, respectively. However, forbidden transitions and hence IC can occur due to spin-orbit coupling. Spin-orbit coupling can be modeled using perturbation theory [Turro et al. 2009]. In case of atoms, spin-orbit coupling depends on the fourth power of the atomic number (z^4). In case of molecules, the coupling is generally enhanced in the presence of a heavier atom but z^4 dependence is also modified by the delocalization of electrons. Transitions forbidden on the grounds of mismatched molecular symmetry, also can be weakly allowed due to the distortion in molecular geometry induced by vibrational motion. This mixing of vibrational and electronic motions is called *vibronic coupling* [Yarkony 2002]. The fact that transitions involving a change of multiplicity are only very weakly allowed results in the long lifetime of triplet states.

2.1.4.5 Dynamics in molecular clusters

Molecular clusters allow for extra channels of dynamics besides those available in isolated molecules. Four significant examples of such dynamics are listed below.

- Formation of excimers - An excimer is a complex that is bound when one member is electronically excited but dissociates when it returns to the ground

state [Hirata et al. 1999]. The lifetime of an excimer is very short (typically nanosecond-order).

- Charge-transfer transitions - These commonly occur in complexes containing both electron donors and acceptors [Boatwright et al. 2007].
- Intra-Penning ionization - If one molecule (A) in a complex is neutrally excited above the ionization potential of another molecule (B) in the cluster, the system can lower its total energy by *autoionizing*. Hence, $A^*B \rightarrow AB^+ + e^-$ [Brutschy 1990].
- Proton Transfer - This is the transfer of a proton from an excited or ionized molecule to a neighboring neutral molecule in a cluster [Meot-Ner 1979, Park et al. 2008]. Proton transfers are commonly observed in irradiated hydrogen-bonded clusters, as discussed in Chapters 4, 5, and 7 of this thesis.

2.2 Ionization and appearance energies

The *ionization energy* (IE) is the amount of energy required to remove an electron from a molecule to form a cation. Unless stated otherwise, the initial molecule is assumed to be in its electronic (S_0) and vibrational ground state and the resultant ion is assumed to be in its lowest electronic state (I_0). Following the principles set out in section 2.1.4, ionization energies can be classed as vertical or adiabatic. In addition to the lowest or *first* ionization energy (the removal of the most weakly bound electron i.e. from the HOMO), higher ionization energies are associated with the removal of electrons from more strongly bound orbitals. Lone pairs are good sources of an ejectable electron, thus the IE of ethanol and dimethyl ether is lower than that of ethane [Gross 2011]. Ionization energies of most neutral molecules are in the range of 7-15 eV.

The *appearance energy* (AE) is the term given to the minimum amount of energy required to produce a fragment ion by excitation of a ground-state molecule to a dissociative ionic state. The analysis of fragment ion production from isolated molecules and clusters are a central part of all four results chapters in this thesis.

2.3 Multi-photon ionization

A molecule can be excited to an ionic state by absorbing a single photon (generally simply referred to as photoionization) or multiple photons. Multi-photon ionization (MPI) processes are typically labeled as (n + m), where n is the number of photons that bring (pump) a ground state molecule into a neutral excited state, and m is the number of photons that are further required to remove (probe) the electron from bound state into the continuum. For example, if it requires only one photon to bring the molecule from the ground state into an excited neutral state, and one further photon to ionize it, that process will be labeled as (1+1). If wavelengths of n and m photon are the same, the scheme is called one colour (or single colour), and if they are different then it is called two colour. Two colour MPI is denoted by putting a prime next to the m number, e.g. (1+2').

Fig. 2.7 shows four types of multiphoton processes [Weickhardt et al. 1996]. In the present work, MPI is used to investigate neutral electronic excited states and dissociative ionic states, with particular interest in delayed (*metastable*) dissociation. All the MPI results presented here are one-colour and obtained using UV-laser pulses of width 7 nanoseconds (ns) (see Chapter 3). In this case, the longer the lifetime of the

neutral electronic excited state accessed, the higher the probability for the molecule to absorb another photon during the 7 ns pulse that can ionize it. If the wavelength of the n photon matches the energy gap between the ground and the excited states, the technique is often referred as Resonance Enhanced Multiphoton Ionization (REMPI). However, this term is not preferred in this thesis as the electronic excitations in the present experiments are relatively broad.

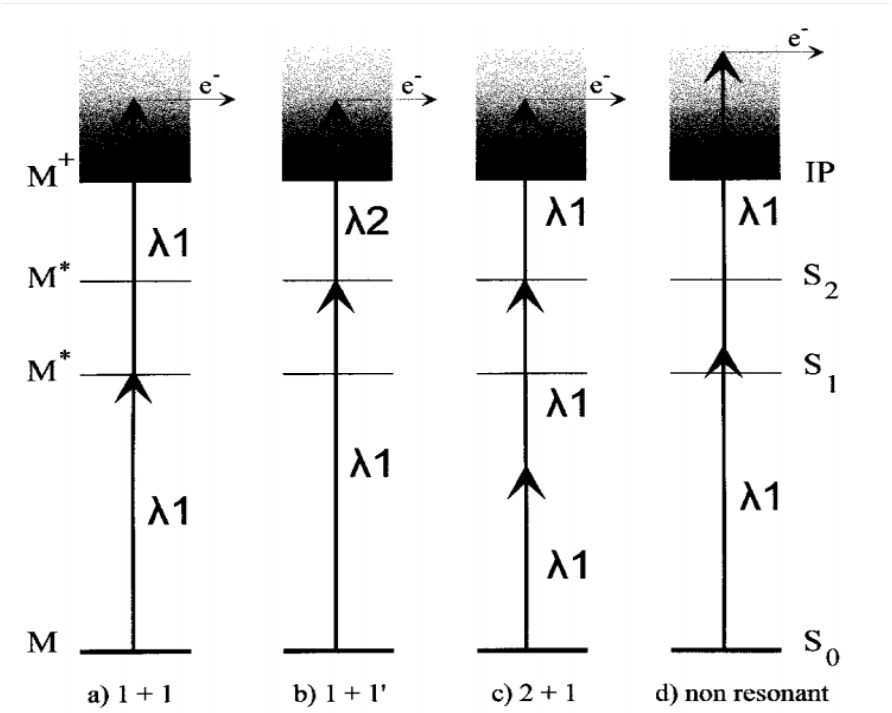

Figure 2.7: Four types of MPI processes: (a) one photon resonant one-colour two photon ionization (1+1), (b) one photon resonant two-colour two photon ionization (1+1'), (c) two photon resonant one-colour three photon ionization, and (d) non-resonant two photon ionization. Adapted from [Ryszka 2015].

MPI can also take place via *virtual* excited states but the short lifetimes of such states mean that processes of this kind are difficult to activate with our laser system. For example, Schechter et al. [1992] reported weak non-resonant MPI of xenon at 266 nm with a laser fluence of 7.49×10^{9} Wcm^{-2}. This is more than one order of magnitude

higher than the maximum average fluence of 2×10^{8} Wcm^{-2} that we can achieve using our UV laser pulses (1 mJ per pulse, pulse width 7 ns, focused to a diameter of 0.3 mm as described in Chapter 3), but still well below the level where field ionization becomes noticeable (10^{13} Wcm^{-2}) [Corkum 1993]).

Pioneered in the 1990s, time-resolved ultrafast pump-probe methods have had an enormous impact on the study of excited state dynamics. This thesis does not present time-resolved experiments but previous work of this kind provides the foundation to rationalize and interpret many aspects of our results. In time-resolved multi-photon ionization, a pump laser pulse supplies n photons and a separate a probe laser pulse provides m photons. The time delay between pump and probe pulses gives the molecule time to evolve before the probe pulse arrives. Typical timeframes for electronic, vibrational and rotational excitations are $< 10^{-15}$, 10^{-14} to 10^{-12}, and 10^{-13} to 10^{-11}s, respectively. Hence very short laser pulses are required for time-resolved study of electronic excited state dynamics, and most experiments of this kind use femtosecond-timescale pulses.

For multi-photon ionization via broad electronic excited states [Morellec et al. 1976], the order of non-linearity, K_0, provides an estimation of the number of photons absorbed (known as the *photon order*) and is given by:

$$K_0 = \frac{\partial \log N_i}{\partial \log I} \qquad \text{[Eq. 2.9]}$$

Where N_i = number of ions produced (ion yield), and I = laser pulse intensity. However, this simple relation is not true near sharp resonances [Held et al. 1973] because the laser-induced electric field can shift molecular energy levels (Stark shift, see section 2.5.1). The laser intensities used to derive photon orders in the present work ($5\text{-}9\times10^{7}$

Wcm^{-2}) (see Chapter 5) overlap with the level where Stark shifts typically become relevant: 5×10^{7}-10^{9} Wcm^{-2} [Morellec et al. 1976]. However as the present MPI experiments involve absorption into broad neutral excited states that will not be affected significantly by Stark shifts [Johnson and Otis 1981], Eq. 2.10 provides valid method to derive photon orders [Wells 2007, Otis and Johnson 1981].

2.4 Electron induced processes

Electron induced processes is a general term for all phenomena initiated by incident electrons. For example, electron attachment (EA) occurs when a free electron attaches to an atom or a molecule to form a transient negative ion, typically in the energy range below 10 eV [Massey 1976, Christophorou 1984]. Electron collisions can initiate so-called optically forbidden transitions between neutral electronic states of molecules with far greater efficiency than photons, as they are not subject to optical selection rules [Chaudhry and Kleinpoppen 2011]. In this thesis, we focus only on *electron impact ionization* (EII). EII mass spectrometry is also a key tool for optimizing our Stark deflection experiment (see Chapter 7).

When a molecule (neutral) interacts with an incident electron, some of the kinetic energy of the electron can be transferred to the molecule. If the energy transferred exceeds the *ionization energy* (*IE*) of the molecule, with the ejection of one electron creating a *molecular ion* as shown below. Depending on the molecular dynamics and on the energy of the incident electron, doubly charged and even triply charged ions may be observed, as well as multiple ions [Märk 1982].

$$M + e^{-} \rightarrow M^{+} + e^{-}\text{ (Incident electron)} + e^{-}\text{ (Ejected electron)} \qquad \text{[Eq. 2.10]}$$

In the electron collision energies used in the experiments in this thesis (e.g. 200 eV in Chapter 7), *single ionization* (the removal of one electron) is the most probable excitation process. This includes the production of fragment ions, metastable ions, and rearrangement ions [Märk 1982]. The probability of electron impact ionization can be characterized by total cross section, partial cross sections and differential cross section. These can be calculated at various levels of theory such as the binary-encounter-Bethe model [Ryszka 2015] and, at collision energies significantly above the lowest ionization energy, they increase with the molecule's size.

2.5 Stark deflection

In an ideal molecular beam experiment, the target should comprise just one type of molecule or cluster in a single and pre-defined state e.g. the electronic, vibrational and rotational ground state of a specific structure (isomer / tautomer / conformer). Charged particles can be manipulated relatively easily using external electric fields, according to their mass-to-charge ratio, or with devices such as ion-mobility spectrometers. The manipulation of neutral molecular beams poses a much greater experimental challenge [Kallmann and Reiche 1921]. The experiments using the *Compact MPI / EII* system (see Chapters 3-6) only provide limited control over the target by changing the expansion conditions of the supersonic jet. Conversely, the experiments in Chapter 7 use the inhomogeneous electric field created by device called a *Stark deflector* to manipulate the motion of neutral species in our molecular beams. This method was first used by Sterns' group to deflect and determine the permanent dipole moment of potassium iodide, which is relatively simple molecule compared to ours [Wrede 1927]. Since the mid-2000s, Meijer, Küpper and co-workers have extended it for the

separation, alignment and orientation of polar molecules on a similar scale to the ones studied in this thesis, notably 3-aminophenol, benzonitrile and iodobenzene [Filsinger et al. 2009A, Filsinger et al. 2009B]. More recently, Küpper and co-workers have also used this technique for the separation of indole-H_2O clusters [Trippel et al. 2012] from indole molecules, water molecules, and larger indole-water clusters in a mixed pulsed molecular beam. As suggested by its name, Stark deflection manipulates the motion of molecules spatially by exploiting the Stark effects of neutral molecules in strong electric fields. The next section (2.5.1) describes the physics of the interaction of neutral polar molecules with DC electric fields. Furthermore, this interaction is quantum-state specific; hence it can allow spatial separation of molecules in beams according to their quantum state. Generally, this method is applicable to all molecules, due to the invariably non-zero polarizabilities, but for non-polar molecules the interaction strength with electric fields is very small. Therefore, we restrict our discussion to polar molecules.

2.5.1 Molecules in inhomogeneous electric fields

A polar molecule exhibits a permanent electric dipole moment. The interaction of this dipole with an external electric field leads to wavefunction hybridization, known as the Stark effect. The resulting energy shift is given by:

$$W = \vec{\mu} . \vec{\varepsilon} = -\mu\varepsilon\langle\cos\theta\rangle = \mu_{eff}\varepsilon \qquad \text{[Eq. 2.11]}$$

Where $\vec{\mu}$ = dipole moment, $\vec{\varepsilon}$ = the electric field, and θ = angle between the two vectors. The angular probability distribution and, hence, the expectation value of $\langle\cos\theta\rangle$ is defined by the molecule's rotational wavefunction [Gordy and Cook 1984]. The resulting *effective dipole moment* is given along the electric field axis is the space-fixed

dipole moment of the molecule. As $\langle \cos\theta \rangle$ is a property of a specific quantum state, so too is $\mu_{eff.}$

In field-free space, the different projections M of the angular momentum onto the laboratory axis are degenerate. The angular probability density is spherical so $\langle \cos\theta \rangle = 0$. The Stark effect lifts this degeneracy and mixes the wavefunctions, hence the value of $\langle \cos\theta \rangle \neq 0$. In this case, Eq. 2.11 shows that the energy of the state depends on external field strength ε. If the external field is inhomogeneous in space, the molecule therefore experiences an attractive force towards weaker or stronger electric field, depending on the sign of $\langle \cos\theta \rangle$ (and hence on the sign of μ_{eff} (ε)). The corresponding states can be described as *low-field-seeking* (lfs) or *high-field-seeking* (hfs).

Under the Born–Oppenheimer approximation [Gordy and Cook 1984], the electronic and nuclear degrees of freedom can be separated. For a rigid closed-shell molecules in a strong electric field, we can then describe the rotational wavefunctions coupling with the molecular frame of fixed dipole moment μ using a fixed effective dipole moment $\mu_{eff.}$ The detailed description of the method used to calculate Stark energies and effective dipole moments for a linear top, a symmetric top and an asymmetric top is described in Chapter 7. Briefly, Fig. 2.8 gives two examples of how Stark energies (W) can increase or decrease as a function of electric field strength ε and, correspondingly, how the effective dipole moments $\mu_{eff}(\varepsilon)$ can be negative or positive.

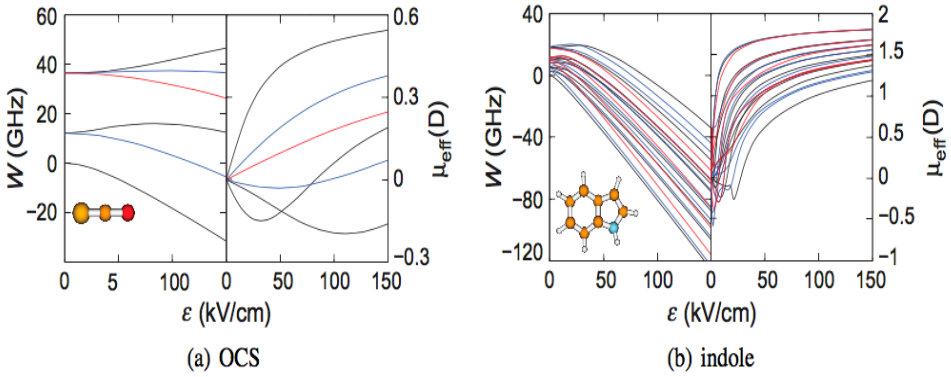

Figure 2.8: Stark energies W and effective dipole moments μ_{eff} of (a) the linear-top molecule OCS and (b) the asymmetric-top molecule indole for the M = 0 (black), M = 1 (blue), and M = 2 (red) levels of all J = 0-2 states calculated using CMIstark [Chang et al. 2014].

The field-strength dependence of the Stark energy together with the principle of minimum energy enables the force $\vec{F}$ exerted on the molecule in a Stark deflector to be calculated using the relation below.

$$\vec{F} = -\vec{\nabla} W = \mu_{eff}(\varepsilon).\vec{\nabla}\varepsilon \qquad \text{[Eq. 2.12]}$$

Ideally, the electric field gradient inside the deflector would exert a strong and constant force in one direction, while there will be absence of any force in the perpendicular direction. A close approximation to this ideal can be achieved using the *two-wire* arrangement of deflector electrodes described in Chapter 3 [Ramsey 2005]. States (with different effective dipole moments) experience different deflection forces in the field. Hence, while traveling through the field they acquire different transverse velocities depending on their effective dipole moment to mass ratio. For example, benzonitrile in a 100 kV/cm field exhibits a Stark shift of −6.71 cm^{-1}, and an effective dipole moment of 0.0759 cm^{-1}/(kV/cm) [Putzke et al. 2012]. Filsinger et al. [2009B] have observed a ≈ 2 mm deflection of benzonitrile at the distance of 0.22 m after their Stark deflector. Moreover, structural isomers of complex molecules and even molecular clusters of different sizes can exhibit different dipole moments, which leads to different dipole

moment to mass ratios. Hence, different structural forms of complex molecules and even molecular clusters can be spatially separated.

2.5.2 Production of rotationally cold molecular beams

In order to achieve a sufficiently high effective dipole moment for Stark deflection, the molecules or clusters of interest must be in low rotational states. Furthermore, the separation of different species within a mixed beam can be achieved most effectively for rotationally cold ensembles with relatively few states occupied with significant populations. The probability p_i that a system having temperature T will be found in a state with energy ϵ_i is given by the Boltzmann rotational distribution and is expressed as [Pullman et al. 1990]:

$$p_i = \frac{\exp\left(-\epsilon_i / k_b T\right)}{Q} \qquad \text{[Eq. 2.13]}$$

Where k_b = Boltzmann constant ($k_b = 8.617 \cdot 10^{-5}$ eV/K), and Q = the system's partition function (the sum of Boltzmann factors for all accessible states). In the experiments in this thesis, molecular cooling is achieved by means of supersonic expansion.

Experimental molecular beams can be separated into two types: effusive or supersonic [Morse 1996]. Effusive beams are formed when the majority of molecules experience no collisions as they leave the reservoir, in other words when their mean free path (λ_0) is much larger that the diameter of the orifice (D) i.e. ($\lambda_0 \gg D$). Hence, effusive beams have similar temperatures to their reservoirs. On the contrary, the molecules in supersonic beams experience collisions during expansion from a higher pressure to a lower pressure. These collisions provide the opportunity to convert internal thermal

energy to translational thermal energy and hence produce internally cold molecules. Supersonic beams are discussed in detail in the next section.

2.5.2.1 Supersonic expansion of gas

A supersonic jet is formed when gas expands through an orifice with diameter (D) significantly larger than the mean free path (λ_0) of the gas particles i.e. $\lambda_0 \ll D$. The expansion can be divided into three stages [Hillenkamp et al. 2003]:

1. Near-nozzle - Due to high density of particles in the jet, collision events are sufficiently frequent to maintain equilibrium conditions. For monoatomic gases, this stage of the expansion can be described in terms of the thermodynamics of an expanding ideal gas.

2. Intermediate stage - The jet density falls to a point where internal degrees of freedom gradually decouple as collision events becomes less frequent.

3 Free molecular flow stage - This is the final stage where jet density has dropped to a point where collision events are so rare that no further cooling occurs.

The transition points from one stage of the expansion to another are gradual. However, in typical experimental supersonic jets, the free molecular flow stage can be considered to extend to a distance of 20 D from the nozzle orifice [Lubman et al. 1982]. This corresponds to 1 mm (with the 50 μm nozzle used in the experiments in Chapters 4 and 5, as well as in some of those in Chapter 7) or 0.6 mm (with the 30 μm nozzle used in the remaining experiments in Chapter 7).

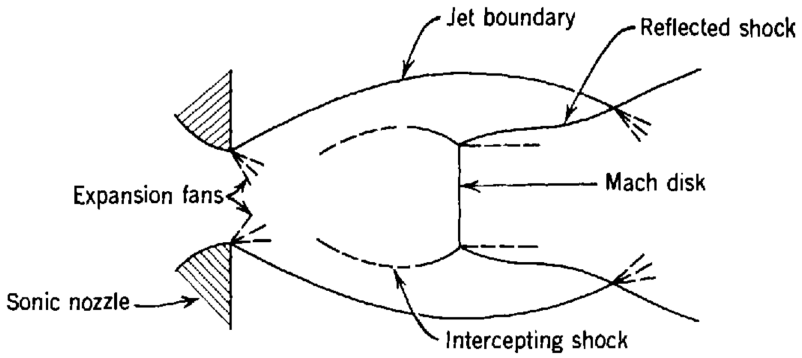

Figure 2.9: Illustration of shocks in a typical experimental free-jet expansion. Adapted from [Ryszka 2015].

As shown in Fig. 2.9, two distinctive shock zones develop due to the interaction of the expansion with the background gas: the *intercepting shock* (often called the barrel shock) and the *Mach disk*. The intercepting shock forms an envelope around the centerline of the propagation of the expansion, whereas the Mach disk is a nearly a flat terminal shock wave perpendicular to the propagation axis. The distance of the Mach disk from the nozzle is given by equation below [Lubman et al. 1982]:

$$x_m = 0.67\ D\ \sqrt{\frac{p_o}{p_B}} \qquad \text{[Eq. 2.14]}$$

Where p_o = pressure in the gas reservoir and p_B = residual pressure in the expansion chamber. The Mack disk position in our Stark experiment is 3.5 cm for p_o = 300 mbar, $p_B = 10^{-4}$ mbar and D = 30 μm. The *zone of silence* is the volume where the expansion can reasonably be assumed to be undisturbed by turbulence and it lies inside the *envelope* defined by the intercepting shock and terminated by the Mach disk. The gas flow is nearly undisturbed before the Mach disk (where significant turbulence is to be expected). A skimmer is typically placed inside the silence zone to perform experiments on the undisturbed molecular beam in high vacuum conditions. This method allows for transmitting the central core of the beam into adjacent chamber. The skimmers in our

experiments have aerodynamic shapes and sharp edges to minimize the possibility of introducing any turbulence. Skimmers are often placed at some distance from the chamber wall to avoid interaction with the gas particles scattered from the back wall; this represents a possible route for improving the supersonic expansion conditions in our experiments in the future.

2.5.2.2 Translational cooling of expanding gas

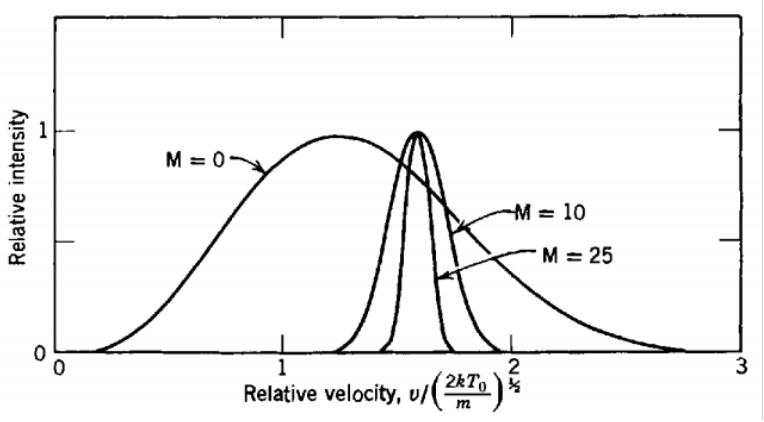

Figure 2.10: Velocity distributions for two Mach numbers in supersonic jets. Maxwell-Boltzmann distribution of the reservoir gas marked as M = 0. Adapted from [Ryszka 2015]

Translational cooling in a supersonic expansion dramatically modifies the velocities of the atoms/molecules with respect to each other. Fig. 2.10 shows a Maxwell-Boltzmann velocity distribution (a typical thermal distribution) for a static gas as well as for two supersonic jets. The ratio of the average flow velocity of the gas to its speed of sound is called the *Mach number*. If the Mach number of a molecular beam is lower than unity then the flow is sub-sonic and if it is higher then it is supersonic. Due to significant cooling of the gas during the supersonic expansion, its local speed of sound is reduced proportionally with $\sqrt{T}$ [Morse 1996]. The enthalpy of the system is conserved during

the expansion under the adiabatic assumption such that:

$$H(x) + \frac{1}{2} mv(x)^2 = \text{constant} \qquad \text{[Eq. 2.15]}$$

Where H(x) = the molar enthalpy of the gas, m = the mass of the atom/molecule, and v(x) = its velocity at position x. Furthermore, the flow of a supersonic jet is directional. Hence, the mean velocity of the gas is not zero. This means that the translational temperature of the gas cannot be determined by the root-mean-square of the velocity distribution, but by the width of said distribution. Eq. 2.15 can be rewritten to obtain the maximum velocity of gas, v_{max}, when all the enthalpy is converted into kinetic energy.

$$v_{max} = \sqrt{\frac{2H(T_0)}{m}} \qquad \text{[Eq. 2.16]}$$

Where $H(T_0)$ = enthalpy of the gas at the temperature of the source reservoir. Typical experimental supersonic jets are formed by seeding a low density of molecules in an expansion of a noble gas. Table 2.2 shows the effect of reservoir temperature kept at 300 and 530 K on maximum velocity of noble gases in a supersonic expansion, calculated using Eq. 2.16.

Table 2.2: Maximum velocities for various noble gases in a supersonic expansion from a reservoir at 300 K (approximately room temperature) and 530 K (a typical temperature of the gas immediately prior to expansion in our experiments in Chapters 4 and 5)

	v_{max} (ms^{-1}) of noble gas atoms in a supersonic expansion				
Temperature (K)	Helium	Neon	Argon	Krypton	Xenon
300	1770	786	559	386	308
530	2300	1032	730	510	406

In this simple model, the expression for the temperature at large distance x/D is given by Eq. 2.17 [Morse 1996]:

$$\frac{T(x)}{T_0} = B\left(\frac{x-x_0}{D}\right)^{-2(\gamma-1)} \qquad \text{[Eq. 2.17]}$$

Where B = a parameter specific for the expanding gas depends on γ [for more details see Morse 1996], x_0= position at which the expansion begins, and γ = the ratio of specific heats of the gas. In reality, the density of the beam soon drops to a level where collisions are rare and this prohibits the gas from maintaining thermal equilibrium and the cooling stops.

The terminal Mach number, M_T, beyond which no further cooling happens, can be expressed in the form of Eq. 2.18 [Morse 1996]:

$$M_T = G\left(\frac{D_\epsilon}{\lambda_0}\right)^{\frac{(\gamma-1)}{\gamma}} \qquad \text{[Eq. 2.18]}$$

Where G = a parameter dependent only on γ. A collisional effectiveness parameter ε denotes the maximum fractional change in the mean random velocity per collision (dependent on the gas). For example, Eq. 2.18 becomes 2.19 [Lubman et al. 1982], when the expanding gas is argon, the pressure p_0 is expressed in bars, and the orifice diameter is expressed in centimeters.

$$M_T = 133.(p_0 D)^{0.4} \qquad \text{[Eq. 2.19]}$$

In fact, the relation above approximates any expansion behavior of any monoatomic gas, with the notable exception of helium [Toennies and Winkelmann 1977]. Classical mechanics calculations for helium give good approximations at low values of p_0D (less than 50 mbar·cm) at room temperature. At higher p_0D values, quantum mechanical calculations must be used. Fig. 2.11 shows the ratios of terminal velocity (i.e. the maximum velocity that a falling body in a gaseous atmosphere can attain) to mean

thermal velocity (directly proportional to terminal temperature) for helium and neon. The quantum-mechanical curve for helium clearly shows improved cooling at high p_0D product values but for neon, this effect is barely observable. In our case the value of p_0D product is only 0.675 torr cm (for p_0 = 300 mbar and D = 30 μm) where classical approximation is adequate.

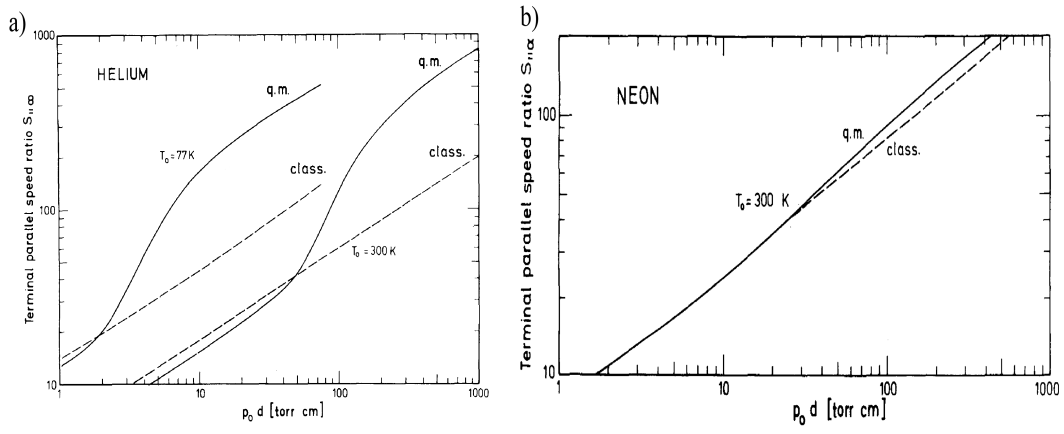

Figure 2.11: Terminal speed ratios ($V_{max}/V_{Thermal}$) of a) helium and b) neon, as a function of p_0D. Solid curves have been produced with quantum-mechanical calculations, whereas the dashed lines represent classical mechanics calculations. Adapted from [Ryszka 2015].

The Eq. 2.17 can be rewritten in terms of Mach number as follows:

$$T(x) = T_0.\left(1 + \frac{\gamma-1}{2}.M(x)^2\right) \qquad \text{[Eq. 2.20]}$$

The terminal translational velocity of the supersonic jet can be obtained by substituting M(x) in Eq. 2.20 and its terminal value given by equation Eq. 2.18 (in case of argon Eq. 2.19). Hence, to obtain the lowest possible translational temperature, it is advantageous to use a colder gas in the reservoir with fewer degrees of freedom (ideally a monoatomic gas), and / or to increase p_0D product. Internal degrees of freedom are critically important in the context of Stark deflection (Chapter 7). See section 2.5.2.6 for

a description of vibrational and rotational cooling in supersonic beams.

2.5.2.3 Mass flow

Using the continuity equation and Bernoulli's equation, mass flow rate (dm/dt) through an orifice can be derived and is given by Eq. 2.21 [Zou et al. 2002]:

$$\frac{dm}{dt} = \sqrt{\frac{\gamma}{R}\left(\frac{2}{\gamma+1}\right)^{(\gamma+1)/(\gamma-1)}} \cdot \frac{p_0}{\sqrt{T_0}} \cdot A \qquad \text{[Eq. 2.21]}$$

Where A = area of the orifice and R = gas constant (R = 8.31 J/mol/K). For a circular orifice of diameter D and grouping the various constants together into a single parameter, C_{gas}, Eq. 2.21 can be expressed simply in the form of Eq. 2.22. Therefore, for any given gas at a stable temperature, the gas load is proportional to the reservoirs' pressure and the square of nozzle diameter.

$$\frac{dm}{dt} = \frac{\pi}{4} \cdot \frac{C_{gas}}{\sqrt{T_0}} \cdot p_0 D^2 \qquad \text{[Eq. 2.22]}$$

2.5.2.4 Molecular beam production and the velocity slip effect

By adding a small amount of a second species (vapor released from a liquid or powder sample in our case) into the carrier gas, a seeded molecular beam is produced. However, if the relative amount of seeded species is small, the behavior of the gas mixture is dominated by the more abundant species. In this case, the carrier gas atoms will impact on the slower and heavier seeded molecules repeatedly, resulting in the molecules attaining nearly the same velocity of the carrier gas atoms. Furthermore, the heavier molecules reach nearly the same terminal translational temperature as the carrier gas. However, if the partial pressures of the two species are relatively similar the *velocity*

slip effect may be observed [Morse 1996]. In this condition, the acceleration of the heavier species (typically the seeded molecules) is incomplete [Amirav 1980] and therefore the two constituents reach different terminal temperatures. The velocity slip effect is more noticeable for the lighter carrier gases. Amirav [1980] investigated this experimentally, and their results suggest that cooling efficiency follows natural order of He<Ne<Ar<Kr<Xe. To achieve the same amount of cooling with He as with Xe, the flow rate of the He should be 400 times greater than Xe [Amirav 1980].

2.5.2.5 Production of clusters

As discussed in section 2.5.2.1, during the first stage of expansion, multi-body collisions are very frequent in a supersonic beam and the temperature of the gas decreases very rapidly. These conditions can enable efficient cluster formation. This phenomena was noticed very early in the studies related to supersonic beams and has led to extensive research [Allan 2007, Berden et al. 1996, Bruny et al. 2012] on molecular (and indeed atomic) clusters formed this way.

The formation of a cluster decreases the total energy of a system significantly and therefore a third body is required to remove this excess of energy. The number of binary collisions varies proportionally with p_0D in the expansion, whereas the number of three-body collisions varies as $p^2{}_0D$. At the same time, the mass throughput varies as p_0D^2. Hence, to maximize the production of clusters without increasing gas flow, the nozzle orifice diameter should be decreased while reservoir pressure is increased (maintaining a constant value of p_0D^2). Additionally, clustering also depends on the nozzle temperature. Yang et al.'s [2007] studies of methane clusters have demonstrated that the

average cluster size was larger for a nozzle temperature of -30° C than for 27° C. However, we use higher nozzle temperatures to produce more molecular clusters in our experiments because we have found that the tendency to increase clustering due to the resultant density of molecules in the expansion dominates over the tendency to decrease clustering due to the hotter nozzle.

2.5.2.6 Rotational and vibrational cooling

All degrees of freedom are coupled together due to near-equilibrium conditions in the near-nozzle stage of the expansion. Collisions with the carrier gas cool internal degrees of freedom in addition to translational cooling. However, as the expansion progresses (into the intermediate stage of expansion), the jet density drops and collisions become less frequent. This causes the degrees of freedom to gradually decouple, and limits the amount of vibrational and rotational cooling. Hence, it is then necessary to introduce the concept of independent translational, vibrational, and rotational temperature. Only a scattering process can cool the internal degrees of freedom. The probability of changing a molecule's vibrational or rotational energy in a collision with an atom can be calculated by solving Schrodinger's equation for the specific molecule, atom and vibrational or rotational state involved. Analysis of the simplest systems can be found in reference [Zener 1931], but the general conclusions can be applied to most atom-molecule collisions.

The translational and vibrational degrees of freedom typically decouple first [Levy 1981] because the intra-molecular binding forces are large compared to inter-molecular repulsion forces at scattering distances. The typically long timescale of vibrational

motion is generally small compared to collision timescales [Zener 1931] further reduces the probability of coupling. Hence the vibrational temperature is usually higher than the translational and rotational temperature in a supersonic molecular beam. Amirav [1980] reported achieving a vibrational temperature T_V = 50 K for supersonic-expanded tetracene ($C_{18}H_{12}$) with p_0D = 2.3. In contrast, the translational temperature was equal to T_T = 7 K. However, as the spacing between vibrational levels of typical molecules is relatively large, even a temperature as high as 50 K leads to a very limited number of vibrational levels being occupied with significant populations.

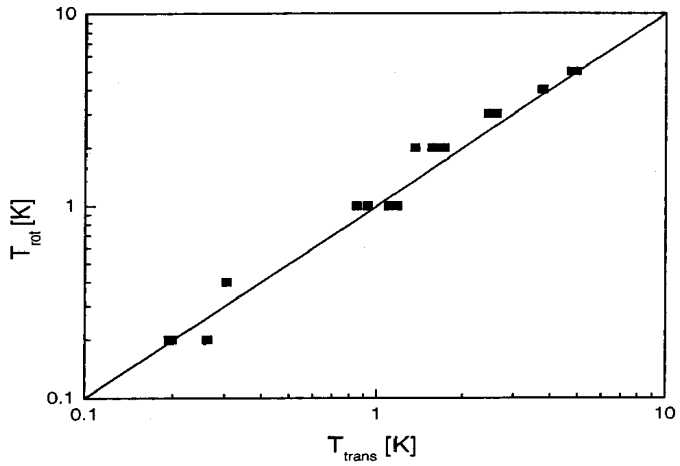

Figure 2.12: Relation between rotational and translational temperatures of aniline in a supersonic expansion. Rotational temperatures have been measured from LIF spectra, while translation temperatures have been calculated based on expansion parameters. Adapted from [Ryszka 2015].

On the other hand, rotational degrees of freedom decouple relatively late [Zener 1931, [Amirav 1980] because rotational relaxation is a much faster process. This increases the probability of changing quanta of rotational energy during a scattering event and hence the rotational temperature in a supersonic beam is typically close to the translational temperature [Amirav 1980]. Fig. 2.12 shows that the translational and rotational

temperatures of aniline follow each other closely. However, a significant number of states can be populated even in a beam with rotational temperature of few K because rotational states in large molecules are separated by very low energies.

2.6 Summary

This chapter gives a brief introduction to the molecular excitation and relaxation processes that are investigated using multi-photon ionization (MPI) in Chapters 4-6. These processes also play critical roles in electron impact ionization (EII) experiments that we use to characterize the Stark deflection experiment in Chapter 7. Particular emphasis is placed on the importance of the concept of a conical intersection in order to understand the electronic excited state dynamics of DNA and RNA bases. Hydrogen bonding is discussed as it is the main mechanism that binds the neutral and positively-charged hydrated thymine clusters investigated in Chapter 5. The Stark effect in strong electric fields and the production of cold molecular beams is described as this provides the fundamental basis for the manipulation of neutral molecular beams using the Stark deflection method. Although the fundamental principles governing the dynamics of excited neutral molecules, ions, and clusters are well established, their complexity is too great to be treated by theory alone in all but the simplest systems. Therefore experiments are essential to characterize radiation damage processes in the biological building blocks investigated in this thesis. The next chapter describes the main experimental tools that I have been exploiting and developed over the course of my PhD.

References:

- A. Abo-Riziq, L. Grace, E. Nir, M. Kabelac, P. Hobza and M. S. de Vries, *Proceedings of the National Academy of Sciences*, 2005, **102**, 20-23.
- M. Allan, *Phys. Rev. Lett.*, 2007, **98**, 123201.
- A. Amirav, U. Even and J. Jortner, *Chem. Phys.*, 1980, **51**, 31-42.
- M. Barbatti, A. C. Borin and S. Ullrich, *Photoinduced Phenomena in Nucleic Acids I: Nucleobases in the Gas Phase and in Solvents (topics in Current Chemistry 355), Springer,* 2014.
- B. Barc, M. Ryszka, J. C. Poully, E. Jabbour Al Maalouf, Z. El Otell, J. Tabet, R. Parajuli, P. J. M. Van Der Burgt, P. Limão-Vieira, P. Cahillane, M. Dampc, N. J. Mason and S. Eden, *Int. J. Mass Spectrom.*, 2014, **365-366**, 194-199.
- P. Bartl, C. Leidlmair, S. Denifl, P. Scheier and O. Echt, *Chem. Phys. Chem.*, 2013, **14**, 227-232.
- G. Berden, W. L. Meerts, M. Schmitt and K. Kleinermanns, *J. Chem. Phys*., 1996, **104**, 972-982.
- J. H. Beynon, J. R. Gilbert, Energetics and Mechanisms of Unimolecular Reactions of Positive Ions: Mass Spectrometric Methods, in *Gas Phase Ion Chemistry*; Bowers, M.T. (ed.); Academic Press, New York, **Vol. II,** 1979.
- A. Boatwright, J. Jeffs and A. J. Stace, *J. Phys. Chem. A*, 2007, **111**, 7481-7488.
- M. Born and J. R. Oppenheimer, *Annalen der Physik*, 1927, **84**, 457-484.
- G. Bruny, S. Eden, S. Feil, R. Fillol, K. El Farkh, M. M. Harb, C. Teyssier, S. Ouaskit, H. Abdoul-Carime, B. Farizon, M. Farizon and T. D. Märk, *Rev. Sci. Instrum.*, 2012, **83**, 013305.
- B. Brutschy, *J. Phys. Chem.*, 1990, **94**, 8637-8647.
- Y. P. Chang, F. Filsinger, B. Sartakov and J. Küpper, *Comp. Phys. Comm.,* 2014, **185**, 339-349.
- A. Chaudhry and H. Kleinpoppen, *Analysis of Excitation and Ionization of Atoms and Molecules by Electron Impact, volume 60 of Springer Series on Atomic, Optical, and Plasma Physics. Springer*, 2011.
- L. Christophorou*, Electron-Molecule Interactions and Their Applications, Academic Press INC*, **Volume 1***,* 1984.
- P. B. Corkum, *Phys. Rev. Lett.*, 1993, **71**, 1994-1997.
- G. H. Dunn, *J. Chem. Phys*., 1966**, 44**, 2592-2594.
- T. R. Dyke, B. J. Howard and W. Klemperer, *J. Chem. Phys.*, 1972, **56**, 2442-2454.

- F. Filsinger, J. Küpper, G. Meijer, J. L. Hansen, J. Maurer, J. H. Nielsen, L. Holmegaard and H. Stapelfeldt, *Angew. Chem. Int. Ed.*, 2009A, **48**, 6900-6902.
- F. Filsinger, J. Küpper, G. Meijer, L. Holmegaard, J. H. Nielsen, I. Nevo, J. L. Hansen and H. Stapelfeldt, *J. Chem. Phys*., 2009B, **131**, 064309.
- J. P. Gallivan and D. A. Dougherty, *Proceedings of the National Academy of Sciences*, 1999, **96**, 9459-9464.
- J. H. Gross, *Mass Spectrometry: A Textbook, Springer*, **2nd edition**, 2011.
- W. Gordy and R. L. Cook, *Microwave Molecular Spectra,* **3rd edition**. *Wiley*, 1984.
- B. Held, G. Mainfray, C. Manus, J. Morellec and F. Sanchez, 1973, *Phys. Rev. Lett.,* **30**, 423-426.
- M. Hillenkamp, S. Keinan and U. Even, *J. Chem. Phys.*, 2003, **118**, 8699-8705.
- T. Hirata, H. Ikeda and H. Saigusa, *J. Phys. Chem. A*, 1999, **103**, 1014-1024.
- J. M. Hollas, *Modern Spectroscopy, John Wiley & Sons,* **4th edition**, 2003.
- P. M. Johnson and C. E. Otis, *Annu. Rev. Phys. Chem.*, 1981, **32**, 139-157.
- B. Johnson and W. Reinhardt, *J. Chem. Phys.*, 1986, **85**, 4538-4556.
- R. L. Johnston, *Atomic and Molecular Clusters, Taylor and Francis*, 2002.
- H. Kallmann and F. Reiche, *Zeitschrift für Physik*, 1921, **6**, 352-375.
- C. Leidlmair, P. Bartl, H. Schöbel, S. Denifl, S. Yang, A. M. Ellis and P. Scheier, *Chem. Phys. Chem.*, 2012A, **13**, 469-476.
- C. Leidlmair, Y. Wang, P. Bartl, H. Schöbel, S. Denifl, M. Probst, M. Alcamí, F. Martín, H. Zettergren, K. Hansen, O. Echt and P. Scheier, *Phys. Rev. Lett.*, 2012B, **108**, 076101.
- D. H. Levy, *Science*, 1981, **214**, 263-269.
- R. H. Lipson, *Ultraviolet and Visible Absorption Spectroscopy, in Encyclopedia of Applied Spectroscopy, Wiley-VCH: Berlin, Andrews,* **D.L. edition***,* 2009.
- M. Liu, T. Li, F. S. Amegayibor, D. S. Cardoso, Y. Fu and J. K. Lee, *J. Org. Chem.*, 2008, **73**, 9283-9291.
- D. M. Lubman, C. T. Rettner and R. N. Zare, *J. Phys. Chem.*, 1982, **86**, 1129-1135.
- J. Makarewicz, *J. Phys. A Math. Gen.*, 1985, **18**, 557-565.
- C. R. Martinez and B. L. Iverson, *Chem. Sci.,* 2012, **3**, 2191-2201.
- S. H. Massey, *Negative Ions, Cambridge University Press*, 1976.
- T. D. Märk, *Int. J. Mass Spectrom. Ion Phys*., **1982,** 45, 125-145.
- M. Meot-Ner, *J. Am. Chem. Soc.*, 1979, **101**, 2396-2403.

- J. Morellec, D. Normand and G. Petite, *Phys. Rev. A*, 1976, **14**, 300-312.
- M. D. Morse. *Methods of Experimental Physics: Atomic, Molecular, and Optical Physics, Academic Press Inc.*, **Vol. II***,* 1996.
- E. Nir, K. Kleinermanns and M. S. de Vries, *Nature*, 2000, **408**, 949–951.
- E. Nir, C. Janzen, P. Imhof, K Kleinermanns and M. S. de Vries, *Phys. Chem. Chem. Phys.*, 2002, **4,** 732-739.
- C. E. Otis and P. M. Johnson, *Chem. Phys. Lett.*, 1981, **83**, 73-77.
- H. S. Park, S. H. Nam, J. K. Song, S. M. Park and S. Ryu, *J. Phys. Chem. A*, 2008, **112**, 9023-9030.
- S. Perun, A. L. Sobolewski and W. Domcke, *J. Am. Chem. Soc.*, 2005A, **127**, 6257-6265.
- S. Perun, A. L. Sobolewski and W. Domcke, *Chem. Phys.*, 2005B, **313**, 107-112.
- R. H. Petrucci, W. S. Harwood, F. G. Herring, J. D. Madura, *General Chemistry: Principles and Modern Applications, Pearson*, **9th edition***,* 2007.
- L. Piela, *Ideas of Quantum Chemistry, Elsevier, Amsterdam,* **1st edition**, 2007.
- S. Pisana, M. Lazzeri, C. Casiraghi, K. S. Novoselov, A. K. Geim, A. C. Ferrari and F. Mauri, *Nat. Mater.*, 2007, **6**, 198-201.
- D. P. Pullman, B. Friedrich and D. R. Herschbach., *J. Chem. Phys.,* 1990, **93**, 3224-3236.
- S. Putzke, F. Filsinger, J. Küpper and G. Meijer, *The Journal of Chemical Physics*, 2012, **137**, 104310.
- N. F. Ramsey, *Molecular Beams The International Series of Monographs on Physics, Oxford University Press London,* 2005.
- D. L. Reger, S. R. Goode and D. W. Ball, *Chemistry: Principles and Practice*, 2009.
- M. Richter, S. Mai, P. Marquetand and L. González, *Phys. Chem. Chem. Phys.*, 2014, **16**, 24423-24436.
- M. Ryszka, Radiation induced processes in biomolecules and clusters in controlled beams, Department of Physical Sciences, The Open University, Milton Keynes, United Kingdom, *PhD thesis*, 2015.
- I. Schechter, H. Schröder and K. L. Kompa, *Chem. Phys. Lett.*, 1992, **194**, 128-134.
- G. Scoles, *Atomic and Molecular Beam Methods. Atomic and Molecular Beam Methods. Oxford University Press*, 1988.
- R. Seiler, *Int. J. of Quant. Chem.,* 1969, **3**, 25-32.
- D. Shemesh, C. Hattig and W. Domcke, *Chem. Phys. Lett.*, 2009A, **482**, 38-43.
- D. Shemesh, A. L. Sobolewski and W. Domcke, *J. Am. Chem. Soc.*, 2009B, **131**,

1374-1375.

- A. L. Sobolewski and W Domcke, *Phys. Chem. Chem. Phys.,* 2006, **8**, 3410-3417.
- N. G. Szwacki, A. Sadrzadeh and B. I. Yakobson, *Phys. Rev. Lett.*, 2007, **98**, 166804.
- J. P. Toennies and K. Winkelmann, *J. Chem. Phys.*, 1977, **66**, 3965-3979.
- S. Trippel, Y.-P. Chang, S. Stern, T. Mullins, L. Holmegaard and J. Küpper, *Phys. Rev. A*, 2012, **86**, 033202.
- N. Turro, V. Ramamurthy and J. Scaiano, *Principles of Molecular Photochemistry: An Introduction. University Science Books,* 2009.
- C. Weickhardt, F. Moritz and J. Grotemeyer, *Eur. J. Mass Spectrom.*, 1996, **2**, 151-160.
- K. Wells, G. Roberts and V. Stavros, *Chem. Phys. Lett.*, 2007, **446**, 20-24.
- C. Woywod, W. Domcke, A. L. Sobolewski and H. J. Werner, *J. Chem. Phys.*, 1994, **100**, 1400-1413.
- E. Wrede, *Z. Phys.*, 1927, **44**, 261-268
- S. Yang, L. Philippe and M. Châtelet, *Int. J. of Mass Spectrom.*, 2007, **263**, 190-194.
- D. R. Yarkony, *Nonadiabatic Derivative Couplings, John Wiley & Sons,* 2002.
- C. Zener, *Phys. Rev.*, 1931, **37**, 556-569.
- X. Zou, X. Wang, C. Luo and M. Han, *IEEE Transac. on Plasma Sci.*, 2002, **30**, 482-487.

CHAPTER 3

Experimental

This chapter describes the two main experimental systems in the Molecular Clusters Laboratory at The Open University and the work that I have carried out to optimize and extend their performance. The experiments use time-of-flight mass spectrometry to detect ions produced by laser or electron beam interactions with molecules and clusters.

3.1 Introduction

This PhD thesis presents results from two different experimental set-ups using *Reflectron time-of-flight* mass spectrometry to study isolated molecules and their clusters. The first approach (*Compact MPI/EII Experiment*) involved using ultraviolet-multi-photon ionization (UV-MPI) and electron impact ionization (EII) mass spectrometry to study isolated DNA/RNA nucleobases and their clusters and also 3-aminophenol. The second approach (*Stark Deflection Experiment*) involved using MPI and EII mass spectrometry on Stark deflected molecules and their clusters.

The *Compact MPI/EII Experiment* configuration produces a CW beam of molecules seeded in a supersonic expansion of argon or helium. The expansion nozzle is only 10 cm apart from the ionizing beam, which results in very strong signals as compared to the *Stark Deflection Experiment*. However, the *Stark Deflection Experiment* brings the key advantage to being able to manipulate polar molecules and clusters within supersonic beams with the aim of selecting specific targets from mixed beams. Hence, the two approaches complement each other in terms of probing UV- and electron-induced processes in molecules and clusters.

The *Compact MPI/EII Experiment* was built mainly by B. Barc (former PhD student in the Molecular Clusters Group) with subsequent modifications by E. al Maalouf (former MSc project student) and M. Ryszka (former PhD student). The system is described in detail in Barc's PhD thesis [2012] and Ryzska's PhD thesis [2015]. Shorter descriptions of the experiment are provided in the Group's recent publications on isolated and hydrated nucleobases [Barc et al. 2013, Barc et al. 2014, Ryszka et al. 2016, Pandey et al. 2017]. Section 3.2 provides a summary of the experimental set-up. In addition to exploiting the techniques that were already used in the *Molecular Clusters Group* before I arrived, I have worked on enhancing the system in three ways. Firstly, I optimized the experiment to gain the best possible signal (see section 3.2.3 and 4.3). Secondly, I have worked on the development of a method to measure fragment ion kinetic energies (see section 3.2.3). I have also extended the Group's technique to study metastable fragmentation of excited ions and cluster ions (see sections 3.2.2, 3.2.4, Chapter 5, and section 6.4.1) by producing *maps* of ion signal against time-of-flight and reflection voltage (Figs. 5.2 and 6.8). Finally, I have built a new source for gas-phase target molecules based on *laser thermal heating* (described in Chapter 6). Results

obtained from the *Compact MPI/EII Experiment* are presented in Chapters 4-6. The last section (3.3) of this chapter gives a description of a new experiment that we have developed in the Molecular Clusters Group to study MPI, EII, and (eventually) electron attachment on Stark-deflected molecules and clusters (*Stark Deflection Experiment*). This experiment was mainly built by Michal Ryszka but I have also made various contributions to its assembly and optimization. In particular, I designed and characterized the moveable lens system necessary for MPI measurements of deflected molecules. Results obtained from the Stark deflection experiments are presented in Chapter 7.

3.2 The Compact MPI/EII Experiment

3.2.1 Overview

Fig. 3.1 shows a schematic of the *Compact MPI/EII Experiment*. The experiment probes ion production when a laser or electron beam crosses a target beam containing isolated molecules and / or molecular clusters. As shown in Fig. 3.1, argon or helium buffer gas seeded with vapor from a heated powder cartridge and / or a liquid reservoir flows continuously through a pinhole nozzle into a pumped chamber to form a supersonic jet. The buffer gas pressure is typically varied between 0.5 and 2 bar. The jet passes through a skimmer into a second pumped chamber and crosses a pulsed UV laser beam for MPI measurements or an electron beam from a commercial gun (Kimball ELG-2) for electron impact ionization experiments (EII). The skimmer is typically kept at 125°C to avoid molecular deposition and its temperature is monitored by another thermocouple. The separation of the nozzle and the skimmer is typically 1 cm. The third harmonic

output (355 nm) of an Nd:YAG laser system (Continuum Powerlight II 8000) provides the pump source for a dye laser (Sirah Cobra-Stretch). Coumarin dyes give access to the wavelength range 220-277 nm after frequency doubling and a diffraction grating with groove density 1,800 lines/mm enables the wavelength to be selected with a resolution better than 10^{-3} nm.

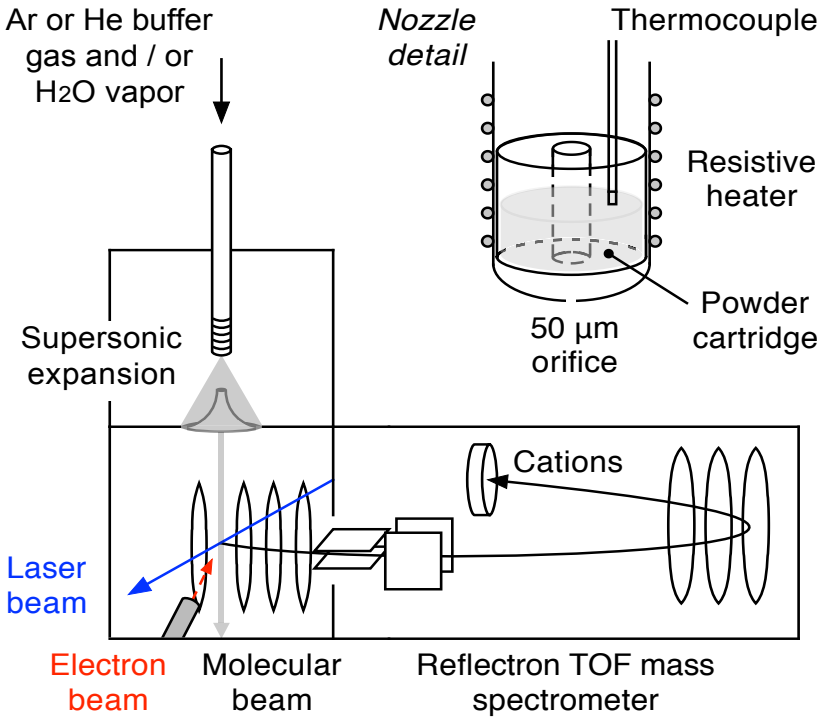

Figure 3.1: Schematic of the *Compact MPI/EII Experiment.* Adapted from [Barc et al. 2013].

The laser pulse width and frequency are 7 ns and 10 Hz. The average pulse energy is adjusted in the range 2 µJ - 2 mJ by changing the delay between the pulses triggering the xenon flash lamps and the Q-switch of the Nd:YAG laser. A convex lens on a slider is used to control the laser spot diameter (3 mm without the lens) at the interaction with the molecular beam. The resulting ions are detected using a *reflectron* time-of-flight (TOF) mass spectrometer. The pre-amplified ion signals are timed using a 250 ps

resolution time-to-digital conversion (TDC) card (Fast Comtec P7887). The data acquisition system is based on a LabView application interfacing with the TDC card and a laser pulse energy meter (Spectrum Detector SPJ-D-8).

The expansion chamber, the interaction chamber (where the beams cross), and the mass spectrometer flight tube are evacuated using turbo pumps with approximate pumping speeds of 500, 500, and 150 ls^{-1}, respectively. The experiments on thymine-water clusters results presented in Chapter 5 were carried out with a second turbo pump (also with approximate pumping speed 500 ls^{-1}) on the expansion chamber. The 50 μm diameter pin hole nozzle was laser-drilled into the closed end of a stainless steel tube (Lennox Laser). The outside of the tube is heated using a coiled resistive heater with an axial clamp in order to sublimate powder samples (uracil, thymine, 5-flurouracil and 3-aminophenol from Sigma-Aldrich with minimum purity 98%, deuterated uracil from CDN isotopes with 98.4% purity) in a stainless steel powder cartridge positioned above the pin hole nozzle. The powder cartridge is attached to two wires that enable the powder cartridge to be removed or reintroduced into the nozzle via a junction in the gas line (referred to as the "top-loading system"). A thermocouple is inserted directly into the powder to monitor the sample temperature. Liquid samples (water from a Milli-Q purification system and nitromethane from Sigma-Aldrich with purity ≥95%) were introduced into a reservoir mounted on the side of the buffer gas line. The reservoir can be isolated using a system of valves. The gas line tubing can be heated using resistive wire and monitored using thermocouples.

The reflectron mass spectrometer was designed and constructed by KORE Technology, whereas its voltage divider system was home-built. Following extraction in a pulsed

electric field (-292 or -271) Vcm^{-1}, depending on which of two available *pulser* units we use), acceleration to high voltage (typically -2 kV), and deflection to compensate for the molecular beam velocity, the cations pass through the field-free region (FFR) of the flight tube and the *reflectron* optics before traversing the FFR for a second time en route to the detector. The detector is a discrete dynode electron multiplier and includes a -10 KV post-acceleration grid to increase the detection efficiency of high-mass ions. The top-loading system enables the powder to be changed in such a way that the beam alignment remains constant. This allows us to distinguish lack of signal due to intrinsic properties of the molecules / clusters from the effects of alignment. Clusters can be formed in the initial stage of the supersonic expansion due to 3-body collisions. The level of clustering in the molecular beam can be varied between measurements; higher argon pressure and higher powder temperature are generally expected to increase clustering [Morse 1996]. However by far the greatest effect is achieved by swapping between helium and argon. With one exception (presented in section 5.4.1), our experiments using helium expansions did not provide any evidence for clusters in helium expansions. The exception was a 270 nm MPI measurement on thymine that included a weak signal of protonated molecules (a characteristic ionization product of thymine clusters).

3.2.2 Exploiting the reflection voltage to determine the position and the diameter of the laser beam / molecular beam intersection

The laser fluence is a key parameter for the interpretation of MPI results and hence it is important to determine the dimensions of the laser spot as accurately as possible. As mentioned in section 3.2.1, a convex lens on a slider was used to control the laser spot diameter (3 mm without the lens) at the interaction with the molecular beam. The laser

spot diameter can be estimated using a ray diagram for partially defocused measurements [Barc et al. 2013] but this simple approach is not effective to determine the spot diameter near the focal point. We overcame with this problem by using the reflection voltage V_R as a tool to measure the spot diameter.

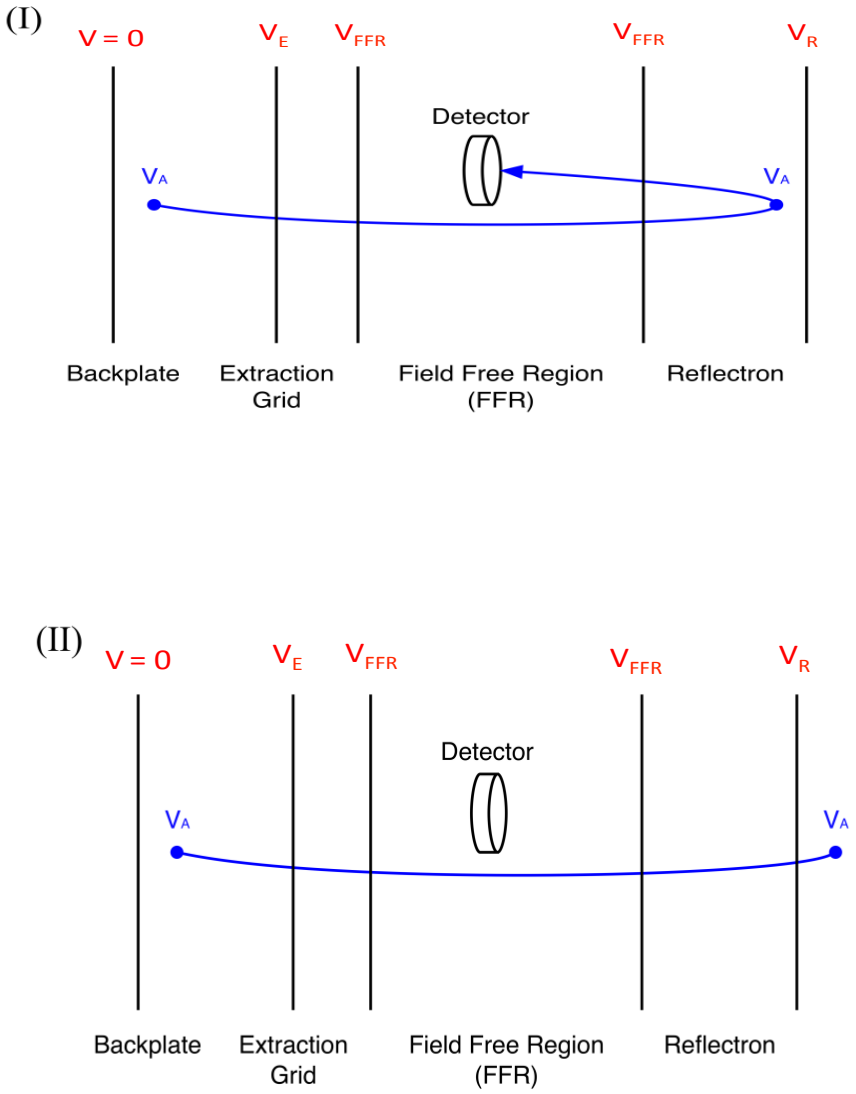

Figure 3.2: Diagrams to aid the explanation of how the reflection voltage can be used to determine ion position at the time of ion extraction. V_A is the voltage at the ion's position when the extraction field is applied. In diagram (I), V_R is in between V_A and 0 so the ion is reflected onto the detector. In diagram (II), V_R is in between V_A and V_E so the ion travels outside the reflectron and never reaches the detector. Note that these diagrams do not include the focusing or deflecting elements of the mass spectrometer.

The experimental concept can be explained with reference to Fig. 3.2 as follows:

- Consider an ion that is at position A (X_A from the backplate) with zero velocity at the instant when the extraction field is applied. We can reasonably ignore the rise time of the extraction voltage (V_E, typically -380 V) as this is very short (several ns) compared with the timeframe of the measurements. Position A corresponds to a specific voltage (V_A) with respect to the backplate (typically grounded). As position A gets closer to the extraction grid, V_A gets closer to V_E.
- The ion is accelerated to the field free region voltage (V_{FFR}, typically -2 kV) and then it is decelerated in the reflectron section of the mass spectrometer. The ion will attain zero velocity at the position that has voltage V_A. If the V_A position is inside the reflectron (as shown in Fig. 3.2(I)) then the ion will be accelerated back into the mass spectrometer's field free region and can be detected. If the V_A position is outside the reflectron then the ion will not be detected (as shown in Fig. 3.2(II)). Therefore we can determine V_A by measuring the ion signal as a function of the reflect voltage (V_R): signal will cut-off at $V_R(0) = V_A$.
- Once we have determined V_A, all we need is to know is how voltage varies with position between the backplate and the extraction grid in order to work out position A (X_A) with respect to the backplate position (X_0). Equation 3.1 below is based the approximation that the field between the backplate and the extraction grid (separated by distance X_E) is uniform.

$$X_A = X_E \times (V_A / V_E) \qquad \text{[Eq. 3.1]}$$

A simulation (QuickField) of the field between the grounded backplate and the grounded extraction grid (-380 V, X_E = 12 mm) is shown Fig. 3.3. Fig. 3.4 demonstrates

the high level of uniformity of the field along the central axis of the extraction. This supports the uniform field assumption and hence equation 3.1.

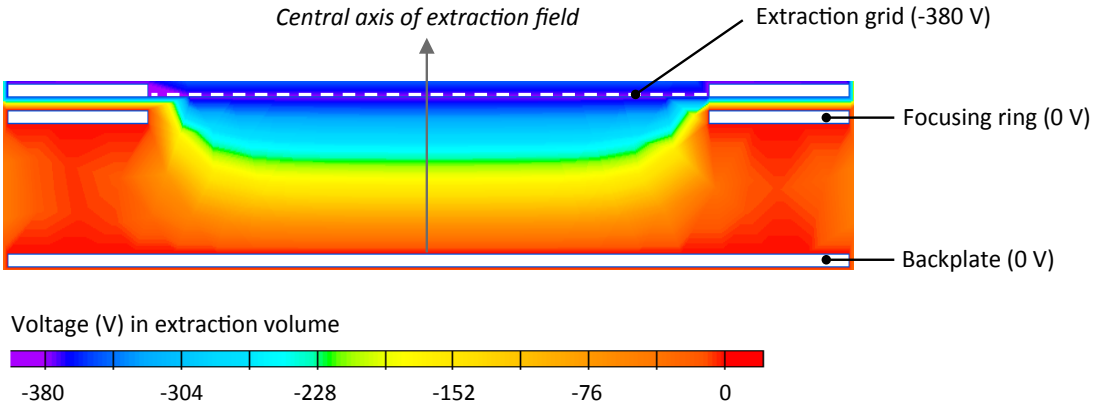

Figure 3.3: A simulation (Quickfield) of the voltage inside the *extraction volume* between the extraction grid and the backplate of the mass spectrometer. The separation of the backplate and the extraction grid (X_E) is 12 mm, the backplate diameter is 90 mm, and the grid diameter (equal to the inner diameter of the focusing ring) is 60 mm. The focusing ring has thickness 1 mm and is separated from the backplate by 10 mm.

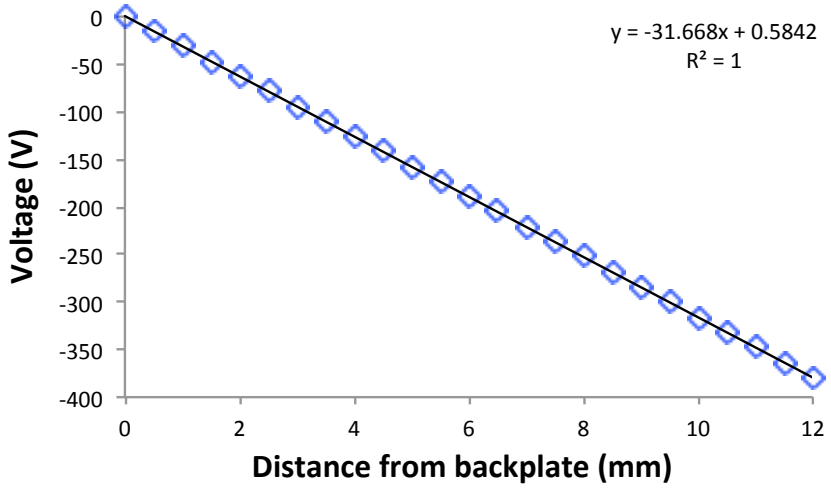

Figure 3.4: Voltage as a function of distance from the backplate along the central axis of the extraction field (grey arrow in Fig. 3.3). The close agreement of the calculated voltages with a linear fit (generated by MS Excel shown as a black line) indicates that a uniform field of -3.17×10^{4} Vm^{-1} is a good approximation for the present ion extraction conditions.

As an example, Fig 3.5 shows the signal of multi-photon ionized uracil as a function of the reflection voltage. The lens was positioned at its focal distance from the molecular beam (50 cm). The uracil$^+$ signal cuts off between V_R = -117±1 V and -126±1 V. Using equation 3.1, this correlates to the focused laser spot having a diameter of 0.29 ± 0.04 mm at the interaction of molecular beam.

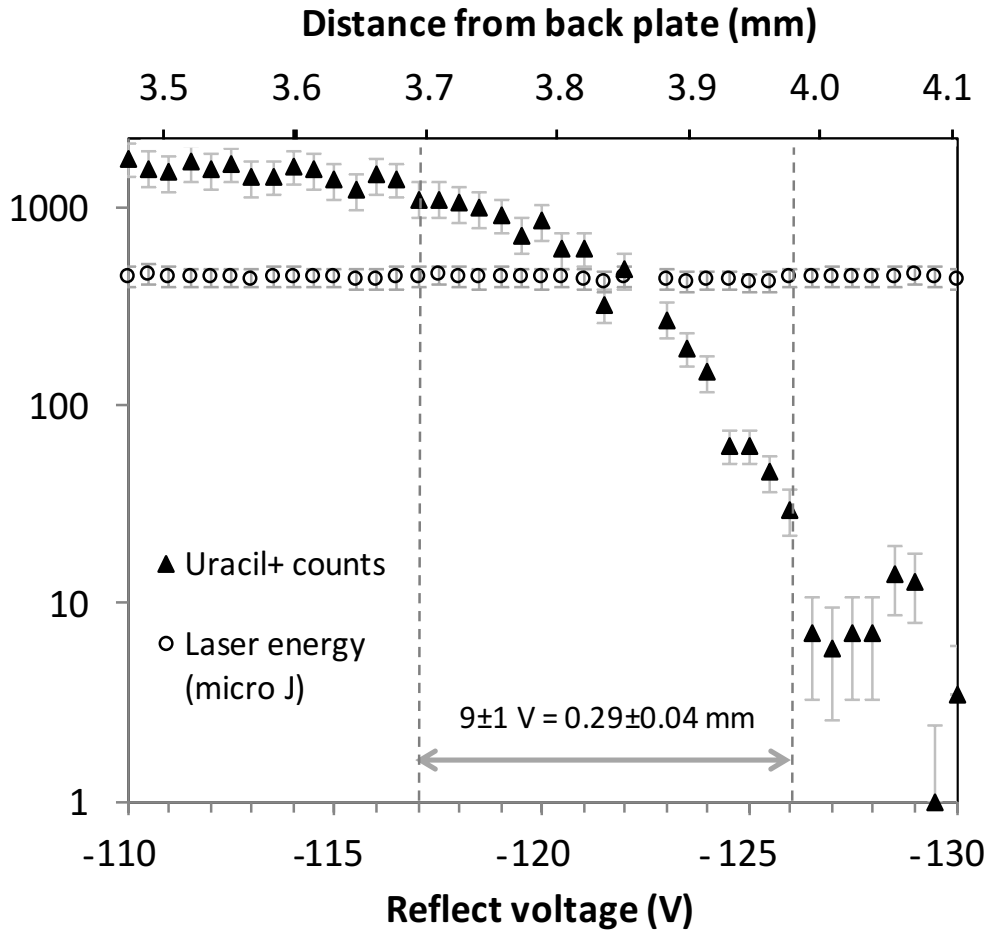

Figure 3.5: Uracil$^+$ production as a function of the reflect voltage (220 nm, He 0.8 bar, powder 264°C). The signal drop width (9±1 V) can be used to determine the diameter (0.29±0.04 mm) of the focused laser spot at the intersection with the molecular beam.

3.2.3 Exploiting the reflection voltage to probe kinetic energy release in dissociative multi-photon ionization

Section 3.2.2 describes how we can use the reflection voltage to determine the position of non-dissociative multi-photon ionization events in the mass spectrometer extraction volume. In this case, the ions have no initial velocity in the direction of extraction field (perpendicular to the molecular beam direction). Conversely, the reflection voltage dependence of the signal for a fragment ion will be modified by dissociative KE release (typically up to several eV for single ionization) [Vredenborg et al. 2011, Vredenborg et al. 2008]. The kinetic energy of a fragment ion can provide valuable information about the dissociation processes itself (for example, helping to distinguish ions that come from double ionization events with Coulomb repulsion contributing to KE), about the ionic excited state from which the ion originated (including its structure), and about the dynamics of the reaction (e.g. indicating a sequential fragmentation pathway) [laskin and Lifshitz 2001]. Continuing the bullet points from sections 3.2.2, our method to gain information on fragment ion KE release is described below:

- Consider a fragment ion with a distribution of initial velocities at the moment that the field is applied. We will call the maximum initial velocity in the direction of the extraction field v_i, giving a maximum initial kinetic energy in the direction of the extraction field of KE_i. Hence, the fragment ion signal will cut-off at $V_R(0) = V_A + KE_i$. With precise voltage control, this provides a direct route to measure KE_i. However, fluctuations of ±1 V on our mass spectrometer voltages meant that a slightly more complicated approach was required for our experiment.

- Suppose we repeat the experiment described in section 3.2.2 with one difference: we wait a certain time (t) after the laser pulse before applying the extraction voltage. During this time, the ions with v_i will have moved to a new position, closer to the extraction grid. Hence, the cut-off reflection voltage for the fragment ion signal ($V_R(0,t)$) will get closer to the extraction voltage (V_E). Now if we measure $\partial V(0,t)/\partial t$, all we need is the spatial variation of V in the extraction volume in order to calculate v_i. As discussed in section 3.2.2, a constant field between the backplate and the extraction grid (separated by distance X_{EX}) is a reasonable approximation. Hence:

$$v_i = (X_E/V_E)\ \partial V(0,t)/\partial t \qquad \text{[Eq. 3.2]}$$

As an example, Fig 3.6 shows how the cut-off reflection voltage ($V_R(0)$) of the NO^+ signal from multi-photon ionized nitromethane (CH_3NO_2) varies with the time of the extraction pulse after the laser pulse (t = 0.25 to 1 μs). This is understood to be 3-photon process [Lemire et al. 1998]: single photon absorption causes neutral dissociation to CH_3 and NO_2* which then pre-dissociates to form NO in its ground electronic state; NO is then 2-photon ionized. Note that these measurements were carried out with the backplate pulsed at +352 V and the extraction grid held at ground, whereas most of our experiments (including all of the measurements in Chapters 4-7) were carried out with the backplate grounded and the extraction grid pulsed at -380 V. This is why the $V_R(0)$ values are positive in Fig. 3.6. The relatively high vapour pressure of nitromethane (CH_3NO_2) without any heating of the liquid sample (e.g. 28 Torr at 20ºC [NIST 2017]) and very strong signal for NO^+ from nitromethane makes it a good test case to measure a cut-off voltage for large delay times in which case the signal dependence is quite

"shallow" and extended. Single-ionization KE release data is most prevalent for relatively small molecules (partly because KE information usually comes at the expense of mass resolution). However, the lowest lying electronic excited states of stable small molecules are generally too high for us to achieve efficient multi-photon ionization. Moreover, our current system is restricted to introducing liquid and solid molecular samples (as well as the inert carrier gas). This prevents us introducing NO directly, for example.

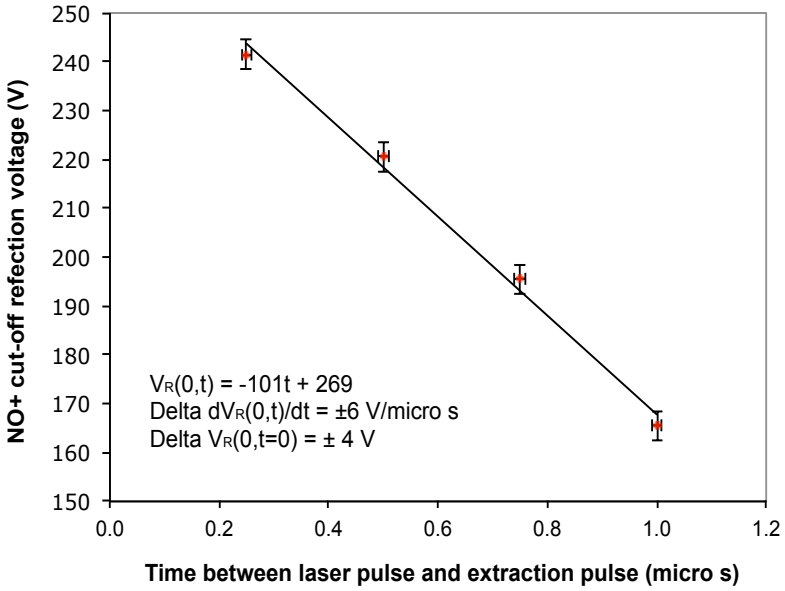

Figure 3.6: Reflectron cut-off voltage ($V_R(0)$) for NO^+ production from multi-photon ionized nitromethane (220 nm, pulse energy 475±35 μJ of the focused beam, Ar pressure 550 mbar, nozzle temperature 230°C) as a function of the time delay between the laser pulse and the extraction pulse. The black line shows a linear weighted fit [Reed 2011].

The linear fit of data points in Fig 3.6 gives $\partial V(0,t)/\partial t = -(1.01\pm0.06)\times10^{8}$ Vs^{-1}. Combined with the uniform field approximation (X_E/V_E = (0.0120±0.005 m / -352±1 V) = $-(3.4\pm0.2)\times10^{-5}$ mV^{-1}), this gives v_i = 3,400±300 ms^{-1} and hence a KE_i for NO^+ of 1.9±0.4 eV. To our knowledge, there are no previous experiments or calculations of the

KE release of NO^+ from nitromethane. However, the KE of NO^+ from NO_2 has been measured [Vredenborg et al. 2011] (maximum 1.3 eV) and so has the KE of NO_2^+ from nitromethane [Vredenborg et al. 2008] (maximum 1.6 eV). Although the mechanism we expect to produce our NO^+ signal begins with neutral NO_2 loss from nitromethane, summing the maximum velocities previously observed for NO_2^+ from nitromethane and NO^+ from NO_2 can provide a first-order estimation of the maximum velocity of NO^+ from nitromethane. Although the resultant velocity of 5,500 ms^{-1} is higher than the present result (3,400±300 ms^{-1}), we consider the agreement to be reasonable considering the indirect nature of the comparison. In particular, it should be noted that the specific MPI scheme (notably total energy absorbed and the time between the absorption of successive photons) and the laser polarization can have strong effects on fragment ion kinetic energies [Vredenborg et al. 2011].

This approach to determine the maximum velocity of a fragment ion in the direction of the extraction field is still at the stage of testing and optimization. In principle, it could be adapted to obtain more information about the velocity distribution of a fragment ion (not just its maximum velocity) by analyzing the specific shape of the ion signal dependence on V_R, not just the cut-off voltage $V_R(0)$. Numerous methods have already been established to probe KE release in dissociative ionization processes, including mass spectrometry techniques based on retarding fields, deflectors, time of flight analysers, deceleration-acceleration systems, and position-sensitive detection systems (most notably velocity map imaging) [Vredenborg et al. 2011, Vredenborg et al. 2008, Steckelmacher 1973]. However, we consider that the present approach has potential to play a useful complementary role due to its relative simplicity and its ability to provide information on fragment ion KE while simultaneously achieving high mass resolution.

3.2.4 Exploiting the reflection voltage to probe and identify metastable dissociation pathways of multi-photon ionized molecules and clusters

Prior to the start of my PhD, the group recorded MPI mass spectra of uracil showing evidence for the dissociation of ions during their first journey through the field free region of the reflectron mass spectrometer [Ryszka 2015, Barc et al. 2013, Barc et al. 2014] (several microseconds after the extraction pulse). This delayed or *metastable dissociation* of uracil$^+$ was not investigated in depth. The present MPI measurements extended our study of the metastable dissociation of uracil, as well as investigating related pathways in thymine, thymine-water clusters, and 3-aminophenol (see Chapters 5 and 6).

The standard flight time (t) to mass (m) calibration (m½ = at + b where a and b are constants) depends on an ion having the same mass throughout its journey in the mass spectrometer. Peaks with non-integer m/z values in a calibrated mass spectrum (the photon energies and laser fluence in the present MPI experiments are not sufficiently high to produce multiply charged ions) can be attributed to the ion dissociating during its flight time in the field free region (FFR). In this case, the (no longer meaningful) calibrated m/z value changes for different optimized mass spectrometer voltages. Dissociation events that take place before the ion has reached the FFR (or in the reflectron part of the mass spectrometer) will lead to a broad distribution of modified flight times. Hence, these dissociations do not manifest themselves as distinct peaks in a mass spectrum; they produce tail features. By contrast, all dissociations of a given type (i.e. from one parent ion to one fragment ion) that take place during the first journey through the field-free-region of the reflectron mass spectrometer will result in one flight time and hence a peak in the mass spectrum that can be KE-analysed. The dissociation

of an ion during its second journey through the FFR only has a minor effect on the measured flight time. Hence, when we refer to *dissociation in the FFR* (for brevity) in the rest of this thesis, we are only talking about the first journey through the FFR.

The TOF spectrometer's reflection electrode voltage V_R (a diagram showing ion optics of the mass spectrometer in shown in Fig. 3.2) enables a cut-off voltage to be determined for any peak in a mass spectrum. For ions produced promptly by the laser pulse, this cut-off voltage is linked to the position at which they were produced, as described in section 3.2.2. The situation changes if a fragment ion is produced some time after the laser pulse. In this case, the kinetic energy of the fragment ion will be lower and hence it can be reflected in a weaker field. Therefore, the cut-off voltage for these metastable fragment ions will be more negative than the extraction voltage, as described in section 3.2.3.

We use a model calculator (built in MS Excel by M. Ryszka [2015]) to identify the pathway responsible for a metastable dissociation in the FFR. Once the mass spectrometer voltages and the crossing position of the laser beam and the molecular beam have been entered into the model, the calculator can be used in three modes:

1. Cut-off voltage determination. Masses of the parent ion and the candidate fragment ion are specified. Then dissociation times are tested iteratively to see if the observed cut-off voltage can be reproduced. The calculations can also be carried out for sequential fragmentations. This typically identifies several possible *parent* and *daughter* ions so the cut-off voltage alone is not enough to determine a metastable dissociation unambiguously.
2. Calculated difference between time-of-arrival of the investigated feature in the

TOF spectrum and a known reference peak (usually the intact ionized molecule) is compared with the equivalent value obtained experimentally. As above, this process is repeated iteratively for different possible dissociations until a good match between the calculated flight time, the measured flight time, and the cut-off analysis (mode 1 above) is obtained.

3. Calculation of absolute values of time-of-flights. This method predicts the time of flight for the investigated ion in a specific dissociation scenario. Several values are calculated corresponding to different dissociation processes taking place in different parts of the mass spectrometer. The experimentally obtained value is then compared. For a well-defined peak, such as a parent ion or the most abundant fragment, this agrees within less than 8 ns, which is the precision of experimental values.

3.3 Multi-photon ionization and electron impact ionization experiments on Stark selected molecules and clusters (*Stark Deflection Experiment*)

3.3.1 Introduction

A major challenge in analyzing radiation-induced processes in clusters is the broad distribution of sizes and configurations produced by supersonic expansion sources (or alternative cluster sources, for example utilizing laser ablation). This can also be a problem for experiments on isolated molecules, as it is not unusual for gas-phase samples to include significant populations of several different structural forms (isomers, tautomers, or conformers). For example, gas phase cytosine has similar populations of its enol and keto forms [Tomic et al. 2005]. The *Stark Deflection Experiment* is

built to investigate electron and photon induced processes in molecules and clusters with *Stark deflection* applied to improve control of the target configuration(s). The Stark deflector uses a strong electric field gradient to deflect molecules and / or clusters in supersonic beams and separate them spatially as a function of their *effective dipole moment* / mass ratio.

The system is shown schematically in Fig. 3.7 and is described in detail in M. Ryzska's PhD thesis [2015]. Briefly, the molecular beam source is based on a CW supersonic expansion of argon, helium or krypton seeded with the molecules of interest. The expansion is skimmed and the resultant beam passes through a Stark deflector built by J. Küpper and co-workers, DESY. This is orientated to deflect polar species vertically, as viewed in Fig. 3.7. The deflected beam then crosses a CW electron beam or a pulsed UV laser beam.

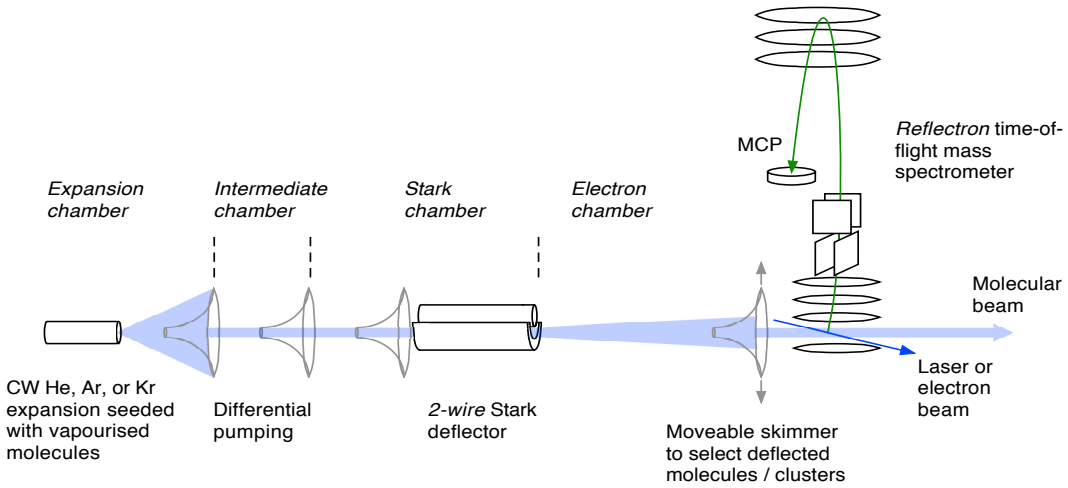

Figure 3.7: Schematic diagram of the *Stark Deflection Experiment*. Typical distances from nozzle to first skimmer (1-5 cm), nozzle to skimmer in front of deflector (45 cm), skimmer in front of deflector to moveable skimmer (70 cm), and moveable skimmer to center of TOF source (13 cm). Adapted from M. Ryzska's PhD thesis [2015].

Different parts of the deflected beam can then be selected using a moveable skimmer before the beam is probed by electron impact ionization or by multi-photon ionization. Alternatively, or as a complement, the focused laser spot can be moved using a lens on vertical movement in order to probe different parts of the deflected beam. The resultant ions are detected using a reflectron time-of-flight mass spectrometer.

M. Ryzska's PhD [2015] tested the capabilities of the experiment to deflect water molecules, benzonitrile molecules, nitromethane molecules, and nitromethane clusters. I extended the work on nitromethane and also studied three more complex molecules: uracil, thymine and 3-aminophenol. This required two key challenges to be addressed. The first challenge (discussed further in section 3.3.2) was to lower the rotational temperature of molecular beam. Controlled deflection depends on producing molecules in low rotational states and the energy separations of J states generally get smaller with increasing complexity of molecules and clusters. The second challenge (discussed further in section 3.3.3) was to ionize and detect the deflected molecules; M. Ryzska's [2015] experiments obtained very low signals outside the un-deflected beam axis.

3.3.2 Producing a beam of rotationally cooled molecules or clusters

Fig. 3.8 shows the carrier gas line and nozzle assembly for the *Stark Deflection Experiment*. Compared the source for the *Compact MPI/EII Experiment*, the horizontal orientation of the nozzle in this system reduced the probability of blocking with impurities or condensed sample molecules. The design also has the advantage the sample cartridge to be refilled without breaking the vacuum.

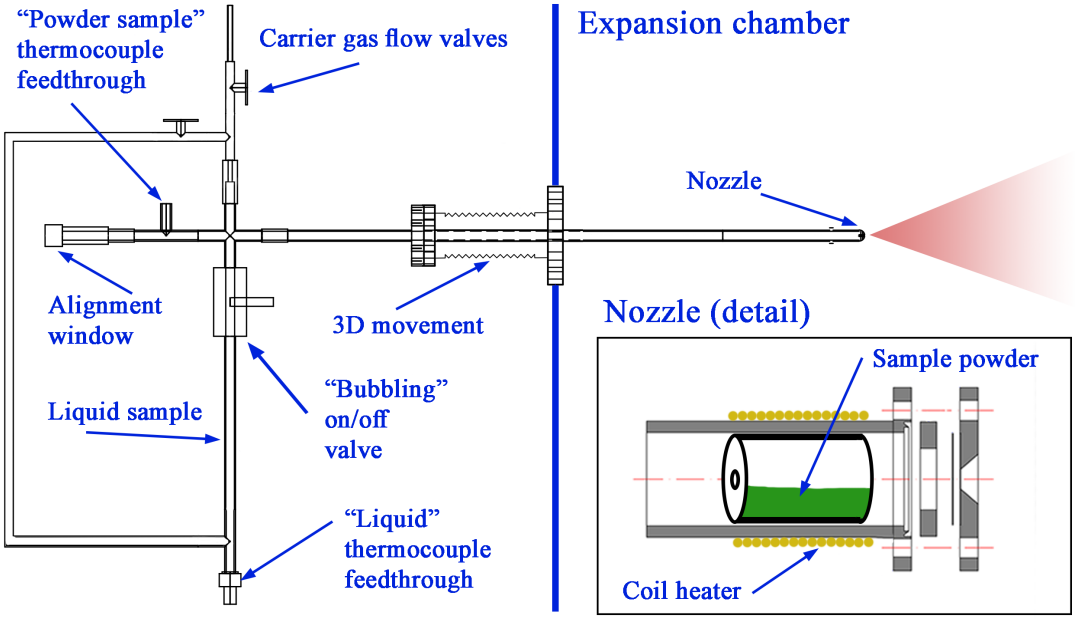

Figure 3.8: Diagram of the carrier gas line and nozzle assembly for the *Stark Deflection Experiment.* Adapted from M. Ryszka's thesis [2015].

This is done normally by opening the gas line close to the alignment window (see Fig 3.8) while there is still just over 1 bar of argon in the gas line. Hence there is a constant flow of argon out of the gas line and no atmospheric air (and hence dust) from the lab flows in towards the nozzle. The entire gas line, including the nozzle, is mounted on a 3D movement. The planar movement allows for precise alignment of the nozzle with respect to the all skimmers. Movement in the third axis has an advantage to modify nozzle and skimmer distance. The carrier gas can either flow through the nozzle directly or it can be directed to pass through stainless steel liquid reservoir see Fig. 3.8. This bubbling system increases the pick-up rate of molecules from the liquid sample and also can be used to produce water-molecule clusters. The reservoir and the gas line can be heated using coiled resistive heater and the temperature is monitored using thermocouples at several control points (inside liquid, inside the powder cartridge, on the outside of tubing on either side of the vacuum feed through, and on the outside of

the nozzle close to the orifice). The resistive heater is wrapped more sparsely around the reservoir than around the gas line in order to prevent condensation.

In order to improve rotational cooling, a more refined nozzle assembly system is required than the laser-drilled nozzles (Lennox Laser) used in the *Compact MPI / EII Experiment*. This is referred to as the "sandwich" nozzle system and is as shown schematically in Fig. 3.8. It includes a precisely engineered circular aperture in a platinum/iridium alloy (95:5%) disk produced by Agar Scientific for an electron microscope. The orifice shape is nearly ideally circular, helping to minimize turbulence in the expansion. The aperture disk is interchangeable but all the measurements in this thesis used a 30 μm orifice. A resistive heater is coiled around the assembly to heat the sample and a thermocouple is inserted into the sample cartridge to measure real sample temperature.

A continuous (generally referred to as CW) expansion is used in order to maximize the signals that can be obtained in interactions with electron beams (the ultimate aim of the experiment). This contrasts with the pulsed molecular beams used in most Stark deflection experiments, notably by our collaborators J. Küpper and co-workers [Filsinger et al. 2009A, Filsinger et al. 2009B, Trippel et al. 2012]. To achieve the best-possible rotational cooling in our CW conditions, the *expansion chamber* (see Fig 3.7) is pumped with three turbo pumps that provide a combined pumping speed of approximately 4,000 ls^{-1}. Typical pressures in the *expansion chamber* with a carrier gas pressure of 500 mbar upstream from the 30 μm orifice are $1.3*10^{-5}$ and $1.6*10^{-5}$ for argon and krypton, respectively. After the expansion, the molecular beam passes through a conical skimmer (Beam Dynamics model 2 skimmer, diameter 1 mm) into a

differential pumping stage referred to here as the *intermediate chamber* (Fig 3.7). The separation of the nozzle and skimmer-nozzle is typically in the range of 1-5 cm. The intermediate chamber is evacuated by a turbo pump with a pumping speed of 600 ls^{-1}, which gives typical pressure of ~10^{-7} mbar during measurements. The beam then passes through a second conical skimmer (orifice diameter 1 mm) into the *deflection chamber* (~10^{-8} mbar during measurements). The first two skimmers in the experiment can be heated up to 125 °C using resistive heaters to prevent condensation and their temperatures are monitored with thermocouples mounted on their assembly systems.

3.3.3 Stark deflection and the detection of deflected molecules

The Deflection chamber is evacuated by a turbo pump (approx. 600 ls^{-1}) and hosts the Stark deflector. The Stark deflector was built by Küpper and co-workers at DESY and comprises a 15 cm long electrode rod positioned above a grounded trough. This arrangement is known as a *2-wire* deflector. A potential difference up to 12 KV can be applied between the rod and the trough [Filsinger et al. 2009A, Filsinger et al. 2009B, Trippel et al. 2012]. The rod and the trough are separated by 1.5 mm and their specific shapes establish the inhomogeneous field (Fig. 3.9 a) necessary to deflect a beam of polar molecules or clusters that passes between them. This strong field gradient accelerates neutral polar molecules and / or clusters as a function of their *effective dipole moment* (a function of their permanent electric dipole moment, polarizability, and rotational excitation) / mass ratio. Stark acceleration is explained in more detail in Chapter 7. Fig. 3.9: (a) shows the cross-section of the Stark deflector with the electric field strength calculated using QuickField for 4 KV on the rod and (b) shows a 3-D drawing of the Stark defector. A skimmer is mounted at the entrance of the deflector to

prevent the molecular beam from hitting the electrodes and to control the width of the deflected beam. The skimmer diameter was 1 mm or 0.5 mm in the present experiments, depending on the desired diameter of the molecular beam. Another skimmer after the deflector (with orifice diameter 1 mm) can be installed to aid alignment. This skimmer has been removed for the present experiments in order to maximize the transmission of deflected molecules. Due to the high field strength in the device, the pressure in the chamber must be $<10^{-6}$ mbar to prevent an arc discharge. Furthermore, a High-Voltage conditioning procedure has to be performed to prepare the electrode surfaces for strong fields after exposure to air (i.e. every time the deflection chamber is vented). The conditioning procedure involves gradually increasing of the voltage on the rod electrode of the deflector (always <1 kV per minute, pausing for 15 mins at 1 kV intervals between 6 and 10 kV, and at 0.5 kV intervals between 10 and 12 kV) while monitoring current flow with a nano-ammeter for any sign of a discharge.

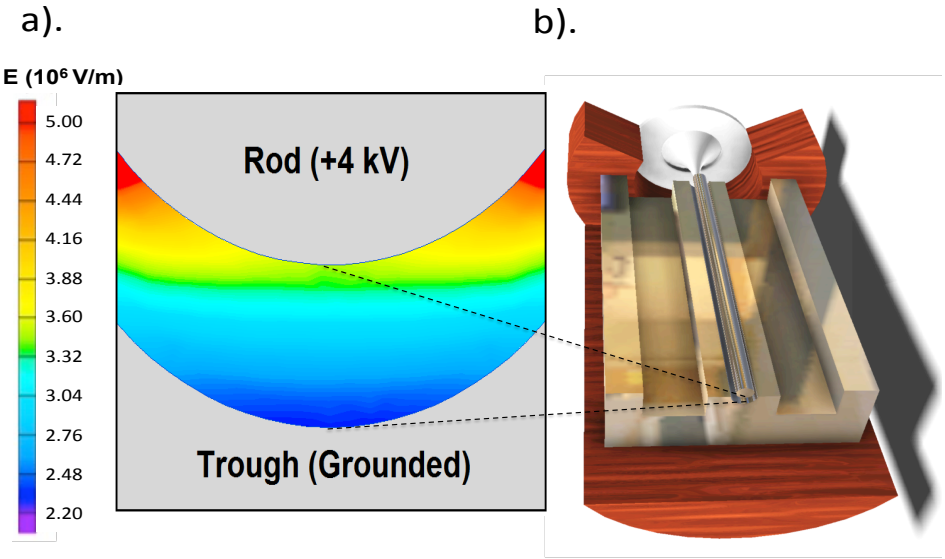

Figure 3.9: (a) Cross-section of the Stark deflector, showing electric field strength calulated with QuickField with 4 KV on the rod. (b) 3-D drawing of the Stark defector. The skimmer in front of the deflector is not shown [Ryszka 2015].

After the deflection chamber, the molecular beam travels 0.5 m to exaggerate any deflection effects. This *drift distance* was chosen to match previous experiments that achieved a 5 mm deflection of trans tautomers of 3-aminophenol using the same deflector design [Trippel et al. 2012] (discussed further in Chapter 7). The drift distance comprises a gate valve, an extension tube, and a chamber referred to here as the *electron chamber*. The electron chamber (~10^{-8} mbar during experiments) is evacuated by a turbo pump (approx. 600 ls^{-1}). The mass spectrometer connected to the electron chamber is pumped additionally by a turbo pump with approximate pumping speed 150 ls^{-1}. The deflection chamber, the electron chamber, and the mass spectrometer share a single oil-free (scroll) backing pump.

Fig. 3.10 shows the design of the electron chamber. Most of the space in the chamber is reserved for an electron monochromator system for planned electron attachment experiments. Stark deflected molecules and clusters can be selected using a moveable skimmer of diameter 1 mm mounted on a 3-way movement (precision 0.01 mm) after the moveable skimmer orifice, the molecular beam (selected or not) crosses a pulsed UV beam or a continuous electron beam (produced by the same commercial laser system and electron gun described in section 3.2.1) in the extraction volume of a TOF mass spectrometer. This enables MPI and EII experiments to be on carried out on the selected species with ionization taking place in TOF extraction volume. EII can be used to ionize the carrier gas and the resultant intense signals are used to optimize the alignment of the system prior to MPI or EII experiments on the molecules and / or clusters in the beam. The design of the *reflectron time-of-flight mass spectrometer* is very similar to the one used in *Compact MPI/EII Experiment.* The extraction voltage pulser (-380 V), the deflectors, the flight tube, and the MCP detector (suitable for cation

or anion detection) were built by KORE Technology. The same home-built voltage divider used in the *Compact MPI/EII Experiment* controls the static voltages. The TOF source has been built in the Science Faculty Workshop following a series of simulations performed using CPO-3D software by M. Dampc (former post-doc in the Molecular Clusters Group). The TOF source electrodes have the same separations as in the *Compact MPI/EII Experiment* but are additionally shielded electrically by a copper tube. The copper tube has six holes around the extraction volume, allowing the passage of the molecular beam, the laser beam and the electron beam.

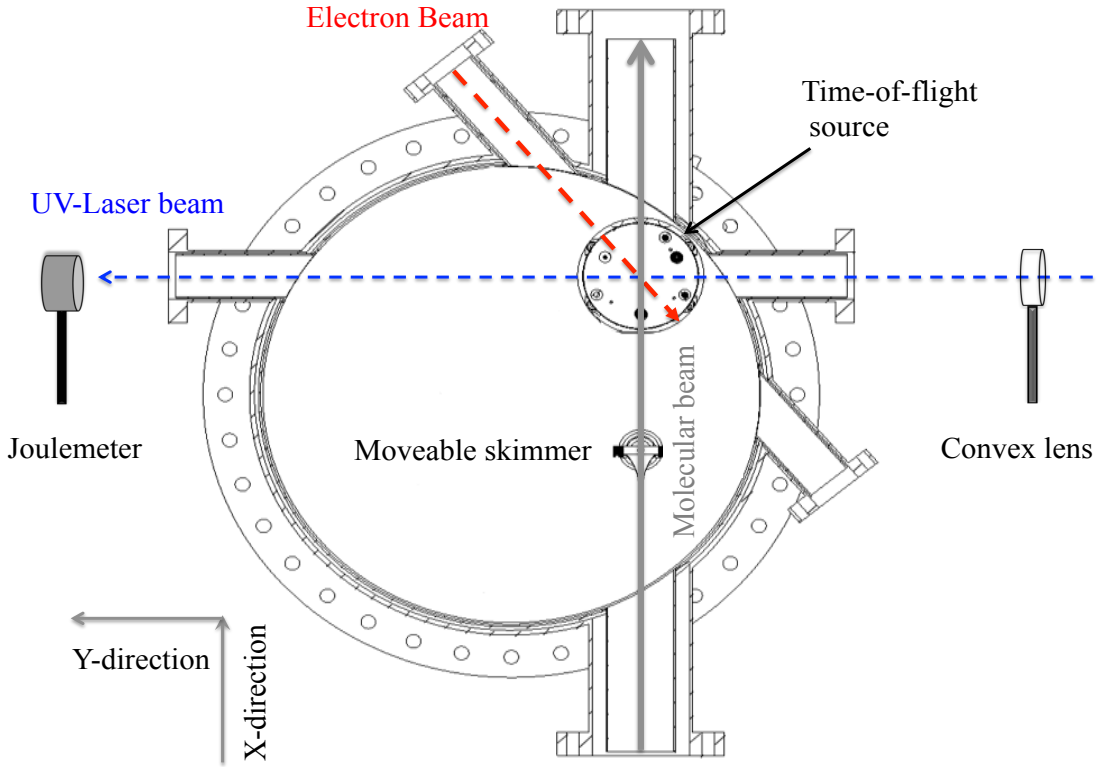

Figure 3.10: Cross section of electron chamber (outer diameter 42 cm, inner diameter 36 cm) showing the crossing of the molecular beam (X-direction, grey) with the laser beam (Y-direction, blue) or the electron beam (red) inside the Time-of-flight source. The convex lens is moveable in the ±Z direction, the molecular beam deflection is in the ±Z direction, and the skimmer is moveable in ±X, ±Y, and ±Z directions. The ions produced by MPI or EII are extracted into the TOF mass spectrometer in the +Z direction (coming out of the page).

The electron chamber is lined with a mu-metal shield to minimize the penetration of magnetic fields (primarily in preparation for the planned electron attachment experiments but also useful for controlling the ionizing electron beam in the present work). This shield has holes for the copper-shielded TOF source, the moveable skimmer, the pumping, and the passage of the key beams. The electron beam is defocused in order to have a diameter that is slightly greater than the 10 mm separation of the backplate and the focusing ring of the TOF source (compare with Fig. 3.3). The alignment of the experiment is such that the undeflected molecular beam passes approximately through the center of the extraction volume. Therefore, deflections up to approximately ±5 mm are observable in the EII experiments when the moveable skimmer is used.

In contrast with the electron beam, the laser beam is tightly focused for the MPI experiments in order to obtain maximum signals. Therefore we used a convex lens (focal distance 300 mm) mounted on a vernier-controlled (precision 0.01 mm) vertically moveable platform in front of the laser entrance window of the electron chamber. Hence the focused UV beam could be moved vertically with respect to the molecular beam in order to probe different parts of the deflected molecular beam. As discussed in section 3.2.2 the reflection voltage, V_R, can be used as a tool to determine the position and the diameter of the laser beam / molecular beam intersection. The separation between grounded backplate and grounded extraction grid is X_{EX} = 12 mm and the applied extraction field is -380 V, giving an approximately uniform electric field of 31.6 Vmm^{-1}. Fig. 3.11 (a) shows the reflection cut-off voltages of the 3-aminophenol$^+$ (3-AP^+) MPI signal from a molecular beam that had been deflected with 10 kV on the deflector. The width of the deflected beam was determined as ~2 mm in a set of electron impact

ionization measurements with the moveable skimmer (see section 7.3.1). The cut-off voltages in Fig. 3.11(a) are -55±5, -150±5 and -215±10 V at lens positions of -2.5±0.01, 0.0±0.01 and 2.0±0.01 mm, respectively (0.0 mm corresponds to the laser beam hitting the center of the convex lens). Converting these cut-off voltages into distances above the grounded backplate gives (55/31.6=) 1.7±0.2, (150/31.6=) 4.7±0.2, and (210/31.6=) 6.6±0.03 mm. These distances are plotted against the lens position as in Fig 3.11 (b) and the linear fit (Origin 6.0) has a gradient of 1.1±0.08. This gradient can be used to convert the lens position into a focused spot position for the MPI deflection experiments.

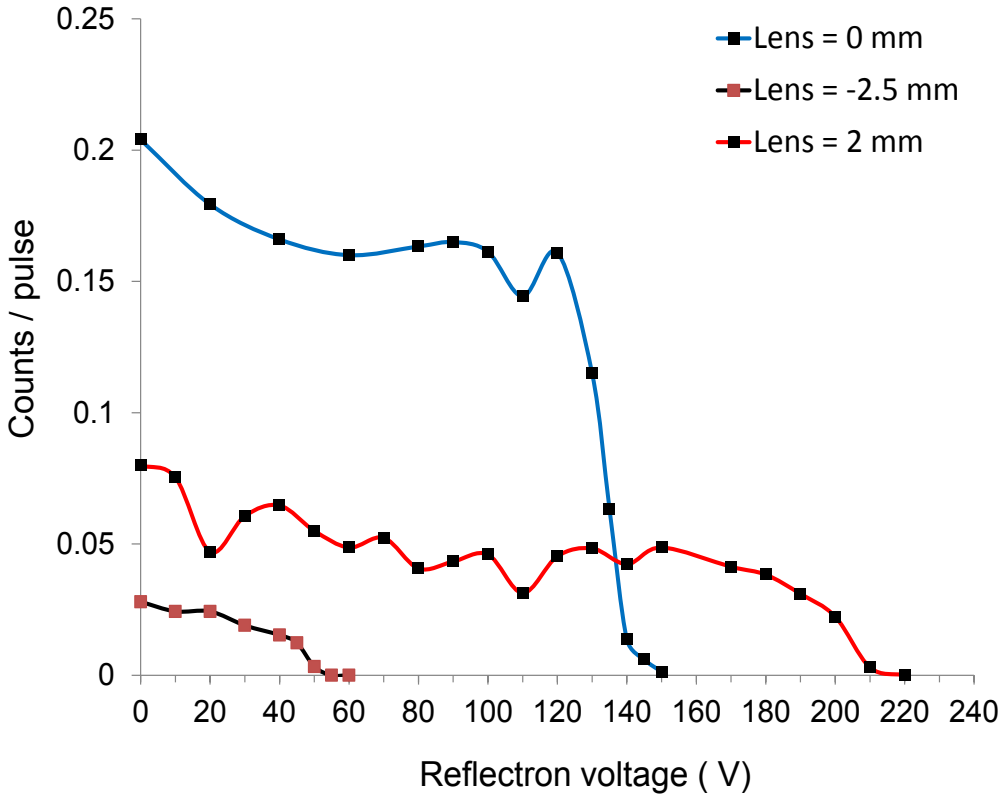

Figure 3.11: (a) Reflection voltage (V_R) dependence of the 3-AP$^+$ signal from multi-photon ionized 3-AP (10 KV stark deflection voltage, 220 nm, 100±25 μJ, Ar = 500 mbar, sample temperature = 105°C) at three different positions of the moveable convex lens.

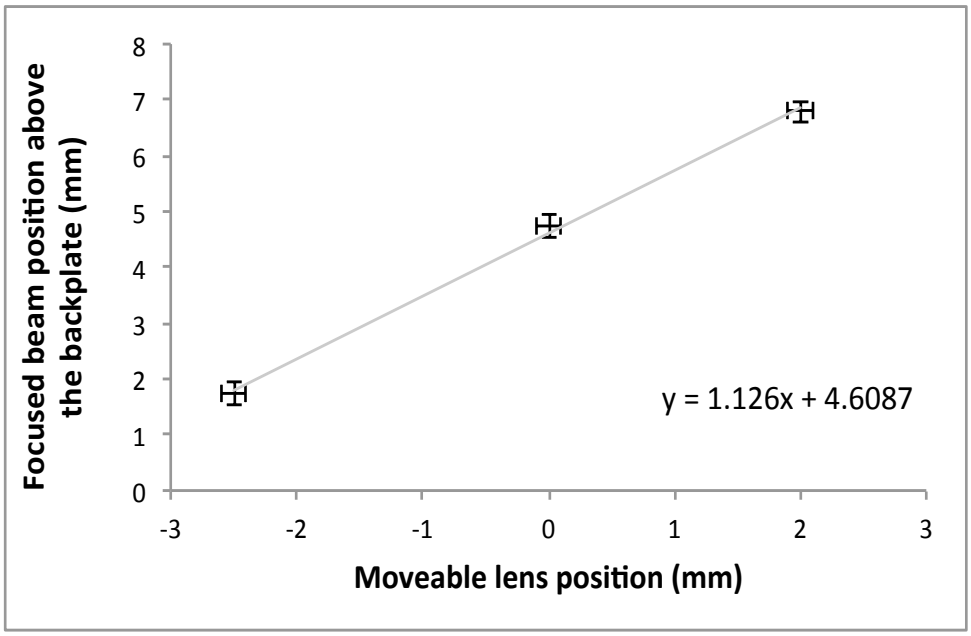

Figure 3.11: (b) Linear fit gradient on focused laser beam position as a function of the moveable lens position.

3.4 Summary

This chapter provides a description of the crossed-beam apparatus at the OU to study *multi-photon ionization (MPI)* and *electron impact ionization (EII)* of isolated and clustered molecules. Further improvement in this *compact MPI/EII experiment* to probe and identify *metastable dissociation* pathway of multi-photon ionized molecule, presented in this chapter. Results obtained using the *Compact MPI / EII experiment* is presented in Chapters 4 and 5.

A new experiment has been designed and built to study MPI and EII of molecules and clusters in Stark-deflected beams (*Stark deflection experiment*). The system is described in detail and a number of MPI/EII results are presented in Chapter 7 to demonstrate its performance to date.

3.5 Contributions by co-workers

The *compact MPI/EII experiment* was mainly built by Bartek Barc (former PhD student). The *Stark deflection experiment* was mainly built by Michal Ryszka (former PhD student). I preformed all the experiments in this chapter, working with Michal Ryszka on the measurements in section 3.2 and PhD student Tiago da Fonseca Cunha on the measurements in section 3.3. PhD student Andre Rebelo carried out the Quickfield simulations of the electric fields inside the TOF source and the Stark deflector.

References:

- B. Barc, Hydrated clusters of nucleic acid bases in supersonic beams probed by multi-photon ionization (MPI) mass spectrometry, Department of Physical Sciences, The Open University, Milton Keynes, United Kingdom, *PhD thesis*, 2012.
- B. Barc, M. Ryszka, J. Spurrell, M. Dampc, P. Limão-Vieira, R. Parajuli, N. J. Mason and S. Eden, *J. Chem. Phys.,* 2013, **139**, 244311.
- B. Barc, M. Ryszka, J. C. Poully, E. J. Al Maalouf, Z. el Otell, J. Tabet, R. Parajuli, P. J. M. van der Burgt, P. Limão-Vieiraf, P. Cahillanea, M. Dampc, N. J. Mason and S. Eden, *Int. J. Mass Spectrom.,* 2014, **194**, 365-366.
- W. Bleakney, *Phys. Rev.,* 1930, **35**,1180-1186.
- Y. P. Chang, F. Filsinger, B. G. Sartakov and J. Küpper, *Comp. Phys. Comm.,* 2014, **185**, 339-349.
- F. Filsinger, J. Küpper, G. Meijer, L. Holmegaard, J. H. Nielsen, I. Nevo, J. L. Hansen and H. Stapelfeldt., *J. Chem. Phys*., 2009A, **131**, 064309.
- F. Filsinger, J. Küpper, G. Meijer, J. L. Hansen, J. Maurer, J. H. Nielsen, L. Holmegaard and H. Stapelfeldt, *Angewandte Chemie International Edition*, 2009B, **48**, 6900-6902.
- H. D. Hagstrum and J. T. Tate, *Phys. Rev*., 1941, **59**, 354-370.
- J. Laskin and C. Lifshitz, *J. Mass Spectrom.,* 2001, **36**, 459-478.
- G. W. Lemire, J. B. Simeonsson and R. C. Sausa, *Anal. Chem.,* 1998, **65**, 529-533.
- M. D. Morse. *Methods of Experimental Physics: Atomic, Molecular, and Optical Physics, Vol. II, Academic Press Inc.*, 1996, 21-47.
- NIST, Chemistry WebBook, 2017, http://webbook.nist.gov (accessed 2017).
- R. Pandey, M. Lalande, M. Ryszka, P. Limão-Vieira, N. J. Mason, J. C. Poully and S. Eden, *Eur. Phys. J. D*, 2017, **in press**
- C. B. Reed, *Physics Education*. 2010, **45**, 93-96.
- M. Ryszka, Radiation induced processes in biomolecules and clusters in controlled beams, Department of Physical Sciences, The Open University, Milton Keynes, United Kingdom, *PhD thesis*, 2015.
- M. Ryszka, R. Pandey, C. Rizk, J. Tabet, B. Barc, M. Dampc, N. J. Mason and S. Eden, *Int. J. Mass Spectrom*. 2016, **396**, 48-54.
- W. Steckelmacher, *J. Phys. E: Sci. Instrum.,* 1973, **6**, 1061-1071.
- K. Tomic, J .Tatchen and C. M. Marian, *J. Phys. Chem. A*, 2005, **109**, 8410-8418.

- S. Trippel, Y. P. Chang, S. Stern, T. Mullins, L. Holmegaard and J. Küpper, *Phys. Rev. A*, 2012, **86**, 033202.
- A. Vredenborg, C. S. Lehmann, D. Irimia, W. G. Roeterdink and M. H. M. Janssen, *ChemPhysChem*, 2011, **12**, 1459-1473.
- A. Vredenborg, W. G. Roeterdink, and M. H. M. Janssen, *J. Chem. Phys*., 2008, **128**, 204311.

CHAPTER 4

Experiments to identify fragment ions from multi-photon ionized uracil: high-resolution mass spectrometry and comparisons with deuterated uracil

This chapter is focused on high resolution multi photon ionization mass spectrometry performed on uracil to identify fragment ions which were subject to debate in previous literature on the basis of their accurate mass determination and also comparison of high resolution results with deuterated uracil measurements.

4.1 Introduction

Ultra Violet Radiation (UVR) induced processes of nucleobases, notably electronic excitation, ionization, and fragmentation, have been studied extensively in recent years to enhance our understanding of the mechanisms that can initiate DNA and RNA lesions [Middleton et al. 2009]. Uracil (U, $C_4H_4N_2O_2$) binds to adenine (A, $C_5H_5N_5$) with two hydrogen bonds in RNA; the other two nucleobases in the macromolecule are

cytosine (C, $C_4H_5N_3O$) and guanine (G, $C_5H_5N_5O$). In DNA, uracil is replaced by thymine (T, $C_5H_6N_2O_2$).

The previous work carried out by Barc et al. (Molecular Clusters Group, The Open University) showed experimental evidence for a new UV damage process in uracil [Barc et al. 2013]. They produced a fragment ion at m/z 84 by 2-photon absorption at photon energies ≥ 5.29 ± 0.06 eV (wavelength ≤ 232 nm). This fragment ion has never been observed in experiments involving the direct excitation of gas-phase uracil to ionic states, for example in single collisions with electrons [Barc et al. 2013, Imhoff et al. 2007, Rice et al. 1965, Denifl et al. 2004, Feil et al. 2004, Manura and Manura 2016, Coupier et al. 2012] or single photon absorption [Jochims et al 2005]. This suggests that 2-photon production of m/z 84 ions must depend on a critical process that occurs in a neutral electronic excited state of uracil (i.e. during the time between the absorption of the two photons).

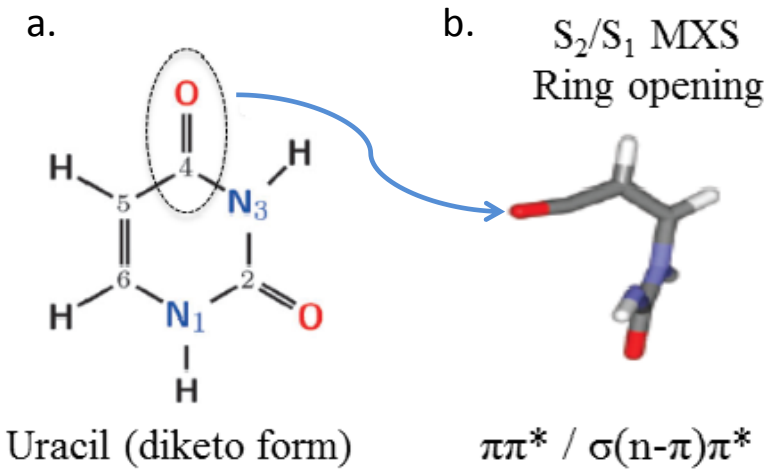

Figure 4.1: (a). Uracil in its diketo tautomer form which is the most abundant form in gas phase [Rejnek et al. 2005] with numbering atoms, b. ring opening at S_2/S_1 crossing seam [Nachtigallova et al. 2011].

Table 4.1: Summary of the characteristics of the calculated ring-opening CIs between the singlet states of uracil. All three involve opening in the same position on the ring.

Initial and final states	**Ring-open structure**	**Energy in eV and method**	**Time after access to initial state**	**Reference**
S_2/S_1	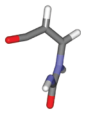	5.25 (CASSCF) 5.84 (MS-CASPT2) 5.97 (MR-CISD)	550 fs	Nachtigallova et al. (2011)
S_1/S_0	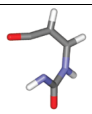	4.43 (CASSCF) 4.76 (MS-CASPT2) 5.25 (MR-CISD)	-	Nachtigallova et al. (2011)
S_1/S_0	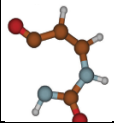	5.25 (CASSCF)	200 fs	Richter et al. (2014)

Barc et al. [2013] assigned the m/z 84 peak based on comparisons with non-adiabatic dynamics simulations. Nachtigallova et al. [2011] revealed a ring-opening decay pathway at the $S_2(\pi\pi^*)$ - $S_1(\sigma(n\text{-}\pi)\pi^*)$ crossing seam and predicted that this would lead to new photochemical products [Nachtigallova et al. 2011]. Richter et al. [2014] also carried out dynamical calculations with non-adiabatic and spin-orbit couplings and reported a ring-opening conical intersection between the S_1 and S_0 states. Similarly, Nachtigallova et al. [2011] reported an S_1/S_0 ring-opening CI but discussed in much less detail than the S_2/S_1 ring-opening CI. Table 4.1 summarizes the characteristics of these calculated ring-opening CIs involving the S_2, S_1, and S_0 states of uracil, including their predicted times and energies. All three CIs involve opening in the same position on the ring and, depending on the calculation method, all can be considered to be energetically consistent with the threshold photon energy (5.29 ± 0.06 eV) for the m/z 84 ion in the MPI experiments [Barc et al. 2013]. Furthermore, the calculated open-ring structure of these CIs have a CO group at one end that appears to be prone to abstraction (see Fig. 4.1). Therefore, Barc et al. [2013] argued that the m/z 84 could be produced by CO loss following the ionization of electronically-excited open-ring uracil. However, while this

is a strong argument, they did not supply any direct experimental proof that the m/z 84 ion really is $C_3H_4N_2O^+$ instead of another possible candidate with the same m/z (notably $C_3H_2NO_2^+$ produced by CNH_2 loss).

The aim of the work presented in this chapter was to find extra evidence to support or counter Barc et al.'s interpretation [2013]. It was also hoped that, the assignments of other fragment ions could be varified, with particular attention to peaks that have been subject to contradicting interpretations in the literature. To achieve these goals, two parallel strategies were adopted as discussed below.

1. MPI spectra were recorded at 220 nm (5.64 eV) with the highest mass resolution that has been achieved using the OU MPI-TOF facility. The strategy was to exploit the small deviations of atomic masses from their nominal mass numbers (the dominant isotopes of hydrogen, carbon, nitrogen, and oxygen have 1.008, exactly 12, 14.003, and 15.995 atomic mass units, respectively [Manura and Manura 2016]) in order to distinguish specific fragment ions.
2. MPI spectra were recorded (also at 220 nm) of fully deuterated uracil and compared them with equivalent measurements on uracil. For isolated peaks (most importantly the m/z 84 peak), this provides a tool to determine the number of hydrogen atoms in a given fragment ion.

Dissociative ionization of uracil has been studied extensively by electron impact [Barc et al. 2013, Imhoff et al. 2007, Rice et al. 1965, Denifl et al. 2004, Feil et al. 2004, Manura and Manura 2016, Coupier et al. 2012] ion impact [Coupier et al. 2012, Tabet et al. 2010, Padellec et al. 2008, Schlathölter et al. 2005, Schlathölter et al. 2006, Vries et al. 2004, Vries et al. 2002, Vries et al. 2003, Markush et al. 2016], and single

photon absorption [Jochims et al. 2005]. Before Barc et al.'s work [2013], the only measurements probing fragment ion production in uracil MPI were carried out using a 260 nm pump (~50 fs) and a 780 nm probe (40 fs) with a variable delay of up to 10 ps [Matsika et al. 2011, Zhou et al. 2012]. Previous fragment ion assignments have been based on photoionization appearance energies [Jochims et al. 2005], thermochemical calculations [Jochims et al. 2005], observations of metastable dissociation pathways as a tool to identify sequential fragmentation (in their discussion, Rice et al. [1965] noted that measurements of this kind had informed their assignments but they did not show the results), and DFT calculations [Arani et al. 2012]. None of the previous mass spectrometric studies stated the mass resolution and fragment ion masses were given to the nearest integer only. In the present data, the mass resolution ($m/\Delta m$, where Δm is the peak FWHM converted to a mass scale) for higher masses ($m/z \geq 84$) is ~1200 and for lower masses ($m/z \leq 44$) is ~600. Rice et al. [1965] carried out measurements on partially deuterated uracil (on the nitrogen sites only) but they did not present the results in detail. To our knowledge, no previous dissociative ionization measurements have been carried out on fully deuterated uracil. Aside from Barc et al.'s MPI experiments [2013], m/z 84 ions from uracil have only been observed in laser-induced plasmas (266 and 1064 nm ns-timescale pulses) [Lopez-Quintas et al. 2014] where multiple collisions can plausibly lead to the ionization of excited neutral isomers. However, it should also be noted that Lopez-Quintas et al.'s experiments [2014] involved laser ablation of compact uracil pellets (1 cm diameter) so the production of specific fragment ions may be affected by intermolecular bonding.

It is interesting to note that Markush et al. [2016] recently observed coincident detection of fragment ions with m/z 42-44 and m/z 38-42 in 36 kV C^{4+} collisions with gas-phase

uracil from an effusive oven source. They argued that these results indicated a common *parent* doubly charged fragment ion with mass 84 and hence m/z 42. As they did not observe any ions with mass 84 (doubly charged or singly charged) from gas-phase uracil, they commented that the lifetime of the $(U\text{-}CO)^{2+}$ must be too short (<500 ns) to be identified using their mass spectrometer. We have never observed evidence for doubly charged ions in our MPI experiments. This is unsurprising in view of the high number of absorbed photons required for double ionization, in the context of the laser fluence available (maximum 10^9 Wcm^{-2} at 220 nm). For an example, van der Burgt et al. [2015] measured electron impact fragmentation of adenine with an appearance energy of 8.0 ± 0.2 eV for parent ion as compared to doubly charged parent ion with an appearance energy of 23.5 ± 1.0 eV.

4.2 Experimental

The compact MPI/EII system has been described in Chapter 3 as well as in previous publications [Barc et al. 2013, Ryszka et al. 2016, Barc et al. 2014, Pandey et al. 2017]. In the present experiments, argon or helium carrier gas (0.5–1.2 bar) seeded with sublimated uracil (Sigma-Aldrich with stated purity ≥99%) and/or deuterated uracil (uracil-d4, CDN isotopes, 98.4%) flowed continuously through a 50 μm diameter pinhole into a pumped chamber (500 l s^{-1}) to form a supersonic jet. The powder temperatures (250–277◦C) were comparable with or lower than those applied in previous mass spectrometry and IR spectroscopy experiments that reported no evidence for thermally driven decomposition (i.e. breakdown process of a single molecule into its two or more elemental parts or to simpler compounds caused by heat), isomerization, tautomerization, or reactivity (i.e. formation of larger and complex molecule from

original molecule(s) caused by heat) in uracil, adenine, or thymine following sublimation in inert gas [Colarusso et al. 1997]. The resulting ions were detected using a reflectron time-of-flight (TOF) mass spectrometer (supplied by KORE Technology and shown schematically in Fig 3.1 and 5.1) with the *field free region* (FFR) held at V_{FFR}= -2,027±1 V kV. The pre-amplified ion signals were timed using a Fast Comtec P7887 time-to-digital conversion (TDC) card with a minimum bin size of 250 ps to achieve maximum resolution that we can attain with our compact MPI/EII experiment.

4.3 High-resolution MPI mass spectra of uracil

Fig. 4.2 shows the sum of five uracil mass spectra recorded under the same conditions. The argon pressure above the nozzle and the pressure in the interaction chamber were 1.214 bar and 6.7×10^{-7} mbar, respectively. The sample was kept at constant temperature (277 ± 1) °C and the average laser pulse energy was (515 ± 32) μJ. In order to obtain the best possible resolution, it was important to keep the timing of the laser pulse with respect to the start pulse of the TOF analysis as constant as possible. Therefore the delay between the pulses triggering the xenon flash lamps and the Q-switch of the Nd:YAG laser (our standard approach to control the pulse energy) was not changed during these measurements. In addition, we did not adjust the position of the frequency doubling crystal (another method to change pulse energy) as this could subtly change the shape and position of the laser spot, both parameters than can affect ion flight time. The laser pulse energy drops steadily with use (we typically adjust the parameters noted above to compensate for this drop) and this can also affect the laser spot shape and hence resolution. Therefore our decisions to not touch the delays or the crystal placed a limit on the number of pulses that we could use for the measurement. Moreover,

notwithstanding our approach of leaving the mass spectrometer voltages to stabilize for at least 12 hours prior to attempting a high-resolution measurement, a longer acquisition time increases the possibility of some drift in mass spectrometer voltages. Therefore there is a compromise between working in optimum resolution conditions and carrying out long measurements to maximise signal. As discussed below, the resolution that we achieved was not sufficient to see separate peaks for different fragment ions with the same nominal mass. However, with good statistics, a symmetric peak shape, and a precise calibration, it is possible to determine the peak maximum with high precision.

We recorded the present mass spectra with the narrowest time bin size available for our TDC (250 ps). This is small compared with the FWHM (full width half maximum) resolution of our peaks. For example, the FWHM of the "m/z 28" peak is 18 ns but the separation of *calculated flight times* (substituting the precise masses [Manura and Manura 2016] into our calibration formula) of the two ions most likely to contribute to this peak (CO^+ and CNH_2^+) is 7 ns. Gaussian fits (Origin 8.5.1) were carried out on all the peaks with intensities > 5% of the maximum peak intensity. The FWHM and the symmetry (the ratio of the total counts on either side of the Gaussian centre) are given in table 4.2. It is interesting to note that the FWHM does not increase significantly for lower mass fragment ions. For example, the similarly intense peaks at m/z 84 (17% of the strongest peak) and 29 (18% of the strongest peak) have respective FWHMs of 22 and 23 ns. As smaller fragment ions have higher kinetic energy release upon fragmentation (due to conservation of momentum), this indicates that kinetic energy release does not have a strong effect on peak width. This can be attributed partially to the action of the reflectron and partially to other factors (for example, the width of laser beam and small fluctuations in the mass spectrometer voltages) having relatively large

effects. Unsurprisingly, Table 4.2. shows that the more intense peaks tend to have narrower FWHM and greater symmetry, corresponding to the most reliable Gaussian centre values.

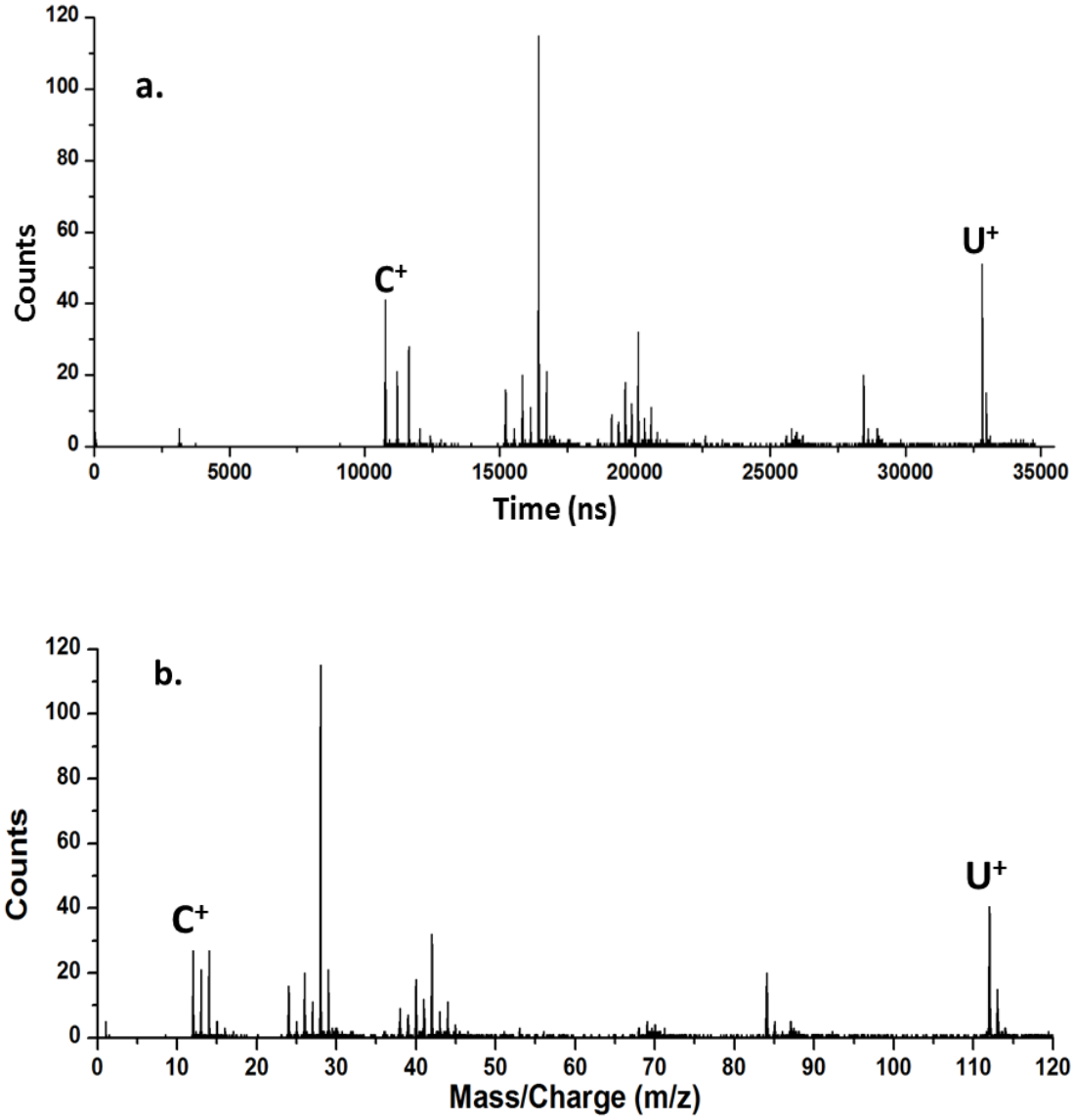

Figure 4.2: (a). Sum of five MPI mass spectra of uracil having arrival time (ns) of fragment ions on the X axis and number of counts arriving in each (250 ps width) bin on the Y axis. (b). Calibrated spectra (a.) having mass/charge (m/z) of fragment ions on x axis; showing carbon$^+$ (C^+, m/z 12.000) and uracil$^+$ (U^+, m/z 112.027).

The calibration is based on a standard linear dependence of detection time (t) against the square root of the ion mass (m in atomic mass units): $\sqrt{m} = At + B$. A and B are

constants that can be determined by identifying reference peaks in the mass spectrum and then solving a simultaneous equation. Approximate flight times can be calculated to check that the peaks have been identified correctly. For the calibration of the uracil mass spectra, The peaks at 10777 and 32844 ns have been picked as references because they are quite strong (36% and 44% of most intense peak, Table 4.2), they are far apart in the mass spectrum, and each can only reasonably be assigned to one ion: carbon$^+$ (C^+, m/z 12.000) and uracil$^+$ (U^+, m/z 112.027) [Barc et al. 2013, Jochims et al. 2005].

The production of UH^+ relative to U^+ is 25% in Fig. 4.2, therefore it shows that the target beams contained some clusters. The most stable uracil dimer configuration features two parallel N3H···OC2 bonds (see Fig. 4.1a) [Pitonák et al. 2008, Hobza et al. 1999]. Previously, MPI mass spectra of pure uracil clusters have been measured using 274 nm ns-timescale laser pulses but no information regarding fragment ions was reported [Kim et al. 2001]. The only experiment in the available literature that report fragment ion production from pure uracil clusters was performed for 100 keV O^{5+} impact ionization [Schlathölter et al. 2006] with an aggregation source that produced larger clusters than the present apparatus. In this experiment, signals at m/z 83 (U^+ minus HCO) and 95 (U^+ minus OH) were interpreted as providing evidence for hydrogen bonding. However, the present MPI measurements did not show any ion production at these m/z values above the background level.

Table 4.2: Summary of the High-Resolution TOF data. The ion assignments in grey are not supported by the high-resolution data; whereas those in bold agree with the present measurements to within the estimated uncertainty ranges.

Gaussian centre (m/z) & intensity % of strongest peak [A, B]	FWHM & peak symmetry (%) w.r.t. Gaussian centre	Possible ions with previous assignments	m/z of possible ions	Notes
113.033 ± 0.013, 13%	17 ns, 88%	**$C_4H_5N_2O_2^+$** **$C_4H_4N_2O_2^+$ with one ^{13}C** [1]*	**113.035** **113.031**	Combination
112.027 ± 0.010, 44%	14 ns, 85%	$C_4H_4N_2O_2^+$	112.027	Calibration reference
84.049 ± 0.011, 17%	22 ns, 96%	$C_3H_4N_2O^+$ [1] $C_4H_4O_2^+$ $C_3H_2NO_2^+$	84.032 84.021 84.009	Deuterated comparison supports $C_3H_4N_2O^+$
44.000 ± 0.009, 10%	20 ns, 86%	$C_2H_4O^+$ CH_2NO^+ [2] CO_2^+	44.026 44.014 43.990	Possible combination
43.004 ± 0.010, 7%	20 ns, 91%	$C_2H_3O^+$ **$CHNO^+$** [3]	43.018 **43.006**	
42.007 ± 0.007, 28%	19 ns, 97%	$C_2H_4N^+$ [2, 4] $CH_2N_2^+$ **$C_2H_2O^+$** [3, 5, 4] CNO^+	42.034 42.022 **42.011** 41.998	Deuterated comparison supports $C_2H_2O^+$
41.016 ± 0.008, 10%	25 ns, 88%	$C_2H_3N^+$ [3, 5] **CHN_2^+** C_2HO^+ [3]	41.027 **41.014** 41.003	Possible combination
40.018 ± 0.007, 16%	26 ns, 88%	$C_3H_4^+$ **$C_2H_2N^+$** [3] CN_2^+ C_2O^+	40.031 **40.019** 40.006 39.995	Deuterated comparison supports $C_2H_2N^+$
39.008 ± 0.010, 6%	33 ns, 99%	$C_3H_3^+$ **C_2HN^+**	39.024 **39.011**	
38.001 ± 0.008, 8%	22 ns, 83%	$C_3H_2^+$ **C_2N^+**	38.016 **38.003**	
29.019 ± 0.006, 18%	23 ns, 98%	CH_3N^+ [3, 4] **HN_2^+** HCO^+ [3]	29.027 **29.014** 29.003	Deuterated comparison supports CH_3N^+
28.013 ± 0.005, 100%	19 ns, 98%	C_2H_4+ CH_2N^+ [3, 5, 4] N_2^+ CO^+ [2]	28.031 28.019 28.006 27.995	Deuterated comparison supports CH_2N^+
27.003 ± 0.008, 10%	23 ns, 87%	$C_2H_3^+$ **CHN^+** [3]	27.023 **27.011**	
26.009 ± 0.006, 17%	26 ns, 98%	$C_2H_2^+$ [3] **CN^+**	26.016 **26.003**	
24.011 ± 0.006, 14%	28 ns, 95%	C_2^+	24.000	
14.013 ± 0.004, 24%	19 ns, 100%	**CH_2^+** [2] N^+ [3]	**14.016** 14.003	
13.005 ± 0.004, 18%	17 ns, 82%	**CH^+**	**13.008**	
12.000 ± 0.002, 36%	20 ns, 94%	C^+	12.000	Calibration reference

*1. Barc et al. 2013, 2. Imhoff et al. 2007, 3. Jochims et al. 2005, 4. Arani et al. 2012, 5. Matsika et al. 2011.

A. The table only includes peaks with intensities >5% of the most intense peak (m/z 28). Further weak peaks were observed at m/z (nearest integer) 1 (H^+), 15 (CH_3^+ [Imhoff et al. 2007), 16 (CH_4^+, H_2N^+, or O^+), 25 (C_2H^+), 45 (CH_3NO^+ or CHO_2^+), 68 ($C_3H_2NO^+$ [Jochims et al. 2005]), 69 ($C_3H_3NO^+$ [Jochims et al. 2005, Matsika et al. 2011, Arani et al. 2012]), 70 ($C_3H_4NO^+$ [Jochims et al. 2005, Arani et al. 2012]), and 85 ($C_3H_5N_2O^+$ or $C_3H_3NO_2^+$).

B. The uncertainty estimations on the Gaussian centre values are based on summing the uncertainties given by fitting software (Origin 8.5.1) and the uncertainty based on the calibration using the reference peaks noted above. Peaks that lie outside the estimated ranges (e.g. for the m/z 84 and 24 peaks) can be attributed to deviations from Gaussian peak shapes.

Figs. 4.3 shows the Gaussian fits (red curves) for the two peaks. The central arrival time (referred to as xc) of each Gaussian fit is labelled with a vertical green line. The xc values with the uncertainties generated by the Origin 8.1 software were 10777.55 ± 0.17 ns and 32844.49 ± 0.11 ns for the C^+ and U^+ peaks, respectively. The uncertainty on the calibrated mass of a given peak in Table 4.2 was generated as a function of (i) the uncertainty on the xc value for that peak and (ii) the uncertainty of the calibration due to the uncertainties on the reference xc values. Further this xc value was used to calculate the calibrated mass of each peak using detection time (t) against the square root of the ion mass (m in atomic mass units) $\sqrt{m} = At + B$.

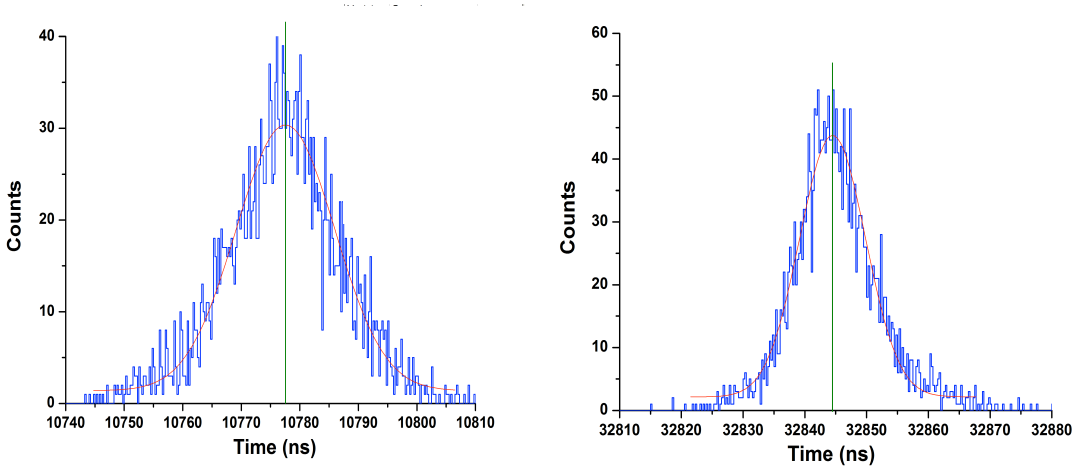

Figure 4.3: Gaussian fitting (red curve) of the peak identified as C^+ (m/z 12.000 ± 0.002) and U^+ (m/z 112.027 ± 0.010). The blue curve outlines a histogram showing the number of counts recorded in each time bin of the mass spectrum. The width of each time bin was 0.25 ns (the minimum possible using the Fast Comtec P7887 TDC). The number of laser pulses (rep rate 10 Hz) used to accumulate the mass spectrum was 30,000. Hence, the count rate per bin (<0.002 per pulse) was far too low for detector or TDC saturation effects to distort the peak shapes.

4.4 MPI mass spectra of uracil and deuterated uracil

Fig. 4.4 (a) and (b) show MPI spectra recorded in matching conditions (220 nm, average laser pulse energy (455 ± 22) μJ, powder 250°C, He 0.8 bar, same lens position and molecular beam alignment) for uracil and fully deuterated uracil. The deuterated results were also discussed in the thesis of Michal Ryzska [2015] but no comparisons were drawn with high-resolution mass spectra.

As noted in the experimental chapter, the deuterated uracil was purchased from CDN Isotopes with a stated purity of 98.4%. However the ratio of the peaks at m/z 115 and 116 in the lower plot of Fig. 4.4 indicates that our molecular beam comprised 20% $C_4D_3HN_2O_2^+$ and 80% $C_4D_4N_2O_2^+$. Rice et al. [1965] studied electron impact ionization of various pyrimidine derivatives, including partially deuterated uracil produced by dissolution in D_2O. They assumed that replacement of hydrogen by deuterium occurred exclusively at nitrogen atoms. Accordingly, we assume that our brief exposure of fully deuterated uracil to air led to some hydrogenation at nitrogen sites only.

The measurements shown in Fig. 4.4 were carried out using helium as the carrier gas. Helium was chosen in order to minimize the possibility of clustering in the supersonic beam. Indeed, we have observed no evidence for clustering in any of our measurements using helium expansions (with one exception presented in section 5.4.1). Fig. 4.4(a) shows that the ratio of the signals at m/z113 and 112 is (6±1)%, in agreement with natural ^{113}uracil / ^{112}uracil ratio of 5.2% [Manura and Manura 2016]. Stronger m/z 113 signals than the natural isotope ratio indicates the production of protonated uracil (UH^+) from uracil cluster ions.

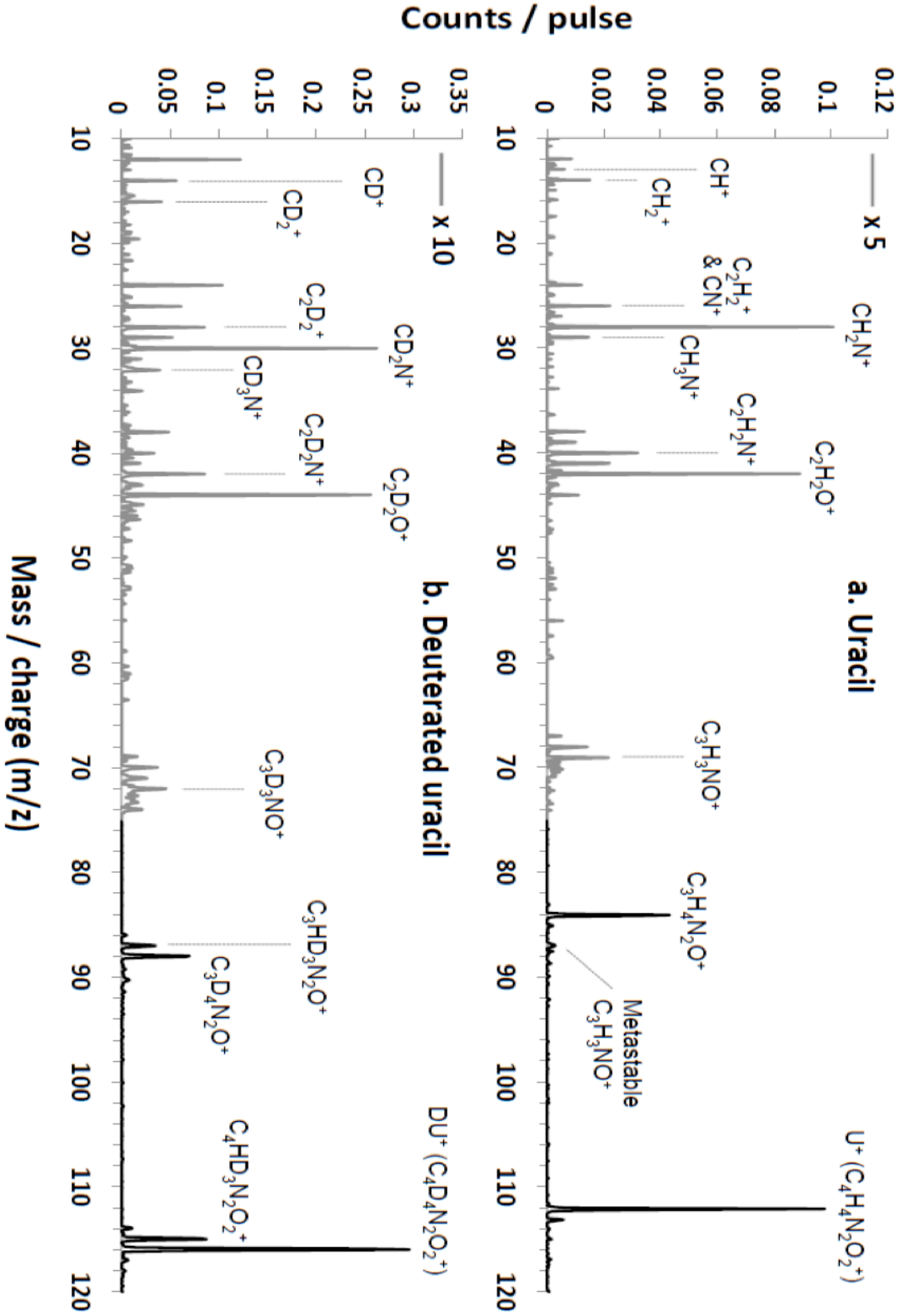

Figure 4.4: MPI mass spectra (220 nm, average fluence 9×10^{7} Wcm^{-2}, He 0.8 bar, powder 250 °C) of a). uracil and b). deuterated uracil. The peak assignments discussed in the text have been labelled.

Reduced clustering in helium expansions compared with argon expansions is a well-know effect. This is associated with relatively inefficient loss of internal energy in collisions with helium atoms than with argon atoms that have kinetic energy that are relatively close to those of the molecules. Hence the energy transfer will then be a maximum when the masses of expansion gas and seeded molecules are comparable [Zener 1931]. Cooling in supersonic expansions is discussed further in Chapters 2 and 7.

By contrast, the high-resolution data in section 4.3 was carried out using an argon expansion. This has the disadvantage that some clusters were present in the expansion, evidenced by the detection of protonated uracil (discussed in section 4.5). However, working with argon beams instead of helium beams is advantageous to achieve high m/z resolution. The seeded molecules have higher velocities in helium expansions (~2200 ms^{-1}) than in argon expansions (~700 ms^{-1}) so a stronger vertical deflection field is necessary to optimise the signals of molecules with low kinetic energy release. This is why the low-mass fragment ion signals are relatively weak in Fig. 4.4; the measurements were optimized for strong detection of un-dissociated ions and large fragment ions. In argon beams, strong signals can be achieved across the full range of product ions from uracil for a single optimization of the mass spectrometer voltages. This is important in order to achieve the largest possible separation of suitably strong calibration peaks and hence the best-possible m/z resolution.

Sadr-Arani et al.'s [2014] dissociative ionization experiments on protonated uracil (UH^+) produced ions with m/z 96, 85, 70, and 68. Similarly, Nelson and McCloskey [1994] reported that the principal dissociation products of protonated uracil had m/z 96,

95, 70, 68, and 67. The peak at m/z 96 was particularly strong in both works [Sadr-Arani et al.'s 2014, Nelson and McCloskey 1994] but it is not visible in Fig. 4.2. Moreover there is small peak at m/z 68 and 70 but they are very small as compared to others. This suggests that the fragment ion peaks observed here did not have significant contributions from dissociated protonated uracil. Schlathölter et al.'s [2005] 100 keV O^{5+} impact experiments on uracil clusters produced fragment ions with m/z 95 and 83. The absence of any prominent peaks at these m/z values in Fig. 4.2 further indicates that clustering did not have a significant effect on the present analysis of fragment ion production.

4.5 Discussion: assignments of fragment ions based on high-resolution mass spectra of uracil and comparison with the uracil/deuterated uracil measurements

I have limited the present discussion to relatively strong peaks because the Gaussian fits for weak peaks give less precisely calibrated central m/z values (referred to here as CM). Table 4.2 summarises the key conclusions from the present measurements. The third column of the table lists the possible ions at each m/z (nearest integer) value and the fourth column lists their masses obtained using the Scientific Instruments Service Isotope Calculator [Manura and Manura 2016]. The ions and masses in bold agree with the present measurements to within the estimated uncertainty ranges. The "possible ions" listed with references correspond to previous assignments in the literature. Clearly, a number of mass spectral peaks have been subject to more than one interpretation. In particular, the peak at m/z 28 (nearest integer) has previously been assigned as CH_2N^+ [Jochims et al. 2005, Matsika et al. 2011, Arani et al. 2012] or CO^+ [Imhoff et al. 2007], while the m/z 29 peak has been assigned as CH_3N^+ [Jochims et al.

2005, Arani et al. 2012] or HCO^+ [Jochims et al. 2005]. The peaks at m/z 41 and 44 (nearest integer) are also subject to contrasting assignments in the literature [Imhoff et al. 2007, Jochims et al. 2005, Matsika et al. 2011].

As an example of how the high resolution data supports a specific assignment, Fig 4.5 shows the Gaussian fit (red line) for to the fragment ion peak centred at xc = 11642.70 ± 0.23 ns (green line), corresponding to CM = 14.013 ± 0.004. The green shaded region represents the uncertainty on the CM value. The black and red lines indicate the masses of the possible ions: CH_2^+ (14.016) and N^+ (14.003). The overlap of present CM uncertainty limits with the mass of CH_2^+ indicates that the peak is dominantly due to CH_2^+, following Imhoff et al.'s interpretation [2007]. If any N^+ (assigned by Jochims et al. [2005]) is produced, it must be relatively weak.

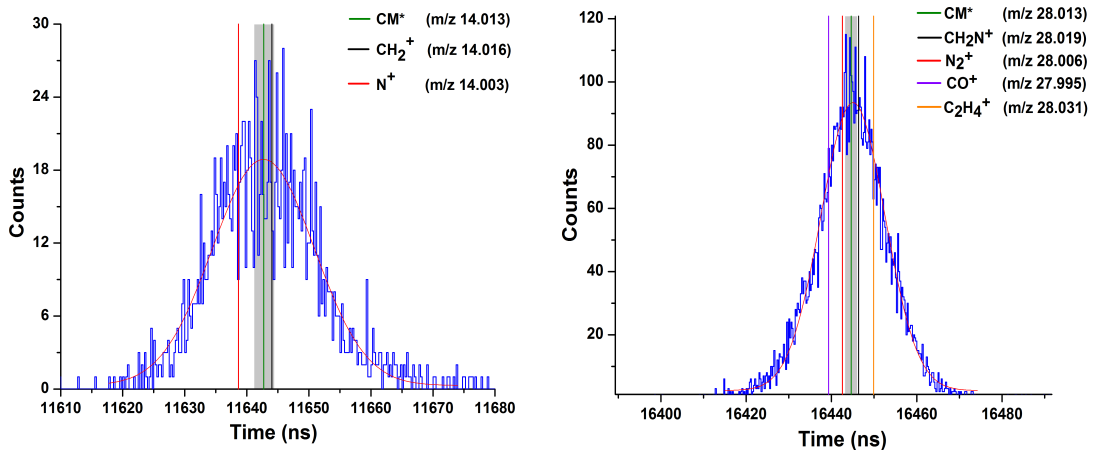

Figure 4.5: Gaussian fitting of the fragment ion peak at m/z 14.013 ±0.004 and at m/z 28.013 ± 0.005, showing calibrated mass CM* (Green line) and other possible ions masses represented by black line and red line, respectively.

Starting at low masses, the first aspect of the uracil / deuterated comparison to note is the absence of any signal at m/z 13 in the deuterated measurement (Fig. 4.4(b)). CH^+

ions were produced from uracil, both in the present data (Fig. 4.4(a) and more strongly in Fig. 4.2) and in previous MPI and EII experiments [Barc et al. 2013, Imhoff et al. 2007]. The fact that negligible CH^+ ions were produced from the deuterated target (approximately 20% $C_4D_3HN_2O_2^+$ and 80% $C_4D_4N_2O_2^+$, as noted above) is consistent with our assumption that the carbon sites on the ring have not experienced D/H exchange. The peak at m/z 14 in Fig. 4.4(b) is assigned to CD^+, although a contribution of N^+ cannot be ruled out. The peak at m/z 16 in the deuterated data (absent in the uracil data) is assigned to CD_2^+. This assignment is consistent with the high-resolution data (Fig. 4.5 and Table 4.2). To our knowledge, no previous work has proposed a specific pathway for CH_2^+ production from uracil.

As weak $C_2H_2^+$ production was previously observed from uracil [Barc et al. 2013, Imhoff et al. 2007], the peak at m/z 26 in Fig. 4.4(b) is expected to contain a contribution of $C_2D_2^+$. Compared with the m/z 25 feature in Fig. 4.4(a), however, the strength of the m/z 26 peak in both plots suggests a contribution of CN^+ (not proposed in any previous works). The high-resolution data (Table 4.2) is consistent with this suggestion as the Gaussian maximum (CM = 26.009 ± 0.006) agrees with the mass of CN^+ (26.003).

The most striking result in the m/z 24-32 ion group is the shift of the strongest peak from m/z 28 in Fig. 4.4(a) to m/z 30 in Fig. 4.4(b). This clearly indicates that the peaks are respectively dominated by CH_2N^+ and CD_2N^+, whereas some previous works have assigned this feature to CO^+ from uracil [Imhoff et al. 2007]. Fig. 4.5 shows the peak whose Gaussian centre (xc = 16444.63 ± 0.10 ns) corresponds to CM = 28.013 ± 0.005. This is close to CH_2N^+ (m/z 28.019) and N_2^+ (m/z 28.006) but significant CO^+ (m/z

27.995) or $C_2H_4^+$ production can be ruled out. Looking at the structure of uracil (Fig.4.1), a rather implausible rearrangement of the molecule would be necessary to produce N_2^+ and no previous studies have suggested this possibility. Furthermore, the narrow FWHM (19 ns) and high symmetry percentage of peak (98%) suggests that it is unlikely to be due to a combination of ions. Therefore the high-resolution data and the uracil / deuterated uracil comparison support the CH_2N^+ assignment.

The only plausible assignment for the clear feature at m/z 32 in Fig. 4.4(b) is CD_3N^+. This provides evidence for a significant contribution of CH_3N^+ to the m/z 29 peak in the uracil mass spectrum, in agreement with Arani et al.'s calculations [2012]. Jochims et al. [2005] assigned the peak to "CH_3N^+ or HCO^+". Our high-resolution data (Table 4.2) shows that the calibrated Gaussian centre of the peak (CM = 29.019 ± 0.006) agrees with the unlikely fragment ion HN_2^+ (m/z 29.014). However the peak is not very strong (18% of the strongest ion) and the agreement with HN_2^+ may be a fortuitous result of overlapping CH_3N^+ (m/z 29.027) and HCO^+ (m/z 29.003) contributions. Arani et al.'s [2012] proposed mechanism for CNH_3^+ production involved direct cleavages of the N1–C2 and C5–C6 bonds (presumably with hydrogen transfer from C5 to C6 (see Fig 4.1)). Note that C5-C6 is a single bond in the radical cation [18], whereas it is a double bond in neutral uracil. By contrast, CNH_2^+ is expected to be stem mainly from $C_3H_3NO^+$ dissociation [Jochims et al. 2005, Arani et al. 2012].

The most intense peak in the m/z 38-45 group is shifted from m/z 42 in Fig. 4.4(a) to m/z 44 in Fig. 4.4(b). This supports assignment to $C_2H_2O^+$ [Jochims et al. 2005, Matsika et al. 2011, Arani et al. 2012] as opposed to $C_2H_4N^+$ [Imhoff et al. 2007 Arani et al. 2012]. The group's second strongest peak (m/z 40 from uracil) is also apparently shifted

by two mass units in the deuterated measurement, consistent with the accepted assignment to $C_2H_2N^+$. Table 4.2 and Fig. 4.6 show that both of these assignments are consistent with the high-resolution data. The main peaks in the m/z 67-74 group are also consistent with the previous assignments to $C_3H_2NO^+$ and $C_3H_3NO^+$ from uracil [Jochims et al. 2005, Matsika et al. 2011, Arani et al. 2012].

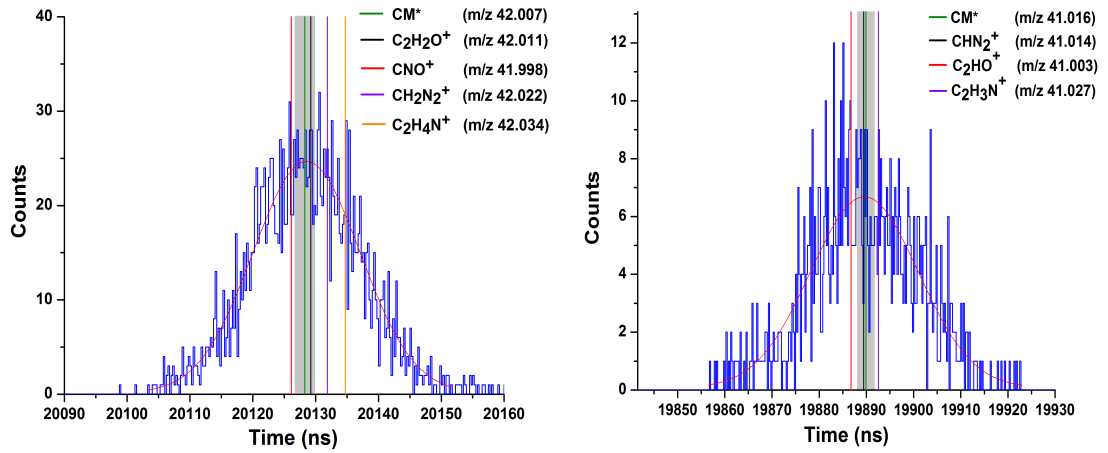

Figure 4.6: Gaussian fitting on fragmented ion peak at m/z 42.007±0.007 and at m/z 41.016 ±0.008, showing CM* (Green line) and other possible ions masses represented by black line, red line and violet line, and orange line respectively.

Fig. 4.6 shows the peak with a calibrated Gaussian centre (CM) at m/z 41.016 ± 0.008. This agrees with CHN_2^+ (m/z 41.014), although the peak's low intensity (10% of the strongest peak) should be noted. Furthermore, the broad FWHM (25 ns) & relatively low peak symmetry percentage (88%) may suggest contributions of more than one ion, most likely the previously proposed ions C_2HO^+ (m/z 41.003) and $C_2H_3N^+$ (m/z 41.027) [Jochims et al. 2005, Matsika et al. 2011]. The uracil / deuterated uracil comparison is inconclusive in this case.

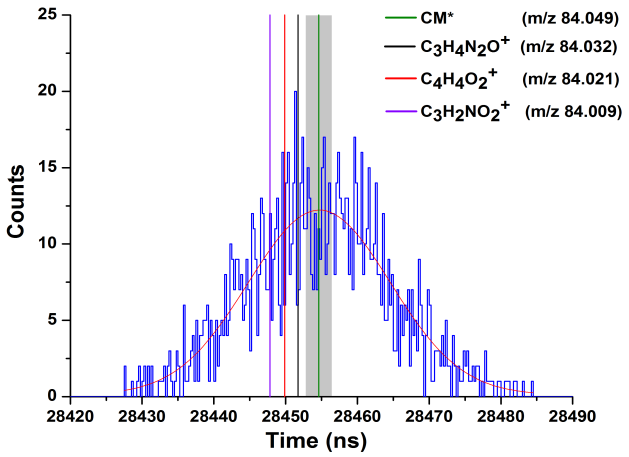

Figure 4.7: Gaussian fitting on fragmented ion peak at m/z 84.049 ± 0.011, showing CM* (Green line) and other possible ions masses represented by black line, red line and violet line, respectively.

The principle motivation for the present measurements was to clarify the assignment of the m/z 84 peak in the uracil MPI mass spectrum. The two plausible assignments are $C_3H_4N_2O^+$ (CO loss from uracil$^+$) [Barc et al. 2013] and $C_3H_2NO_2^+$ (CNH_2 loss from uracil$^+$). The comparison of the uracil and deuterated uracil data in Fig. 4.4 is conclusive. The peak at m/z 84 in Fig. 4.4(a) is replaced by two peaks at m/z 87 and 88 in Fig. 4.4(b). The substitution of hydrogen atoms in $C_3H_2NO_2^+$ with deuterium atoms cannot produce an ion with mass greater than m/z 86 ($C_3D_2NO_2^+$) so this channel can be ruled out. The observation of two peaks for this fragmentation pathway in Fig. 4.4(b) is due to some D/H exchange at ND sites in our deuterated sample (see section 4.4).

There is one other possible ion formula that could account for the results in Fig. 4.7 $C_4H_4O_2^+$ (neutral N_2 loss). This is even less plausible than N_2^+ production (discussed above) as it necessitates the N loss from two completely separate sites on the ring (both with attached H atoms) without the loss of any other atoms. Accordingly, the high-resolution data provides evidence against this implausible pathway. Fig. 4.7 shows the peak with Gaussian centre (CM) at m/z = 84.049.011 ± 0.005. Although the estimated uncertainty range does not overlap with the m/z value of $C_3H_4N_2O^+$ (84.032), the agreement is better than with $C_4H_4O^+$ (84.021) or $C_3H_2NO_2^+$ (84.009).

The peak at m/z 113 (nearest integer) in the high resolution mass spectrum can be attributed to a combination of protonated uracil (UH^+) and the isotopomer of U^+ with one ^{13}C replacing a ^{12}C atom [Imhoff et al. 2007, Manura and Manura 2016]. The natural ratio of ^{113}uracil / ^{112}uracil is 5.2% [Manura and Manura 2016], whereas the ratio of (m/z 113) / (m/z 112) in the high mass resolution measurement of uracil is 25.27 ± 0.17 %. This shows that the m/z 113 (nearest integer) peak was dominantly produced by UH^+ ions. UH^+ is traced to barrierless proton transfer in uracil cluster ions (notably the dimer ion) followed by dissociation producing a protonated uracil ion and a *deprotonated uracil* neutral fragment (U-H) [Imhoff et al. 2007, Mota et al. 2005]. Table 4.1 shows that the CM of the peak is 113.033 ± 0.013. This is in between the m/z values of UH^+ (113.035) and uracil$^+$ with one ^{13}C (113.031), as expected for a peak containing two different ions. The fact that the peak CM value is further than expected from the UH^+ value may be due to quite low statistics.

4.6 Summary

High-resolution MPI of uracil has been studied and compared with uracil/deuterated uracil results for the assignment of fragment ions from uracil at 220 nm (5.64 eV). The main conclusions of present work are listed below:

- For peaks with good statistics, the high-resolution data and the uracil / deuterated uracil comparison are in excellent agreement in terms of identifying specific fragment ions.
- We have definitively assigned the m/z 84 (nearest integer) peak. This agrees with the interpretation of the new fragmentation pathway that we reported in our previous work [Barc et al. 2013, Ryszka et al. 2016]. Hence we see evidence for CO loss due

to ring opening in neutral excited states and three conical interactions have been calculated (see table 4.1) with ring opening in a plausible place to explain this. The energies of these CIs are also consistent with wavelength threshold observed by Barc et al. [2013]. However, we do not know which (if any) of these CIs are responsible for our results.

- We have provided evidence supporting the production of the following ions that were subject to debate in the literature, m/z (nearest integer): 14 (CH_2^+), 28 (CH_2N^+), 29 (CH_3N^+), 42 ($C_2H_2O^+$). It should be noted that these results do not rule out possible weaker additional contributions of alternative ions.

This chapter shows how the combined information provided by deuterated measurements and high-resolution measurements allows fragment ions to be identified unambiguously. This is a powerful analytical approach. The present measurements also show that the precise definition of peak maxima provides valuable information even when the mass resolution is not high enough to completely separate peaks from different ions that have equal m/z to the nearest integer.

4.7 Contributions by co-workers and publication

I preformed all the experiments in this chapter, working with PhD students Michal Ryszka (now graduated) and Chris Rizk (master's student). I analyzed the experimental data and devised interpretations, working primarily with Samuel Eden. Marcin Dampc, Jean Tabet, and Nigel J. Mason contributed to the journal manuscripts based on this chapter: The results in this chapter have been published in International Journal of Mass Spectrometry [Ryszka, Pandey et al. 2016].

References:

- L. S. Arani, P. Mignon, H. Abdoul-Carime, B. Farizon, M. Farizon and H. Chermette, *Phys. Chem. Chem. Phys.*, 2012, **14**, 9855-9870.
- L. Sadr-Arani, P. Mignon, H. Chermette and T. Douki., *Chem. Phy. Lett.*, 2014, **605-606**, 108-114.
- B. Barc, M. Ryszka, J. Spurrell, M. Dampc, P. Limão-Vieira, R. Parajuli, N. J. Mason and S. Eden, *J. Chem. Phys.*, 2013, **139**, 244311.
- B. Barc, M. Ryszka, J.-C. Poully, E. Jabbour Al Maalouf, Z. el Otell, J. Tabet, R. Parajuli, P. J. M. van der Burgt, P. Limão-Vieira, P. Cahillane, M. Dampc, N. J. Mason and S. Eden, *Int. J. Mass Spectrom*., 2014, **365-366**, 194-199.
- P. J. M. van der Burgt, S. Finnegan and S. Eden, *Eur. Phys. J. D*, 2015, **69**, 173.
- P. Colarusso, K. Q. Zhang, B. J. Guo and P. F. Bernath, *Chemical Physics Letters.,* 1997, **269**, 39-48.
- B. Coupier, B. Farizon, M. Farizon, M. J. Gaillard, F. Gobet, N. V. de Castro Faria, G. Jalbert, S. Ouaskit, M. Carré, B. Gstir, G. Hanel, S. Denifl, L. Feketeova, P. Scheier and T. D. Märk, *Eur. Phys. J. D*, 2002, **20**, 459-468.
- S. Denifl, B. Sonnweber, G. Hanel, P. Scheier and T. D. Märk, *Int. J. Mass Spectrom*., 2004, **238**, 47-53.
- S. Feil, K. Gluch, S. Matt-Leubner, P. Scheier, J. Limtrakul, M. Probst, H. Deutsch, K. Becker, A. Stamatovic and T. D. Märk, *J. Phys. B*, 2004, **37**, 3013-3020.
- P. Hobza, J. Sponer, *Chem. Rev.,* 1999, **99**, 3247-3276.
- M. Imhoff, Z. Deng, and M. Huels, *Int. J. Mass Spectrom*., 2007, **262**, 154-160.
- H. W. Jochims, M. Schwell, H. Baumgartel and S. Leach, *Chem. Phys.,* 2005, **314**, 263-282.
- N. J. Kim, H. Kang, G. Jeong, Y.S. Kim, K.T. Lee and S.K. Kim, *Proc. Natl. Acad. Sci.,* 2001*,* **98**, 4841-4843.
- A. Les and L. Adamowicz, *J. Phy. Chem.*, 1989, **93**, 7078-7081.
- I. Lopez-Quintas, M. Oujja, M. Sanz, A. Benitez-Cañete, C. Hutchison, R. de Nalda, M. Martin, R. Ganeev, J. Marangos and M. Castillejo., *App. Surf. Sci.*, 2014, **302**, 299-302.
- J. J. Manura and D. J. Manura, Scientific Instrument Services Isotope Distribution Calculator, http://www.sisweb.com/mstools/isotope.htm, accessed 2016.

- P. Markush, P. Bolognesi, A. Cartoni, P. Rousseau, S. Maclot, R. Delaunay, A. Domaracka, J. Kocisek, M. C. Castrovilli, B. A. Huber and L. Avaldi, *Phys.Chem.Chem.Phys.*, 2016, **18**, 16721-16729.
- S. Matsika, C. Y. Zhou, M. Kotur and T. C. Weinacht, *Faraday Discuss.*, 2011, **153**, 247-260.
- C. T. Middleton, K. de La Harpe, C. Su, Y. K. Law, C. E. Crespo- Hernandez and B. Kohler, *Annu. Rev. Phys. Chem.*, 2009, **60**, 217-239.
- R. Mota, R. Parafita, A. Giuliani, M.-J. Hubin-Franskin, J. M. C. Lourenço, G. Garcia, S. V. Hoffmann, N. J. Mason, P. A. Ribeiro, M. Raposo and P. Limão-Vieira, *Chem. Phys. Lett.*, 2005, **416**, 152-159.
- D. Nachtigallova, A. J. A. Aquino, J. J. Szymczak, M. Barbatti, P. Hobza and H. Lischka, *J. Phys. Chem. A*, 2011, **115**, 5247-5255.
- C. C. Nelson and J. A. McCloskey, *J. Am. Soc. Mass Spectrom.*, 1994, **5**, 339-349.
- A. Le Padellec, P. Moretto-Capelle, M. Richard-Viard, J. P. Champeaux and P. Cafarelli, *J. Phys. Conf. Ser.*, 2008, **101**, 012007.
- R. Pandey, M. Lalande, M. Ryszka, P. Limão-Vieira, N. J. Mason, J. C. Poully and S. Eden, *Eur. Phys. J. D*, 2017, **in press.**
- M. Pitonák, K. E. Riley, P. Neogrády, P. Hobza, *Chem. Phys. Chem.,* 2008*,* **9**, 1636-1644.
- J. Rejnek, M. Hanus, M. Labelac, F. Ryjacek and P. Hobza, *Phys. Chem. Chem. Phys*, 2005, **7**, 2006-2017.
- J. M. Rice, G. O. Dudek and M. Barber, *J. Am. Chem. Soc.*, 1965, **87**, 4569-4576.
- M. Richter, S. Mai, P. Marquetand and L. González, *Phys. Chem. Chem. Phys.*, 2014, **16**, 24423-24436.
- M. Ryszka, Radiation induced processes in biomolecules and clusters in controlled beams, Department of Physical Sciences, The Open University, Milton Keynes, United Kingdom, *PhD thesis*, 2015.
- M. Ryszka, R. Pandey, C. Rizk, J. Tabet, B. Barc, M. Dampc, N. J. Mason and S. Eden, *Int. J. Mass Spectrom.*, 2016, **396**, 48-54.
- T. Schlathölter, F. Alvarado and R. Hoekstra, *Nucl. Instrum. Methods Phys. Res. B*, 2005, **233**, 62-69.
- T. Schlathölter, F. Alvarado, S. Bari, A. Lecointre, R. Hoekstra, V. Bernigaud, B. Manil, J. Rangama and B. Huber, *Chem. Phys. Chem.*, 2006, **7**, 2339-2345.
- J. Tabet, S. Eden, S. Feil, H. Abdoul-Carime, B. Farizon, M. Farizon, S. Ouaskit and T. D. Mark, *Phys. Rev. A*, 2010, **81**, 012711.

- J. de Vries, R. Hoekstra, R. Morgenstern and T. Schlathölter, *J. Phys. B*, 2002, **35**, 4373-4381.
- J. de Vries, R. Hoekstra, R. Morgenstern and T. Schlathölter, *Phys. Rev. Lett.*, 2003, **91**, 053401.
- J. de Vries, R. Hoekstra, R. Morgenstern and T. Schlathölter, *Phys. Scr.*, 2004, **T110**, 336-339.
- C. Zener, *Phys. Rev.*, 1931, **37**, 556-569.
- C. Zhou, S. Matsika, M. Kotur, and T. C. Weinacht, *J. Phys. Chem. A*, 2012, **116**, 9217-9227.

CHAPTER 5

Metastable dissociation processes in nucleobase radical cations and their hydrated clusters: insights into neutral excited state energies and cluster ion stabilities

This chapter investigates the metastable dissociation of uracil$^+$, thymine$^+$, and thymine-water cluster ions. Photon energy thresholds for metastable HNCO loss from multi-photon ionized uracil and thymine have been observed. We argue that these can be attributed to accessing the molecules' S_1 states with vibrational energy matching the threshold for HNCO loss from the radical cation. Combined with previous photoionization energies this provides a new route to deduce the S_1 adiabatic energies. In addition, metastable H_2O loss has been observed in multi-photon ionization experiments on thymine-water clusters. This result is compared with minimum energies required for single water molecule removal from thymine-water cluster ions ($T^+(H_2O)_n$) that have been calculated by our collaborators at CIMAP/GANIL (Research Centre on Ions, Materials, and Photonics / Large Heavy Ion National Accelerator, Caen, France). The experiments and the calculations both support a steady fall in the outermost H_2O binding energy with n.

5.1 Introduction

The valence excited state dynamics of DNA and RNA bases have been studied extensively in recent years [Kleinermanns et al. 2013] with the particular aim of understanding the response of these biological building blocks to UV irradiation. Dynamical calculations [Fingerhut et al. 2014] and time-resolved spectroscopic measurements on isolated pyrimidine nucleobases [Hudock et al. 2007] have revealed a great deal of information on the relaxation pathways from their optically bright $S_2(\pi\pi^*)$ states. Internal conversion to the electronic ground state (either directly or via S_1 states of mainly $n\pi^*$ character) dominates $S_2(\pi\pi^*)$ deactivation [Yamazaki et al. 2012, Ullrich et al. 2004], although intersystem crossing to long-lived triplet states has also been reported [Wu et al. 2004, Ligare et al. 2015]. The majority of previous experiments have probed the relaxation dynamics of nucleobases following access to low vibrational levels of S_2, for example pumping with the third harmonic of a Ti-sapphire laser (4.65 eV compared with the calculated S_2 origin of thymine at 4.49 eV [Serrano-Perez et al. 2007]). In the present multiphoton ionization (MPI) experiments, isolated thymine and uracil are excited at photon energies of 5.39-5.64 eV, where significant vibrational excitation increases the range of possible relaxation pathways. In particular, tautomeric transitions and ring opening conical intersections have been predicted theoretically [Shukla et al. 2002, Nachtigallová et al. 2011]. Our recent studies of uracil indicate that the analysis of fragment ion production from multiphoton ionized molecules can provide evidence for structural changes in neutral excited states (see Chapter 4 as well as Barc et al. [2013] and Ryszka et al. [2016]). Matsika and co-workers [Matsika et al. 2011, Kotur et al. 2012, Matsika et al. 2013] have also studied fragment ion production from multiphoton ionized nucleobases and argued that uracil$^+$ detection in 260 nm

pump - 780 nm probe experiments could only be traced to ionization from S_2, whereas the $C_3H_3NO^+$ yield (uracil$^+$ less HNCO) could provide information about the wavepacket evolution on both S_2 and S_1. The first part of this chapter (sections 5.2 and 5.4.1) investigates the metastable dissociation of multiphoton ionized nucleobases for the first time and considers its potential to provide new insights into the valence excited state energies and dynamics of these important biomolecules.

Although studying DNA bases in the gas phase can lead to relatively clear interpretations, it represents a major step away from condensed macromolecular systems. Complementary studies of nucleotides [Stavros et al. 2016], base pairs [Hunig et al. 2004], and hydrated clusters [Rasmussen et al. 2010, Nosenko et al. 2011, Barc et al. 2014] can enable closer analogies to be drawn with irradiated biological material. However, as cluster sources generally produce a broad distribution of conformations and sizes, characterizing the precursor of a specific product can present a significant challenge in experiments probing radiation-induced processes in clusters. Mass spectrometry measurements of metastable product ions can help to address this challenge by simultaneously defining the ion cluster mass before and after dissociation. Furthermore, they can provide information on binding energies, as the microsecond-order time delay implies that the vibrational energy of the cluster ion was very close to the relevant dissociation barrier. Metastable dissociation experiments have therefore played an important role in cluster research for many years [Continetti 1998, Cooks et al. 1973, Bruzzi et al. 2014], notably by means of UV irradiation [Ishiuchi et al. 2007, Kim et al. 2002]. The second part of this chapter (sections 5.3 and 5.4.2) investigates the stabilities of *nanohydrated* thymine radical cations based on metastable dissociation

measurements and detailed comparisons with *ab initio* calculations carried out by Jean-Christophe Poully and Mathieu Lalande (CIMAP/GANIL).

The majority of previous UV irradiation experiments on thymine have probed the relaxation dynamics following access to quite low vibrational levels of its optically bright S_2 state, for example pumping with the third harmonic of a Ti-sapphire laser (4.65 eV compared with the calculated S_2 origin of at 4.49 eV [Serrano-Perez et al. 2007]). In the present ns-timescale UV multiphoton ionization (MPI) experiments, thymine is excited at a photon energy of 5.64 eV (220 nm), where significant vibrational excitation increases the range of possible relaxation pathways after ionization. In addition to proton, hydrogen and hydride transfers that have been observed [Khistyaev et al. 2013, Golan et al. 2012] or predicted [Duncan Lyngdoh et al. 2009] in DNA building blocks, diverse fragmentation and evaporation processes can occur. While the decrease in ionization energy of thymine with nanohydration has been experimentally and theoretically studied by several groups [Khistyaev et al. 2011, Close et al. 2008], scarce reports can be found on the structure and decay processes of thymine-water cluster ions [Kim et al. 2002]. Here we investigate the metastable evaporation of one water molecule from UV multiphoton ionized thymine-water clusters by mass spectrometry. This experimental result inspired our collaborators to perform the most extensive set of *ab initio* quantum-chemical calculations of optimized hydrated thymine radical cation conformers to date. The relative intensities of the metastable signals in the MPI experiments are discussed here in the context of the calculated binding energies of the precursor cluster ions.

5.2 Experimental

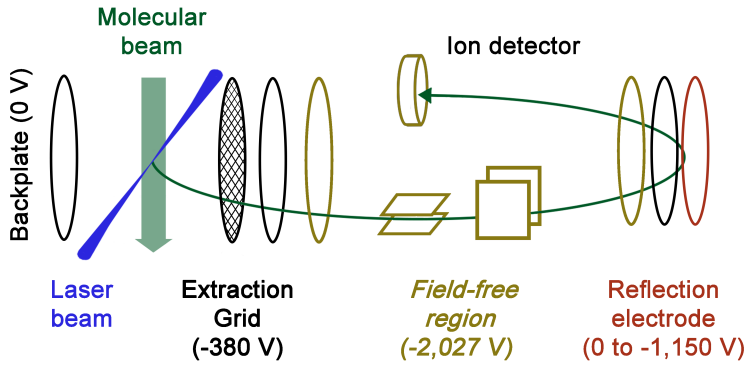

Figure 5.1: Schematic diagram of the reflectron mass spectrometer.

The compact MPI/EII system has been described in Chapter 3 as well as in previous publications [Barc et al. 2013, Ryszka et al. 2016, Barc et al. 2014, Pandey et al. 2017]. In the present experiments, argon or helium carrier gas (0.8-1.1 bar) seeded with sublimated thymine or uracil (both Sigma-Aldrich with stated purity ≥99%) flowed continuously through a 50 µm diameter pinhole into a pumped chamber (500 ls^{-1} in the experiments on isolated uracil and thymine; 1000 ls^{-1} in the experiments on nanohydrated thymine to achieve better clustering) to form a supersonic jet. Water vapor from a heated reservoir could be introduced to the carrier gas via a valve. The powder temperature (250 °C) was comparable with or lower than those applied in previous mass-spectrometry and IR spectroscopy experiments that reported no evidence for thermally driven decomposition, isomerization, tautomerization, or reactivity in uracil or thymine following sublimation in an inert gas [Colarusso 1997]. The ions produced by multi-photon ionization in the diagnostic chamber of the experiment were detected using a reflectron time-of-flight (TOF) mass spectrometer (shown schematically in Fig. 5.1) with the *field free region* (FFR) held at V_{FFR}= -2,027±1 V.

The voltage on the reflection electrode could be adjusted to test for metastable dissociation, as described in detail in section 5.4.

5.3 Theoretical methods

The central aim of the theoretical work was to obtain binding energies for single H_2O loss from nanohydrated thymine radical cations $T^+(H_2O)_n$ (n=1-4). The uMP2/6-31+g(d,p) level of theory was chosen as this has been demonstrated to provide enthalpy changes for water evaporation from nanohydrated pyridine in very good agreement with experimental values [Ibrahim et al. 2007]. All the calculations were performed with the Gaussian 09 package [R. A. 1 Gaussian 09] at CIMAP/GANIL. The first step was to calculate the adiabatic ionization energies (IE) as the difference between the zero-point vibrational energy (ZPE) corrected ground-state potential energies of the lowest-energy optimized conformers of $T(H_2O)_n$ and $T^+(H_2O)_n$. Basis set superposition errors (BSSE) were calculated for n=1 and found to be small; the IE changed from 8.72 eV to 8.75 eV. Moreover, these corrections were computationally unaffordable for n>1 so the results presented here have not been BSSE-corrected. Table 5.1 compares the present IEs with earlier calculations [Khistyaev et al. 2011] and with experimental photoionization [Jochims et al. 2005, Belau et al. 2007, Choi et al. 2005] and electron impact ionization results [Kim et al. 1996]. Despite the lower level of theory used here compared to Khistyaev et al. [2011], there is a fair agreement with their calculations as well as with their experimental data. This provides further support for applying this level of theory, and indicates that it is suitable for studying larger clusters for which higher-level methods such as CCSD are not computationally affordable. The water binding energy (BE) is defined as the difference between the ZPE-corrected ground-state potential

energies of the optimized conformers of $T^+(H_2O)_n$ and $T^+(H_2O)_{n-1} + H_2O$. Poully and Lalande used chemical intuition as well as previously reported structures (Kim et al. 2006, Close et al. 2008, Khistyaev et al. 2011) to build the initial geometries, and optimized them with the default algorithm. No imaginary frequency was found for all conformers studied, showing that they are true minima of the potential energy surface. For radical cations, spin contamination by higher spin-states was found to be negligible since the spin operator value after annihilation was 0.7573 on average and always lower than 0.763.

Table 5.1: Calculated ionization energies (IE; adiabatic zero point corrected energy difference between the lowest-energy optimized ionic and neutral conformations; MP2/6-31+g(d,p) level) of thymine-water clusters compared with previous photoionization [Khistyaev et al. 2011, Jochims et al. 2005, Belau et al. 2007, Choi et al. 2005] and electron impact [Kim et al. 1996] measurements.

Neutral species	Calculated adiabatic IE (eV)		Experimental IE (eV) *
	Present work	Khistyaev et al. [2011]	
Thymine	9.08	8.90	8.9178 ± 0.001 [Choi et al. 2005]
			8.82 ± 0.03 [Jochims et al. 2005]
			8.85± 0.05 [Khistyaev et al. 2011]
			8.90 ± 0.05 [Belau et al. 2007]
			9.15 ± 0.15 [Kim et al. 1996]
$T(H_2O)$	8.72	8.51	8.75 ± 0.05 [Belau et al. 2007]
			8.60 ± 0.05 [Khistyaev et al. 2011]
			8.85 ± 0.15 [Kim et al. 1996]
$T(H_2O)_2$	8.57	8.52	8.6 ± 0.1 [Belau et al. 2007]
			8.55 ± 0.05 [Khistyaev et al. 2011]
			8.65 ± 0.15 [Kim et al. 1996]
$T(H_2O)_3$	8.34	8.35	8.6 ± 0.1 [Belau et al. 2007]
			8.40 ± 0.05 [Khistyaev et al. 2011]
			8.50 ± 0.15 [Kim et al. 1996]
$T(H_2O)_4$	8.30	-	-

* Choi et al. [2005], Jochims et al. [2005], Khistyaev et al. [2011] and Belau et al. [2007] interpreted their photoionization data as providing adiabatic IEs. Kim et al. [1996] noted that their measurements for isolated nucleobases match Hush and Cheung's [1975] photoelectron spectroscopic results (9.14 eV for thymine), indicating that their IEs can be regarded as vertical.

For neutral species, three conformers were found for n=1-3, and two for n=4. For radical cations, we considered 4, 11, 17 and 12 conformers for n=1, 2, 3 and 4, respectively. Only the diketo tautomer of neutral thymine was considered, since it was established by previous work as the only one present in supersonic jets of isolated [Lopez et al. 2007] or nanohydrated molecules [Nosenko et al. 2011, Lopez et al. 2010]. After multiphoton ionization of these species, tautomerization might occur by overcoming barriers calculated to be on the order of 1 eV by DFT methods [Kim 2006], but since these conformers are predicted to have very similar energies compared to diketo tautomers, their water binding energy will also be similar. The average of all possible evaporations (with minimum rearrangement) for a given conformer was calculated, and the average of all conformers gave the average binding energy (BE_{ave}). The minimum binding energy (BE_{min}) is the difference between the lowest-energy conformers of $T^+(H_2O)_n$ and $T^+(H_2O)_{n-1} + H_2O$. A value of 0.77 eV was obtained for n=1, slightly higher than that measured by Ibrahim et al. [2007] for the pyridine radical cation (0.59 eV) and consistent with water being bound to an NH group in both cases and to the adjacent C=O group in thymine (see Fig. 5.4).

5.4 Results and Discussion

5.4.1 Metastable dissociation of multi-photon ionized thymine and uracil

Fig. 5.2 shows MPI TOF mass spectra of thymine and uracil as a function of the reflection voltage, V_R. To our knowledge, *mapping* ion signal against time-of-flight and reflection voltage in this way is a new way to present metastable dissociation data, with potential value in recognizing weak channels. The seeded helium expansion conditions

were chosen to minimize clustering. The mass spectra have not been calibrated in the fig. because the proportionality of flight time against $\sqrt{\frac{m}{z}}$ breaks down for delayed fragmentation. Each band falls to zero at a characteristic reflection voltage, $V_R(0)$. The difference between $|V_{FFR}|$ and $|V_R(0)|$ gives the ion's kinetic energy (KE) in eV immediately prior to entering the reflectron optics. For thymine$^+$ and uracil$^+$, $V_R(0)$= -212±1 V. This corresponds to the voltage at the point in space where the focused laser beam crossed the molecular beam (explained in detail in section 3.2.2). Hence, the KE of the radical cations in the field free region (FFR) was 1815±2 eV. For fragment ions produced *promptly*[1] after ionization, $V_R(0)$ is slightly more negative due to dissociative KE release (typically up to several eV for single ion production by MPI [Vredenborg et al. 2009]) but fluctuations of ±1 V on the mass spectrometer voltages prevented a detailed analysis of this effect.

The *metastable bands* extending to more negative V_R values in Fig. 5.2 are due to the fragmentation of ions during their first journey through the FFR (1.3-15.7 μs after the laser pulse). The resultant ions have relatively low kinetic energies and so can be reflected by a weaker field. $V_R(0)$= -830±1 and -907±1 V for the metastable bands in Fig. 5.2a and b, respectively. Hence the KE of the relevant ions immediately before entering the reflectron optics were ($|V_{FFR}|$ - $|V_R(0)|$ =) 1197±2 and 1120±2 eV, corresponding to 65.9±0.2% and 61.7±0.2% of the KE prior to fragmentation (1815±2 eV). Comparisons between the calculated and measured flight times ruled out metastable dissociation of a fragment ion. This defines the metastable fragment ion m/z values as 83.1±0.3 from thymine$^+$ and 69.1±0.3 from uracil$^+$.

[1] The present experiments were only sensitive to delays ≥100 ns between ionization and dissociation. Hence, we have chosen to describe more rapid dissociation as *prompt*.

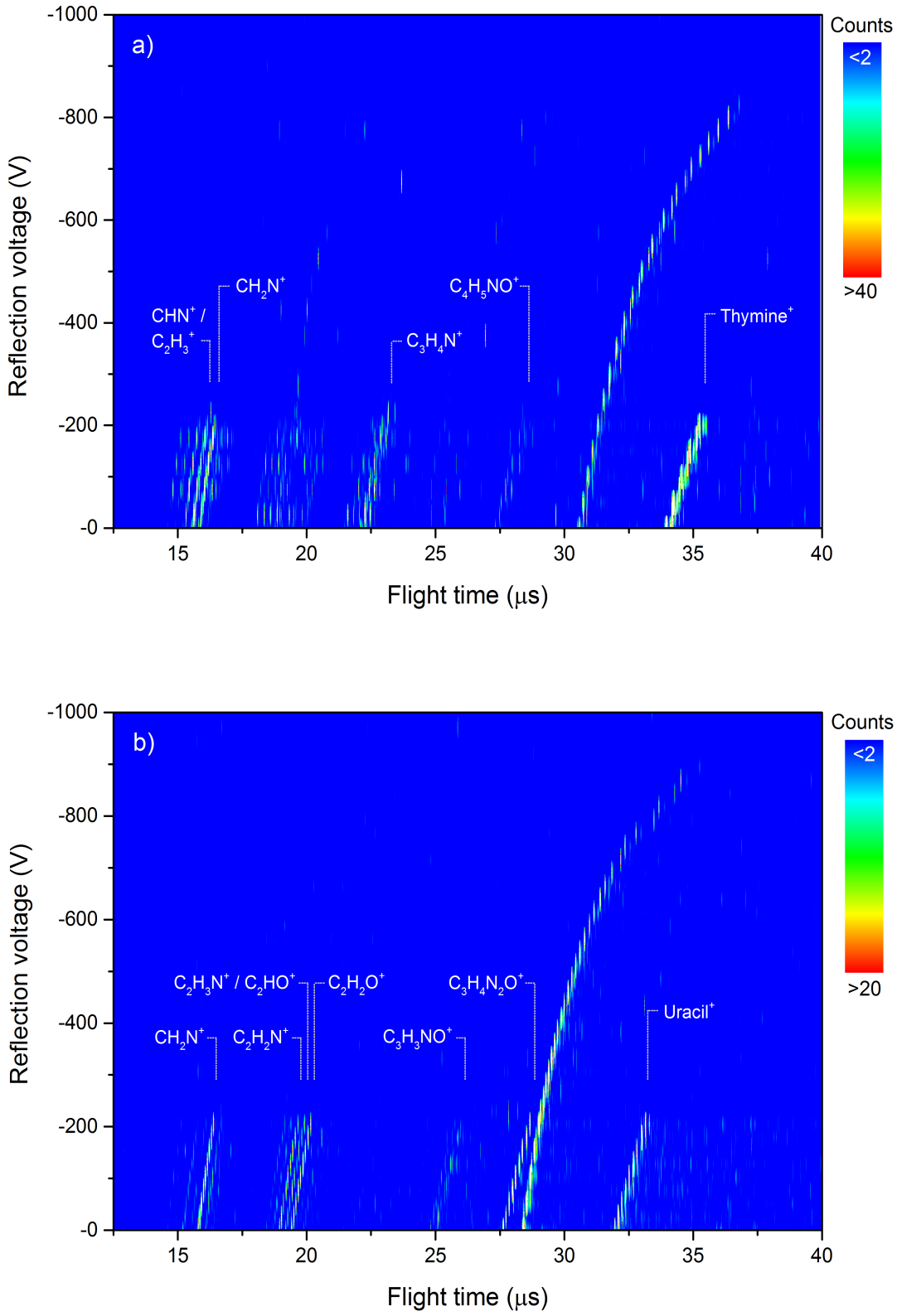

Figure 5.2: MPI (220 nm, average fluence 9×10^{7} Wcm^{-2}, He 0.8 bar) time-of-flight contour plots of (a) thymine and (b) uracil as a function of the reflection voltage. Selected bands are labelled in accordance with assignments by Jochims et al. [2005] and Ryszka et al. [2016]. The strong metastable bands in plots (a) and (b) extend to reflection voltages of -830±1 and -907±1 V, respectively.

Based on thermochemical [Jochims et al. 2005] and DFT [Arani et al. 2012] calculations, the m/z 83 and 69 ions can be assigned to $C_4H_5NO^+$ and $C_3H_3NO^+$ following HNCO loss from the respective radical cations. HNCO loss is widely recognized as the first step in the main sequential fragmentation pathways of both thymine$^+$ and uracil$^+$. The ions at m/z 83 and m/z 69 are also notable for having the lowest appearance energies of any fragment ions from the thymine and uracil radical cations [Jochims et al. 2005, Van Der Burgt et al. 2014].

Rice et al. [1965] carried out electron impact ionization (EII) studies on a range of pyrimidine derivatives and were able to recognize metastable fragmentation processes using a double focusing mass spectrometer. Although they did not show their data in detail (for example, no timeframes were mentioned), they reported delayed HNCO loss from uracil$^+$ and stated that the fragmentation of thymine$^+$ was "perfectly analogous" to uracil$^+$ with respect to the first step of the main sequential fragmentation pathways. Therefore, our observation of metastable HNCO loss from multi-photon ionized thymine$^+$ and uracil$^+$ is broadly consistent with the EII literature. However, Rice et al. [1965] did not discuss the mechanism for metastable HNCO loss in contrast with prompt dissociative ionization. The photon energy and fluence dependence of these channels in MPI measurements can provide insights that are not available from EII experiments. Barc et al. [2013] observed metastable HNCO loss from multi-photon ionized uracil and demonstrated that this was a 2-photon process at 220 nm but did not offer a mechanistic interpretation.

Fig. 5.3 shows the metastable HNCO loss signal from thymine at 220 nm (5.64 eV) as a function of the laser pulse energy. The photon order (α) can be estimated from the ion counts per pulse (I) and the pulse energy (E) using the perturbation theory expression $I=cE^{\alpha}$, where c is a constant [Nam et al. 2007]. To within the experimental uncertainty limits, the photon order for the metastable pathway (1.4±0.2) matched the photon order for thymine^{+} production (1.7±0.3) in the same measurements. The fact that the photon orders are less than 2 indicates some level of saturation. The key conclusion here is that the same number of photons was required for both processes, while thymine^{+} production can reasonably be assumed to be a 2-photon process.

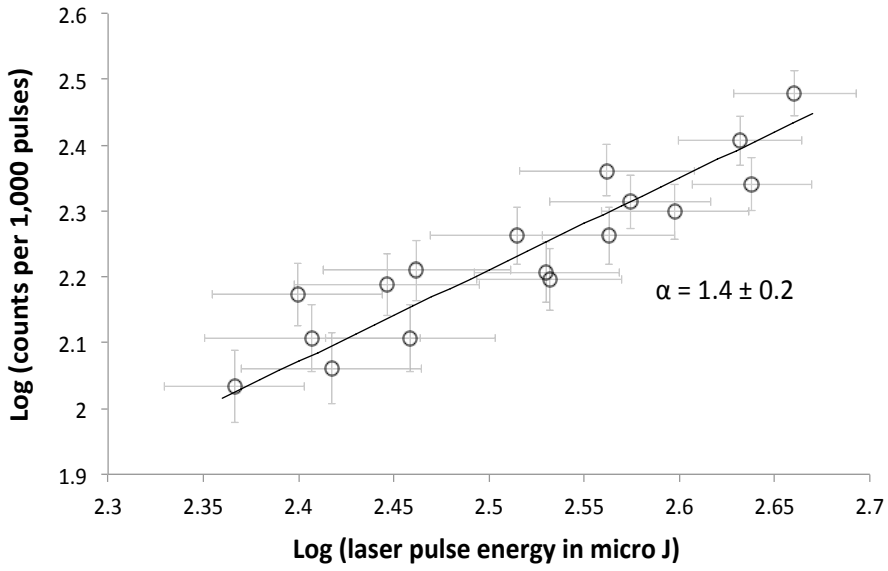

Figure 5.3: Power dependence (α) for metastable $C_4H_5NO^+$ production on laser pulse energy (average fluence 5-9×10^7 Wcm^{-2}, 220 nm, He 0.6 bar). As α(*meta* $C_4H_5NO^+$) = 1.4±0.2 matches α(thymine$^+$) = 1.7±0.3 from the measurements to within the uncertainties, this result supports metastable $C_4H_5NO^+$ production being a 2-photon process.

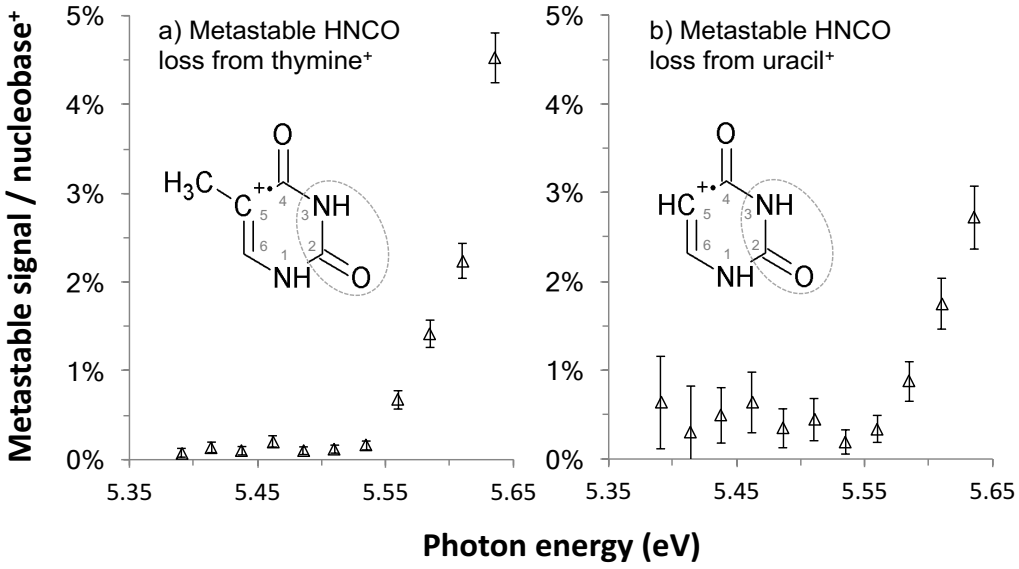

Figure 5.4: Photon energy dependence for metastable HNCO loss from multi-photon ionized (a) thymine and (b) uracil (220-230 nm, average fluence 9×10^7 Wcm^{-2}, He 0.8 bar). The metastable HNCO loss signals are shown as percentages of the intact parent ion signals. The presently calculated structures of the radical cations are shown schematically. Arani et al. [2012] proposed that the encircled HNCO group is removed from uracil$^+$ and we have assumed here an analogous dissociation of thymine$^+$.

Fig. 5.4 shows the dependence of the metastable HNCO loss channels on the laser photon energy, at the same average fluence of 9×10^7 Wcm^{-2}. Clear thresholds are visible at 5.55±0.02 and 5.57±0.02 eV from thymine and uracil, respectively (notwithstanding reduced signal-to-noise ratios in the uracil data below 5.51 eV). These energies were determined as the midpoints between the highest energy at which the signal overlapped with the background level and lowest energy at which the signal was clearly higher than the background level. The uncertainty was then estimated as the energy spacing between the data points. The observation of a photon energy (i.e. wavelength) threshold for an MPI fragment ion is a strong indicator of a critical process in the neutral excited state dynamics [Barc et al. 2013]. Ionic state thresholds do not manifest themselves as photon energy thresholds because ionization can take place with

various photon orders in the same measurement. If the total energy delivered by two photons is not sufficient to produce a given fragment ion, then the absorption of three or four photons can achieve this as long as the laser fluence is sufficiently high. To illustrate this crucial point, Fig. 5.5 compares MPI fragment ion production from thymine at 220 and 270 nm, at the same fluence of 9×10^{7} Wcm^{-2}. Previous electron impact and single photon ionization studies of thymine revealed particularly strong signals at m/z 27, 28, 39, 54, and 55 [Jochims et al. 2005, Rice et al. 1965]. As expected for channels that can be accessed efficiently by direct excitation from the neutral electronic ground state [Barc et al. 2013], we see no evidence for threshold behaviour in the MPI production of these fragment ions. The $C_3H_3^+$ (m/z 39) signal is worthy of particular attention as the single photon ionization appearance energy for this ion (14.4±0.1 eV [Jochims et al. 2005]) is comfortably attainable with 3 photons at 220 nm (5.64 eV) but requires 4 photons at 270 nm (4.59 eV). This change in the required photon order does not manifest itself as a photon energy threshold.

Accordingly, we are confident that the photon energy thresholds for metastable HNCO loss shown in Fig. 5.4 are linked to critical processes in neutral excited states prior to the absorption of the ionizing photon. The agreement of the photon energy thresholds for metastable HNCO loss from the two molecules (to within the experimental uncertainty of ±0.02 eV) provides a further indicator that that they cannot be understood solely in terms of ionic state energetics. The single-photon ionization energies of uracil are systematically higher than the equivalents of thymine [Jochims et al. 2005]. In particular, the adiabatic energy for dissociative ionization with HNCO loss is 0.25±0.07 eV higher [Jochims et al. 2005] from uracil than from thymine. In contrast with the significant differences in their ionization energies, the most recent calculated adiabatic

energies of the lowest-lying singlet states of thymine and uracil agree to within ≤0.03 eV [Etinski and Marian 2010].

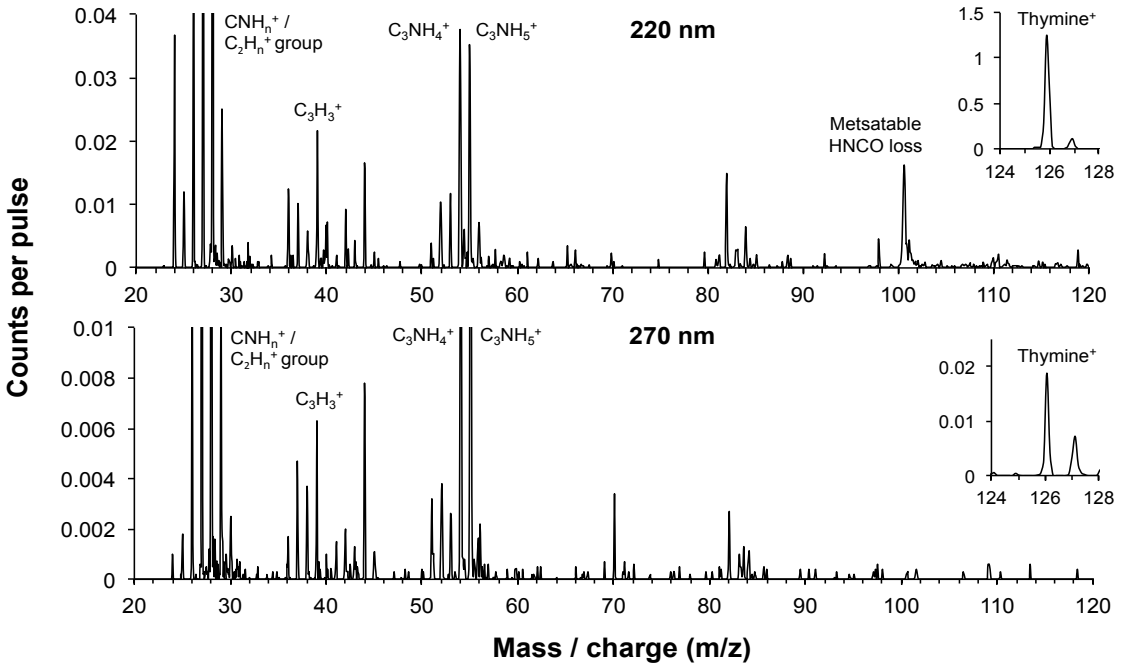

Figure 5.5: Comparison of MPI mass spectra of thymine at 220 and 270 nm (respective photon energies 5.64 and 4.59 eV, average fluence 9×10^7 Wcm^{-2}, powder 250 °C, He 0.8 bar, reflection voltage -80 V). The strongest peaks observed in single photon ionization experiments are labelled with the previous assignments [Jochims et al. 2005] and show no evidence for threshold behaviour. Metastable HNCO loss from thymine$^+$* is also labelled in the 220 nm measurement but the mass calibration does not apply to this feature.

HNCO loss from thymine$^+$ and uracil$^+$ are understood to proceed via cleavage of the N_3-C_4 and N_1-C_2 bonds [Jochims et al. 2005, Arani et al. 2012] (see schematic structures in Fig. 5.4). Arani et al. [2012] calculated the potential energy barrier needed for HNCO loss from uracil$^+$ as 2.11 eV. Improta et al. [2000] calculated the transition states of two reaction paths for HNCO loss from thymine$^+$ with potential energy barriers of 1.83 and 2.00 eV. The difference between the adiabatic photoionization energy of thymine and the appearance energy of $C_4H_5NO^+$ is 1.88±0.06 eV [Jochims et al. 2005]. This is very close to the corresponding value of 1.80±0.06 eV for HNCO loss from uracil$^+$ [Jochims

et al. 2005]. The similar energy requirement for HNCO loss from the two radical cations is not surprising as the HNCO group in question is relatively far from the methyl group that differentiates the two ions.

Our interpretation for the present threshold behaviour is centred on the vibrational excitation of the nucleobase cation. If the total vibrational energy of the ion in its ground state (I_0) is at the threshold required for HNCO loss then a suitable redistribution of the activated modes can lead to delayed dissociation. The delay can be due to tunnelling through a low potential barrier or a low rate constant for unimolecular fragmentation when the excess internal energy is small [Cooks et al. 1973]. Electronic excitation of neutral thymine and uracil by single photon absorption in the present energy range results in significant vibrational excitation. Due to the inefficient conversion of energy from vibrational modes to electronic modes, this vibrational energy *survives* the second photon absorption and results in an (at least) equivalently vibrationally hot ionic state. Competition with energy removal by the emitted electron means that the absorption of the ionizing photon is expected to be a far less efficient mechanism for vibrational excitation than the first photon absorption. Therefore we propose that the thresholds shown in Fig. 5.4 correspond to producing electronically excited thymine and uracil with exactly the additional vibrational energy required to dissociate the respective radical cations in their ground states (I_0).

If the interpretation above is correct, we can deduce the adiabatic energies of the electronic excited states that absorb the ionizing photon: (5.55±0.02 - 1.88±0.06 =) 3.67±0.07 eV for thymine and (5.57±0.02 - 1.80±0.06 =) 3.77±0.07 eV for uracil. These agree with the most recent calculations (at RI-CC2/aug-cc-pVDZ level [Etinski and

Marian 2010]) for the S_1 states: 3.72 eV for thymine (earlier 3.73-4.03 eV at various levels of theory [Etinski et al. 2009]) and 3.69 eV for uracil (earlier 3.74-4.04 eV [Etinski et al. 2009]). By contrast, the present values are clearly lower than the calculated adiabatic energies for S_2 (4.49 eV for thymine [Serrano-Perez et al. 2007] and 4.48 eV for uracil [Climent et al. 2007]) and higher than those for T_1 (2.84-3.16 eV for thymine and 2.87-3.31 eV for uracil [Serrano-Perez et al. 2007, Etinski and Marian 2010, Etinski et al. 2009]). Aside from S_1, the only calculated band origins that are close to the present values correspond to the T_2 states: 3.84-3.93 eV for thymine [Serrano-Perez et al. 2007] and 3.84-3.91 eV for uracil [Etinski et al. 2009]. He et al.'s [2004] pump (267 nm) - probe measurements showed that hydration significantly repressed access to the long-lived dark states of thymine and methyl-substituted uracil.

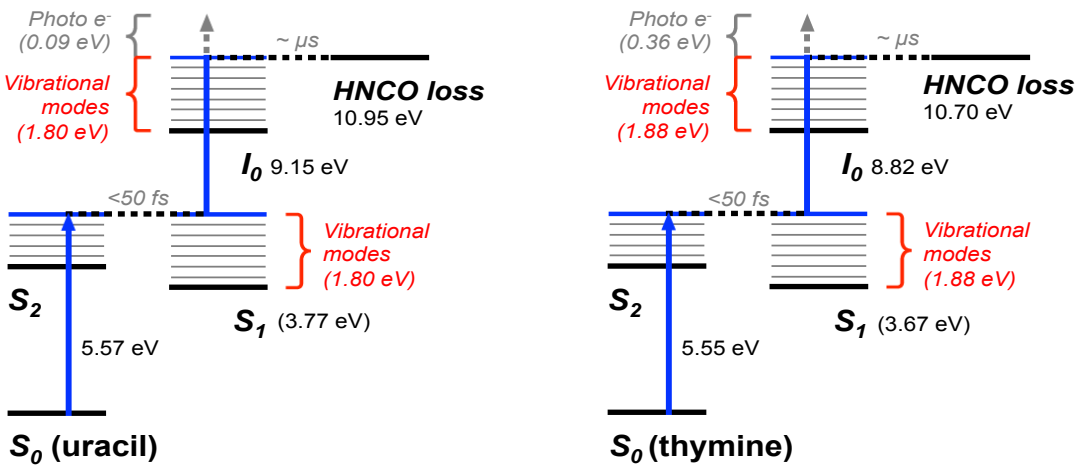

Figure 5.6: Illustration of the proposed interpretation for the present photon energy thresholds for metastable HNCO loss from multi-photon ionized uracil and thymine (5.57±0.02 and 5.55±0.02 eV, respectively). The key premise is that the minimum vibrational energy in the excited radical cation matches the vibrational energy in the neutral excited molecule immediately prior to the absorption of the ionizing photon. The adiabatic ionization energies (I_0) and the appearance energies for HNCO loss from the excited radical cations are from Johims et al.'s [2005] photoionization measurements. The energies in brackets are derived from the present interpretation. For simplicity, the numerical uncertainties are not shown in the Fig.

However, hydration does not have a significant suppressive effect on the MPI signals from thymine (see section 5.4.2.1) and uracil [Barc et al. 2013] using the present experimental system. This suggests that ionization from triplet states did not contribute significantly to the present results. Hence, our interpretation of the present photon energy thresholds for metastable HNCO loss from multi-photon ionized uracil and thymine is summarized schematically in Fig. 5.6.

To our knowledge, the only previous experimental adiabatic energies of uracil and thymine's low-lying electronic excited states were reported by Tsuchiya et al. [1988]. They identified two bands of vibronic peaks in the fluorescence spectra of each nucleobase and attributed these to the S_1 states of different tautomers. The origins of the lower-energy vibronic band for each molecule (3.833 eV for uracil and 3.857 eV for thymine) are close to the values deduced from the present analysis (the differences are of the order of a single quantum of C=O stretching [Tsuchiya et al. 1988]) and also to the calculated S_1 adiabatic energies of the diketo tautomers. Hence the most recent calculations suggest that the lower-energy vibronic bands are traced to diketo tautomers, whereas Tsuchiya et al. [Tsuchiya et al. 1988] assigned them to unspecified keto-enol forms. It is worth noting that ionization of a given S_1 tautomer state does not imply that metastable HNCO loss took place from the equivalent tautomer of the radical cation. The high level of vibrational excitation (≥1.8 eV) of the radical cations in the present experiments means that numerous tautomeric transitions (barriers ~1 eV [Kim 2006]) can be expected in the microseconds prior to dissociation.

The count rate of the metastable channel is significantly higher in the thymine measurements than for the uracil data. Indeed, the total MPI signal from thymine is

approximately five times greater than from uracil in the present experiments. Uracil and thymine are similar in terms of their vapour pressures [Tabet et al. 2010], their calculated photoabsorption cross-sections, and the vertical energies of their S_1 and S_2 states [Etinski et al. 2009, Barbatti et al. 2010]. Therefore, we attribute thymine's relatively high MPI efficiency to the combined effect of lower ionization thresholds (e.g. adiabatic IE = 8.82±0.03 eV compared with 9.15±0.03 eV for uracil [Jochims et al. 2005]) and slower relaxation from its low-lying singlet states (average exponential decay time constant following 267 nm photo-excitation = 6.4 ps compared with 2.4 ps for uracil [Kang et al. 2002]).

5.4.2 Thymine-water cluster ions

5.4.2.1 MPI of nanohydrated thymine

Fig. 5.7 shows MPI (220 nm, 8×10^7 Wcm^{-2}) production of hydrated thymine monomer ions, while larger complexes were observed up to m/z 288 ($T_2^+(H_2O)_2$ or $T^+(H_2O)_9$). Previous MPI experiments (266 nm, 7×10^5 Wcm^{-2}) have produced $T^+(D_2O)_n$ and $T_2^+(D_2O)_n$ with n up to 10 and 6, respectively [Kim et al. 2002]. The insert in Fig. 5.6 compares the signals for thymine$^+$ and protonated thymine (TH^+) recorded in *dry* and *hydrated* expansion conditions (before and after opening the valve to the heated water reservoir, respectively). Prior to the *dry* measurement, the nozzle and the carrier gas line were pumped overnight using a scroll pump and then purged for two hours in a flow of argon carrier gas while the powder temperature was increased and stabilized. Water is transparent at 220 nm [Mota et al. 2005] and thermochemical calculations have shown that proton transfer from T^+ to T in a dimer cation is exothermic [Liu et al. 2008].

Therefore, the present TH^+ signals are attributed to the dissociation of thymine dimer ions (or possibly larger thymine cluster ions), with or without associated water molecules. Due to the relatively weak binding between thymine and water molecules [Rasmussen et al. 2010], T_m^+ (where m is the number of thymine molecules) fissure within a hydrated cluster is expected to involve extensive water loss. Accordingly, the weak features with one m/z unit above the $T^+(H_2O)_n$ values (12±1% of these peaks) can be attributed to approximately equal proportions of $TH^+(H_2O)_n$ and cluster ions containing ^{13}C isotopes (6%) [Manura and Manura 2016].

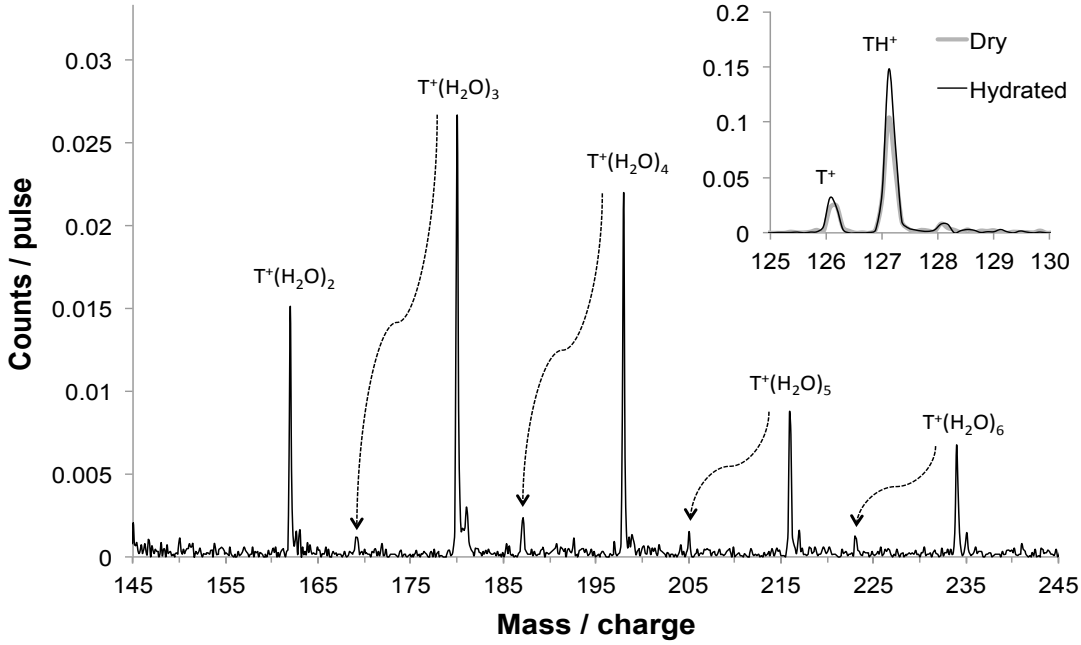

Figure 5.7: MPI (220 nm, average fluence 8×10^7 Wcm^{-2}, water 50 °C, Ar 1.1 bar) mass spectrum of thymine-water clusters. The dotted arrows signify metastable H_2O loss (note that the mass calibration does not apply to these peaks). The insert compares a detail of the mass spectrum with an equivalent measurement recorded in *dry* conditions (before opening the valve to add water vapor to the expansion).

Comparing ion signals in dry and hydrated conditions can provide insights into the neutral excited state dynamics that take place during the present MPI processes. Previous dynamical calculations and time-resolved spectroscopic measurements on

isolated nucleobases have revealed a great deal of information on the relaxation pathways from their optically bright S_2 states [Kang et al. 2002, González-Vázquez et al. 2009]. Internal conversion to the electronic ground state (either directly or via S_1 states of mainly nπ* character) dominates $S_2(\pi\pi^*)$ deactivation, although intersystem crossing to long-lived triplet states has also been reported. Kang et al.'s [2003] transient ionization experiments revealed a slow decay component of thymine with a time constant of >100 ps. Similarly, He et al.'s [2004] pump-probe measurements (267 nm pump) showed a dark state with a lifetime of several tens to hundreds of ns, depending on the probe wavelength (220-273 nm). Kang et al. [2003] assigned the slow decay to ionization from a triplet state, while recent double resonance spectroscopy experiments and *ab initio* calculations support a $^3\pi\pi^*$ character [Ligare et al. 2015]. He et al. [2004] reported that hydration significantly repressed access to the long-lived dark state. Therefore, the fact that thymine radical ion production was not suppressed due to the formation of thymine-water clusters (Fig. 5.7 insert) provides a strong indicator that the dominant MPI pathways in the present experiments do not involve ionization from triplet states. On the contrary, the total MPI signal (summing all counts from cluster ions, TH^+, T^+, and fragment ions with m/z lower than T^+) increased by 56±10%. This increase can be attributed partially to the reduction in ionization energy due to clustering with water (see the calculated and experimental data in Table 5.1). Furthermore, the predicted shifts in the vertical excitation energies of S_2 (calculated red shift of 0.02-0.19 eV) and S_1 (blue shift of 0.21-0.80 eV) due to hydration [Etinski and Marian 2010] are expected to affect MPI efficiency.

Fig. 5.7 shows a series of peaks in between the $T^+(H_2O)_n$ ($2\leq n\leq 6$) features. Comparisons between calculated and measured flight times enabled these peaks to be

assigned to metastable loss of a single H_2O molecule from $T^+(H_2O)_n$ ($3 \leq n \leq 6$) complexes in the *field-free region* (FFR) of the mass spectrometer (1.5-21.4 μs after ionization). Metastable dissociation events that take place before the ions have reached the FFR or in the reflecting part of the mass spectrometer lead to a broad distribution of modified flight times and hence do not manifest themselves as distinct peaks in a mass spectrum. The flight-time calculations were based on a simple model of the electric fields in between the various electrodes in the mass spectrometer [Ryszka 2015]. Different possible dissociations in the FFR were tested iteratively until a good match was achieved between the calculated and measured flight times. The intensities of the metastable peaks are listed as percentages of the respective *parent* (or *original*) cluster ion signals in Table 5.2. The signal-to-noise ratio was insufficient to obtain a useful result for metastable H_2O loss from $T^+(H_2O)$ and there is no clear peak for H_2O loss from $T^+(H_2O)_2$. Indeed, the most striking result in Table 5.2 is an increase of >400% in metastable H_2O loss relative to *parent* $T^+(H_2O)_n$ detection over the cluster size range n=2-4. Kim et al. [2002] observed an increase of around 100% in this cluster size range; the more pronounced effect in the present work may be linked to differences in the ionizing laser conditions applied in the two experiments. Increased metastable dissociation of clusters is widely viewed as a possible indicator of a lower energy threshold for the removal of a single molecule, helping to recognize particularly stable cluster sizes (so-called *magic numbers* often linked to shell structures) [Heinbuch et al. 2007]. Kim et al. [2002] observed a particular increase in metastable H_2O loss for n>4 and stated that this might indicate that the first solvation shell around the thymine radical cation is composed of four water molecules. Belau et al.'s [2007] single-photon ionization mass spectrum of a supersonic beam containing various clusters comprising thymine, water, and / or adenine molecules only showed clear $T^+(H_2O)_n$ peaks up to

n=4. At a first look, this appears to support Kim et al.'s [2002] shell closure proposal based on their metastable dissociation results. However, an equivalent *direct* consideration Kim et al.'s [2002] 2-photon ionization mass spectra reveals no distinct step in sequential peak heights for $T^+(D_2O)_n$ in the range n=1-10. Similarly, Kim et al.'s [2002,1996] electron impact ionization and 2-photon ionization mass spectra of thymine-water clusters did not provide any suggestion of shell structures up to n=6 (above which the singly hydrated cation peaks overlap with the $T_2^+(H_2O)_n$ peaks). This highlights the main limitation of directly comparing cluster ion peak heights in a mass spectrum as a means to extract information about relative stabilities: the peak heights reflect both the abundance of neutral clusters in the target and the stability of the ionized clusters. By contrast, mass spectrometry measurements of metastable product ions simultaneously define the ion cluster mass before and after dissociation. Our collaborators from CIMAP/GANIL have carried out *ab initio* quantum-chemical calculations of optimized $T^+(H_2O)_n$ conformers in order to see if the water binding energies can help to explain the experimental metastable evaporation results.

Table 5.2: Signals for metastable single H_2O loss from $T^+(H_2O)_n$ expressed as percentages of the signals for the original cluster ions. The signal-to-noise ratio was insufficient to obtain a useful result for metastable H_2O loss from $T^+(H_2O)$. * To be hidden by the background level in Fig. 2, the metastable H_2O loss signal must be <3.7% of the $T^+(H_2O)_2$ signal.

Original cluster ion formula	Metastable H_2O loss signal / original cluster ion signal
$T^+(H_2O)_6$	18.6 ± 5.4 %
$T^+(H_2O)_5$	12.5 ± 3.3 %
$T^+(H_2O)_4$	17.5 ± 2.6 %
$T^+(H_2O)_3$	8.1 ± 1.4 %
$T^+(H_2O)_2$	No metastable peak*

Figs. 5.8-5.10 show the lowest-energy optimized structures of $T(H_2O)_n$ and $T^+(H_2O)_n$ (n=1-4). We also depict the $T^+(H_2O)_n$ conformers within 100 meV of the minimum ZPE corrected energy, as well as two additional higher-energy conformers for n=1. This has been shown to be the typical uncertainty of MP2 methods in predicting interaction energies of biologically relevant non-covalent clusters [Riley et al. 2007]. The neutral structures are consistent with previous experiments for n=1 [Gonzalez-Vazquez et al. 2009] and calculations for n=1, 2, [Lopez et al. 2010, Kabelác et al. 2007] and 4 [Kim et al. 2006]. Close et al. [2006] found a different lowest-energy $T(H_2O)_3$ conformer than the one in Fig. 5.8 which is 9 kJ/mol (93 meV) higher according to their DFT calculation method.

5.4.2.2 *Ab initio* quantum-chemical calculations on nanohydrated thymine neutrals and radical cations

To the best of our knowledge, no spectroscopic studies of $T^+(H_2O)_n$ are available in the literature and only two theoretical studies have been reported. Kim's [2006] optimized geometry of the lowest-energy conformer of $T^+(H_2O)$ is similar to the present result. Close et al. [2008] and Khistyaev et al. [2011] presented structures for ionized hydrated thymine up to n=3. They used the lowest-energy $T(H_2O)_n$ structures as the starting points for their $T^+(H_2O)_n$ structure optimization. This approach is entirely reasonable for assessing the ionization energies of neutral clusters (the main aim of their work) but it does not necessarily consider the entire phase space of conformations accessible following ionization several eV above threshold, as occurs in the present MPI experiments (compare the ionization thresholds in Table 5.1 with 11.27 eV shared between the excited cluster ion, the released electron, and any neutral dissociation products in 2-photon ionization at 220 nm). Therefore, while their $T^+(H_2O)$ (and

$T^+(H_2O)_2$ for Khistyaev et al. [2011]) geometries match the present result (Fig. 5.8), it is not very surprising that their optimized geometries differ from ours at n=3 (Fig. 5.9). Indeed, the present lowest-energy $T^+(H_2O)_n$ conformers (Figs. 5.8-5.10) all differ significantly from their neutral counterparts at n=2-4 (at least one major rearrangement of a water molecule).

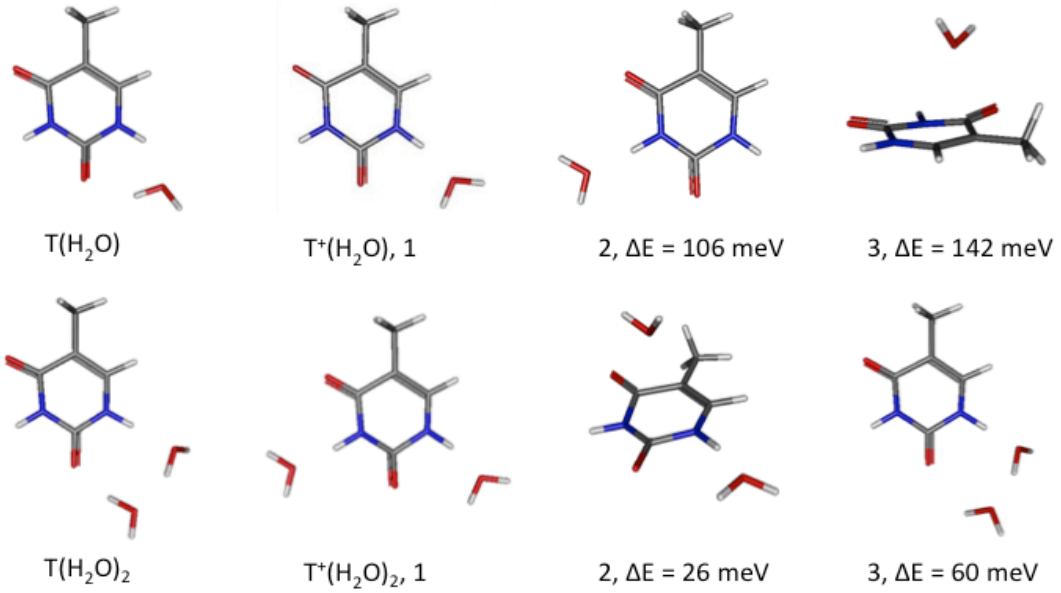

Figure 5.8: Structures of the lowest-energy conformers of $T(H_2O)_n$ and $T^+(H_2O)_n$ (n=1-2), optimized at the MP2/6-31+g(d,p) level. Relative $T^+(H_2O)_n$ conformer energies (ΔE, zero-point vibrational energy corrected) are indicated. The $T^+(H_2O)_n$ conformers are labeled 1-3 in order of increasing ΔE.

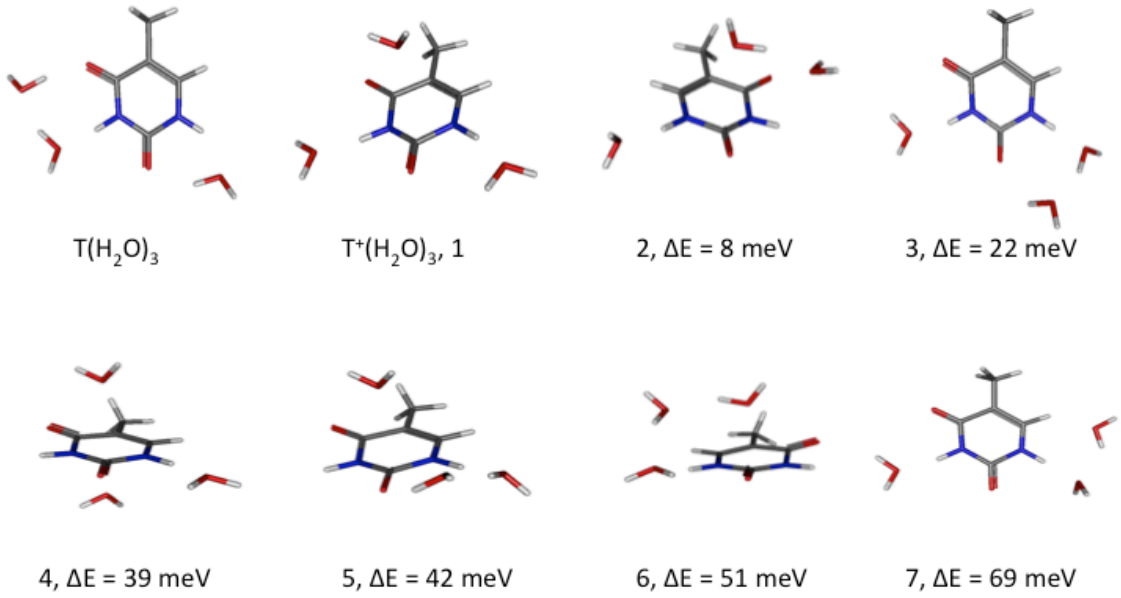

Figure 5.9: Structures of the lowest-energy conformers of $T(H_2O)_3$ and $T^+(H_2O)_3$ (numbered 1-7), optimized at the MP2/6-31+g(d,p) level. Relative $T^+(H_2O)_3$ conformer energies (ΔE, zero-point vibrational energy corrected) are indicated.

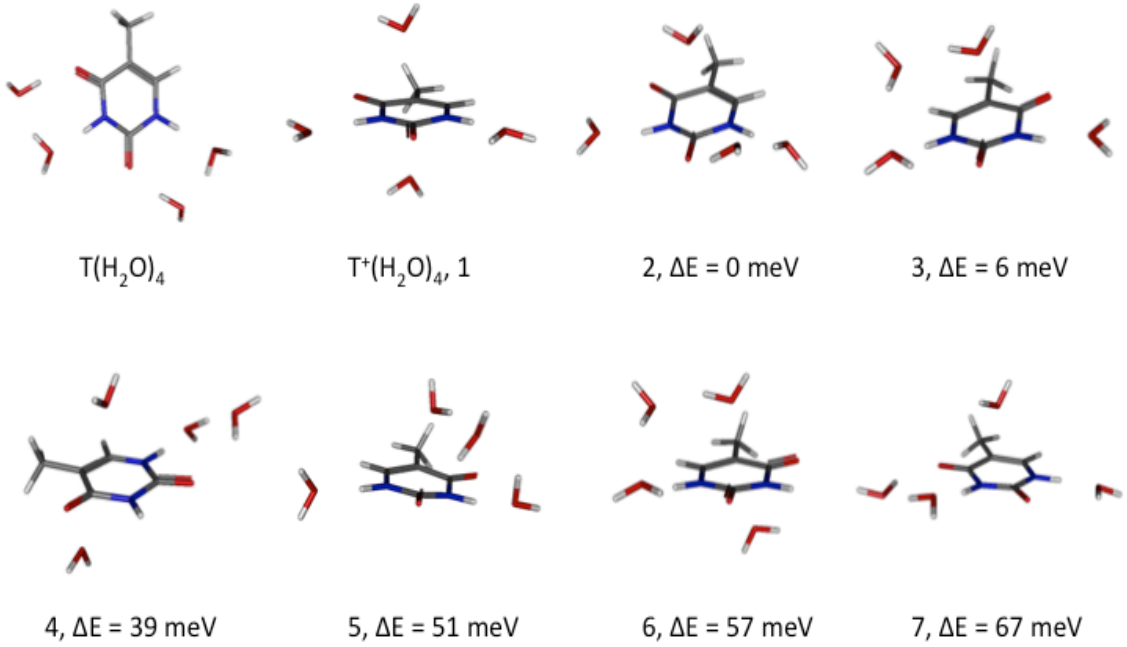

Figure 5.10: Structures of the lowest-energy conformers of $T(H_2O)_4$ and $T^+(H_2O)_4$ (numbered 1-7), optimized at the MP2/6-31+g(d,p) level. Relative $T^+(H_2O)_4$ conformer energies (ΔE, zero-point vibrational energy corrected) are indicated.

The present and previous calculations of neutral hydrated thymine clusters support essentially planar hydrogen-bonded structures. While the most stable conformers of $T^+(H_2O)$ and $T^+(H_2O)_2$ also involve hydrogen bonding at both nitrogens, the present calculations show that alternative binding interactions and non-planar geometries are important in the cluster ions. Indeed, ΔE is only 26 meV between the $T^+(H_2O)_2$ minimum and the lowest-energy structure with a water molecule located *above* the thymine$^+$ ring (such molecules are referred to as *ring-bound* in this discussion). This conformer ($T^+(H_2O)_2$ conformer 2 in Fig. 5.8) is consistent with stabilization via a charge-dipole interaction, while the present calculations indicate that the positive charge on the radical cation is mainly located at the carbon bound to the methyl group (referred to here as C_M). For $T^+(H_2O)_3$ and $T^+(H_2O)_4$ (Figs. 5.9 and 5.10) ring-bound water molecules feature in the most stable conformers. Interestingly, the charge at C_M increases in conformers with two ring-bound water molecules ($T^+(H_2O)_3$ conformer 4 and $T^+(H_2O)_4$ conformers 1, 4, and 6), while some additional charge appears at the methyl carbon. Such ring-bound conformers have been reported for hydrated benzene radical cations [Dopfer et al. 2005], but not for nucleobases. It is also noteworthy that there is no clear indication of a closed shell of four water molecules around the thymine radical cation to support Kim et al.'s [2002] suggested interpretation of their metastable dissociation experiments. The calculated binding energies (BE) required for single H_2O loss from $T^+(H_2O)_n$ (n=1-4) are given in Fig. 5.11. The Fig. 5.11 shows BE_{min} between the lowest-energy configurations of $T^+(H_2O)_n$ and $T^+(H_2O)_{(n-1)}+H_2O$ as well as the average BE_{ave} of all possible evaporations (with minimum rearrangement).

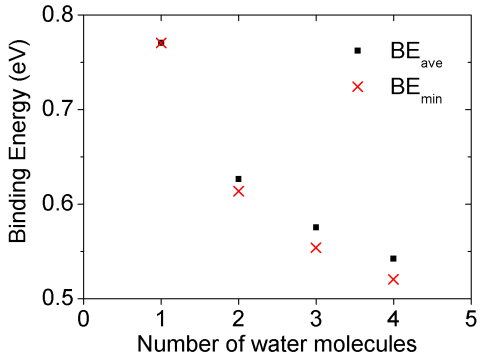

Figure 5.11: Binding energies (BE) of $T^+(H_2O)_n$ calculated at the MP2/6-31+g(d,p) level as a function of the number of water molecules bound to thymine. Average (BE_{ave}) as well as minimum (BE_{min}) binding energies are plotted (see the text for more detail).

In both cases, BE decreases smoothly with n, with the greatest change (20%) between n=1 and 2. This is consistent with the general trend of increasing metastable H_2O loss in the present experimental data, as well as in Kim et al.'s [2002] results. In the range n=2-4, BE_{min} falls by 6-10% and BE_{ave} by 6-8%. These changes appear to be quite small in the context of the dramatic increase in metastable H_2O loss observed in the present experiment across the same cluster ion size range (Table 5.2). This suggests that caution is required when attempting to associate the strength of metastable dissociation signals with cluster ion binding energies. In particular, we expect the number of available pathways for the loss of a molecule to play a role in determining the relative probability of metastable dissociation. This expectation is based on the premise that the vibrational energy in the cluster ion's intermolecular modes needs to be very close to a dissociation barrier in order for metastable dissociation to occur. The number of possible dissociation pathways, each with its own barrier potential, rises with cluster size so this will tend to increase the probability that a given vibrating cluster will meet the condition for metastable dissociation. Another reason for the much weaker metastable evaporation from $T^+(H_2O)_n$ with $n \leq 3$ might be their lower internal energy after evaporation of a higher average number of water molecules compared to $n \geq 4$. Such a cooling effect has

been observed in pure nucleobase clusters after ion impact ionization [Vizcaino et al. 2014].

5.5 Summary

Strong signals for metastable HNCO loss from multi-photon ionized thymine and uracil molecules have been observed with clear photon energy thresholds. We do not observe threshold behaviour of this kind in the signals of any fragment ion channels that can be produced efficiently by direct excitation from neutral electronic ground state, notably in electron impact ionization. Therefore, the present thresholds are strongly indicative of critical processes in neutral excited states. More specifically, we propose that they can be attributed to accessing the neutral molecules' S_1 states with vibrational energy matching the threshold for HNCO loss from the radical cation. If this interpretation is correct, the present results can be combined with existing photoionization energies to deduce the excited states' adiabatic energies: 3.67±0.07 eV for thymine and 3.77±0.07 eV for uracil. These are close to the origins of the lowest-lying vibronic bands observed in previous LIF spectra and agree with the most recent calculated adiabatic energies of the diketo S_1 states. More generally, the present results suggest that the study of metastable fragment ion production in MPI experiments has considerable potential to provide insights into the dynamics of molecules in high vibronic states.

H_2O loss from hydrated thymine radical cations has been observed in single-colour MPI experiments; the second result of this kind in the literature. This chapter compares these measurements with the most extensive set of optimized $T^+(H_2O)_n$ geometries to date (up to n=4). The binding energies for single water molecule removal fall with n, broadly

consistent with increasing metastable dissociation in the MPI experiments. The lowest energy $T^+(H_2O)_n$ conformers differ significantly from their neutral counterparts for $n \geq 2$, with charge-dipole interactions playing important roles and no indication of preferential closed-shell structures. Additional experimental and theoretical work (for example IR laser action spectroscopy in the fingerprint regions of m/z selected cluster ions combined with quantum-chemical calculations of IR spectra) would be required to prove the existence of these interactions in hydrated thymine radical cations.

5.6 Contributions by co-workers and forthcoming publications

I preformed all the experiments in this chapter, working with PhD students Michal Ryszka (now graduated) and Tiago da Fonseca Cunha. Mathieu Lalande and Jean-Christophe Poully carried out the calculations. I analyzed the experimental data and the calculations and devised interpretations, working primarily with Samuel Eden and Jean-Christophe Poully. Michal Ryszka, Marcin Dampc, and Tiago da Fonseca Cunha also contributed to the data analysis. Paulo Limão-Vieira and Nigel J. Mason contributed to the journal manuscripts based on this chapter: *Stabilities of nanohydrated thymine radical cations: insights from multiphoton ionization experiments and ab initio calculations* [Pandey et al. 2017] and *Threshold behavior in metastable dissociation of multi-photon ionized thymine and uracil* (submitted to Chemical Physics Letters). Following referees' reports and a positive interim decision from the editor, a revised version of the Chem. Phys. Lett. manuscript is being considered by the editor at the time of writing.

References:

- L. S. Arani, P. Mignon, H. Abdoul-Carime, B. Farizon, M. Farizon and H. Chermette, *Phys. Chem. Chem. Phys.*, 2012, **14**, 9855-70.
- M. Barbatti, A. J. A. Aquino and H. Lischka, *Phys. Chem. Chem. Phys.*, 2010, **12**, 4959-4967.
- B. Barc, M. Ryszka, J. Spurrell, M. Dampc, P. Limão-Vieira, R. Parajuli, N. J. Mason and S. Eden, *J. Chem. Phys.*, 2013, **139**, 244311.
- B. Barc, M. Ryszka, J. C. Poully, E. Jabbour Al Maalouf, Z. El Otell, J. Tabet, R. Parajuli, P. J. M. Van Der Burgt, P. Limão-Vieira, P. Cahillane, M. Dampc, N. J. Mason and S. Eden, *Int. J. Mass Spectrom.*, 2014, **365-366**, 194-199.
- L. Belau, K. R. Wilson, S. R. Leone and M. Ahmed, *J. Phys. Chem. A*, 2007, **111**, 7562-7568.
- E. Bruzzi, G. Raggi, R. Parajuli and A. J. Stace, *J. Phys. Chem. A*, 2014, **118**, 8525-8532.
- K. W. Choi, J. H. Lee and S. K. Kim, *J. Am. Chem. Soc.*, 2005, **127**, 15674-15675.
- S. K. Choi, W. Lee and D. R. Herschbach, *J. Phys. Chem.*, 1996, **100**, 7933-7937.
- T. Climent, R. Gonzalez-Luque, M. Merchan and L. Serrano-Andres, *Chem. Phys. Lett.*, 2007, **441**, 327-331.
- D. M. Close, C. E. Crespo-Hernández, L. Gorb and J. Leszczynski, *J. Phys. Chem. A*, 2008, **112**, 4405-4409.
- D. M. Close, C. E. Crespo-Hernández, L. Gorb and J. Leszczynski, *J. Phys. Chem. A*, 2006, **110**, 7485-7490.
- P. Colarusso, K. Zhang, B. Guo and P. E. Bernath, *Chem. Phys. Lett.*, 1997, **269**, 39-48.
- R. G. Cooks, J. H. Beynon, R. M. Caprioli and G. R. Lester, *Metastable Ions*, Elsevier, Amsterdam, 1973.
- R. E. Continetti, *Int. Rev. Phys. Chem.*, 1998, **17**, 227-260.
- R. H. Duncan Lyngdoh and H. F. Schaefer, *Acc. Chem. Res.*, 2009, **42**, 563-572.
- O. Dopfer, *Zeitschrift Fur Phys. Chemie-International J. Res.*, 2005, **219**, 125-168.
- M. Etinski, T. Fleig and C. M. Marian, *J. Phys. Chem. A*, 2009, **113**, 11809-11816.
- M. Etinski and C. M. Marian, *Phys. Chem. Chem. Phys.*, 2010, **12**, 4915-4923.
- B. P. Fingerhut, K. E. Dorfman and S. Mukamel, *J. Chem. Theory Comput.*, 2014, **10**, 1172-1188.

- R. A. Gaussian 09, M. J. Frisch, G. W. Trucks, H. B. Schlegel, G. E. Scuseria, M. A. Robb, J. R. Cheeseman, G. Scalmani, V. Barone, B. Mennucci, G. A. Petersson, H. Nakatsuji, M. Caricato, X. Li, H. P. Hratchian, A. F. Izmaylov, J. Bloino, G. Zheng, J. L. Sonnenberg, M. Hada, M. Ehara, K. Toyota, R. Fukuda, J. Hasegawa, M. Ishida, T. Nakajima, Y. Honda, O. Kitao, H. Nakai, T. Vreven, J. A. Montgomery, Jr., J. E. Peralta, F. Ogliaro, M. Bearpark, J. J. Heyd, E. Brothers, K. N. Kudin, V. N. Staroverov, R. Kobayashi, J. Normand, K. Raghavachari, A. Rendell, J. C. Burant, S. S. Iyengar, J. Tomasi, M. Cossi, N. Rega, J. M. Millam, M. Klene, J. E. Knox, J. B. Cross, V. Bakken, C. Adamo, J. Jaramillo, R. Gomperts, R. E. Stratmann, O. Yazyev, A. J. Austin, R. Cammi, C. Pomelli, J. W. Ochterski, R. L. Martin, K. Morokuma, V. G. Zakrzewski, G. A. Voth, P. Salvador, J. J. Dannenberg, S. Dapprich, A. D. Daniels, O. Farkas, J. B. Foresman, J. V. Ortiz, J. Cioslowski, and D. J. Fox, *Gaussian, Inc., Wallingford CT*, 2009.
- A. Golan, K. B. Bravaya, R. Kudirka, O. Kostko, S. R. Leone, A. I. Krylov and M. Ahmed, *Nat. Chem.*, 2012, **4**, 323-329.
- J. González-Vázquez, L. González, E. Samoylova and T. Schultz, *Phys. Chem. Chem. Phys.*, 2009, **11**, 3927-3934.
- Y. He, C. Wu and W. Kong, *J. Phys. Chem. A*, 2004, **108**, 943-949.
- N. S. Hush and A. S. Cheung, *Chem. Phys. Lett.*, 1975, **34**, 11-13.
- H. R. Hudock, B. G. Levine, A. L. Thompson, H. Satzger, D. Townsend, N. Gador, S. Ullrich, A. Stolow and T. J. Martinez, *J. Phys. Chem. A*, 2007, **111**, 8500-8508.
- I. Hunig, C. Plutzer, K. A. Seefeld, D. Lowenich, M. Nispel and K. Kleinermanns, *Chemphyschem*, 2004, **5**, 1427-1431.
- S. Heinbuch, F. Dong, J. J. Rocca and E. R. Bernstein, *J. Chem. Phys.*, 2007, **126**, 244301.
- Y. Ibrahim, R. Mabrouki, M. Meot-Ner and M. S. El-Shall, *J. Phys. Chem. A*, 2007, **111**, 1006-1014.
- R. Improta, G. Scalmani and V. Barone, *Int. J. Mass Spectrom.*, 2000, **201**, 321-336.
- S. Ishiuchi, M. Sakai, K. Daigoku, K. Hashimoto and M. Fujii, *J. Chem. Phys.*, 2007, **127**, 234304.
- H. W. Jochims, M. Schwell, H. Baumgärtel and S. Leach, *Chem. Phys.*, 2005, **314**, 263-282.
- H. Kang, K. T. Lee, B. Jung, Y. J. Ko, S. K. Kim, H. Kang, K. T. Lee, B. Jung, Y. J. Ko and S. K. Kim, *J. Am. Chem. Soc.*, 2002, **124**, 12958-12959.
- K. Khistyaev, A. Golan, K. B. Bravaya, N. Orms, A. I. Krylov and M. Ahmed, *J. Phys. Chem. A*, 2013, **117**, 6789-6797.
- K. Khistyaev, K. B. Bravaya, E. Kamarchik, O. Kostko, M. Ahmed and A. I. Krylov, *Faraday Discuss.*, 2011, **150**, 313-330.

- N. J. Kim, *Bull. Korean Chem. Soc.*, 2006, **27**, 1009-1014.
- N. J. Kim, Y. S. Kim, G. Jeong, T. K. Ahn and S. K. Kim, *Int. J. Mass Spectrom.*, 2002, **219**, 11-21.
- S. Kim, W. Lee and D. Herschbach, *J. Phys. Chem.*, 1996, **3654**, 7933-7937.
- K. Kleinermanns, D. Nachtigallová and M. S. De Vries, *Int. Rev. Phys. Chem.*, 2013, **32**, 308-342.
- S. Kim, S. E. Wheeler and H. F. Schaefer, *J. Chem. Phys.*, 2006, **124**, 204310.
- M. Kotur, T. C. Weinacht, C. Zhou and S. Matsika, *IEEE J. Sel. Top. Quantum Electron.*, 2012, **18**, 187-194.
- M. Kabelác and P. Hobza, *Phys. Chem. Chem. Phys.*, 2007, **9**, 903-917.
- M. Ligare, F. Siouri, O. Bludsky, D. Nachtigallová and M. S. de Vries, *Phys. Chem. Chem. Phys.*, 2015, **17**, 24336-24341.
- J. C. Lopez, M. I. Pena, M. E. Sanz and J. L. Alonso, *J. Chem. Phys.*, 2007, **126**, 191103.
- J. C. Lopez, J. L. Alonso, I. Pena and V. Vaquero, *Phys. Chem. Chem. Phys.*, 2010, **12**, 14128-14134.
- M. Liu, T. Li, F. S. Amegayibor, D. S. Cardoso, Y. Fu and J. K. Lee, *J. Org. Chem.*, 2008, **73**, 9283-9291.
- S. Matsika, C. Zhou, M. Kotur and T. C. Weinacht, *Faraday Discuss.*, 2011, **153**, 247-260.
- S. Matsika, M. Spanner, M. Kotur and T. C. Weinacht, *J. Phys. Chem. A*, 2013, **117**, 12796-12801.
- R. Mota, R. Parafita, A. Giuliani, M. J. Hubin-Franskin, J. M. C. Lourenco, G. Garcia, S. V. Hoffmann, N. J. Mason, P. A. Ribeiro, M. Raposo and P. Limao-Vieira, *Chem. Phys. Lett.*, 2005, **416**, 152-159.
- J. J. Manura and D. J. Manura, *Scientific Instrument Services Isotope Distribution Calculator*, http://www.sisweb.com/mstools/isotope.htm, 2016.
- S. H. Nam, H. S. Park, J. K. Song and S. M. Park, *J. Phys. Chem. A*, 2007, **111**, 3480-3484.
- D. Nachtigallová, A. J. A. Aquino, J. J. Szymczak, M. Barbatti, P. Hobza and H. Lischka, *J. Phys. Chem. A*, 2011, **115**, 5247-5255.
- Y. Nosenko, M. Kunitski and B. Brutschy, *J. Phys. Chem. A*, 2011, **115**, 9429-9439.
- R. Pandey, M. Lalande, M. Ryszka, P. Limão-Vieira, N. J. Mason, J. C. Poully and S. Eden, *Eur. Phys. J. D*, 2017, **in press**.
- A. M. Rasmussen, M. C. Lind, S. Kim and H. F. Schaefer, *J. Chem. Theory Comput.*,

2010, **6**, 930-939.

- J. M. Rice, G. Dudek and M. Barber, *J. Am. Chem. Soc.*, 1965, **87**, 4569-4576.
- K. E. Riley and P. Hobza, *J. Phys. Chem. A*, 2007, **111**, 8257-8263.
- M. Ryszka, R. Pandey, C. Rizk, J. Tabet, B. Barc, M. Dampc, N. J. Mason and S. Eden, *Int. J. Mass Spectrom.*, 2016, **396**, 48-54.
- M. Ryszka, Radiation Induced Processes in Biomolecules and Clusters in Controlled Beams, PhD Thesis, The Open University, 2015.
- J. J. Serrano-Perez, R. Gonzalez-Luque, M. Merchan and L. Serrano-Andres, *J. Phys. Chem. B*, 2007, **111**, 11880-11883.
- M. K. Shukla and J. Leszczynski, *J. Phys. Chem. A*, 2002, **106**, 8642-8650.
- V. G. Stavros and J. R. R. Verlet, in *Annual Review of Physical Chemistry, Vol 67*, eds. M. A. Johnson and T. J. Martinez, 2016, 67, 211-232.
- J. Tabet, S. Eden, S. Feil, H. Abdoul-carime, B. Farizon, M. Farizon, S. Ouaskit and T. D. Märk, *Nucl. Instruments Methods Phys. Res. B*, 2010, **268**, 2458-2466.
- Y. Tsuchiya, T. Tamura, M. Fujii and M. Ito, *J. Phys. Chem.*, 1988, **92**, 1760-1765.
- S. Ullrich, T. Schultz, M. Z. Zgierski and A. Stolow, *Phys. Chem. Chem. Phys.*, 2004, **6**, 2796-2801.
- P. J. M. Van Der Burgt, F. Mahon, G. Barrett and M. L. Gradziel, *Eur. Phys. J. D*, 2014, **68**, 151.
- A. Vredenborg, W. G. Roeterdink, C. A. De Lange and M. H. M. Janssen, *Chem. Phys. Lett.*, 2009, **478**, 20-27.
- V. Vizcaino, J. C. Poully, J. Y. Chesnel, A. Domaracka, S. Maclot, A. Méry, J. Rangama, P. Rousseau, L. Adoui and B. A. Huber, *Int. J. Mass Spectrom.*, 2014, **365-366**, 181-186.
- S. Yamazaki and T. Taketsugu, *J. Phys. Chem. A*, 2012, **116**, 491-503.

CHAPTER 6

Laser thermal desorption mass spectrometry

This chapter describes the development of a new system at the Open University to study biomolecules brought into the gas phase by *laser thermal desorption*. The system was tested using MPI mass spectrometry of 3-aminophenol. Further MPI measurements on uracil confirmed that the CO-loss channel investigated in Chapter 4 is not dependent on the specific mechanism of producing the gas-phase target. This test was necessary to enable the most direct comparisons possible with time-resolved pump-probe experiments carried out by our collaborators at Heriot-Watt University.

6.1 Introduction

In 2013, the Molecular Clusters Group reported the production of a new fragment ion with m/z 84 from multi-photon ionized uracil [Barc et al. 2013]. The absence of this peak in electron impact ionization mass spectra and its threshold behaviour in the MPI experiments show that this MPI channel depends on a critical process in a neutral excited state. As demonstrated in Chapter 4, the m/z 84 ion is derived from CO loss

from the excited ion system instead of CNH_2 loss [Ryszka et al. 2016]. This result is consistent with the structures of three ring-opening conical intersections that have been predicted in dynamical calculations (see table 4.1) [Nachtigallova et al. 2011, Richter et al. 2014]. The m/z 84 ion in MPI experiments therefore represents a potential marker for a ring opening CI in uracil and brings the exciting possibility of carrying out time-dependent experiments to track this process in real time. Hence, measuring the time-dependence of the m/z 84 ion in pump-probe experiments offers the opportunity to identify which (if any) of the theoretically predicted ring-opening CIs is responsible for its production. Accordingly, the Molecular Clusters Group started collaboration with Townsend and co-workers at Heriot Watt (HW) University to carry out ultrafast pump-probe experiments on uracil.

In 2015, former OU PhD student Michal Ryszka participated in measurements at HW of mass spectra from uracil as a function of the time delay between electronic excitation at 200 nm and ionization at 400 nm [Ryszka 2015]. More recently, the HW group have carried out equivalent experiments with a 220 nm pump beam in order to draw a closer analogy with the OU MPI measurements presented in Chapter 4. The HW probe wavelength of 400 nm provides a reasonably similar ionizing energy for the excited uracil molecules with 2 photons (6.20 eV) as the ionizing step of the OU measurement at 220 nm (5.64 eV). The measurement covered the pump-probe delay range from *zero* (overlapping pump and probe beams of approximate width 50 fs) to 100 ps (in 30 fs steps up to a delay of 1260 fs and then 30 exponentially increasing steps up to 100 ps). The HW group also measured one mass spectrum with a pump-probe delay of 330 ps. No evidence was observed for m/z 84 ions in any of these results [Ghafur et al. 2017]. Our main possible hypothesis to explain this result are:

1) The critical neutral excited state process responsible for the m/z 84 channel in the OU MPI experiments occurs predominantly >0.3 ns after the initial S_2 excitation. This would rule out the CIs in table 1 and suggests that similar (but not yet identified theoretically) structural changes in long-lived triplet states may be responsible.
2) The production of the m/z 84 ion from excited uracil is dependent on the specific characteristics of the neutral uracil target prior to excitation. This could conceivably be linked to different populations of tautomers and / or different vibrational temperatures in the OU target compared with the HW target.

The HW group [Ghafur et al. 2017, Ryzska 2015] bring uracil into the gas phase in a different way to the OU experiments in Chapter 4. Whereas the OU experiments involved heated uracil powder to 250 ºC in a flow of argon or helium (typically 0.5-1.0 bar) prior to supersonic expansion into vacuum to produce a molecular beam, the HW group use the *laser thermal desorption* (LTD) method. Therefore, to test hypothesis 2 above and to enable the best possible comparisons between the OU experiments and the HW experiments, we have built a new LTD system at the OU. The background and principles of LTD are described in section 6.2 and the specific design of the new OU system is described in section 6.3. Section 6.4.1 presents our first successful LTD experiments at the OU, using 3-aminophenol (3-AP) as a test case. We chose 3-AP because it can be brought into the gas phase effectively at much lower temperatures than a nucleobase. In addition, it is useful for us to characterize its MPI mass spectrum in preparation for Stark deflection experiments on the molecule (see Chapter 7). Section 6.4.2 presents our MPI mass spectrum of uracil using the OU LTD source.

Making direct comparisons with time-resolved experiments at HW is not our only motivation for developing this new system. In the future, we want to exploit it to look at biomolecules that we cannot study with our current supersonic molecular beam source due to thermal decomposition and / or reactivity. Nucleobases are at the limit of the biomolecular complexity that we can study using the supersonic beam sources described in Chapter 4. The nucleobase targets that we have been able to produce with adequate density for extended experiments (notably exploring wavelength dependence, photon orders, and clustering effects) are adenine, thymine, uracil, and 5-fluorouracil [Barc 2012, Barc et al. 2013, Barc et al. 2014, Ryszka et al. 2016]. For cytosine, avoiding thermal reactivity limited us to a very weak target [Ryszka 2015]. The Group's previous experiments on 5-chlorouracil and 5-bromouracil were unsuccessful due to thermal reactivity, while we have not attempted to study guanine in view of its well-known sensitivity to thermal damage [Periquet et al. 2000]. By contrast, LTD has been used successfully to produce gas-phase targets of nucleosides for ultrafast pump-probe experiments [De Camillis et al. 2015] and ion impact experiments [Poully et al. 2015].

6.2 Laser thermal desorption – background and principles

Currently the dominant technique to bring large fragile molecules into the gas phase for action spectroscopy experiments without molecular breakup is electrospray ionization [Fenn et al. 1989]. In this case, the target molecules are charged via protonation or deprotonation, often leading to substantially different properties compared to those of the neutral. Laser desorption / ablation methods (including matrix-assisted laser desorption, MALDI [Tanaka et al. 1988]) typically generate a low proportion of ions in addition to the neutrals [Merrigan et al. 2009, Puretzky and Geohegan 1998], internal

energies are generally high, and the resultant molecular cloud is often contaminated by matrix molecules and associated solvents. Laser induced acoustic desorption (LIAD) provides an alternative system to bring intact complex species into the gas phase, extending to macromolecules and even viruses [Peng et al. 2006]. In this method, a pulsed laser beam impinges on a metallic foil and initiates the desorption of molecules from a condensed sample on the other side of the foil [Bald et al. 2008]. This is typically described in terms of photoacoustic shock waves in the foil coupling with intermolecular vibrational modes in the sample and thus breaking intermolecular bonds on a faster timescale than thermalisation [Lucchese and Tully 1984]. However, Zinovev et al.'s [2007] experimental studies of LIAD systems indicated a more complex combination of processes was responsible, including the formation of cracks in microscale or nanoscale crystals and non-equilibrium electronic states on the foil surface that are repulsive to the adsorbed molecules. While further research is required to fully understand LIAD, a practical limitation is that very thin molecular deposits are required and these are typically depleted in only a few hundred pulses of the focused laser [Bald 2017]. Although this can be mitigated by moving foil and / or laser focus systems, it nonetheless presents a significant barrier to many types of experiment.

Having previously built a LIAD system [Calvert et al. 2010], Greenwood and co-workers at Queen's University Belfast modified the method by replacing the pulsed laser with a CW laser and using thicker sample deposits for ultrafast pump-probe experiments on nucleosides [De Camillis et al. 2015]. In this case, the molecular desorption process can reasonably be assumed to be thermal so they called it *laser thermal desorption* (LTD) [Poully et al. 2015]. Unlike conventional molecular beams produced by heating in an effusive oven [Tabet et al. 2010] or in a supersonic expansion

nozzle (such as in the experiments in Chapters 4 and 5), evaporation using LTD has the advantage that the desorbed molecules do not undergo several cycles of condensation and re-evaporation. Furthermore, they do not scatter from hot surfaces or gas-phase atoms / molecules. The foil can be positioned very close to the interaction region (e.g. just 1-2 mm from the MPI laser in our experiments in section 6.4) so the journey time from desorption to the experimental interaction is short (microsecond-order). These effects reduce the likelihood of thermal decomposition. Accordingly, Greenwood et al. [De Camillis et al. 2015, Poully et al. 2015] reported no evidence for thermal decomposition in the gas-phase nucleoside targets from their LTD source.

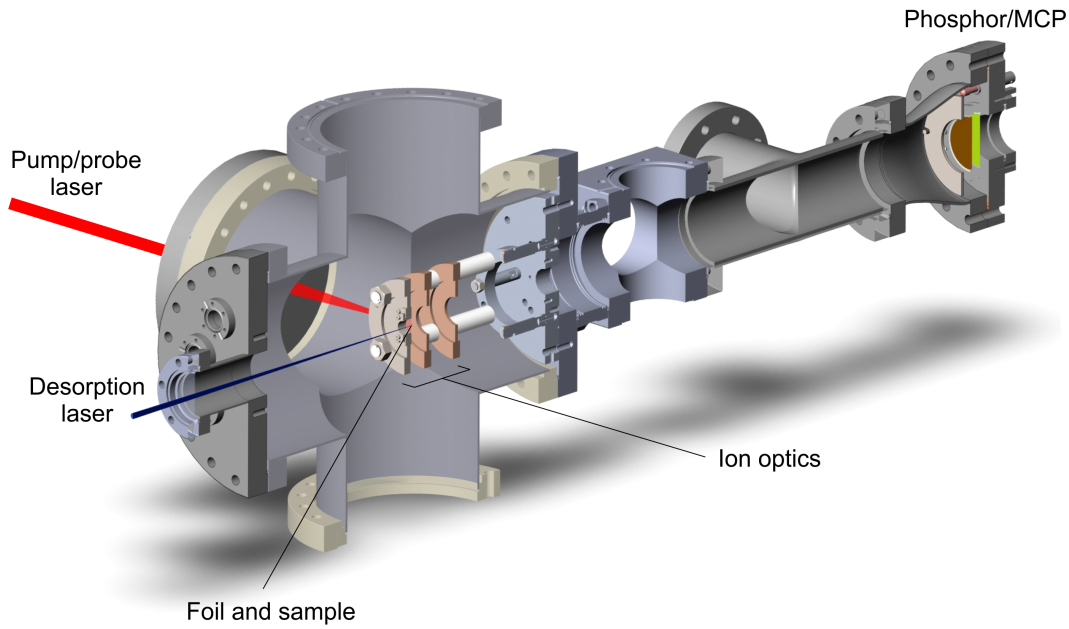

Figure 6.1: Schematic of the Heriot-Watt experiment, including their first LTD system. [Ghafur et al. 2017].

Townsend and co-workers at Heriot Watt (HW) University collaborate with Greenwood and adopted the LTD approach for their pump-probe experiments on gas-phase biomolecules. The HW experiments on uracil described in section 6.1 were carried out

using a CW focused beam of power 300 mW [Kalecnc 445 nm 1.5 W Laser Module, model 44513FPA5 with an added potentiometer for controlling the power]. The focused spot was approximately 1 mm in diameter. Fig. 6.1 shows the first LTD system that was built by the HW group and used for most of their experiments on uracil [Ghafur et al. 2017]. Further details are provided in Michal Ryzska's PhD thesis [2015]. Townsend and co-workers have recently upgraded their experiment to include a rotating foil sample, thus reducing the regularity of having to open the experiment to replenish the sample.

6.3 The OU laser thermal desorption (LTD) system

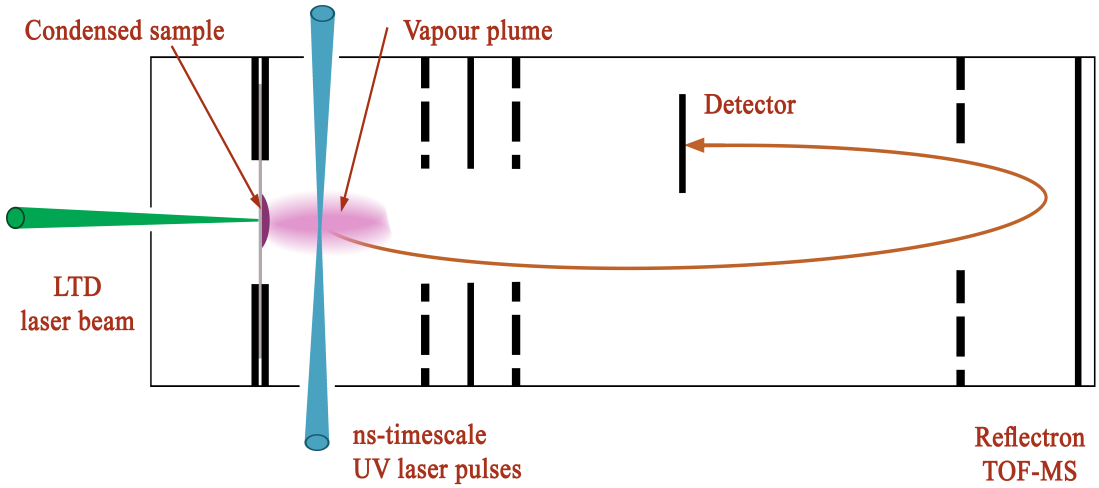

Figure 6.2: Schematic of the new laser thermal desorption experiment at the OU. The LTD beam was 532 nm (green, as shown in the diagram) in the experiments on 3-aminophenol and 450 nm (blue) in the experiments on uracil.

Fig. 6.2 shows a schematic view of the new LTD experiment at the OU. The design of the LTD source is based on adapting the compact MPI/EII experiment (Chapter 3) to incorporate the most important features of the first HW system (itself inspired by the

Queen's University Belfast system [De Camillis et al. 2015, Poully et al. 2015]). The LTD laser used in the experiments on 3-aminophenol was a Ventus 532 system (532 nm, maximum power 0.12 W). To achieve greater heating of the foil for the uracil experiments, this was replaced with a DLM-445-1000 OEM Blue Laser Module (445 nm, maximum power 1 W supplied by Eksma Optics with an EO-PS-II adjustable power supply). In addition to delivering greater power, the relatively small dimensions and mass of the DLM-445-1000 enable easier alignment. An external interlock system was built by the OU electronics team (Robert Seaton and co-workers) to cut off the power supply to the LTD laser if the laboratory doors are opened. The optical power outputs of the lasers were tested and calibrated as a function of the adjustable currents from their power supplies using a Gentec UNO laser power meter.

The LTD laser beam passes through a convex lens mounted 4 cm in front of a window of diameter 15 mm (a standard DN16CF viewport) on an aluminium profile connected to the support frame of the compact MPI/EII experiment. The window is connected to a zero-length DN25CF/DN100 adapter that has been customized by the OU mechanical workshop team (Chris Hall and co-workers). This customization involved welding three high-voltage electrical feedthroughs (MHV 5kV) and adding four tapped holes; three to support the *TOF source* assembly and one for a grounding connection. As shown in Fig. 6.3, the TOF source includes the grounded backplate, the (pulsed) extraction grid assembly, a focusing ring electrode, and the first grid defining the field free region (FFR) of the reflectron mass spectrometer. These parts were re-used from the original KORE technology system (described in Chapter 3), except for a new backplate built by the OU mechanical workshop team. The new backplate system enabled a piece of foil to be installed using the *sandwich* system shown in Fig. 6.4.

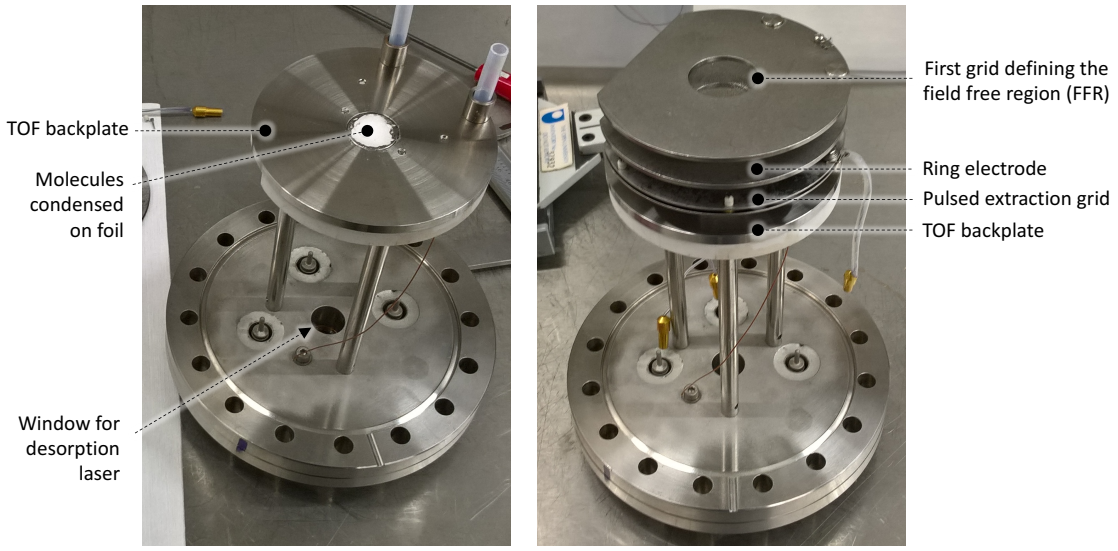

Figure 6.3: Photographs of the *TOF source* used for the LTD experiments at the OU. The left-hand diagram shows the TOF source at a stage of partial construction. The powder deposit on the foil is clearly visible. The right-hand diagram shows the almost-fully-assembled TOF source (only the electrical connections need to be made).

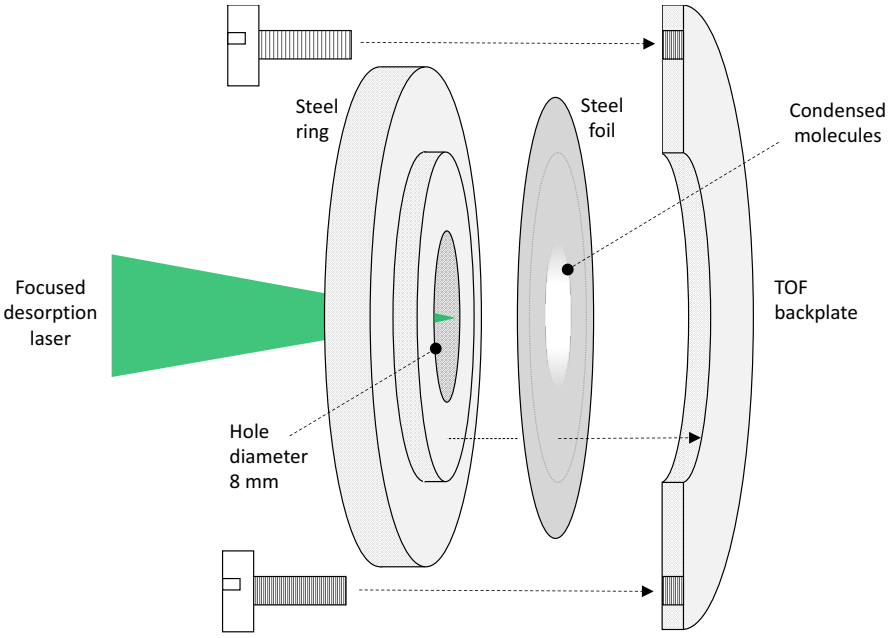

Figure 6.4: Schematic diagram illustrating the OU *sandwich* system used to mount the foil for LTD experiments. The foil is pulled tight across the *front* (the right side in the diagram) of the steel ring before both are mounted on the TOF backplate as shown. The front of the foil (with the condensed molecules) is then level with the front surface of the TOF backplate. Finally, the experiment is pumped down and the laser shines through the hole in the ring onto the back of the foil.

The effect of the *sandwich* system is to replace part of the TOF backplate surface with a layer of stainless steel foil of thickness 10 μm (supplied by Hollinbrow). Prior to assembly, a layer of condensed molecules is deposited on the side of the foil that will face into the mass spectrometer. This deposit is achieved by dropping 30-40 mg of powder on the foil using a spatula. A drop of methanol is then added to the powder, creating a supersaturated solution. Subsequent evaporation of the methanol in air leaves a layer of solid sample of approximate diameter 18 mm that remains attached to the foil when the TOF source is turned 90° and installed in the experiment. A shallow arc-shaped piece of copper sheet (220×110×0.5 mm, bent with an approximate radius of 50 mm) is placed below the TOF source to prevent any dislodged fragments of the solid sample falling into the turbo pump.

The lens for the LTD laser is typically placed at its focal distance (20.0 cm) away from the foil with an estimated precision of ±5 mm. However, we found that the signal did not change noticeably when we used the lens or when we worked with the unfocused beam (an ellipse of approximately 2×4 mm from the 445 nm laser or a circle of diameter ~0.8 mm from the 532 nm laser). The lens was not used in the experiments on 3-AP shown in section 6.2. Nonetheless, the lens is used is most LTD experiments at the OU as it aids alignment and enables a closer analogy with the HW system. The pulsed UV laser beam was positioned 1-2 mm away from the condensed sample surface (tested using the method described in section 3.2.2). The resulting ions were detected and analysed using reflectron time of flight mass spectrometry, as described in Chapter 3.

The 3-AP and uracil samples used in the experiments in section 6.4 were supplied by Sigma-Aldrich with stated purity of 98% and ≥99%, respectively. The melting points given by the supplier are 120-124°C for 3-AP and >300°C for uracil; hence a significantly lower LTD laser power can be used to produce an adequate gas-phase target of 3-AP than uracil.

6.4 Results and Discussion

6.4.1 MPI mass spectra of 3-aminophenol from the OU LTD system

Aminophenol is the chromophore in the amino acid tyrosine and is also closely related the neurotransmitter dopamine [Shinozaki et al. 2003]. It is therefore somewhat surprising that the experimental and theoretical work in the literature on the electronic states, ionic states, and fragmentation of 3-AP is extremely sparse (unlike 4-AP which is no more relevant in a biological context). Shinozaki et al. [2003] performed REMPI experiments on 3-AP in the photon energy range 4.2-4.6 eV, as well as LIF measurements and quantum chemical calculations to support their assignments of vibronic structure. These REMPI assignments enabled Küpper, Meijer and co-workers to demonstrate the complete separation of the molecule's cis and trans conformers (which exist in approximately equal proportions in the gas phase and are shown in Fig. 6.5) using Stark deflection [Filsinger et al. 2009]. More recently, Yatsyna et al. [2016] have performed IR action spectroscopy measurements on the full set of aminophenol isomers. However, to our knowledge only one mass spectrum of 3-AP has been reported: an electron impact ionization (EII) measurement on the Japanese AIST/NIMC

Database (2017 – reproduced in the NIST database). This is shown in Fig. 6.6c(a). We are not aware of any proposed assignments for the fragment ions.

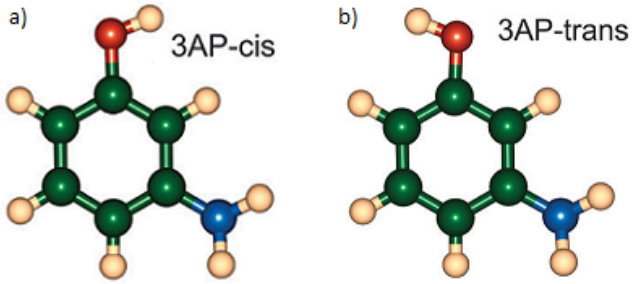

Figure 6.5: Cis- and trans- conformers of 3-aminophenol [Yatsyna et al. 2016].

Our first experiment on 3-AP was to measure its MPI mass spectrum using the supersonic beam source described in Chapter 3 with a single 500 ls^{-1} pump on the expansion chamber. The powder temperature of 108ºC is lower than 150ºC used in the EII measurement (AIST/NIMC 2017) but higher than the nozzle temperature of 80-100ºC used in the previous action spectroscopy experiments [Shinozaki et al. 2003, Yatsyna et al. 2016]. As shown in Fig. 6.6(b) and (c), we repeated our MPI measurements in helium and argon expansions. Neither mass spectrum revealed any evidence for clustering in the target beam. As in the EII data (Fig. 6.6(a)), the MPI mass spectra are dominated by the m/z 109 peak corresponding to the intact 3-AP^+ ion ($C_6H_7NO^+$). The fragment ion patterns are also similar in the three measurements, with the peak at m/z 80 ($C_5H_6N^+$ or $C_5H_4O^+$) particularly prominent. The differences in the relative intensities of the fragment ions are most likely due to variations in the acceptance of the mass spectrometer configurations and differences in energy deposition in the excited ion. No new peak stands out in the MPI measurements that could indicate a critical process in a neutral excited state.

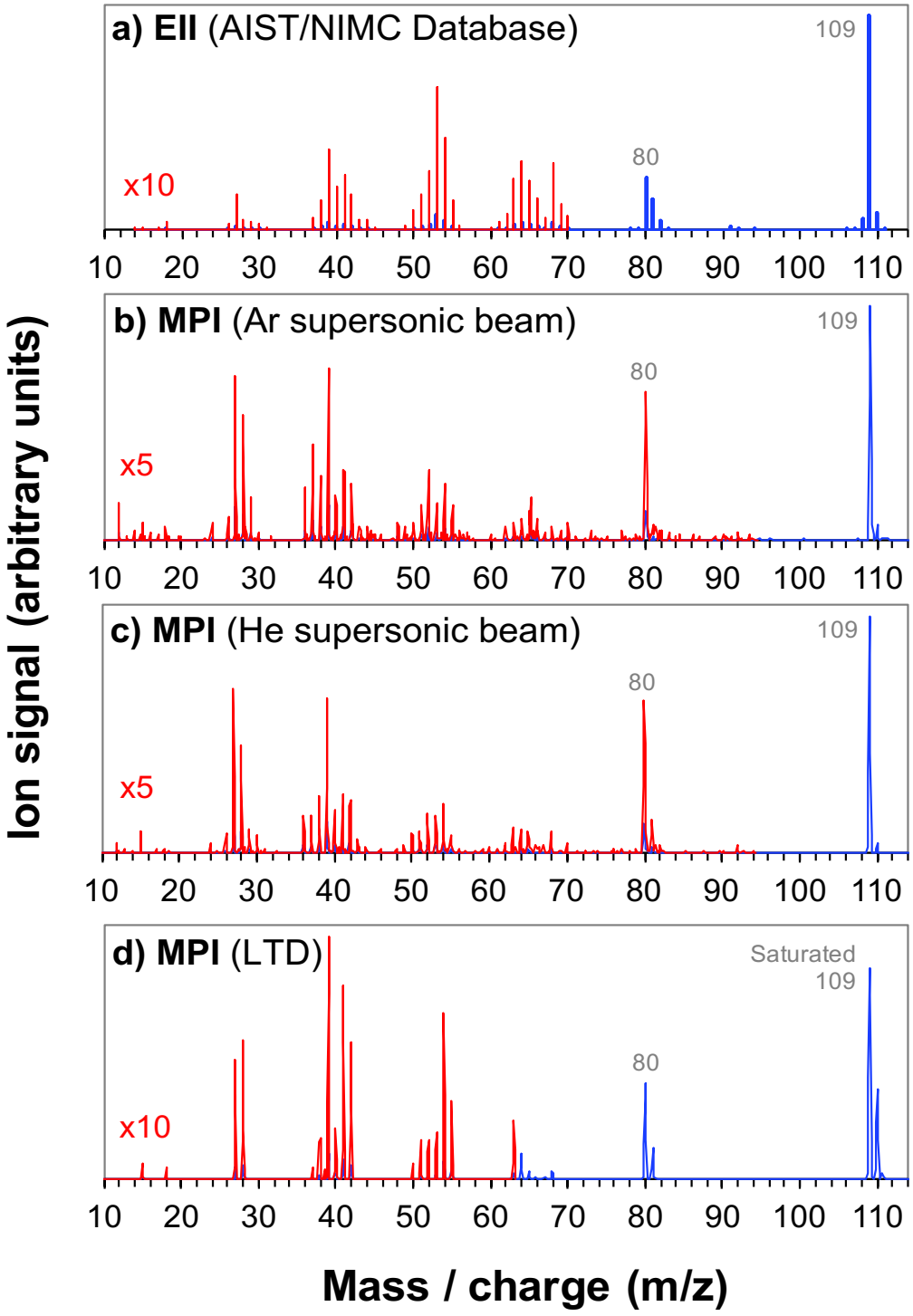

Figure 6.6: Comparison of mass spectra of gas-phase 3-AP. (a) 75 eV electron impact ionization mass spectrum, sample 150°C (AIST/NIMC 2017). (b)/(c) MPI (220 nm, average fluence 2×10^{7} Wcm^{-2}) in a supersonic beam of helium / argon (1 bar, powder 108°C). (d) MPI (220 nm, average fluence 7×10^{5} Wcm^{-2}) using the LTD system (533 nm, 120 mW, unfocused).

Fig. 6.6(d) shows the MPI mass spectrum of 3-AP produced using the new LTD source. The 3-AP^+ signal was saturated even though the energy per pulse of the focused MPI laser was 30 times lower than in the supersonic beam measurements. Based on the signal of the isotopomer ion at m/z 110 and the known proportion of 3-AP including one ^{13}C atom (7.0% [Manura and Manura 2016]), we can determine that the number of 3-AP^+ ions hitting the detector per MPI laser pulse was 32. For comparison, the 3-AP^+ signal in the helium beam measurement (Fig. 6.6(c) – with a much more intense MPI beam) was 0.63 counts per pulse. The strong signal in Fig. 6.6(d) demonstrates the efficacy of the OU LTD system and suggests that it has considerable potential to study weak MPI processes. Accordingly, we decided to test for metastable dissociation signals by recording TOF spectra as a function of the reflection voltage in the same way as we did for uracil and thymine (section 5.4.1). Fig. 6.7 shows two time-of-flight measurements with the reflection voltage (V_R) set on either side of the cut-off for the detection of 3-AP^+ and fragment ions produced by its *prompt* dissociation (≤100 ns after ionization). A clear metastable ion signal is visible in the V_R= -200 V data. This feature is superimposed on the m/z 64 *prompt* fragment ion signal in the V_R = -25 V result. The time-of-flight scale is not mass-calibrated in Fig. 6.7 so a direct comparison can be made with the 2-D plot in Fig. 6.8.

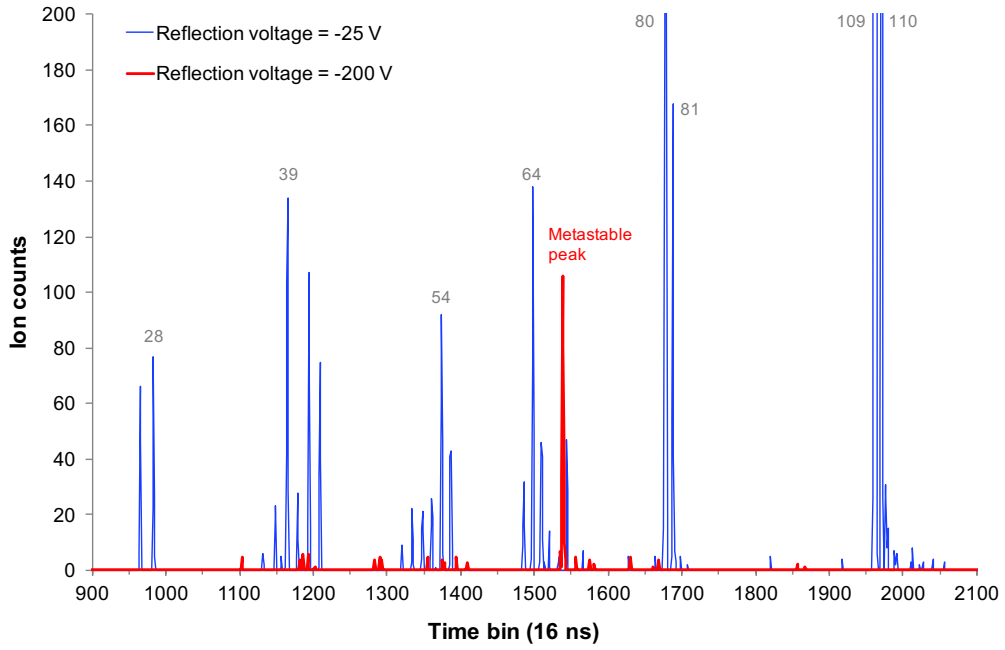

Figure 6.7: MPI time-of-flight spectra of 3-AP (MPI and LTD laser parameters as in Fig. 6.6(d)) with reflection voltages V_R = -25 V and -200 V. The m/z values of several prominent peaks in the 25 V result are labelled in grey. The peak in the -200 V result is due to metastable dissociation in the field-free-region (FFR) of the mass spectrometer.

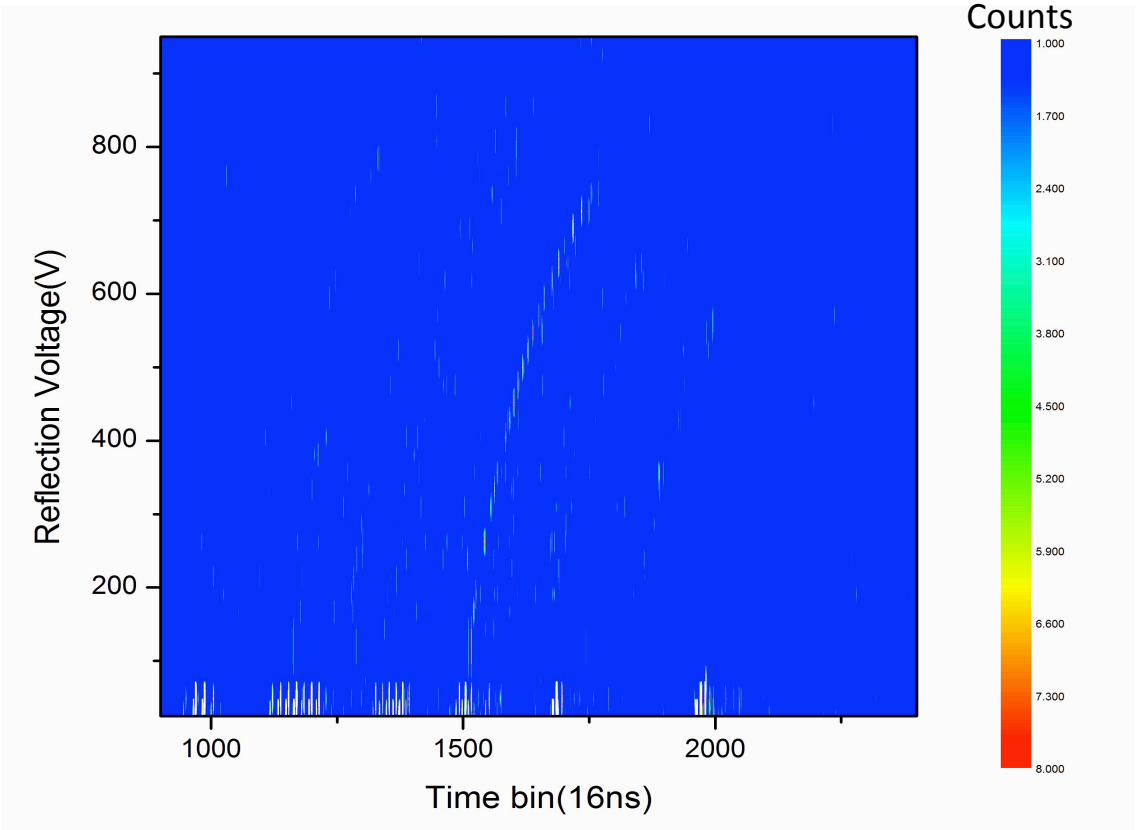

Figure 6.8: MPI time-of-flight contour plot of 3-AP (MPI and LTD laser parameters as in Fig. 6.6(d)) as a function of the reflection voltage. The band extending to more negative reflection voltages corresponds to the metastable dissociation peak in Fig. 6.7.

As explained in Chapters 3 and 5, the *metastable band* extending to more negative V_R values in Fig. 6.8 is due to fragmentation of ions during their first journey through the FFR. The resultant ions have relatively low kinetic energies and so can be reflected by a weaker field. The V_R steps in Fig. 6.8 are 25 V. The *prompt* fragment ion signals cut-off between -50 and -75 V and the metastable band cuts off between -750 and -775 V. The FFR voltage was -2028±1 V so the mass of the product ion is ((2028±1 – 762.5±12.5) / (2028±1 – 62.5±12.5) =) (65.7±1.1)% of the mass of the parent ion before its dissociation in the FFR. Comparisons between the calculated and measured flight times ruled out the possibility that a metastable dissociation of 3-AP^+* could be responsible. On the contrary, the metastable dissociation can only be from a parent with m/z 80-81 to a product with m/z 52-54. Metastable dissociation from m/z 80 to m/z 52 gives the best agreement of KE and TOF. This can be explained as one of two plausible sequential dissociation pathways:

	First step – *prompt*	Second step - *metastable*
(1)	3-AP^+* loses COH → $C_5H_6N^+$*	$C_5H_6N^+$* loses CNH_2 → $C_4H_4^+$
or (2)	3-AP^+* loses CNH_3 → $C_5H_4O^+$*	$C_5H_4O^+$* loses CO → $C_4H_4^+$

Pathway 1 requires no hydrogen rearrangements before or during the *prompt* dissociation step. However, *prompt* here means ≤100 ns (a very long time in the context of intramolecular hydrogen transfer) so we see no convincing intuitive argument to support either pathway ahead of the other. Our collaborator Jean-Christophe Poully is currently running *ab initio* calculations to assign the metastable dissociation process with confidence.

6.4.2 Uracil

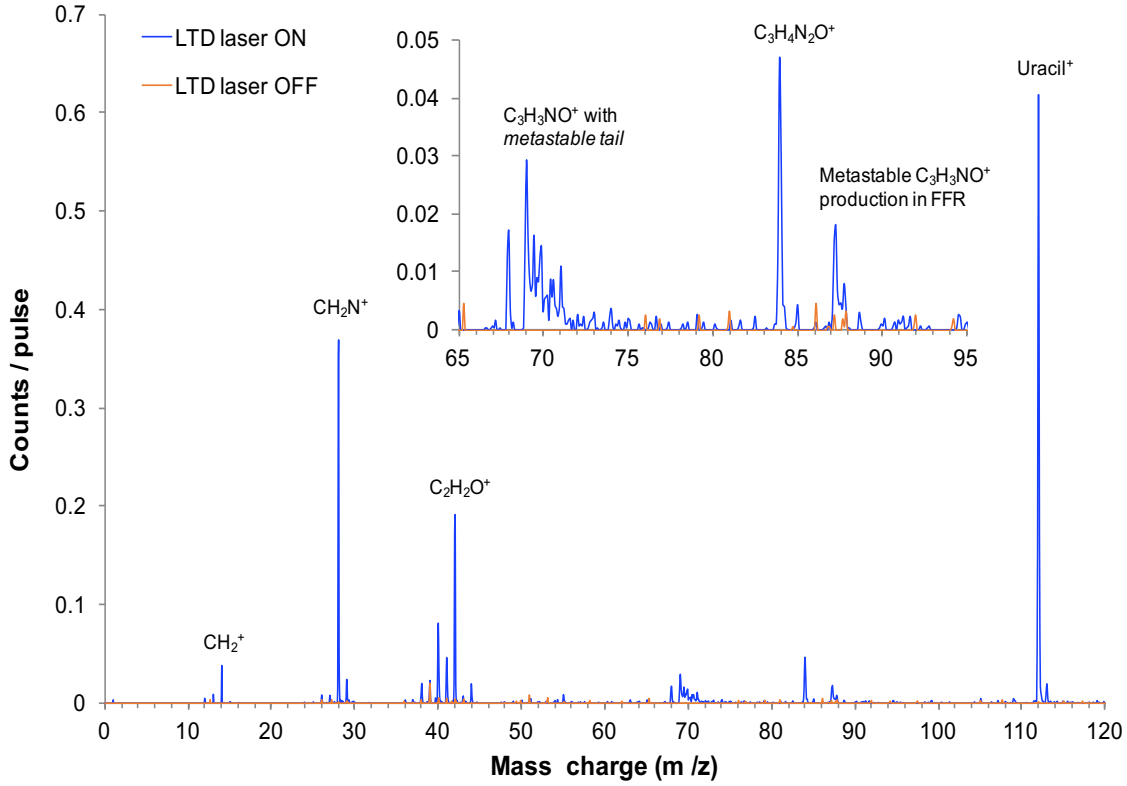

Figure 6.9: MPI mass spectrum of uracil at 220 nm (average fluence 1.26×10^{7} Wcm^{-2}) using new LTD system (445 nm, 160 mW) at the OU. The mass m/z 84 peak is clearly present, demonstrating that its absence in the HW time-resolved experiments is not due to differences between the gas-phase targets.

Fig. 6.9 shows the 220 nm MPI mass spectrum of uracil recorded using our new LTD system. The background signal with the LTD laser turned off is also shown and only contributes significantly to the uracil measurement at m/z 39. Fig. 6.9 can be compared with the MPI mass spectrum of uracil in a supersonic helium beam in Fig. 4.4. The agreement is excellent in terms of the fragment ion pattern, with $C_2H_2O^+$ and CH_2N^+ standing out as particularly strong. There is no evidence for thermal decomposition or reactivity. The ratio of m/z 113 / 112 counts is (4±1)%, in agreement with the natural ^{113}uracil / ^{112}uracil ratio of 5.2% [Manura and Manura 2016]. As protonated uracil is a

major ionization product of hydrogen-bonded uracil dimers [Ryzska et al. 2016], this provides strong evidence for the absence of clusters in the neutral target. The peak due to metastable HNCO loss from uracil^{+}* in the FFR (investigated in depth in Chapter 5) is clearly visible between m/z 87 and 88 in Fig. 6.9 (although the m/z calibration does not apply to this peak). Metastable HNCO loss from uracil^{+}* as it travels between the ionization region and the entrance of the FFR is also evidenced by a tail feature extending from the $C_3H_3NO^+$ peak (m/z 69) to higher m/z values.

The key result in Fig. 6.9 is the clear presence of the m/z 84 peak corresponding to $C_3H_4N_2O^+$ (uracil$^+$ less CO). This shows that the absence of m/z 84 ion production in the time-resolved experiments at Heriot Watt University is not linked to the method of bringing the uracil into gas phase. This is not surprising when we consider that infrared spectra of uracil vapour from powder heated at 200-325ºC into 13-20 mbar of static argon only showed evidence for a single tautomer: the diketo form [Colarusso et al. 1997]. Furthermore, while the level of vibrational excitation in the uracil molecules released by LTD will be higher than in our supersonic beam experiments, it will still be very minor in comparison with the vibrational excitation caused by photoexcitation to S_2 at 220 nm, 1.16 eV above the state's calculated adiabatic energy [Etinski et al. 2009]. However, the result leaves the identification of the specific neutral excited state process responsible for the m/z 84 channel in the present MPI experiments unresolved.

6.5 Summary

This chapter provides a description of the newly built *laser thermal desorption* (LTD) system at the OU to study multi-photon ionization (MPI) of isolated biomolecules. The LTD system was demonstrated to be effective for 3-aminophenol (3-AP); a solid biomolecule that can be brought into the gas phase effectively at relatively low temperatures. Furthermore, the intense signals in our LTD experiments on 3-AP have revealed a metastable dissociation channel of a fragment ion (the first observation of this kind from any molecule using compact MPI/EII experiment at the OU). To our knowledge, this is the first experimental insight into the sequential dissociative ionization pathways of 3-AP^+.

The original motivation for building the LTD source was to test if the m/z 84 fragment ion channel from multiphoton ionized uracil shows a significant dependence on the system for producing the gas-phase target. Such a dependence could have explained why time-resolved pump-probe experiments by our collaborators at Heriot-Watt University did not produce this fragment ion. However, the m/z 84 signal was clear in our MPI experiments using the new LTD system. This suggests that its production depends on a so-far unidentified critical process that takes place predominantly on a longer timescale than the time-resolved experiments (>0.3 ns). Further experiments are currently in progress exploiting LTD to probe larger gas-phase biomolecules than we can study using our supersonic expansion source. Our aim is to study how specific processes in biomolecular subunits evolve when that subunit is integrated into sequentially more complex biomolecules. Our first step in complexity is comparing the MPI of uracil with its nucleoside: uridine.

6.6 Contributions by co-workers and forthcoming publications

I designed and built the new LTD system, working with PhD students Michal Ryszka (now graduated), Tiago da Fonseca Cunha, and Jana Bockova. Tiago da Fonseca Cunha, Jana Bockova, and I performed the experiments. I analyzed the data and devised interpretations, working mainly with Sam Eden. The uracil result presented here will be included in a collaborative paper that we are currently preparing with Dave Townsend's group at Heriot-Watt University and Jason Greenwood's group at Queen's University Belfast [Ghafur et al. 2017].

References:

- AIST/NIMC Database-Spectrum MS-IW-4311, http://sdbs.db.aist.go.jp (National Institute of Advanced Industrial Science and Technology, accessed 2017.
- I. Bald, J. Langer, P. Tegeder and O. Ingólfsson, *International Journal of Mass Spectrometry*, 2008, **277**, 4-25.
- I. Bald, University of Potsdam, *Private Communication*, 2017.
- B. Barc, Hydrated clusters of nucleic acid bases in supersonic beams probed by multi-photon ionization (MPI) mass spectrometry, Department of Physical Sciences, The Open University, Milton Keynes, United Kingdom, *PhD thesis*, 2012.
- B. Barc, M. Ryszka, J. Spurrell, M. Dampc, P. Limão-Vieira, R. Parajuli, N. J. Mason and S. Eden, *J. Chem. Phys.,* 2013, **139**, 244311.
- B. Barc, M. Ryszka, J. C. Poully, E. Jabbour Al Maalouf , Z. el Otell, J. Tabet, R. Parajuli, P. J. M. van der Burgt , P. Limão-Vieiraf, P. Cahillanea, M. Dampc , N. J. Mason and S. Eden, *Int. J. Mass Spectrom.,* 2014, **194**, 365-366.
- P. Colarusso, K. Zhang, B. Guo and P. F. Bernath, *Chem. Phys. Lett.,* 1997, 269, 39-48.
- S. De Camillis, J. Miles, G. Alexander, O. Ghafur, I. D. Williams, D. Townsend and J. B. Greenwood, *Physical Chemistry Chemical Physics*, 2015,**17**, 23643-23650.
- M. Etinski, T. Fleig and C. M. Marian, *J. Phys. Chem. A*, 2009, **113**, 11809-11816.
- J. B. Fenn, M. Mann, C. K. Meng, S. F. Wong and C. M. Whitehouse, *Science*, 1989, **246**, 64-71.
- F. Filsinger, J. Küpper, G. Meijer, J. L. Hansen, J. Maurer, J. H. Nielsen, L. Holmegaard and H. Stapelfeldt, *Angewandte Chemie International Edition*, 2009, **48**, 6900-6902.
- M. Gerhards and C. Unterberg, *Appl. Phys. A*, 2001, **72**, 273-279.
- O. Ghafur, S. W. Crane, M. Ryszka, J. Bockova, R. Pandey, A. Rebelo, L. Saalbach, S. De Camilis, J. B. Greenwood, S. Eden and D. Townsend, *Time-dependent photoionization yield study of uracil: Non-adiabatic dynamics over the 267-200 nm excitation region*, in preparation, 2017.
- A. Jansen and M. Gerhards, *J. Chem. Phys.,* 2001, **115**, 5445-5453.
- J. J. Manura and D. J. Manura, *Scientific Instrument Services Isotope Distribution Calculator, http://www.sisweb.com/mstools/isotope.htm*, 2016.
- T. L. Merrigan, C. A. Hunniford, D. J. Timson, M. Catney and R. W. McCullough, *Biochem. Soc. Trans*., 2009, **37**, 905-909.

- D. Nachtigallova, A. J. A. Aquino, J. J. Szymczak, M. Barbatti, P. Hobza and H. Lischka, *J. Phys. Chem. A*, 2011, **115**, 5247-5255.
- W.-P. Peng, Y.-C. Yang, M.-W. Kang, Y.-K. Tzeng, Z. Nie, H.-C. Chang, W. Chang, and C.-H. Chen, *Angew. Chem. Int. Ed.,* 2006, **45**,1423-1426.
- V. Periquet, A. Moreau, S. Carles, J.P. Schermann, C. Desfrancois, *J. Electron Spectrosc. Relat. Phenom.,* 2000,**106**, 141-151.
- J.-C. Poully, J. Miles, S. De Camillis, A. Cassimi and J. B. Greenwood, *Phys. Chem. Chem. Phys.,* 2015, **17**, 7172-7180.
- A. A. Puretzky and D. B. Geohegan, *Chem. Phys. Lett.,* 1998, **286**, 425–432.
- M. Richter, S. Mai, P. Marquetand, L. González, *Phys. Chem. Chem. Phys.*, 2014, **16**, 24423-24436.
- M. Ryszka, R. Pandey, C. Rizk, J. Tabet, B. Barc, M. Dampc, N. J. Mason and S. Eden, *Int. J. Mass Spectrom.*, 2016, **396**, 48-54.
- M. Ryszka, Radiation Induced Processes in Biomolecules and Clusters in Controlled Beams, Department of Physical Sciences, The Open University, Milton Keynes, United Kingdom, *PhD thesis*, 2015.
- M. Shinozaki, M. Sakai, S. Yamaguchi, T. Fujioka and M. Fujii, *Phys. Chem. Chem. Phys.,* 2003, **5**, 5044-5050.
- J. Tabet, S. Eden, S. Feil, H. Abdoul-Carime, B. Farizon, M. Farizon, S. Ouaskit and T. D. Märk, *Nuclear Inst. and Methods in Physics Research B,* 2010, **268**, 2458-2466.
- K. Tanaka, H. Waki, Y. Ido, S. Akita, Y. Yoshida, T. Yoshida and T. Matsuo, Rapid Commun. Mass Spectrom., 1988, **2**, 151-153.
- V. Yatsyna, D. J. Bakker, R. Feifel, A. M. Rijs and V. Zhaunerchyk, *Phys. Chem. Chem. Phys.,* 2016, **18**, 6275-6283.

CHAPTER 7

Stark deflection of continuous molecular beams

This chapter presents the main progress achieved during this PhD in the manipulation of continuous (CW) molecular beams using *Stark deflection*. Stark deflection depends on producing polar neutrals in low rotational states that can subsequently be accelerated in an electric field gradient in space. Electron impact ionization (EII) experiments on nitromethane demonstrate the level of deflection and cooling that we can attain in helium beams using the new system at the OU. Multi-photon ionization (MPI) measurements on 3-aminophenol (3-AP), thymine, and uracil show that more complex biomolecules can be manipulated in CW beams of argon and krypton. Conversely, the thymine and uracil clusters in these beams are minimally affected. This provides a route to trace specific product ions to monomers and / or clusters.

7.1 Introduction

Distributions of different species within neutral target beams can present a major challenge in interpreting irradiation experiments and drawing rigorous comparisons with theory. For example, the Molecular Clusters Group has previously performed experiments using to the *Compact MPI/EII* system looking at the production of fragment ions from nucleobases in different molecular beam conditions with increased or decreased clustering [Barc 2012, Barc et al. 2013, Barc et al. 2013, Ryszka 2015, Ryszka et al. 2016]. These experiments have indicated some interesting trends such as a decrease in the relative production of m/z 84 ions from hydrated uracil clusters [Barc et al. 2013]. However, we cannot give more precise information such as whether or not a specific fragment ion channel is completely quenched by clustering or if different cluster configurations have different effects. *Stark deflection* experiments provide a route to answering questions of this kind, ideally by producing pure targets of a specific cluster configuration. For example, the Watson-Crick guanine-cytosine can, in principle, be separated from the main alternative hydrogen-bonded geometry of the base-pair (see Fig. 7.1) as well as from π-stacked guanine-cytosine due to the differences in the permanent dipole moments of these complexes. If a complete separation is not possible with the level of rotational cooling, narrowing the range of different configurations in a mixed beam using Stark deflection can also be extremely valuable in refining data interpretations.

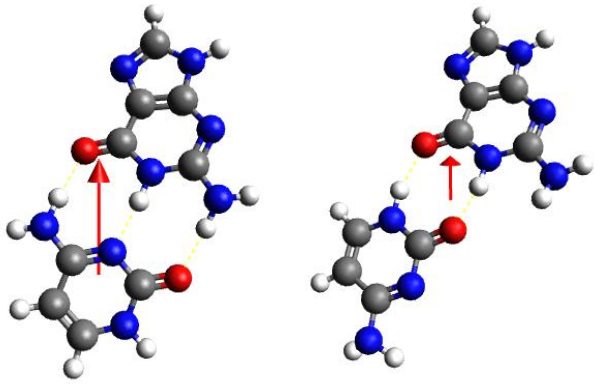

Figure 7.1: Left: Watson–Crick pair of Guanine-Cytosine with permanent dipole moment 2.5 D [Riahi et al. 2010], Right: alternative hydrogen-bonded Guanine-Cytosine configuration with permanent dipole moment 1.2 D. Drawn and optimized using *Avigadro* [Hanwell et al. 2012].

In addition to the challenge presented by numerous different configurations in beams containing clusters, many molecules exhibit a combination of different structural conformers in the gas phase. Examples include para and ortho H_2, cyclohexane, glycine, tryptophan and 3-aminophenol (3-AP) [Suenram and Lovas 1980, Rizzo et al. 1985]. These can convert into each other through the rotation about covalent bond, often leading to significant changes in permanent dipole moment. The specific structure of a molecule can determine some of the most important aspects of its functionality. It is well established that different conformers can show distinct chemical reactivities [Barton 1953, Dunathan 1966, Eliel and Wilen 1994]. Furthermore, the response of a molecule to irradiation can be modified by its specific geometry (isomers, tautomers, and structural conformers). For example, shifts in the energies, photoabsorption cross sections, and dynamics of valence excited states of different tautomers of biologically relevant molecules have been reported on numerous occasions [Nir et al. 2002]. As different molecular geometries generally lead to different permanent dipole moments, the Stark effect can be exploited to select specific structural conformers of isolated

molecules from rotationally-cold beams [Filsinger et al. 2009].

Küpper, Meijer, and their co-workers have demonstrated that Stark deflection can control the motion of several quite complex polar molecules with rotational temperatures as low as 1 K [Filsinger et al. 2009A] in pulsed helium beams. For example, they have separated individual quantum states of benzonitrile [Filsinger et al. 2009A] (4.515 D). Using a *2-wire* Stark deflector (matching the OU deflector - see section 3.3.2) or alternatively using a quadrupole *filter* with alternating electric fields, they have separated cis (2.3 D) and trans (0.7 D) conformers of 3-aminophenol (Fig. 6.5) and probed them by vibrationally-resolved REMPI spectroscopy [Filsinger et al. 2008A, Filsinger et al. 2009B]. Furthermore, they have shown that the reaction rate with Ca+ ions is different for these two conformers of 3-AP [Chang et al. 2013]. From the perspective of our aims, it is particularly interesting that they have also separated indole-H_2O clusters from a beam containing H_2O, indole, and indole-$(H_2O)_2$ using a 2-wire deflector [Trippel et al. 2012].

Pulsed molecular beams are suitable for action spectroscopy experiments with pulsed lasers but are much less applicable to studies of collision-induced processes with relatively low cross sections and / low intensity of the incident projectiles. In the future, we aim to carry out dissociative electron attachment (DEA) experiments on Stark-selected clusters. The experimental literature on the effects of clustering on DEA is very sparse but major effects have been predicted theoretically such as an order-of-magnitude difference in the cross section for Cl^- abstraction from different geometries of $CF_3Cl(H_2O)_3$ [Fabrikant et al. 2012]. Due to space charge effects, low energy electron beams can only be controlled effectively with very low currents (e.g. nA) so a

pulsed target beam would not be a viable option. Therefore, our new experiment at the OU uses a Stark deflector built by Küpper and co-workers to manipulate CW beams. The principles of Stark deflection are introduced in the section 2.5 and the OU experiment is described in section 3.3.

In addition to Küpper and Meijer's groups, further researchers exploiting Stark deflection and / or Stark deceleration of molecules in pulsed beams to produce controlled targets include Softley, [Willitsch et al. 2008], Kressin [Moro et al. 2006], van de Meerakker [Vogels et al. 2015] and their respective co-workers. However, the literature is much more sparse with respect to the Stark manipulation of CW beams (Jankunas and Osterwalder 2015). Rempe and co-workers [Rangwala et al. 2003, Junglen et al. 2004, Reiger et al. 2005, Reiger et al. 2006, Motsch et al. 2007, Motsch et al. 2009, Sommer et al. 2009, van Buuren et al. 2010] controlled formaldehyde (H_2CO, 2.34 D), deuterated ammonia (ND_3), and water using a static quadrupole Stark filter. The OU Molecular Clusters Group have also manipulated water molecules in CW beams of helium and argon using the Stark effect [Ryszka 2015]. The group then extended their deflection experiments to nitromethane (CH_3NO_2, 3.46 D) and benzonitrile (C_6H_5CN, 4.52 D). To our knowledge, these were the largest and most complex molecules to have been Stark manipulated in CW beams prior to my PhD. I have extend this complexity further by demonstrating the first Stark deflection DNA and RNA bases.

In Ryszka's [2015] experiments, the deflected beams were probed using EII mass spectrometry. Most of the experiments involved measuring the signal of the intact molecular ion along the axis of the argon or helium beam as a function of the voltage on

the deflector. Hence Stark deflection was demonstrated by removal of molecules from the beam axis. The greatest *Stark removal* (60%) was achieved for nitromethane in argon and hence this was chosen as the test beam for experiments aiming to observe the deflected molecules using the moveable skimmer system (see section 3.3). Stark deflection of up 1 mm was observed in the high-field seeking direction. However, it was not possible to observe the full profile of the deflected beam because the majority of the molecules that had been removed from the beam axis were *lost*. This loss limited the experimental capabilities for target selection and the comparisons that we could draw with calculated Stark curves (described in section 7.2). Therefore, a key aim of my PhD work was to measure the profile of a Stark-deflected CW beam with full recovery of the deflected molecules.

7.2 Calculated Stark Curves

7.2.1 Calculation method

The CMIStark [Chang et al. 2014] package was used by my colleague Andre Rebelo to simulate the Stark effect on the asymmetric top molecules studied experimentally in this chapter. This package was developed by the Controlled Molecule Imaging group (CMI – Küpper and co-workers) at the Centre for Free Electron Laser Science (CFEL), Hamburg. It has been applied previously to calculate the adiabatic energies of the low rotational states of asymmetric top molecules such as benzonitrile [Wohlfart et al. 2008] as a function of the external electric field strength (*Stark curves*). The calculations are based on the numerical diagonalization of analytically obtained Hamiltonian matrices in the perturbing case of the external electric field. The reader is referred Chang et al.

[2014] for a detailed description of the method.

Table 7.1: Summary of the input parameters for the present CMIStark calculations of Stark curves.

Molecule	**Rotational constants (GHz)**	**Reference**	**Dipole moment components (Debye)**	**Reference**
Nitromethane	A = 12.26 B = 10.54 C = 5.87	Schwettmann et al. (2005)	μ_x = -3.46 μ_y = 0 μ_z = 0	Schwettmann et al. (2005)
3-AP cis	A = 3.73 B = 1.82 C = 1.23	Filsinger et al. (2008 B)	μ_x = 1.77 μ_y = 1.52 μ_z = 0	Filsinger et al. (2008 B)
3-AP trans	A = 3.73 B = 1.82 C = 1.23	Filsinger et al. (2008 B)	μ_x = 0.56 μ_y = 0.54 μ_z = 0	Filsinger et al. (2008 B)
Thymine	A = 3.17 B =1.39 C = 0.97	Present work: MP2/cc-pVDZ//MP2/cc-pVTZ	μ_x = 0.99 μ_y = -4.71 μ_z = 0	Present work: MP2/cc-pVDZ//MP2/cc-pVTZ
Uracil	A = 3.88 B = 2.02 C = 1.33	Vaquero et al. (2007)	μ_x = -1.41 μ_y = 4.77 μ_z = 0	Present work: MP2/cc-pVDZ//MP2/cc-pVTZ

The five molecular structures considered here are all asymmetric tops (rotational constants A ≠ B ≠ C). The essential input parameters for CMIStark are the rotational constants of the molecule along its principle axes A, B, and C. In addition, it is necessary to specify the components of the molecule's permanent dipole moment along the molecule-fixed axes x, y, and z, where z is the direction of the external electric field. The input data for the present calculations were either obtained from the literature (experimental values, when available) or calculated using an *ab initio* method in the Gaussian09 package [2009]. The Stark effect on nitromethane in low rotational states has previously been calculated by Schwettmann et al. [2005] with the assumption that

centrifugal distortion does not have a major effect. Considering their aromatic ring structures, 3-AP, thymine, and uracil can reasonably be assumed to be more rigid than nitromethane. Therefore, we assumed that all the molecules studied here could be treated as rigid rotors, i.e. rotation did not affect their structure significantly. Similarly, Küpper and co-workers did not include centrifugal distortion constants in their Stark curve calculations for the conformers of 3-AP (Filsinger et al. 2008A, Filsinger et al. 2009B).

7.2.2 Stark curves of nitromethane, 3-aminophenol, uracil, and thymine

The first molecule studied in this chapter is nitromethane, building on the previous experiments by Ryszka [2015]. As mentioned above, Schwettmann et al. [2005] carried out a theoretical study of the Stark shifts of the molecule and stated that it is suitable for Stark manipulation (they specifically discussed Stark slowing). Fig. 7.2 (right) shows Schwettmann et al.'s [2005] curves for *low* J and M=2 in the energy range -1.0 to 7.5 cm^{-1} (relative to J=0 with no external field) and in the field strength range 0 to 100 kV/cm. To test that we have applied CMIStark correctly, Andre Rebelo used the same rotational constants and dipole moments as Schwettmann et al. [2005] (see Table 7.1) to calculate Stark curves for the J=0-5, M=2 states. The calculation was performed for J up to 10 (although only the J=0-5, M=2 states are plotted) but repeating the calculation including J states up to 32 was found to make no discernible difference. Therefore, to enable time-efficient calculations using a standard desktop computer, all the calculations shown here were performed including J states up to 10 only. Fig. 7.2 shows that our calculations using CMIStark agree with Schwettmann et al.'s [2005] calculations (including up to J=12).

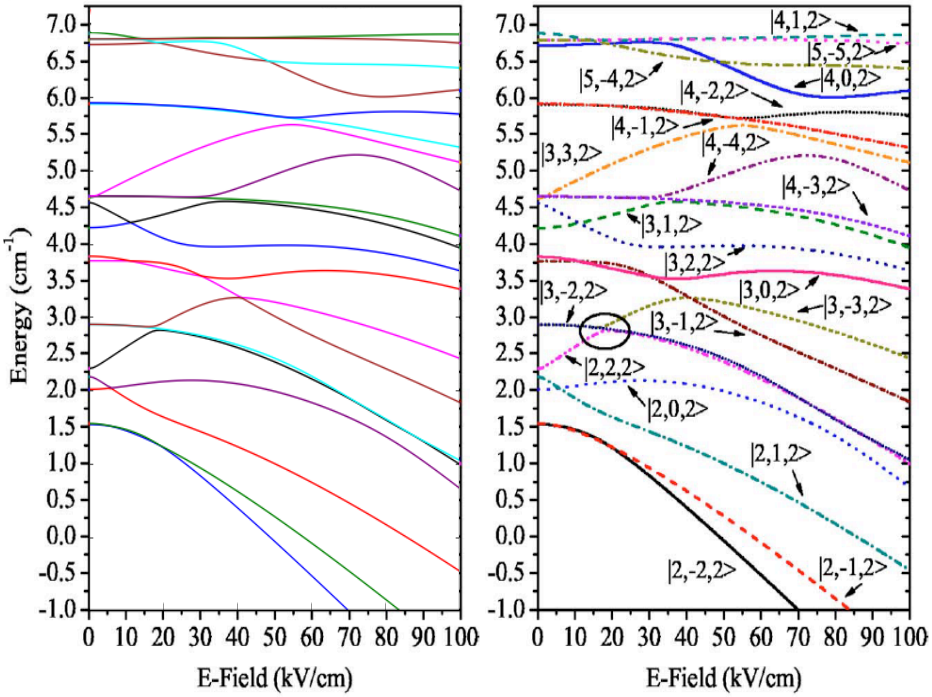

Figure 7.2: Comparison between the Stark curves generated using the CMIStark package (left) and Schwettmann et al.'s [2005] calculations (right). The states are labelled in the right-hand plot according to Schwettmann et al.'s [2005] nomenclature |J,τ,M>, where τ is a pseudo-quantum-number with integer values from −J to J for fixed J and M.

To compare the Stark effects of the different molecules studied here, Fig. 7.3 shows the curves for the J=0-1 states using the same axis scales (energy -6 to 2 cm^{-1} and field strength 0 – 100 kV/cm). The J=0 state is shown by a dashed line. The first point to note is that the separation of the J=0 and J=1 states at 0 kV/cm is 5-10 times greater for nitromethane than for the 3-AP conformers, thymine, and uracil. Therefore nitromethane can be prepared in low J states at much higher rotational temperatures than the other four molecular structures. Secondly, as a first order approximation, the steepness of the Stark curves increases with the permanent dipole moment of the molecule (see Table 7.1). Thirdly, all of the curves have negative gradients (albeit very weak ones for trans-3AP) above certain critical electric field strengths. Hence, all the

states shown are high field seekers (HFS) above this critical field strength. Three different voltages have been applied to the Stark deflector rod in the present experiments: 4 kV (nitromethane), 10 kV (3-AP and thymine), and 12 kV (uracil - the maximum voltage advised without risking significant discharges). These correspond to electric field ranges of 25-35, 60-90 and 72-108 kV/cm, respectively, from the bottom of the trough vertically upwards to the rod (calculated using Quickfield – see Fig. 3.9).

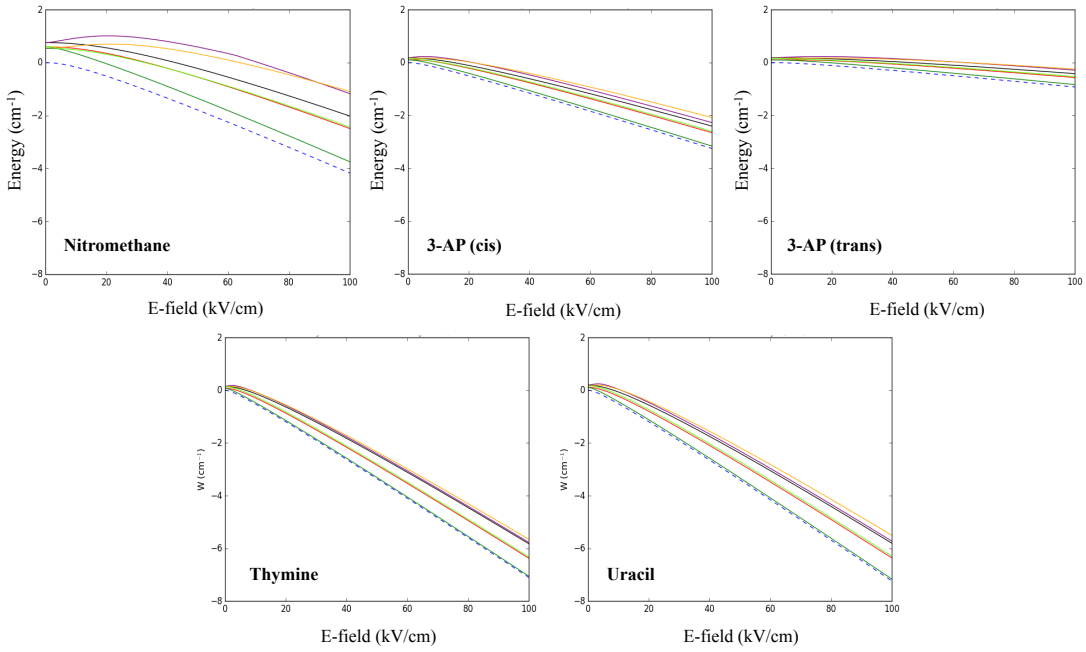

Figure 7.3: Stark curves for the J=0-1 states of nitromethane, cis 3-AP, trans-3AP, thymine, and uracil. The curves were calculated using the CMIStark package. In all the plots, the energy scale is -6 to 2 cm^{-1} and the E-field scale is 0-100 kV/cm.

Figs. 7.4-7.7 show the Stark curves for J=2-5 states of nitromethane, cis and trans 3-AP, thymine, and uracil. Whereas Fig. 7.3 demonstrates that 4 kV on the rod (25-35 kV/cm) is sufficient to eliminate low-field seeking (LFS) deflection of all the molecules in J=0-1 states, Figs. 7.4-7.7 show that various states are LF seekers or have negligible Stark effects even with the strongest fields achievable in our deflector. Conversely, even at

J=5 there are some states that exhibit negative gradients (i.e. HFS deflection) that are as steep as the J=0 state.

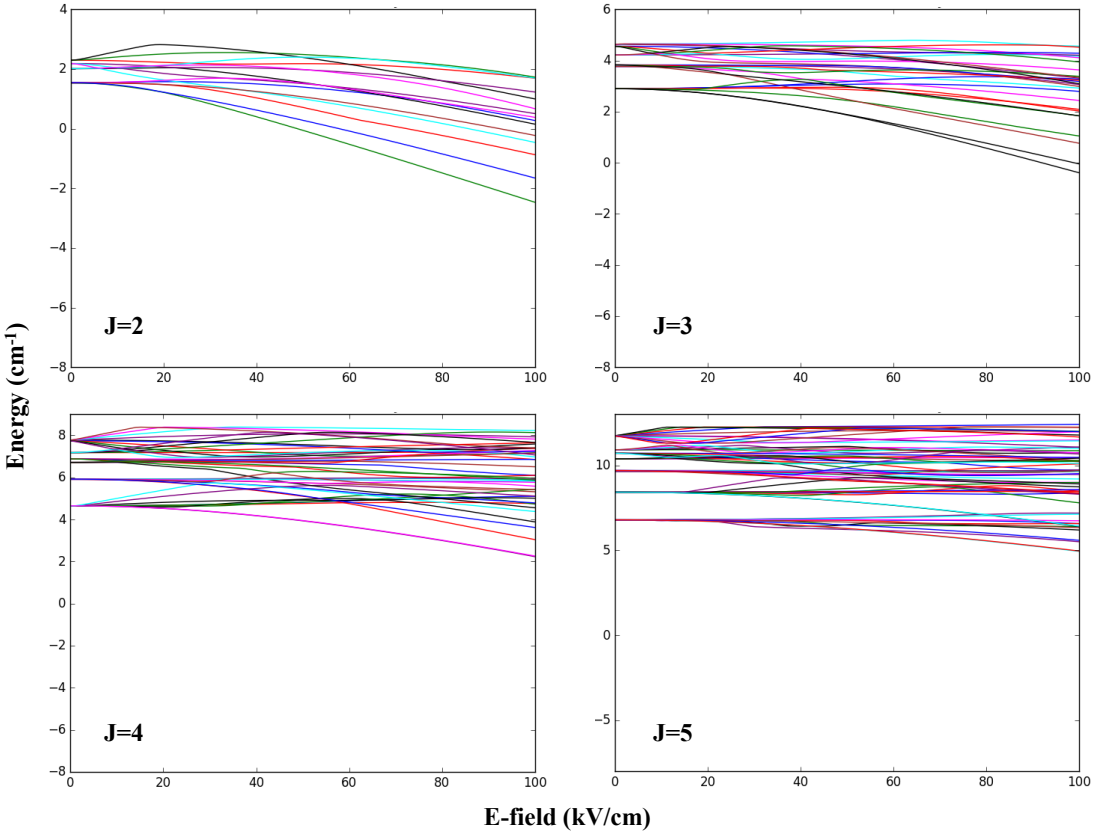

Figure 7.4: Stark curves for the J=2-5 states of nitromethane. Note that the maximum energy on the axis of each plot is different.

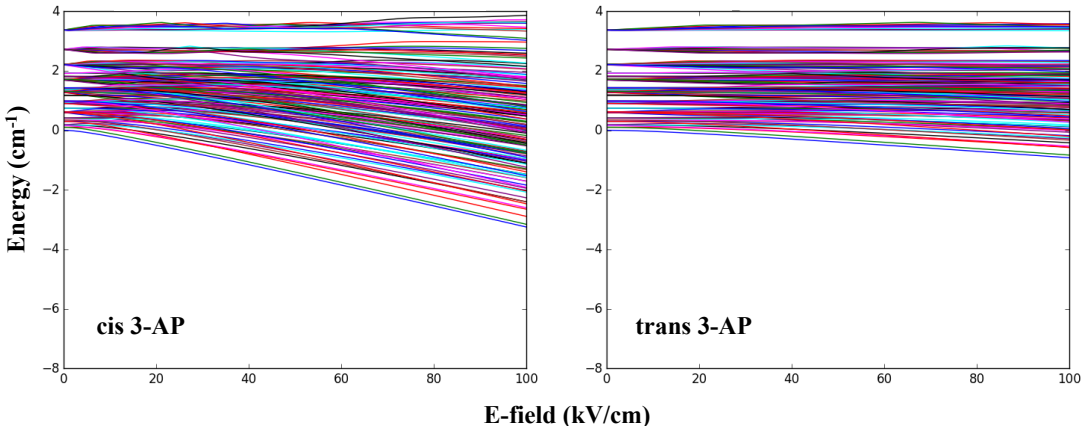

Figure 7.5: Stark curves for the J=2-5 states of cis and trans 3-AP.

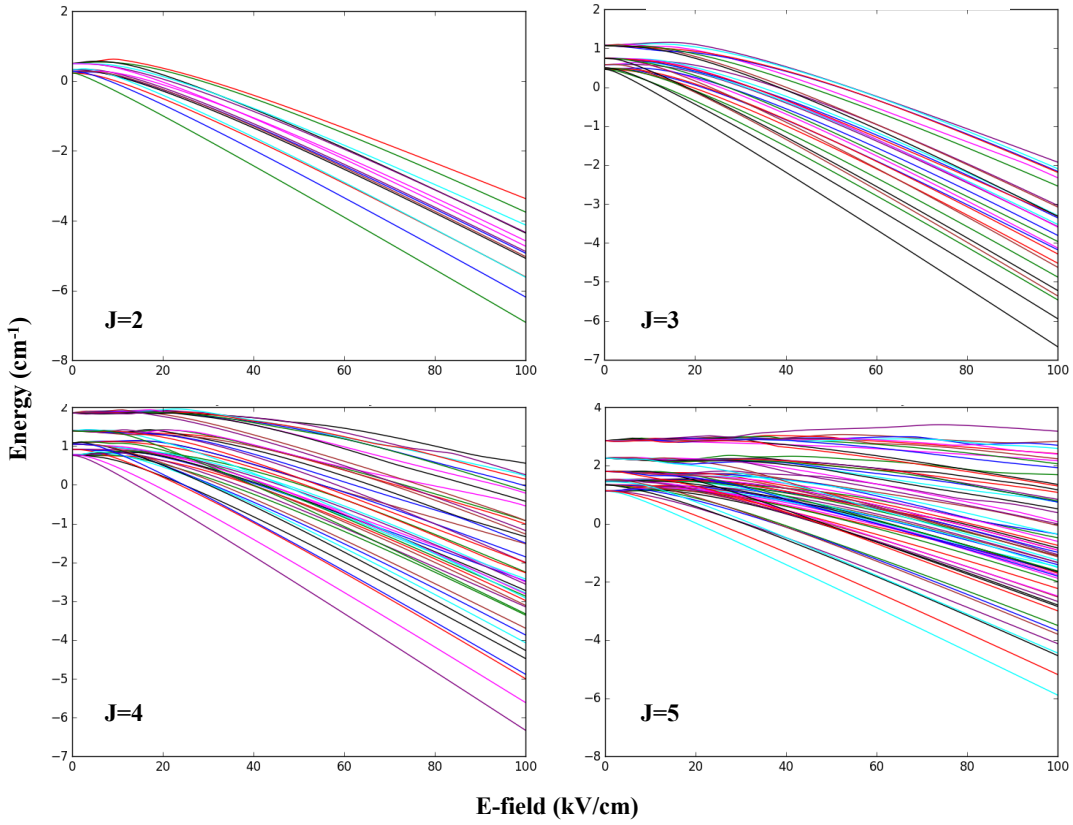

Figure 7.6: Stark curves for the J=2-5 states of thymine (note different energy ranges).

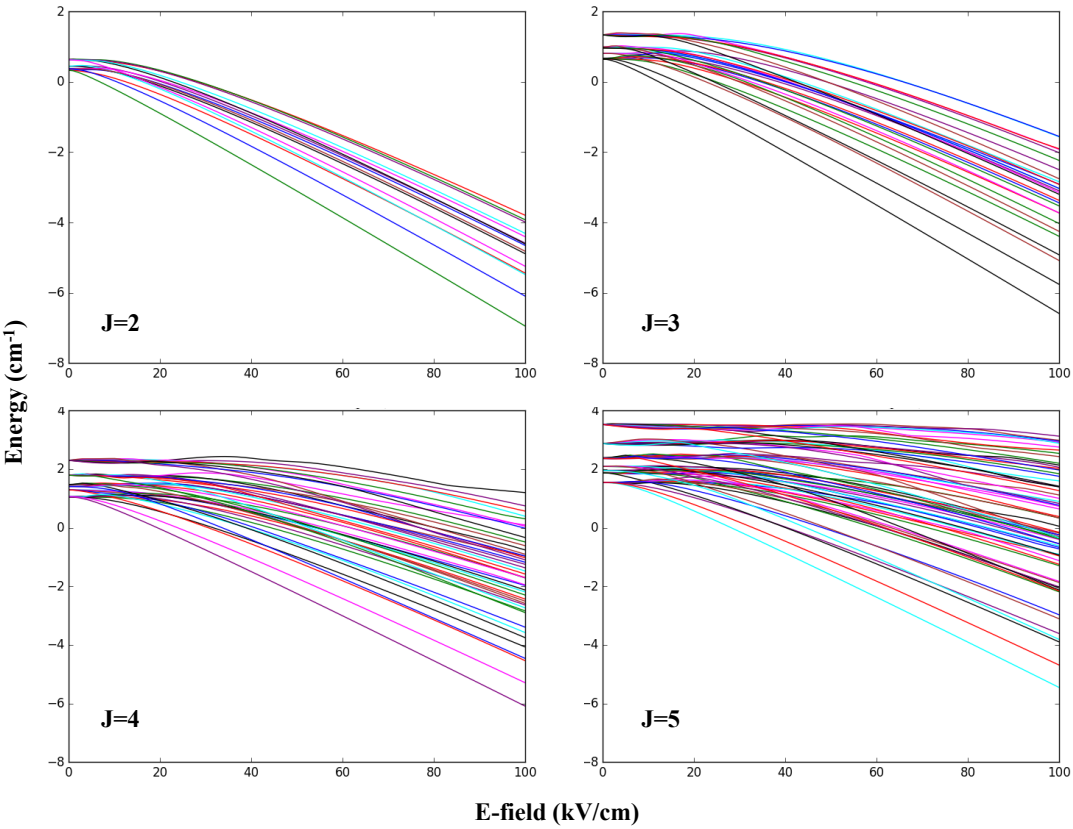

Figure 7.7: Stark curves for the J=2-5 states of uracil (note different energy ranges).

7.3 Results and Discussion

7.3.1 Stark deflection of nitromethane in a CW helium beam

Nitromethane has the largest permanent dipole moment / mass ratio (3.46 D / 71 a.m.u.) of the molecules studied here. Furthermore, its high vapour pressure at room temperature means it can be seeded in our molecular beams without heating the nozzle. As the temperature attainable in a supersonic expansion is directly proportional to the initial temperature of the gas (see section 2.5.2.2), this makes nitromethane a particularly good candidate for our optimization of CW beam deflection. The aim of the experiments in this section was to observe Stark-deflection with the maximum recovery possible of the deflected molecules.

The Stark curves in section 7.2 can be combined with our calculations of the electric field strength inside the deflector and the experimental dimensions to predict the deflection of different rotational states of nitromethane as a function of the voltage on the deflector rod. This is based on a simple calculation of the force that the molecule feels due to its Stark energy gradient in the deflector and the velocity of the molecule (assumed to be equal to the carrier gas velocity and hence calculable using Eq. 2.12 in Chapter 2 [Morse 1996]). In Stark removal and deflection experiments on nitromethane in argon and helium beams, Ryzka [2015] achieved the greatest effects (corresponding to the lowest rotational temperatures) using a refined circular aperture disk (the *sandwich* nozzle system described in section 3.3.2) and a carrier gas pressure of 0.5 bar (the lowest that we can stabilize in our experiments). In these conditions, J=0 nitromethane in an argon beam with 4 kV on the deflector rod will be deflected 21 mm

in the HFS direction at the position of the moveable skimmer. This is far outside the range observable in our experiment (limited by the 1 cm entrance hole in the copper shield). By contrast, the equivalent deflection of J=0 nitromethane in a helium beam will be 2.2 mm. Such a deflection is readily observable using the OU experiment.

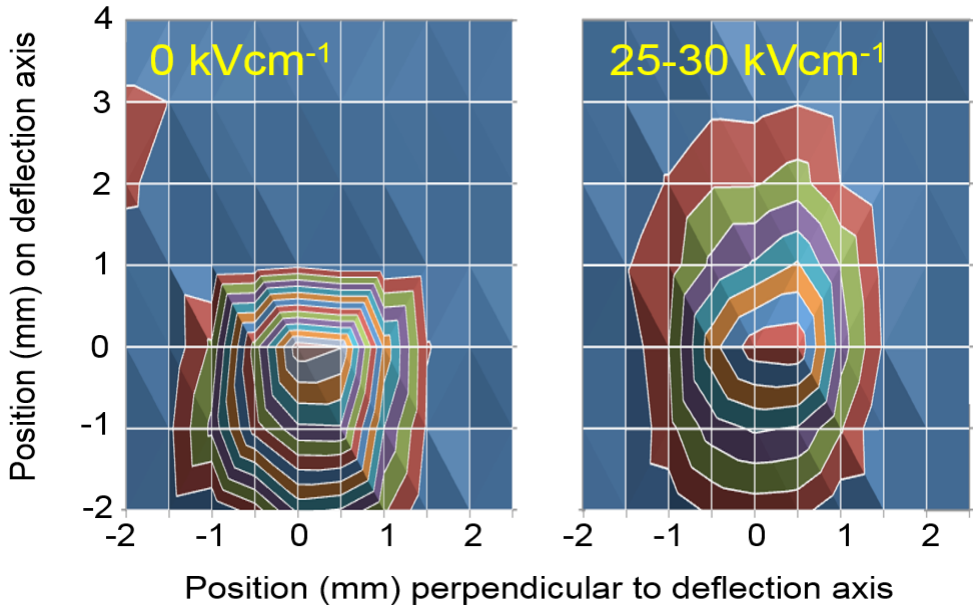

Figure 7.8: EII (200 eV) profiles of nitromethane in a helium beam (nozzle and sample at room temperature, nozzle diameter 30 μm, helium pressure 0.5 bar) with and without a Stark deflecting field. Deflection of 2 mm (+ve deflection axis = HFS) and (94±5)% recovery of deflected molecules was achieved with 4 kV on the Stark deflection rod (Ɛ = 25-30 kV/cm).

Fig. 7.8 shows how the nitromethane$^+$ signal obtained in electron impact ionization experiments in a helium beam varied as a function of the moveable skimmer position with and without a deflecting field. The experiments were carried out using a 30 μm diameter aperture disk in the *sandwich* nozzle and with 4000 ls^{-1} pumping on the expansion chamber (double the pumping speed in Ryszka's experiments). The moveable skimmer has diameter 1 mm and the approximate diameter of the ionizing electron beam is 10 mm. The left-hand plot shows the undeflected beam profile. As expected for a well-aligned beam, the profile is approximately symmetrical. The measured profile is ~3 mm in diameter, corresponding to a molecular beam diameter of

~2 mm (considering the diameter of the moveable skimmer). This is consistent with the diameter (1 mm) of the skimmer in front of the deflector and its position with respect to the nozzle and the moveable skimmer.

High field seeking (HFS) deflection corresponds to an extension of the measured beam profile towards the positive values of "position on the deflection axis". This is clearly visible in the Fig. 7.8, with a maximum HFS deflection of ~2 mm (comparing the upper edge of the undeflected profile with that of the deflected profile). This maximum deflection is consistent with the steepest Stark curves of the J=0-5 states of nitromethane (Figs. 7.3 and 7.4). Reassuringly, no deflection is observed perpendicular to the *deflection axis*. However, the most important result in Fig. 7.8 is that the total ion signal in the deflected measurement is only 6% lower than in the undeflected measurement, with an uncertainty of ±5% based on the count statistics and the background subtraction.

The high recovery rate of the deflected molecules means that the absence of any evidence for LFS deflection cannot be attributed to experimental limitations. Fig. 7.4 shows that LFS deflection should occur for a large proportion of the J=4 states in an external field of 25-30 kV/cm. Therefore, we can be confident that the nitromethane molecule in the present experiments were predominantly in J states <4. Fig. 7.4 also shows that the position of maximum nitromethane$^+$ signal did not change due to the deflecting field so most of the molecules were in rotational states that did not exhibit significant Stark effects at 25-30 kV/cm. Therefore, we conclude that the nitromethane molecules were mainly in J=2 and J=3 states. This provides our first measure to date of the rotational cooling that we can achieve using the CW supersonic expansion system at

the OU.

7.3.2 *Stark removal* of 3-aminophenol, thymine, and uracil in CW argon and krypton beams

7.3.2.1 3-aminophenol

3-AP was chosen as a target molecule for the present experiments because its aromatic structure and mass (109 a.m.u.) are comparable with a nucleobase. However, it has a much higher vapour pressure at any given temperature than a nucleobase and hence the nozzle only requires heating to 110-120 °C to seed a suitable quantity of molecules into our carrier gas expansions. Furthermore, our experiments in Chapter 6 show that it can be multi-photon ionized using the OU ns laser system with high efficiency. MPI is particularly convenient for our experiments characterising Stark deflection because it produces better signal-to-noise ratios and mass resolution than EII. The method to move the focused laser spot across the target molecular beam in the direction of the deflection axis (±X) is described in Chapter 3. Finally, we have chosen to study 3-AP because if we can achieve significant deflection it should be possible to separate the cis and trans conformers, as achieved by Küpper, Meijer and co-workers in pulsed helium beams [Filsinger et al. 2009A].

Fig. 7.9 compares MPI measurements of 3AP at 0 kV and 10 kV with the focused laser positioned in the centre of the undeflected beam. The experiments were performed using the same nozzle assembly as the nitromethane measurements and with three different carrier gasses: helium, argon, and krypton. The Stark removal achieved in helium was just 18±5%. Considering the Stark curves in Fig. 7.5, the small effect of the

Stark deflection voltage on 3-AP in the helium beam result suggests that a large proportion of the molecules were in rotational states >5. This is entirely consistent with our experiments on nitromethane. The reduced energy spacing of the J states in 3-AP relative to nitromethane will the result in the population of higher J states in similar expansion conditions. Moreover, the gas temperature before the expansion was higher in the experiments on 3-AP than nitromethane. Therefore, we did not attempt further deflection experiments on 3-AP in CW helium beams.

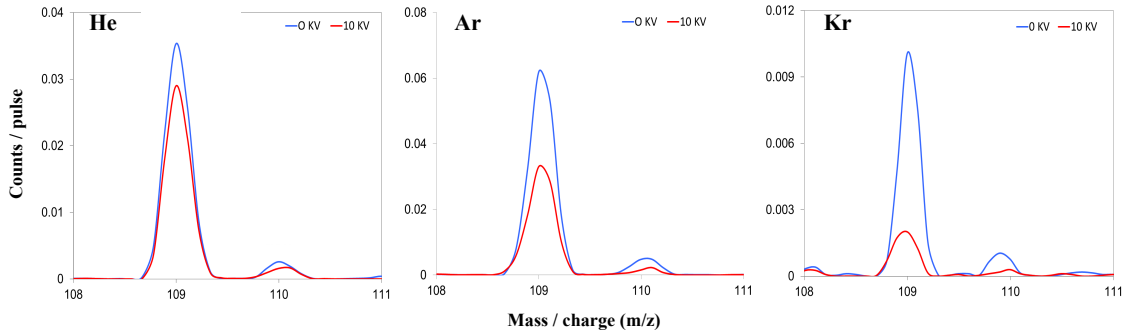

Figure 7.9: 220 nm (average pulse energy 70±15 μJ, maximum focus) MPI signals of 3-AP$^+$ with zero and 10 kV on the deflector rod. The molecules are seeded in helium, argon, and krypton beams with 0.5 bar in the nozzle (diameter 30 μm, temperature 117ºC). The laser was aligned with the centre of the undeflected beam. Hence, the measurements demonstrate *Stark removal* of 3-AP molecules from the undeflected beam axis.

In contrast with the helium result (44±5)% and (76±13)% Stark removal of 3-AP was observed in argon and krypton beams, respectively (Fig. 7.9). These results are particularly striking when we consider that half of the 3-AP molecules are trans conformers with weak Stark effects (Fig. 7.5). Therefore, we measured the 3-AP$^+$ signal from the argon beam at different positions of the focused laser beam to obtain a profile of the molecules deflected with 0 and 10 kV on the deflector rod. Fig. 7.10 shows that (89±3)% of the 3AP$^+$ signal in the 0 kV measurement was retrieved at 10 kV in the range accessible using the moveable laser spot (±3 mm from the centre of the

undeflected beam). However, the shape of the $3AP^+$ profile at 10 kV does not show a strong enhancement of HFS deflection (to positive laser spot positions) compared with LFS deflection. Considering the Stark curves at Ɛ = 60-90 kV/cm (corresponding to 10 kV on the rod) in Fig. 7.5, this suggests significant occupation of states with J>5. We are not able to assign different parts of the deflected profile explicitly to cis or trans 3-AP.

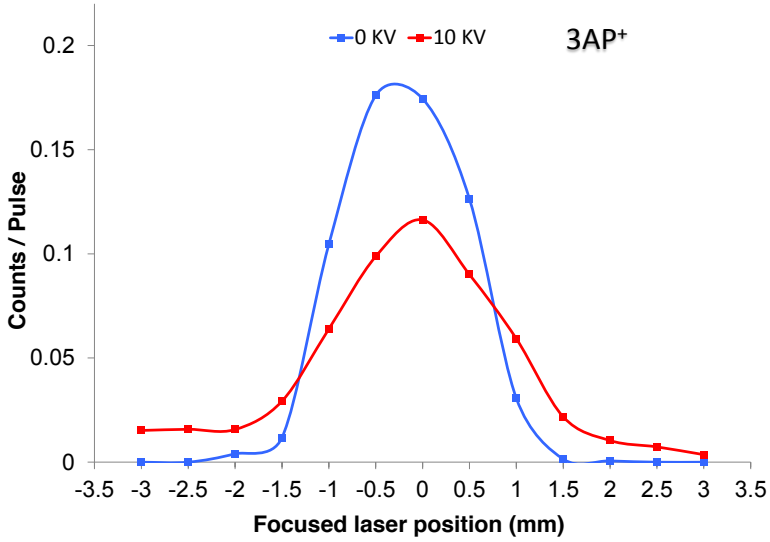

Figure 7.10: MPI (220 nm, average pulse energy 70±15 μJ, maximum focus) profiles of 3AP in an argon beam (nozzle and sample at 115°C, nozzle diameter 30 μm, argon pressure 0.5 bar) with and without a Stark deflecting field. 10 KV on the deflection rod (Ɛ = 60-90 kV/cm) resulted in a broadening of the beam with (89±3)% recovery of signal observed at 0 kV.

The O-ring in the *sandwich* system (see Chapter 3) cannot withstand the high nozzle temperatures required for experiments on nucleobases. Therefore, we carried out experiments on 3-AP to assess the deflection that can be achieved using the laser drilled nozzle (50 μm diameter). As shown in Fig. 7.11, the Stark removal was significantly reduced (23±3)% compared with the refined 30 μm aperture disk nozzle (44±5)% (the same result shown in Fig. 7.9.). Adapting the *sandwich* system to withstand higher

temperatures provides a route to achieve enhanced Stark manipulation of nucleobases in the future.

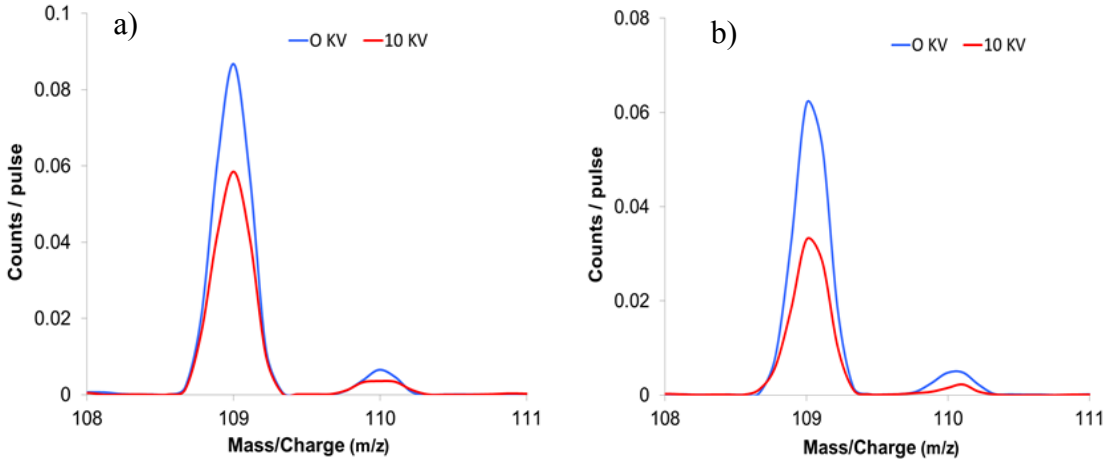

Figure 7.11: MPI comparison of *Stark removal* of 3-AP from an argon beam achieved using the laser drilled nozzle (50 µm diameter) and the relatively refined aperture disk nozzle (30 µm diameter). All other experimental conditions match Fig. 7.9.

7.3.2.2 Thymine and uracil

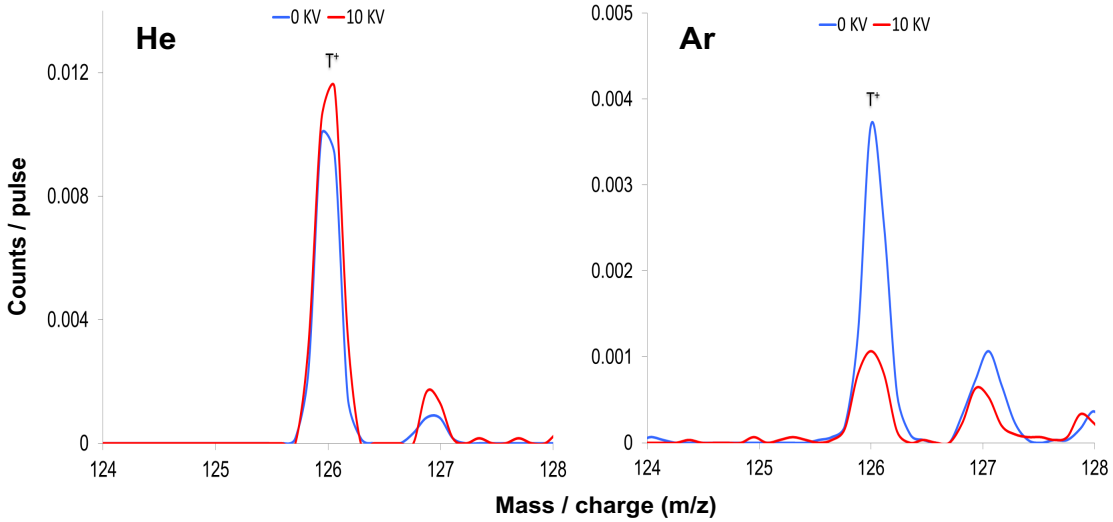

Figure 7.12: 220 nm (average pulse energy 250±20 µJ, maximum focus) MPI signals of thymine$^+$ with 0 and 10 kV on the deflector rod. The molecules were seeded in helium or argon beams with 2 bar in the nozzle (diameter 50 µm, temperature 235ºC). The laser was aligned with the centre of the undeflected beam.

Thymine was chosen as the first nucleobase to study using Stark deflection because its MPI signals using the OU ns laser system are higher than those from uracil (see section 5.4.1). Nonetheless, the thymine$^+$ (T^+) signals are typically an order of magnitude weaker than the 3-AP$^+$ signals presented in the section above. Fig. 7.12 compares the Stark removal of thymine from the centre of the helium and argon beams. There is no evidence for Stark removal in the helium beam measurement (the fact that T^+ signal in the 10 kV result is marginally higher than in the 0 kV result can be attributed to statistical uncertainties). By contrast, (65±17)% removal of the T^+ signal is observed from the centre of the argon beam. The removal is greater than that of 3-AP from Ar beams (for example, (23±3)% using the 50 μm nozzle in Fig. 7.11) despite the higher gas temperature. This result is consistent with the steeper Stark curves of the J=0-5 states of thymine compared with either conformer of 3-AP (see Figs. 7.4-7.6).

The OU Molecular Clusters group has previously observed that thymine forms clusters readily in CW argon expansions [Barc 2012]. As noted in Chapter 5, proton transfer from thymine$^+$ to thymine in a hydrogen-bonded dimer cation is exothermic [Liu et al. 2008] and protonated thymine (TH^+) signals are attributed to the dissociation of thymine dimer ions (or possibly larger thymine cluster ions) in the present MPI mass spectra. The argon beam result in Fig. 7.12 shows a relative increase in the m/z 127 signal (TH^+ and T^+ isotopomers) compared with the m/z 126 signal (T^+). To investigate Stark manipulation of thymine monomers and clusters further, Stark removal experiments were carried out on thymine seeded in argon beams with enhanced clustering conditions (Fig. 7.13). These conditions were achieved by raising the nozzle temperature to 257°C, increasing the density of thymine molecules in the expansion. The difference between the response of the thymine molecules and the thymine clusters

is striking: (40±9)% of the T^+ signal is removed in the 10 kV measurement, whereas the TH^+ signal is unaffected to within the statistical uncertainties. The absence of a clear Stark effect on the TH^+ signal can be explained by the fact that hydrogen-bonded thymine dimers are symmetric [Ding et al. 2013] with no permanent electric dipole moment.

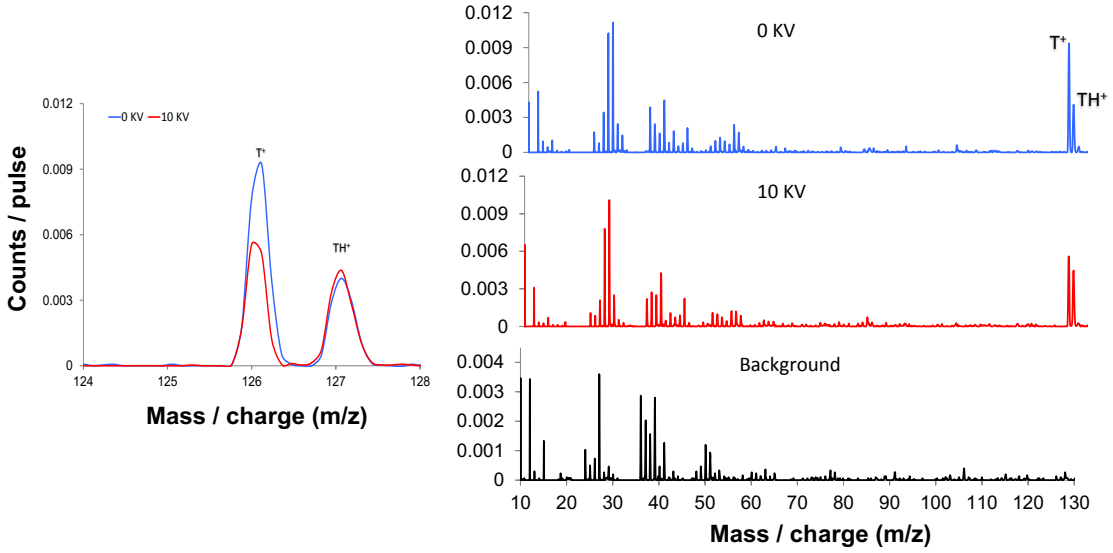

Figure 7.13: 220 nm (average pulse energy 250±20 μJ, maximum focus) MPI mass spectra of thymine with 0 and 10 kV on the deflector rod, as well as a background measurement recorded with the molecular beam blocked using a gate valve. The left-hand plot shows a detail of the thymine$^+$ and the protonated thymine signals. The molecules were seeded in an argon beam with 1 bar in the nozzle (diameter 50 μm, temperature 257ºC). The laser was aligned with the centre of the undeflected beam.

In principle, the measurements in Fig. 7.13 can enable specific fragment ions to be traced to multi-photon ionized monomers, clusters, or a combination of both. If a fragment ion of interest comes from the same neutral precursor as T^+ then the Stark removal of its signal should match that of T^+. T^+ is not expected to be produced efficiently from hydrogen-bonded cluster ions due to competition with barrierless proton transfer [Liu et al. 2008], but it can plausibly be produced from ionized stacked clusters. If the fragment originated from the same neutral source as TH^+ (necessarily

clusters) then its Stark removal will be negligible. If it comes from a combination of both ionized monomers and hydrogen-bonded clusters then its Stark removal will be in between that of T^+ and TH^+. However, the strong background signal at low masses prevents a detailed analysis of this kind in the Fig. 7.13 data.

Due to the relatively low MPI signals from uracil, we have performed fewer Stark manipulation experiments on this molecule. However, our particular interest in the m/z 84 ion ($C_3H_4N_2O^+$, investigated in Chapters 4 and 6) motivated us to attempt a Stark removal measurement to assess whether or not it can be produced from hydrogen-bonded clusters. Fig. 7.14 shows MPI mass spectra of uracil in an argon beam recorded with 0 and 12 kV on the deflector rod, as well as background measurement. Importantly, there is no significant background signal at m/z 84.

Fig. 7.15 shows the same results with the background subtracted, as well as showing the production of uracil$^+$ (U^+) and protonated uracil (UH^+) in detail. The UH+ signal is unaffected by the voltage on the deflector rod to within the experimental uncertainties. As with TH^+ in the discussion above, the absence of any discernible Stark effect on the UH+ signal is consistent with protonated uracil being traced to theoretically-predicted barrierless proton transfer in dimer cations [Zadorozhnaya and Krylov 2010] followed by the dissociation of the resultant complex. Hydrogen-bonded uracil dimers are not completely symmetric [Ding et al. 2013] but the Stark effect on these complexes can still be assumed to be very small.

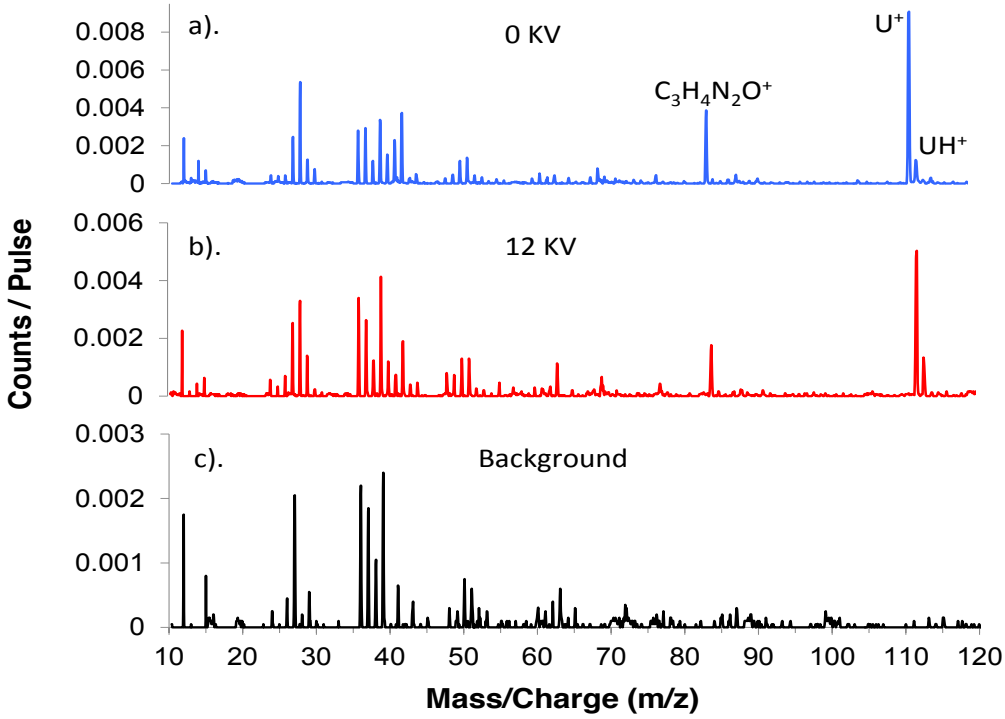

Figure 7.14: 220 nm (average pulse energy 250±20 µJ, maximum focus) MPI mass spectra of uracil with 0 and 12 kV on the deflector rod, as well as a background measurement recorded with the molecular beam blocked. The molecules were seeded in an argon beam with 0.5 bar in the nozzle (diameter 50 µm, temperature 257ºC). The laser was aligned with the centre of the undeflected beam.

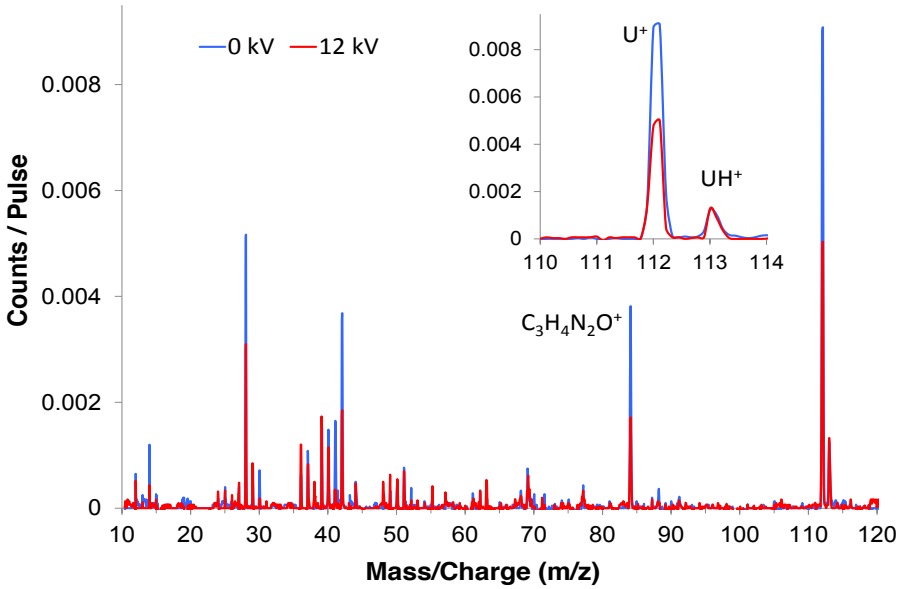

Figure 7.15: Background-subtracted MPI mass spectra of uracil recorded with 0 kV and 12 kV on the deflector rod. The details of the measurements are given in the Fig. 7.14 caption.

In contrast with the UH+ signal, the Stark removal of the U^+ signal in Fig. 7.15 is (46±7)%. The Stark removal of the m/z 84 ($C_3H_4N_2O^+$) signal is (51±11)%, matching the U^+ removal to within the experimental uncertainties. This demonstrates that most of the observed $C_3H_4N_2O^+$ ions came from the same neutral precursor(s) as the U^+ ions (from uracil monomers and possibly stacked clusters). However, the statistical uncertainties and the apparently quite low level of clustering in the beam (the ratio of m/z 113 counts over m/z 112 counts is (24±3)% at 12 kV) means that we cannot rule out a possible weak contribution of $C_3H_4N_2O^+$ ions from hydrogen-bonded clusters. In the future, we plan to repeat this measurement with higher levels of clustering in the target beam.

7.4 Summary

This chapter reports two main advances in the Stark manipulation of molecules in CW beams. Firstly, high-field-seeking deflection of 2 mm of nitromethane (CH_3NO_2) has been achieved in a helium beam with only (6±5)% loss of molecules and negligible low-field seeking deflection. This is the first time that the Molecular Clusters Group has simultaneously achieved significant Stark deflection of simultaneously with high recovery of the deflected molecules. Furthermore, the ability to view the full *profile* (the cross section) of the deflected beam enables us to draw useful comparisons with calculated Stark curves. The maximum observed deflection (2 mm) is consistent with the steepest calculated Stark curves. Any low-field-seeking deflection in the experiments must be negligible, indicating that most of the molecules were in J=2 and 3 states.

The second main advance in this chapter is the Stark manipulation of three relatively complex aromatic biomolecules (3-AP, thymine, and uracil) in CW argon and krypton beams. These beams have been probed using MPI-TOF mass spectrometry (all the previous experiments using the Stark deflector at the OU have been based on EII). The most effective experiments we can carry out using argon and krypton with the current experimental geometry are based on *Stark removal* of molecules from the centre of the undeflected beam. (65±17)% removal of thymine molecules was achieved from an argon beam and (76±13)% removal of 3-AP was achieved from a krypton beam. By contrast, the protonated nucleobase signals due to the ionization of hydrogen-bonded clusters were unaffected by the deflection voltage. This demonstrates for the first time that the relative populations of isolated and clustered nucleobases (uracil and thymine) can be modified using Stark deflection. Moreover, it offers a route to testing if a specific fragment ion originates from neutral isolated molecules, clusters, or a combination of both in mixed beams.

We have analysed $C_3H_4N_2O^+$ production from a beam containing isolated and clustered uracil with and without a deflecting field. The results show that any $C_3H_4N_2O^+$ production of the m/z 84 ion from multi-photon ionized hydrogen-bonded uracil clusters must be weak. This result appears to be consistent with the fact that the most stable uracil dimer configuration features hydrogen bonding on either side of the expected ring-opening position in electronically-excited uracil [Ding et al. 2015, Nachtigallová et al. 2011, Richter et al. 2014]. Local intermolecular bonding of this kind is expected to affect possible ring-opening, while competition with proton transfer in the excited hydrogen-bonded dimer [Zadorozhnaya and Krylov 2010] may also play a significant role.

7.5 Contributions by co-workers

I preformed the experiments in this chapter, working with PhD students Andre Rebelo and Tiago da Fonseca. Andre Rebelo generated the Stark Curves in CMIStark, working with Jean-Christophe Poully on the calculations for the rotational constants and dipole moments. I analysed and interpreted the experiments, working mainly with Sam Eden.

References:

- R. Antunes, D. Almeida, G. Martins, N. J. Mason, G. Garcia, M. J. P. Maneira, Y. Nunesa and P. Limaõ-Vieira, *Phys. Chem. Chem. Phys*., 2010, **12**, 12513-12519.
- B. Barc, Department of Physical Sciences, Hydrated clusters of nucleic acid bases in supersonic beams probed by multi-photon ionization (MPI) mass spectrometry, The Open University, Milton Keynes, United Kingdom, *PhD thesis*, 2013.
- B. Barc, M. Ryszka, J. Spurrell, M. Dampc, P. Limão-Vieira, R. Parajuli, N. J. Mason and S. Eden, *J. Chem. Phys.*, 2013, **139**, 244311.
- B. Barc, M. Ryszka, J.-C. Poully, E. Jabbour Al Maalouf, Z. el Otell, J. Tabet, R. Parajuli, P. J. M. van der Burgt, P. Limão-Vieira, P. Cahillane, M. Dampc, N. J. Mason and S. Eden**,** *Int. J. Mass. Spectrom*., 2014, **365-366**, 194-199.
- D. H. R. Barton, *J. Chem. Soc.,* 1953, 1027-1040.
- Y. P. Chang, K. Długołecki, J. Küpper, D. Rösch, D. Wild and S. Willitsch, *Science*, 2013, **342**, 98-101.
- Y.-P. Chang, F. Filsinger, B. G. Sartakov and J. Küpper, *Comp. Phys. Comm.*, 2014, **185**, 339-349.
- N. Ding, X. Chen, C.-M.L. Wu, H. Li, *Phys. Chem. Chem. Phys.*, 2013, **15**, 10767–10776.
- H. C. Dunathan, *Proceedings of the National Academy of Sciences*, 1966, **55**, 712-716.
- E. L. Eliel and S. H. Wilen, *Stereochemistry of organic compounds, John Wiley & Sons, New York,* 1994.
- I. I. Fabrikant, S. Caprasecca, G. A. Gallup and J. D. Gorfinkiel, *J. Chem. Phys*., 2012, **136**, 184301.
- J.B. Fenn, *Annu. Rev. Phys. Chem*., 1996, **47**, 1-41.
- F. Filsinger, U. Erlekam, G. von Helden, J. Kupper and G. Meijer, *PRL*, 2008**A**, **100**, 133003.
- F. Filsinger, K. Wohlfart, M. Schnell, J.-U. Grabowb and Jochen Küpper, *Phys. Chem. Chem. Phys*., 2008**B**, **10**, 666-673.
- F. Filsinger, G. Meijer, H. Stapelfeldt and H. N. Chapman, J. Küpper, *Phys. Chem. Chem. Phys*., 2011, **13**, 2076-2087.
- F. Filsinger, J. Küpper, G. Meijer, L. Holmegaard, J.H. Nielsen, I. Nevo, J.L. Hansen, and H. Stapelfeldt, J. Chem. Phys., 2009**A**, **131**, 064309.
- F. Filsinger, J. Küpper, G. Meijer, J. L. Hansen, J. Maurer, J. H. Nielsen, L. Holmegaard, and H. Stapelfeldt, *Angew. Chem. Int. Ed*., 2009**B**, **48**, 6900-6902.

- R. A. Gaussian 09, M. J. Frisch, G. W. Trucks, H. B. Schlegel, G. E. Scuseria, M. A. Robb, J. R. Cheeseman, G. Scalmani, V. Barone, B. Mennucci, G. A. Petersson, H. Nakatsuji, M. Caricato, X. Li, H. P. Hratchian, A. F. Izmaylov, J. Bloino, G. Zheng, J. L. Sonnenberg, M. Hada, M. Ehara, K. Toyota, R. Fukuda, J. Hasegawa, M. Ishida, T. Nakajima, Y. Honda, O. Kitao, H. Nakai, T. Vreven, J. A. Montgomery, Jr., J. E. Peralta, F. Ogliaro, M. Bearpark, J. J. Heyd, E. Brothers, K. N. Kudin, V. N. Staroverov, R. Kobayashi, J. Normand, K. Raghavachari, A. Rendell, J. C. Burant, S. S. Iyengar, J. Tomasi, M. Cossi, N. Rega, J. M. Millam, M. Klene, J. E. Knox, J. B. Cross, V. Bakken, C. Adamo, J. Jaramillo, R. Gomperts, R. E. Stratmann, O. Yazyev, A. J. Austin, R. Cammi, C. Pomelli, J. W. Ochterski, R. L. Martin, K. Morokuma, V. G. Zakrzewski, G. A. Voth, P. Salvador, J. J. Dannenberg, S. Dapprich, A. D. Daniels, O. Farkas, J. B. Foresman, J. V. Ortiz, J. Cioslowski and D. J. Fox, Gaussian, Inc., Wallingford CT, 2009.
- M. D Hanwell, D. E. Curtis, D. C Lonie, T. Vandermeersch, E. Zurek and G. R. Hutc hison, *Journal of Cheminformatics*, 2012, **4**:17.
- J. Jankunas and A. Osterwalder, *Annual Review of Physical Chemistry*, 2015, **66**, 241-262.
- T. Junglen, T. Rieger, S. A. Rangwala, Pinkse and G. Rempe, *Eur. Phys. J. D*, 2004, **31**, 365-73.
- I. Kulakowska. M. Geller. B. Lesyng and K. L. Wierzchowski, *Biochimica et Biophysica Acta,* 1974, **361**, 119-130.
- G. W. Lemire, J. B. Simeonsson and R. C. Sausa, *Anal. Chem.*, 1993, **65**, 529-533,
- M. Liu, T. Li, F. S. Amegayibor, D. S. Cardoso, Y. Fu and J. K. Lee, *J. Org. Chem.*, 2008, **73**, 9283–9291.
- R. Moro, R. Rabinovitch, C. Xia, V. V. Kresin, *Phys. ReV. Lett.,* 2006, **97**, 123401.
- M. D. Morse. *Methods of Experimental Physics: Atomic, Molecular, and Optical Physics, Academic Press Inc.*, **Vol. II***,* 1996.
- M. Motsch, M. Schenk, L. D. van Buuren, M. Zeppenfeld, P. W. H. Pinkse and G. Rempe, *Phys. Rev. A*, 2007, **76**, 061402.
- M. Motsch, L. D. van Buuren, C. Sommer, M. Zeppenfeld, G. Rempe G and P. W. H. Pinkse, *Phys. Rev. A*, 2009, **79**, 013405.
- E. Nir, M. Muller, L.I. Grace and M.S. de Vries, *Chem. Phy. Lett.*, 2002, **355**, 59-64.
- NIST Chemistry WebBook, http://webbook.nist.gov; accessed 2017.
- G. Quéméner and P. S. Julienne, *Chem. Rev.*, 2012, **112**, 4949-5011.
- S. A. Rangwala, T. Junglen, T. Rieger, P. W. H. Pinkse and G. Rempe, *Phys. Rev. A*, 2003, **67**, 043406.

- S. Riahi, S. Eynollahi ,M. R. Ganjali and P. Norouzi, *Int. J. Electrochem. Sci*., 2010, **5,** 355-366.
- T. Rieger, T. Junglen, S. A. Rangwala, P. W. H. Pinkse and G. Rempe, *Phys. Rev. Lett.*, 2005, **95**, 173002.
- T. Rieger, T. Junglen, S. A. Rangwala, G. Rempe, P. W. H. Pinkse and J. Bulthuis, *Phys. Rev. A*, 2006, **73**, 061402.
- T. R. Rizzo, Y. D. Park, L. Peteanu and D. H. Levy, *J. Chem. Phys*., 1985, **83**, 4819-482.
- M. Ryszka, R. Pandey, C. Rizk, J. Tabet, B. Barc, M. Dampc, N. J. Mason and S. Eden, *Int. J. Mass Spectrom.*, 2016, **396**, 48-54.
- M. Ryszka, Radiation induced processes in biomolecules and clusters in controlled beams, Department of Physical Sciences, The Open University, Milton Keynes, United Kingdom, *PhD thesis*, 2015.
- A. Schwettmann, J. Franklin, K. R. Overstreet and J. P. Shaffer., *J. Chem. Phys*., 2005, **123**, 194305.
- G. Scoles, *Atomic and Molecular Beam Methods, Vol. 1 & 2, Oxford University Press, New York,* 1988 & 1992.
- C. Sommer, L. D. van Buuren, M. Motsch, S. Pohle, J. Bayerl and P. W. H. Pinkse Faraday Discuss., 2009, **142**, 203–20.
- R. D. Suenram and F. J. Lovas, *J. Am. Chem. Soc.*, 1980, **102**, 7180-7184.
- S. Trippel, Y.P. Chang, S. Stern, T. Mullins, L. Holmegaard, and J. Küpper, *Phys. Rev. A*, 2012, **86**,033202.
- L. D. van Buuren, C. Sommer, M. Motsch, S. Pohle, M. Schenk, J. Bayerl, P. W. H. Pinkse and G. Rempe, Phys. Rev. Lett., 2009, **102**, 033001.
- S. Y. T. van de Meerakker, H. L. Bethlem, N. Vanhaecke and G. Meijer, *Chem. Rev*., 2012, **112**, 4828-4878.
- V. Vaquero, M. Eugenia Sanz, J. C. López and J. L. Alonso, *J. Phys. Chem. A*, 2007, **111**, 3443-3445.
- S. N. Vogels, J. Onvlee, S. Chefdeville, A. van der Avoird, G. C. Groenenboom and S. Y. T. van de Meerakker, *Science*, 2015, **350**, 787-790.
- S. Willitsch, *Int. Rev. Phys. Chem*., 2012, **31**, 175-199.
- S. Willitsch, M. T. Bell, A. D. Gingell, S. R. Procter and T. P. Softley, *Phys. Rev. Lett.*, 2008, **100**, 043203.
- K. Wohlfart, M. Schnell, J.-U. Grabow and J. Küpper. *J. Mol. Spectrosc*., 2008, **247**, 119-121.
- A. A. Zadorozhnaya and A. I. Krylov, *J. Chem. Theory Comput*., 2010, **6**, 705-717.

CHAPTER 8

Conclusions & Outlook

This thesis applies multi-photon ionization (MPI) using ns-timescale laser pulses to investigate UV-induced processes in biomolecules and hydrated clusters that represent model systems for biological environments. Furthermore, it reports advances in applying Stark deflection to control and manipulate CW beams of molecules and clusters for irradiation experiments. Section 8.1 describes the five most important contributions of this thesis. Section 8.2 provides a more exhaustive summary of the conclusions from the experiments and analysis work presented in each chapter. Finally, section 8.3 discusses the future experiments and development work that I recommend to build on the progress presented in this thesis and strengthen the proposed physical and chemical interpretations.

8.1 Highlights

High-resolution mass spectra of multi-photon ionized uracil from a supersonic expansion source combined with data from measurements on deuterated uracil have enabled several fragment ions to be identified unambiguously that were previously

debated in the literature. In particular, the results demonstrate that the m/z 84 ion is due to CO loss from ionized uracil instead of CNH_2 loss. This MPI channel has previously been demonstrated to depend on a critical process in a neutral excited state [Barc et al. 2013]. The calculated structures of three ring-opening CIs between the molecule's lowest-lying singlet states all leave a CO group at one end of the resultant *open* structure that is expected to be vulnerable to abstraction upon ionization [Nachtigallova et al. 2011, Richter et al. 2014]. Therefore, our new result is consistent with the hypothesis that the m/z 84 ion from multi-photon ionized uracil is a marker for a ring-opening CI (or possibly several similar CIs) between neutral excited states.

Previous ultrafast time-resolved pump-probe experiments on uracil from a laser thermal desorption (LTD) source at Heriot Watt (HW) University had not revealed m/z 84 ions [Ryszka 2015]. Therefore, we have built a new LTD source at the Open University to test if the m/z 84 channel in MPI experiments using our ns-timescale laser system is significantly dependent on the method of bringing uracil into the gas phase (LTD vs seeding in supersonic expansion). It is not. This suggests that the critical neutral-excited-state process responsible for MPI production of m/z 84 ions from uracil takes place predominantly on a longer timescale than the HW experiments (>0.3 ns after excitation). A so-far unidentified CI between triplet states appears to be a plausible candidate.

Photon energy thresholds have been observed for metastable HNCO loss from multi-photon ionized uracil and thymine. We argue that these can be attributed to accessing the molecules' S_1 states with vibrational energy matching the threshold for HNCO loss

from the radical cation and can provide a new method to deduce the S_1 adiabatic energies.

Metastable H_2O loss from $T^+(H_2O)_n$ was observed in multi-photon ionization experiments for n≥3. *Ab initio* binding energy calculations by our collaborators are consistent with the general trend of increasing metastable H_2O loss with n in the experimental data but do not explain the step between n=2 and 4. This suggests that caution is required when attempting to associate the strength of metastable dissociation signals with cluster ion binding energies. We hypothesize that the number of available pathways for the loss of a molecule also plays a role in determining the relative probability of metastable dissociation.

The OU experiment to gain control over CW beams of molecules and clusters using Stark deflection has been advanced significantly. Measuring MPI and EII (electron impaction ionization) signals from nucleobases in supersonic argon beams as a function of the deflection voltage has demonstrated *Stark removal* of up to 65% of the isolated molecules from the centre of the undeflected beam. By contrast, the protonated nucleobase signals traced to the ionization of clusters were unaffected by the deflection voltage. To our knowledge, this is the first time that DNA/RNA constituents have been manipulated using the Stark effect. The only molecule of similar complexity that has been deflected previously in CW beams was benzonitrile (also by the OU Molecular Clusters Group [Ryszka 2015]).

8.2 Specific conclusions from Chapters 3-7

8.2.1 Experimental developments (Chapter 3)

Chapter 3 primarily describes apparatus and methods that were already established in the Molecular Clusters Group before I started my PhD. The main innovation of the *Compact MPI/EII* experiment in this thesis is the development of a method to measure the kinetic energy of fragment ions produced by multi-photon ionization. In the absence of metastable dissociation, the *cut-off* reflection voltage ($V_R(0)$) for an ion signal in the mass spectrometer defines the ion's distance from the extraction grid. Therefore, measuring $V_R(0)$ as a function of time after ionization can determine the ion's velocity. Preliminary tests on nitromethane have provided plausible maximum velocities of NO^+ but further tests and optimization are required to exploit the method fully. While numerous other experimental techniques are already available to measure fragment ion kinetic energies, this method will be a useful addition to the capability of the *Compact MPI/EII* system at the OU and has the advantage of simultaneously providing KE information and high mass resolution.

Further developments of experimental and analytical methods in this PhD include extending our study metastable fragmentation of excited ions and cluster ions by producing *maps* of ion signal against time-of-flight and reflection voltage. To our knowledge, this is a new way to present metastable dissociation data visually. It has potential to be particularly useful for recognizing weak metastable dissociation channels. Furthermore, a moveable lens system has been built and characterized to enable MPI experiments on Stark-deflected molecules. The previous Stark deflection

experiments in the group were limited to electron impact ionization [Ryszka 2015].

8.2.2 High-resolution mass spectrometry of uracil and comparisons with deuterated uracil results (Chapter 4)

MPI-TOF experiments have been performed on uracil with the highest mass resolution obtained to date using the OU *Compact MPI/EII* system: m/Δm ~1200 for the largest fragment ions from uracil. This was not sufficient to completely separate peaks of different fragment ions with the same nominal m/z. However, for peaks with good statistics and a symmetric shape it was possible to determine the peak maximum with sufficiently high precision to identify the main ion that contributed to the signal. Hence, combined with information from experiments on fully deuterated uracil, the high-resolution measurements enabled various fragment ions to be identified unambiguously for the first time. The standout result was the identification of the m/z 84 ion, as highlighted in section 8.1. Further prominent fragment ion signals from uracil that had been the subject of debate in the literature [Jochims et al. 2005] have been identified as being dominantly due to CH_2^+ (m/z 14), CH_2N^+ (m/z 28), CH_3N^+ (m/z 29), and $C_2H_2O^+$ (m/z 42).

8.2.3 Metastable dissociation processes in nucleobase radical cations and their hydrated clusters (Chapter 5)

Multi-photon ionization experiments have been carried out on thymine, uracil and thymine-water clusters in the gas phase. As highlighted in section 8.1, threshold behaviour in the metastable dissociation of multi-photon ionized thymine and uracil has been observed for the first time. We propose that these thresholds are due to the

molecules being ionized via neutral electronic excited states with vibrational energy matching the threshold for HNCO loss from the radical cation. Combined with existing photoionization energies, this enables us to deduce the adiabatic energies of these electronic excited states as 3.65±0.07 eV for thymine and 3.72±0.07 eV for uracil. These are close to the origins of the lowest-lying vibronic bands observed in previous LIF spectra and agree with the most recent calculated adiabatic energies of the diketo S_1 states. 2-photon ionization via the S_1 state is a very plausible MPI pathway for uracil and thymine using our ns laser system. The credibility of this interpretation suggests that the study of metastable fragment ion production in MPI experiments has considerable potential to provide insights into the dynamics of molecules in high vibronic states.

Our observation of H_2O loss from hydrated thymine radical cations is the second result of this kind in the literature. We have compared our measurement, as well as the previous MPI measurement by Kim et al. [2002], with the most extensive set of optimized $T^+(H_2O)_n$ geometries to date (up to n=4). The calculated binding energies for single water molecule removal fall with n, broadly consistent with increasing metastable dissociation in the MPI experiments. However, as noted in the highlights above, the calculations do not explain the step in our experimental data between n=2 and 4. Furthermore, the calculations do not support a closed hydration shell around thymine$^+$ that could explain the step between n=4 and 5 in Kim et al.'s [2002] data. Indeed, we consider that the relative stability of different cluster ion configurations is only one of the factors that can determine the relative intensity of metastable dissociation signals in mass spectra. Finally, it is noteworthy that the lowest energy $T^+(H_2O)_n$ conformers differ significantly from their neutral counterparts for n≥2, with charge-dipole

interactions playing important roles.

8.2.4 Laser thermal desorption mass spectrometry (Chapter 6)

We have designed, built, and optimized a new *laser thermal desorption* (LTD) system at the OU to study MPI of isolated biomolecules. This was tested using 3-aminophenol (3-AP, C_6H_7NO), providing the first MPI mass spectrum of the molecule and revealing metastable dissociation of a fragment ion ($C_5H_6N^+$* or $C_5H_4O^+$*) for the first time in our laboratory. As highlighted in section 8.1, we performed MPI experiments on uracil from the LTD source to compare with our earlier experiments on uracil seeded in supersonic beam. The m/z 84 channel was clearly visible in both sets of experiments, showing that this MPI fragment ion is not significantly dependent on the method of bringing uracil into the gas phase. LTD has previously been demonstrated to be a more *gentle* method of bringing molecules into the gas phase than heating in a conventional oven or nozzle [De Camillis et al. 2015] with respect to thermal decomposition. Therefore, the new LTD source will enable us probe more complex and fragile biomolecules than we can study using our supersonic expansion source.

8.2.5 Stark deflection of continuous molecular beams (Chapter 7)

Perhaps the most striking progress achieved in this PhD is in manipulating CW beams of molecules and clusters using the Stark effect. The key motivation for this work is to select specific structural configurations of neutral biomolecules or clusters from mixed supersonic beams for irradiation experiments, notably probing dissociative electron attachment (DEA) processes. *Stark selection* of this kind will make it possible to trace

specific irradiation products to specific precursors, as required for the clearest mechanistic interpretations and comparisons with calculations. This has been achieved previously using pulsed supersonic beams [Filsinger et al. 2009, Trippel et al. 2012] but such targets are not well suited to experiments using low radiation beam intensities and / or probing processes with low cross sections. This thesis reports the following achievements in the Stark deflection of CW beams.

High-field seeking deflection of 2 mm of nitromethane (CH_3NO_2) has been achieved in a helium beam with only 6% loss of molecules and negligible low-field seeking deflection. Nitromethane deflection has been observed previously by the Molecular Clusters Group before my PhD [Ryszka 2015] but never with high recovery of the deflected molecules. This is critically important both to achieve the best-possible selection and to make comparisons with calculated Stark curves. Comparing the beam profile with the calculations indicates that a large proportion of the molecules were in J=2-3 states and relatively few were in higher J states where low-field seeking deflection would be significant.

The level of rotational cooling achieved for nitromethane in a helium expansion can be useful in various conceivable experiments (for example, separating monomers from clusters in mixed beams). However, it is not expected to enable significant deflection of nucleobases and related biological building blocks due to the relatively small separations of their J states. Accordingly, our experiments on 3-AP and thymine in a helium beam did not demonstrated significant deflection. To achieve increased rotational cooling, we seeded thymine, uracil, and 3-AP in argon expansions. As

highlighted in section 8.1, MPI experiments as a function of the voltage on the deflector demonstrated *Stark removal* of up to 65% of the isolated molecules from the beam axis.

Even greater Stark removal was achieved for 3-AP in a krypton expansion (76% removal of 3-AP compared with 44% removal in an equivalent argon expansion). Unfortunately, it was not possible to achieve good recovery of deflected molecules when they were seeded in argon expansions. This is because the geometry of the deflector (the length and separation of the electrodes) and the *drift distance* from the deflector to the ionizing beam was designed for experiments on helium beams with velocities >3 and >4 times greater than argon and krypton beams, respectively. Future experiments are planned with a modified deflector and drift distance to study deflected molecules in argon and krypton.

With the current experimental geometry, the most effective experiments we can carry out using argon and krypton are based on *Stark removal* from the beam axis. As highlighted in section 8.1, this can be a powerful method to trace product ions to different neutral precursors in a mixed beam. For the first time, this thesis shows that the relative populations of isolated and clustered nucleobases (uracil and thymine) can be modified using Stark deflection. In the absence of significant background signals, this can enable fragment ions to be traced to isolated molecules, clusters, or a combination of both. In the case of uracil, it is interesting that the m/z 84 ion signal was removed from the centre of an argon beam by a deflecting field of 72-108 kV/cm with equal efficiency (to within experimental uncertainties) as the uracil$^+$ signal. This shows that any production of the m/z 84 ion from multi-photon ionized pure uracil clusters must be very weak. The result appears to be consistent with the fact that the most stable

uracil dimer configuration features hydrogen bonding on either side of the expected ring-opening position in electronically-excited uracil [Ding et al. 2015, Nachtigallová et al. 2011, Richter et al. 2014]. Local intermolecular bonding of this kind can reasonably be expected to have a significant effect on this radiation damage process, while competition with efficient proton transfer in the excited hydrogen-bonded dimer [Liu et al. 2008] is also expected to play a role. However, further deflection experiments in stronger clustering conditions are required to assess whether or not weak production of m/z 84 ions is possible from hydrogen-bonded clusters.

8.3 Outlook

The results in this thesis add to our detailed understanding of how uracil and thymine respond to UV irradiation in wavelength range 220-230 nm. Some of the new information, for example the identification of specific fragment ions, can be directly useful in models of radiation damage in biological environments or astrochemical environments. However, the most interesting results require further investigation to attain definitive interpretations. Similarly, the development of the OU laser thermal desorption source and our advances in Stark deflection of CW beams are most exciting when considered in terms of the opportunities they open for future experiments. I particularly recommend the following activities to extend my PhD research.

1) The specific neutral excited state process responsible for the CO loss channel from multi-photon ionized uracil has not yet been identified. One possibility is a ring-opening process in a long-lived triplet state (or at the CI from such a state to the electronic ground state). This hypothesis can be tested in time-resolved experiments that extend to longer delay times than the Heriot-Watt measurements (ns delays and

longer). As a first test, the Molecular Clusters Group plans to run pump-probe measurements using two ns lasers with a variable delay.

2) Further evidence is required to test our interpretation of the photon energy thresholds for HNCO loss from multi-photon ionized uracil and thymine. A simple approach that does not require new experimental developments will be to look for comparable threshold behaviour in the metastable dissociation of molecules with different neutral excited state energies.

3) The LTD source can be exploited to study how specific processes in biomolecular subunits evolve when that subunit is integrated into sequentially more complex biomolecules. Naturally, the most important fundamental processes from the applied perspective will be those that are not significantly quenched within larger biomolecules. A particularly interesting process to investigate will be possible CO loss from multi-photon ionized uridine (the RNA nucleoside containing uracil). The Group is currently performing experiments of this kind and has acquired a compact pulsed YAG laser from the University of Iceland to bring nucleotides and even larger DNA/RNA subunits into the gas-phase by laser induced acoustic desorption (LIAD).

4) A shorter Stark deflector will be built and the mass spectrometer system will be brought to a new position just ~10 cm after the deflector. This will enable a systematic study of the Stark deflection profiles of biomolecules (notably nucleobases) and their clusters in argon beams. The reduced length of the experiment and the reduced velocity of the molecules in argon compared with helium will help to achieve good signals. Once satisfied with the deflection and the signal intensity, the Group will work on adapting their low-energy electron beam system for the new experimental geometry. The aim will be to carry out the first electron attachment experiments on Stark selected molecules and clusters.

References:

- B. Barc, M. Ryszka, J. Spurrell, M. Dampc, P. Limão-Vieira, R. Parajuli, N. J. Mason and S. Eden, *J. Chem. Phys*., 2013, **139**, 244311.
- S. De Camillis, J. Miles, G. Alexander, O. Ghafur, I. D. Williams, D. Townsend and J. B. Greenwood, *Physical Chemistry Chemical Physics*, 2015, **17**, 23643-23650.
- F. Filsinger, J. Küpper, G. Meijer, J. L. Hansen, J. Maurer, J. H. Nielsen, L. Holmegaard and H. Stapelfeldt, *Angew. Chem. Int. Ed*., 2009, **48**, 6900-6902.
- H. W. Jochims, M. Schwell, H. Baumgärtel and S. Leach, *Chem. Phys.*, 2005, **314**, 263-282.
- N. J. Kim, Y. S. Kim, G. Jeong, T. K. Ahn and S. K. Kim, *Int. J. Mass Spectrom.*, 2002, **219**, 11-21.
- M. Liu, T. Li, F. Sedinam Amegayibor, D. S. Cardoso, Y. Fu and J. K. Lee, *J. Org. Chem.,* 2008, **73**, 9283-9291.
- D. Nachtigallová, A. J. A. Aquino, J. J. Szymczak, M. Barbatti, P. Hobza and H. Lischka, *J. Phys. Chem. A*, 2011, **115**, 5247-5255.
- M. Richter, S. Mai, P. Marquetand and L. González, *Phys. Chem. Chem. Phys.*, 2014, **16**, 24423-24436.
- M. Ryszka, Radiation Induced Processes in Biomolecules and Clusters in Controlled Beams, Department of Physical Sciences, The Open University, Milton Keynes, United Kingdom, *PhD thesis*, 2015.
- S. Trippel, Y. P. Chang, S. Stern, T. Mullins, L. Holmegaard and J. Küpper, *Phys. Rev. A,* 2012, **86**,033202.